Théorie de perturbation à N corps de Bogolioubov pour les noyaux : Génération et évaluation automatique des diagrammes et premiers calculs ab initio

Pierre Arthuis

DE LA RECHERCHE À L'INDUSTRIE
cea

UNIVERSITÉ PARIS SUD
Comprendre le monde, construire l'avenir®

Thèse de doctorat de l'Université Paris-Saclay préparée à l'Université Paris-Sud

École doctorale n°576 PHENIICS
Particules, Hadrons, Énergie, Noyau, Instrumentation, Imagerie, Cosmos et Simulation

Spécialité de doctorat :
Structure et réactions nucléaires

par

M. Pierre Arthuis

Bogoliubov Many-Body Perturbation Theory for Nuclei: Systematic Generation and Evaluation of Diagrams and First *ab initio* Calculations

Thèse présentée et soutenue à Gif-sur-Yvette, le 27 septembre 2018.

Composition du Jury :

M. Denis Lacroix	Directeur de Recherche UPSaclay, IPN Orsay	Président du jury
M. Piotr Piecuch	University Distinguished Professor Université d'État du Michigan	Rapporteur
M. Carlo Barbieri	Reader Université du Surrey	Rapporteur
M. Robert Roth	Professor Université de technologie de Darmstadt	Examinateur
M. Jean-Paul Ebran	Ingénieur de recherche CEA, DAM, DIF	Examinateur
M. Thomas Duguet	Professeur, ingénieur de recherche UPSaclay, IRFU, CEA	Directeur de thèse

À mes grands-parents,
À René et Gundel Blondel,

Acknowledgements

As you are about to start reading this section of the manuscript, please let me start with an apology. The language used to write these acknowledgements will indeed vary between English and French, and the reader looking for a clear structure and progression might get upset. I invite them to be patient, and hope the rest of this work will reach their expectations. As the acknowledgements traditionnally are a much more relaxed section of the manuscript, especially maybe in France, I would like them to be as the discussions I had with the people cited below: often informal, sometimes messy, and always full of life.

Because some form of protocol always subsists, let me first thank the members of the jury. May Piotr Piecuch be thanked for accepting to be available at 5 in the morning to cope with the busy schedule of the lecture halls in Saclay, his numerous constructive remarks and his continuous enthusiasm. I would like to thank Carlo Barbieri for crossing the Channel to take part in my defense and allowing me to cross the Channel as well, though in an opposite direction, to work with him for the next two years, even after a ten-minute video feed break during the interview. I hope our ongoing project will meet our shared expectations. Crossing in his case not the Channel but the Rhine, a warm thank you to Robert Roth for accepting to be part of my jury, but most and foremost for two years of collaboration, his always warm welcome in Darmstadt, his sushi-related knowledge and the numerous discussions on various matters. Now moving to the French members of the commitee, a big thank you to Denis Lacroix, for numerous conversations in various occasions over these three years, as well as offering me the first opportunity to present my work during a workshop in Trento, in April 2017. Even though he is just credited as 'examinateur' for administrative reasons, a very warm thank you to Jean-Paul Ébran, my co-supervisor. Though the evolution of this project had me moving away from the originally intended Energy Density Functional application, thus limiting our collaboration to more restricted occasions, I really appreciated all the time we spent together, from this memorable two-day session to figure out the properties of Time-Structure Diagrams to this moving-out and -in session in the Essonian suburbs, not to forget numerous (possibly gossipy) discussions. May his unstoppable energy radiates around him, in B3 and elsewhere.

Finally, a very particular thank you to Thomas Duguet. One always says that the relationship between a student and their PhD supervisor is one of its kind, and now I can say that it is true indeed. Thank you for trusting me in the first place though my curriculum was kind of odd and the forced leap year was not helping, and then figthing to get the funding (I am not forgetting Jean-Paul nor Valérie for that matter, but we will come back to that) and giving me a taste of many-body theory even before I could start at the ESNT workshop on near-degenerate systems, though I must confess I did not understand much (if any) of it at the time. Thanks for those three years of working together, for accommodating to my odd working process of asking only few questions, and in the end showing me that it was possible to work with someone efficiently while sometimes having divergences but being able to overcome them. Those who have known me for long know I had my share of troubles with team-working before. Thanks for this week

of teaching-training in Grenoble, which really helped me approach both science and teaching from a new perspective, while enjoying pizzas and discussions along the Isère river. Thanks for the countless political, philosophical or sports-related discussions, up to the point that we sometimes did not start working before lunch. You helped make Saclay a second home for me, and it was at once all that and more than what I needed. I am confident our paths will cross again, be it in a scientific context, or, even better, a less formal one.

Let us now go on with acknowledgments in English. My first thoughts and thanks are for Hans-Werner Hammer, who was the first to give me a chance, when I was just a young physics student from an "engineering school", which of course seems odd to anyone but a Frenchman. A warm thank you to the members of his group, with whom I always enjoy having a Nougattaller when visiting Darmstadt, especially Artëm, Fabian and Marcel. Thank you to Bira van Kolck as well, who discussed the possibility of having me as a student when I came back from Darmstadt, even though the fundings where lacking in the end. Both Hans-Werner and Bira encouraged me to stay in the field, and my decision to do so eventually was influenced by such kind support. A warm thank you to Heiko Hergert for his kindness, his availability despite the jetlag and several warm discussions, either in Gif-sur-Yvette, in Darmstadt or in Vancouver, may they have been centered on many-body methods or Michael Schur sitcoms. Thank you to Achim Schwenk and Kai Hebeler, as well as all the members of their group, for welcoming me in Darmstadt for a seminar at the beginning of the year and discussing my projects with me. Thank you to Petr Navratil and Jason Holt for having me at the TRIUMF workshop in Vancouver, and particularly to Jason and Hope for welcoming us at home. A kind thought for Gaute Hagen and his life-and-death lessons looking over the city from the 12th floor. Thank you to Bruce Barrett and Marek Ploszajczak for their workshops in GANIL and the friendly and active atmosphere there then. A warm thank you to Tomás Rodriguez, Luis Robledo and Alfredo Poves for the organization of the Gogny Conference in Madrid and their warm welcome there. Not everyone can claim to have witnessed Luis mastering table football, and I am among the lucky ones.

A warm thank you to my new colleagues at University of Surrey for their welcome as I am writing these acknowledgements a few weeks after my start in Guildford. Apart from Carlo Barbieri, already metionned, a big thank you to Arnaù Rios for his optimistic spirit and the help provided with settling on the first few days after my arrival. Thank you to Kai Wen for his energy, his tips for living around Guildford and a sociable atmosphere in our shared office. Thank you to Chris Mc Illroy for allowing me to keep doing desperate PhD students joke even now that I am a postdoc. Thank you to James Keeble for sharing the social media exposure with me on our first day in the group and taking the spot of the indispensable PhD student of the group. Thank you to Natasha Timofeyuk for the help organizing our visit with Mehdi in July and knowledge of the Guildford area. Thank you to Paul Stevenson for playing the tough role of the mean field practitioner in an overwhelmingly *ab initio* group. And finally, thank you to Joanna Moore and Natasha Fey for keeping everything moving around here and the help around the University on my first few days.

A deep and sincere thank you to the people taking time to organize summer (or not) schools for physics students and teaching there. So thank you to Jacek Dobacewski, Allessandro Pastore, Nicolas Schunck and Andrea Idini for the TALENT school on Energy Density Functionals in York, and managing to set up three weeks so intense and so friendly at the same time. Thank you to Omar Benhar and Georges Ripka for the Doctoral Training Program in Trento,

and particularly Georges for numerous relaxed discussions, sassy comments and a memorable pizza-eating session. Thank you to the organizers of the Paris-Saclay HPC training program for three intense and productive weeks. Finally, thank you to Angela Bonaccorso and her colleagues for organizing the Galileo Galilei Institute school in Florence. Being able to learn in such an environment was a chance rarely seen.

Finally, a warm thank you to all the people I have met and chatted with during workshops, schools or seminars: Kristina Liautey, Jutta Escher, Paul Fanto, Jerry Yang, Baishan Hu, Patrick Reinert, Dean Lee, Sebastian König, Andreas Ekström, Christian Forssen, Daniel Gazda, Harald Griesshammer, Manuel Pavon Valderrama, Kevin Fossez, Jimmy Rotureau, Ania Zdeb, Ruchi Garg, Claudia Gonzales-Boquera, Archana Saxena, Pawel Baczyk, Kyle Godbey, James Curbiss, Matthew Shelley, David Muir, Pierre Becker, Tiia Haverinen. Though I am definitely forgetting some of them here, I hope they will forgive me.

And now, my apologies to the non-French-speaking readers, as one moves from English to French. Comment en effet remercier aussi bien les gens que dans leur langue maternelle ? Si certains ont déjà eu le droit à leur lot de louanges en anglais pour des raisons protocolaires (on ne se défait pas des traditions pour quelque chose d'aussi sérieux que des remerciements de thèse), il est temps pour tous les autres d'obtenir leur dû. Et par qui commencer, si ce ne sont les membres du groupe de théorie du DPhN (SPhN, comme on disait de mon temps !). Nous commencerons par renvoyer le lecteur avide de compliments sur Thomas Duguet à chausser son meilleur anglais et se référer aux paragraphes précédents. A partir de là, commençons par proximité géographique. De francs et chaleureux remerciements à Mehdi Drissi donc, mon compagnon de joies et de peines pour ces trois ans en pièce 103 A, pour avoir réussi à supporter mes obsessions, ma maniaquerie et mon rapport parfois assez distendu à la rigueur mathématique. Trois ans de complicité et de proximité dupond-et-dupontesque qui en ont déconcerté plus d'un, malgré quelques mois de retraite tactique et spirituelle du jeune homme en salle 45 pour sa rédaction, et qui devraient continuer puisque l'histoire aura voulu que nous partagions encore un bureau pour notre premier post-doc. Mehdi aura beau jeu d'affirmer que c'est moi qui l'y ait suivi puisqu'il a été accepté en premier, les données de l'université du Surrey pourront prouver que j'avais déposé ma candidature avant lui !

Éloignons-nous un petit peu et traversons le couloir pour remercier Vittorio Somà. L'accent a son importance, bien qu'il aura la gentillesse de ne pas vous le faire remarquer. Si Thomas est l'élément flamboyant du groupe, Vittorio vient y apporter l'équilibre par son calme et sa douceur jamais remis en cause. Merci à lui pour sa patience, sa présence et sa disponibilité indéfectibles et son humour. Un peu plus loin, autre bureau. Let's switch back to English to thank warmly Alexander Tichai, as he keeps trying to convince all of us he cannot speak French, even though he is probably now the französichste Deutscher I might know (and I've known a pretty Frenchish Saarländer). His arrival in the group made my work in Saclay on this project go from a mainly bilateral relation with Thomas to a real team work, only for the best. But most importantly, offered me the possibility to abuse his stock of free, good freshly-ground coffee as well as an opportunity to fight what could only be described as Thomas' skepticism towards Germany. Additionally to a lot of friendly (and sometimes a bit boozy) conversations. Repassons en français pour le passager clandestin du DPhN, Julien Ripoche. Fraîchement débarqué (échappé ?) de Bruyères avec sa bonne humeur et son énergie à toute épreuve, son amour de la chanson, ses accueillants canapés et sa capacité sans cesse renouvelée pour les gaffes auront fini de parfaire l'ambiance au sein du groupe. Un grand merci à lui ! Puisque nos

chemins se sont croisés, un grand merci et bienvenue à la fois à Francesco Raimondi, qui vient renforcer le désormais célèbre contingent des italiens du DPhN. Bon courage à lui pour ces deux ans à venir, et j'espère me montrer digne du bureau qu'il m'a laissé à Guildford. S'ils ne sont arrivés que tout récemment au sein du groupe, trop récemment en tout cas pour que je ne puisse les apprécier à leur juste valeur, mes plus sincères encouragements vont à Mikaël Frosini et Pepijn Demol pour la lourde tâche qu'ils s'apprêtent à affronter. Enfin, finissons par remercier celle qui est membre honoraire du groupe de théorie de structure nucléaire, Egle Tomasi, qui a tenu à merveille sur ces trois ans son rôle d'attentive grand-mère catholico-syndicaliste, depuis le prêt de plaques de cuisson jusqu'aux petits cadeaux de retour de voyage. Merci à elle pour tout ça, pour les nombreuses discussions scientifiques ou politiques et les histoires de famille !

S'ils ont quitté le groupe de théorie, ils sont toujours présents dans nos cœurs. Un fraternel remerciement à Benjamin Bally et Marco Martini, nos deux vaillants post-docs ESNT de la promotion 2015. Merci à Marco pour sa présence souriante et chaleureuse, sa bonhomie et son incroyable capacité à être connu de l'ensemble des chercheurs rencontrés sur le plateau de Saclay et ailleurs. Merci à Benjamin pour ses saillies, sa mégalomanie[1] et ses nombreuses visites en 103A, parfois agaçantes, très souvent excuse bien commode pour arrêter de travailler une demie-heure (voire plus dans les grands jours) et avant tout occasion de poser les questions naïves que nous, jeunes première année complexés, n'aurions osé poser à quelqu'un d'autre. Il aura joué ce rôle de grand frère astucieux et magouilleur durant mes débuts au DPhN, depuis le couloirs du 703 jusqu'aux abord du château de Trente en pleine nuit, et avouons que c'était bien pratique, que ce soit pour enfin comprendre cette histoire de variation après projection ou pour exfiltrer une agrafeuse du LSCE. Pour finir, il m'aura permis d'accomplir le rêve de tout thésard en insérant une mention "Private communication" dans la présentation de ma soutenance.

De chaleureux remerciements, ensuite, pour la double colonne vertébrale du DPhN, à savoir Danielle Coret et Isabelle Richard. Si l'on sait qu'il n'y a pas de science sans cité scientifique, il n'y a pas de cité scientifiques sans elles. Un grand merci à elles, pour les nombreuses requêtes administratives ou autres, les nougats et les bonbons, et qu'elles se rassurent, j'ai toujours des pâtes dans le placard au cas où, et oui, ce manuscrit finira bien par être imprimé un jour. Merci également à Patrick Champion pour son travail de l'ombre à maintenir le DPhN en état de marche, à Valérie Payeton pour son travail pour la formation et son aide pour les posters. Une pensée sincère pour tous les employés d'entretien et de ménage anonymes qui font en sorte que la ruche du CEA puisse travailler dans de bonnes conditions. Merci également aux directions passées et présentes du DPhN, Héloïse Goutte, Jacques Ball, Franck Sabatié et Christophe Theisen, pour les discussions occasionnelles et avoir fait en sorte, et le faire encore, que tout ceci soit possible. Je me permets, entorse à l'organigramme, d'associer à ce petit monde Valérie Lapoux, au co-pilotage de l'ESNT. Merci beaucoup à elle pour son énergie inégalée, son rôle joué dans l'obtention de mon financement COPHYNU et les chocolats Antton ramenés de congés. Enfin, merci aux gens de Bruyères, en particulier Éric Bauge et Stéphane Hilaire, pour avoir rendu cette thèse possible. J'espère que la qualité de ce manuscrit rachètera à leurs yeux mon faible nombre de visites à B3.

Mais le DPhN n'est pas peuplé que de théoriciens de structure nucléaire ou assimilés ou de son équipe de direction (et assimilés). Un chaleureux merci donc à Diane Doré, qui aura

[1] J'invite les lectrices et lecteurs interloqués à aller lire le manuscrit du sieur Bally.

bien voulu accepter le rôle ô combien ingrat et flou de "tutrice DPhN", et qui aura en plus eu l'élégance de l'assumer avec la gentillesse et la douceur qui la caractérisent, à coup de petites discussions informelles par-ci par-là. Merci à Nicole D'Hose pour les nombreuses discussion pleines d'humour en salle café autour de la petite bande des thésards et post-docs du LSN. Merci à Hervé Moutarde pour les rencontres en salle café (décidément), les sympathiques taquineries sur la longueur des présentations de Nabil et la promotion de l'humour gotlibien. Merci à Maxime Defurne pour les astuces pour se faire rembourser ses vacances par l'ACAS, et l'espoir donné à toute une génération de pouvoir être recrutés après une thèse. Merci à Antoine Drouart pour sa permanente énergie, son sens de l'humour et la galette des rois. Merci à Anna Corsi et Alain Gillibert pour les innombrables discussions autour du repas, leur optimisme indéfectible, leurs renseignements sur les environs palaisiens et leur éternelle bonne humeur. Merci à Thomas Materna pour les discussions sur la Belgique et la Pologne et les "Il reste du café ?". Merci à Alexandre Obertelli pour les séances de théorie quantique des champs. Merci à Anthony Marchix pour sa sympathie douce et calme, à Barbara Sulignano pour son énergie, à Marine Vandebroucke pour son éternel sourire, à Wolfram Korten pour sa présence apaisée, à Franck Gunsing pour sa gentillesse réservée.

Comment ne pas mentionner maintenant la joyeuse bande de thésards et post-docs du DPhN, auto-proclamés "précaires" désormais ? Un grand merci à Jason Hirtz, à l'origine de tout ce bazar, pour son humour, son appétence pour les pauses l'après-midi et ses alcools maisons. Merci à Loïc Thulliez pour être parti puis revenu, son optimisme, ses plantes vertes et son rire passé trois verres. Merci à Aurélie Bonhomme pour nos chemins de thèse en commun, de la signature simultanée de nos contrats jusqu'à l'organisation partagée de nos pots de thèse, sa gentillesse, son rire un peu gêné, ses dessins sublimes et les tartines biocools à Anthony. Merci à Tino pour l'accueil lors de la dégustation des dites tartines biocools. Merci à Raphaël Briselet pour les nombreuses discussions sur HFB et les discussions encore plus nombreuses sur les jeux vidéos ou le communisme, et ses nombreuses joutes politico-oratoires avec Benjamin. Merci à Nabil Chouika pour sa présence calme, son rire éclatant, la devise de la France, les soirées dans son appart à Anthony et les bouteilles de cidre. Merci à Valérian Sibille pour son intransigeance, les burgers bostoniens, l'aide pour la vidéo-conférence en amphi Bloch et la coopération interculturelle. Merci à Georg Schnabel pour son éternelle joie de vire, son français impeccable et les pas de danse sur du Schlager. Merci à Nancy Paul pour les nombreuses discussions pleines de rires, les réflexions sur la famille et les enfants, les chants de Noël au clavier dans un appartement essonnien, la petite Marie-Hélène dans mes bras et m'avoir montré que les républicains catholiques de Pennsylvanie rurale sont des gens fréquentables. Merci à Simon Bouteille pour les échanges sur les modules PHENIICS lors de trajets en bus et les répétitions de soutenance. Merci à Michal Rapala pour les discussions rugbystiques autour de l'espoir avorté de reprendre en corpo, les trajets en commun dans le 91.06 et les chocolats polonais. Merci à Antoine Vidon pour sa sassyness, les séances de thérapie assis dans son bureau avec un thé et les histoires de date improbables. Merci à Saba Ansari pour son sourire et son allemand bien meilleur qu'elle ne veut l'affirmer. Merci à Alessandro Minotti pour les nombreuses bières, les échanges pleins d'humour et une mémorable tentative de soirée à la maison de l'Inde de la Cité Universitaire. Merci à Michalina Komorowska pour les échanges trop peu nombreux à se plaindre du MOOC PHENIICS. Merci à Christopher Filosa pour sa veste de sapeur, les memes hamonistes, les réflexions sur le pastis, les emballages en slides de conférence sur la muographie et le service de livraison de Micromegas à domicile. Merci

à Benjamin Magnin pour les réflexions sur les RPG et les trajets en 106 Kid. Merci à Yelei Sun et Hongna Liu pour leur gentillesse discrète et un mémorable attrapage de RER au sortir du déménagement de Nancy. Merci à Guillaume Christiaens pour les discussions au long de ses aller-retours d'expérimentateur en co-tutelle. Merci à Adrien Blanchet pour son humour et les bons plans pour voir Franck Lepage, auxquels je n'ai malheureusement jamais donné suite. Merci à Marco Meyer pour son calme serein et son contrepoint apaisant à l'énergie d'Antoine. Merci à Nicolas Pierre pour sa maîtrise du sel et son contrepoint énergique au calme d'Antoine. Merci à Charles-Joseph Naïm pour sa présence sereine et un retour mémorable à pied à travers le plateau enneigé en commun avec Marco et Mehdi. Merci à Zoé Favier pour son enthousiasme, les trajets en bus vers Gif et l'orga bienvenue pour les cadeaux de thèse de Mehdi. Merci à Andreina Chietera pour son accent italien et les 25 degrés dans son bureau partagé avec Christopher. Merci à Jinesh Kallunkathariyil-Sebastian pour les échanges entre ses allers-retours au GANIL et son éternel sourire. Merci à Arkadiusz Trawinski pour son enthousiasme à s'enquérir des spécificités culturelles françaises et sa bonne humeur. Ma capacité à socialiser et les contraintes de la dernière année de thèse étant ce qu'elles sont, mes échanges auront été plus limités avec pas mal des derniers arrivés au sein du département. Mes excuses et mes remerciements mêlés à eux donc. Qu'ils soient sûrs que j'ai apprécié les discussions que nous avons pu avoir autour d'un déjeuner du vendredi. Et à tous ceux que j'aurais pu oublier, mes excuses les plus sincères.

Plus bas dans la vallée, un grand merci à tous les gens de l'IPN Orsay pour leur accueil régulier et les discussions occasionnelles. Si Denis Lacroix et Bira van Kolck ont déjà été cités précédemment, que Marcella Grasso soit remerciée pour sa sympathie, et avoir permis elle aussi, en sa qualité de co-organisatrice, ma participation à ce tout premier workshop à Trente. Merci à Jérémy Bonnard pour les échanges au détour de workshops. Merci à David Régnier pour les conversations diverses et son désespoir rieur à attendre la poster session d'une conférence SSNET à laquelle l'équipe de Saclay s'était rendue en toute discrétion. Mais la fission ne vent pas autant que la structure cristalline des noyaux apparemment. Merci à Guillaume Hupin pour les innombrables commentaires acerbes, les parts de pizza au détour d'un déménagement et les verres de vin chaud en période de Noël. Merci beaucoup à Monsieur Pierre, à savoir Petar Marevic, pour son élégance à toute épreuve, son admirable volonté de maîtriser les réflexions françaises les plus vulgaires et ne pas m'avoir laissé seul dans le club des daltoniens. Merci à Antoine Boulet pour son auto-dérision, son anglais irréprochable et ses talents de mime. Merci beaucoup à Olivier Vasseur de venir apporter une contrepartie apaisante et rationnelle au bouillonnement d'Antoine. Un immense merci enfin à Raphaël-David Lasseri, pour son énergie déconcertante, sa curiosité insatiable, les discussions innombrables sur tous les sujets, le trajet en commun un jour de déménagement, le barbecue à Palaiseau, le discours de remerciements post-soutenance. J'espère que nos trajectoires seront amenées à se recroiser dans le futur.

Parmi les quelques francophones non encore nommés, merci à Maxime Mougeot pour les longues marches de nuit et de jour à York, les discussions sur le couple, la famille et l'immobilier britannique, les bières descendues au pub et ce mémorable moment à attendre la fin d'une averse interminable sous l'abri bien fragile d'un arbre en bord d'Ouse, face au Millenium Bridge. Merci à Marc Verrière pour son enthousiasme, ses précieux conseils Python et C++, son anglais sans peur et sans reproche et sa gentillesse. Merci au petit comité de Bruyères à la Gogny conference, Nathalie Pillet, Marc Dupuis, Rémi Bernard, Guillaume Blanchon et évidemment Stéphane Hilaire pour les discussions dans les bars madrilènes. Merci à Sophie Péru pour les

discussions régulières au fil de ses visites à Saclay pour travailler avec Marco Martini. Merci à Adeline Ébran pour son accueil et sa gentillesse.

Au-delà de la communauté scientifique, cette thèse n'aurait pas été possible sans le soutien de mes proches. Un grand merci à mes parents pour avoir toujours cultivé ma curiosité et m'avoir offert la possibilité de mener mes études telles que je le voulais, y compris au fil de quelques changements de plan auxquels ce double-diplôme en Allemagne ne fût pas étranger ou de cette année vide entre mon retour de Darmstadt et le début de cette thèse. Une pensée bien évidemment pour mes grands-parents, eux-mêmes à l'origine de cette trajectoire familiale. Un grand merci à mes frères, Louis et Charles. Si mes études nous ont mené à passer peu de temps ensemble, je suis fier de pouvoir me dire le grand frère de ces deux jeunes adultes drôles, intelligents et pleins d'humanité, bien que ma contribution à tout cela soit plus que limitée.

Une thèse peut-elle se traverser sans le soutien et la présence inconditionnels de vieux amis ? Rien n'est moins sûr, aussi je veux exprimer ici ma gratitude à Alexandre, Hervé, Jéromine et Philippe. Que notre petite bande ait tenu des bancs du collège Paul Éluard jusqu'à aujourd'hui en dit long, je crois, sur notre capacité à rester proches malgré les années et les kilomètres. A Julien, je veux dire combien je suis sincèrement désolé de toujours le rappeler avec plusieurs semaines de retard, et combien je le remercie de ne jamais s'en effaroucher. A tous les amis rencontrés par la suite, que ce soit à Saint-Louis, à Nantes, à Darmstadt, sur Twitter ou en manif, et que je ne listerai pas ici autant par concision que pour laisser croire que je suis un être profondément sociable, je veux dire merci. Mes dispositions naturelles à ne pas donner de nouvelles ne ce sont en rien améliorées avec la thèse, et je sais à quel point cela peut être agaçant. A ceux que je vois régulièrement, qui m'ont soutenu ces dernières années, voire ont même pris la peine de bouleverser leur planning pour venir assister à ma soutenance, un immense merci et toute ma reconnaissance. A ceux avec qui le contact a été plus distant, mes plus sincères excuses et le vœu que le futur puisse nous amener à nous recroiser plus régulièrement et rattraper le temps perdu.

Enfin, pour finir, un immense merci à Pauline pour ces dix années passées à mes côtés. A elle qui a su supporter mon indisponibilité en prépa, la distance à Nantes puis en Allemagne, et mon air renfrogné la plupart du temps, merci pour sa gentillesse, sa patience et sa magnanimité. Drôle de couple que celui formé par une musicienne toujours occupée le week-end et un scientifique toujours à l'étranger. Mais s'il a su survivre à dix ans de distance et d'incertitudes, j'ose espérer qu'il tiendra de nombreuses années encore. Merci à toi pour tout.

Contents

Introduction

0.1. State of the art and challenges of nuclear physics

A common misconception about nuclear physics is that, more than forty years after the Nobel Prize awarded to Bohr, Mottelson and Rainwater, the field now consists only of applied work. The truth is that the detailed properties of nuclei are still not fully understood, and nuclear physics has recently undergone major changes both from a theoretical and an experimental point of view.

A first specificity of the nuclear system is that the internucleonic force driving the construction of nuclei cannot be derived directly from Quantum Chromodynamics (QCD). Though attempts at connecting the nuclear interaction to QCD through lattice calculations are being made [1, 2, 3], results of physical relevance are still to be obtained. Thus, more phenomenological or effective methods are used to perform actual calculations. Additionally, the structure of the nuclear interaction itself, i.e. central, spin-orbit, tensor, quadratic spin-orbit, etc., terms, is particularly complex. Furthermore, there are two sources of non-perturbative character. The strong short-range repulsion associated with interpenetration of nucleons generates an ultraviolet source of non-perturbativeness. The large scattering lengths associated with the existence of a weakly bound proton-neutron state (i.e. the deuteron) and of a virtual di-neutron state induces an infrared source of non-perturbativeness. Additionally, the treatment of nucleons as point-like particles require three-nucleon-, four-nucleon-, etc., forces to be consistently considered. Various investigations over the past two decades came to reinforce this statement, as they focused on differential nucleon-deuteron cross-sections [4, 5, 6], triton and light-nuclei binding energies [7], the Tjon line [8], the violation of the Koltun sum rule [9] or the saturation of symmetric nuclear matter [10, 11, 12, 13, 14, 15] related to the Coester line problem [16, 17, 18].

Another problem is due to the atomic nucleus as a system. Ranging from few nucleons to approximately 300 of them, most of the nuclei can be considered to be neither very-little– nor very-many-body systems. Hence, exact methods available for few-body systems find their theoretical and computational limits, while physical effects stemming from the finite size of nuclei prevent the use of statistical methods. Furthermore, a unified description of the nuclear system requires a description of close- and open-shell systems, small- and large-amplitude collective motions, interfacing structure and reaction to access spontaneous and induced fission, fusion, nucleon emission at the drip-line...

The atomic nucleus study aims at describing ground- (mass, radius, deformation, multipolar moments...) and excited-states (single-particle, vibrational, shape and spin isomers, high-spin and super-deformed rotational bands...) properties as well as their various decay modes (strong, electromagnetic and electroweak) and reaction properties (elastic and inelastic scattering, transfer and pickup, fusion...). This challenge is to be achieved over the whole nuclear chart, i.e. for the roughly 3400 nuclei observed [19] and the thousands still to be discovered. A

common effort from experimental and theoretical groups is thus critical, as a new generation of radioactive-ion-beam (RIB) facilities is being built to produce very short-lived systems, using high-precision detectors designed for low-statistics and high-noise-to-signal-ratio measurements. Such facilities, based on in-flight fragmentation, stopped and reaccelerated beams will extend the limits of our knowledge towards the drip-lines, i.e. the limits of stability against nucleon emission. Studies near the neutron drip-line especially should help understanding the conjectured r-process responsible for half of the nucleosynthesis of elements heavier than iron. Recent studies around the drip-lines have already observed a weakening of some magic numbers, and possible apparitions of others [20]. Other phenomena have been observed due to the proximity of the Fermi energy with the continuum in this area, e.g. nuclear halos [21, 22, 23, 24, 25] or di-proton emitters [26]. While experiments near the drip-lines are critical, investigations around the valley of stability remain key to understanding some processes. For example, Penning traps [27] or Schottsky spectrometry [28] precision mass measurements have refined and extended mass difference formulae [29], leading to a better understanding of pairing correlations. At the same time, the study of the first 2^+ state in even-even nuclei along with the associated $B(E2)$ transition to the ground state provide key information about the magic character of nuclei [30] while experiments dedicated to the study of rotational or vibrational bands [31], shape coexistence [32, 33], fission properties of actinides [34] or collective modes [35] remain of primer interest even near the valley of stability. Finally, the quest for superheavy elements and the island of stability beyond the $Z = 82$ magic number [36] is another attempt at expanding the limits of existence of the nuclear chart.

0.2. Recent progress of *ab initio* methods

0.2.1. On *ab initio*

While bulk properties of nuclei can be mainly described using macroscopic approaches like the liquid drop model (LDM) [37], microscopic methods are needed for a coherent description of static and dynamical properties. This leads to defining *ab initio* methods that can be characterized by a common set of properties, namely

1. They consider nucleons to be the elementary degrees of freedoms, i.e. quarks and gluons are not explicitly accounted for, such that nucleons are treated as point-like objects. At the same time, collective degrees of freedom (e.g. as done in the collective Hamiltonian model) are meant to emerge from the description of interacting nucleons.

2. They use interactions rooted in the underlying theory, i.e. Quantum Chromodynamics, to preserve the link with higher-energy physics. The current paradigm is to use interactions derived from chiral Effective Field Theory (see Sec. 4.2.1) and fitted only in the two-body sector for two-body forces, three-body sector for three-body forces, etc.

3. They expand the solution of the Schrödinger equation in a systematic way, thus providing control over the truncation of the result and an assessment of associated uncertainties.

4. The truncation mentioned before is then effected analytically at a given order, and numerical calculations are performed.

5. They eventually estimate the error on the result, coming both from the input Hamiltonian, the analytical truncation and the numerical treatment of the calculations.

All those characteristics distinguish *ab initio* methods from other approaches relying on phenomenological Hamiltonians or more collective degrees of freedom, in which the error assesment is often complicated by the fact that the method is not systematically formulated. *Ab initio* methods like Fadeev-Yakubovski [38, 39, 40], Green's function Monte Carlo [41, 42, 43], no-core shell model [44, 45, 46, 47, 48] have been limited to light nuclei up to $A \sim 12$ due to their factorial scaling. Through the development of methods scaling polynomially, the past fifteen years have witnessed a significant extension of *ab initio* methods both with respect to accessible mass numbers and to the open-shell character of the targeted system.

0.2.2. Non-perturbative methods

Approaches applicable to closed-shell systems typically start from a single-determinantal, e.g., Hartree-Fock (HF), reference state and account for *dynamic correlations* via the inclusion of particle-hole excitations on top of it. The simplest method in this context is many-body perturbation theory (MBPT). However due to the hard-core character of the nuclear Hamiltonian, it proved inefficient and was abandoned early on by the nuclear physics community.

In this context, a plethora of many-body frameworks resumming all order contributions beyond MBPT have been developed to describe medium-mass systems, e.g., coupled-cluster (CC) theory [49, 50, 51, 52, 53], self-consistent Green's functions theory (SCGF) [54, 55, 56] or the in-medium similarity renormalization group approach (IMSRG) [57, 58, 59, 60]. For doubly closed-shell nuclei, all of these non-perturbative methods agree well with quasi-exact no-core shell model (NCSM) calculations for ground-state energies of nuclei in the $A \sim 20$ regime, and are considered to constitute the reference methods for mid-mass nuclei.

Coupled-cluster theory

Coupled-cluster (CC) theory [49, 50, 61, 51, 52, 53] is based on an expansion over the reference state[1] via the exponentiation on a connected cluster operator T

$$|\Psi\rangle = e^T |\Phi\rangle \ , \tag{0.1}$$

where T is defined as a linear combination of n-particle n-hole excitations operators T_n

$$T \equiv T_1 + T_2 + T_3 + \dots \ . \tag{0.2}$$

The truncation scheme for CC consists of restricting the set of excitation operator to a certain n-particle-n-hole rank, i.e. up to a certain T_n, thus resumming infinite set of terms whose particle-hole degree is less than n. Initially formulated in nuclear physics [62, 63, 64, 65] and developed in quantum chemistry [66, 67], the method has proven succesful to describe medium-mass doubly-closed-shell nuclei, and was extended to neighboring nuclei as well as excited states through the use of Equation of Motion (EOM) techniques [52].

[1] For the sake of concision, the ingredients introduced here are only defined rigorously in the following chapter.

The extension of the CC formalism to open-shell nuclei has been made in two different ways: in a multi-reference approach with MR-CC in quantum chemistry [68, 69, 70, 71, 72], as well as using symmetry-adapted formalisms for quasi-degenerate systems [73, 74, 75], or more recenty in a symmetry-breaking-and-restoring approach with Bogoliubov CC, which breaks either the symmetry associated to the angular momentum [76] or to the particle number [77]. The only available calculations so far have been made in small model spaces and for two-body-only interactions without symmetry projection, though [78]. The spin-projected CC version of this formalism [76] has been transferred and implemented successfully on the Hubbard model and on molecule dissociation [79]. The particle-number-projected BCC method is currently been (succesfully) tested on the schematic pairing, or BCS, Hamiltonian problem [80].

In-medium Similarity Renormalization Group

As suggested by its name, In-Medium Similarity Renormalization (IMSRG) [57, 58, 59, 60] is an approach based on the very idea behind the use of Similarity Renormalization Group (SRG) [81, 82, 83, 84, 85, 86, 87] in nuclear physics, i.e. the use of a continuous unitary transformation

$$H(s) = U(s)H(0)U^{\dagger}(s) \tag{0.3}$$

driving the Hamiltonian, or any other operator, towards a band-diagonal structure with respect to a given basis as exemplified in Fig. 0.1. Coupled to the use of normal-ordered operators that recast higher-body forces at low level via density matrices, which explains the naming In-Medium SRG. Eventually, the transformation decouples the reference state from its particle-hole excitations, such that the flowing Slater determinant is mapped onto the exact eigenstate of the original Hamiltonian at the end of the flow.

IMSRG was then extended to open-shell nuclei by the incorporation of multi-determinantal reference states in the Multi-Reference IMSRG (MR-IMSRG) [88]. The first MR-IMSRG applications used particle-number-projected (PNP) HFB states [89, 90, 88]. More recently, solutions of no-core shell model (NCSM) calculations [48, 85, 91] in a small model space were employed, leading to the so-called in-medium no-core shell model (IM-NCSM) [92], and proof-of-principle calculations with angular-momentum projected HFB states were presented in [93].

Self-Consistent Green's Function

Self-Consistent Green's Function (SCGF) [54, 55, 56, 94] recast the information on the many-body system into a set of k-body ($k \leq A$) Green's function. In particular, the one-body Green's function or propagator carries information regarding the total ground-state energy, one-body observables, the spectroscopy of a $A \pm 1$ system as well as elastic nucleon-nucleus scattering. In its symmetry-conserving Dyson formulation, many-body correlations are included by solving iteratively the Dyson equation relating the unpertubed propagator and the dressed or correlated propagator via the so-called one-nucleon self-energy. The Dyson equation is represented diagrammatically in Fig. 0.2. Part of the correlations are thus iteratively integrated into the reference state. Solving this non-linear equation corresponds eventually to resumming an infinite series of terms involving the self-energy, i.e. an infinite series of many-body perturbation theory diagrams.

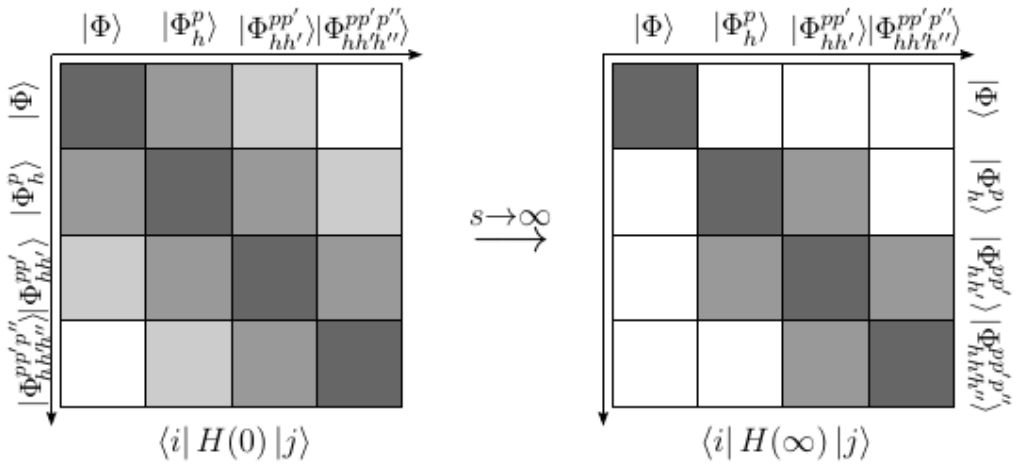

Figure 0.1. Schematic view of IMSRG decoupling in a many-body Hilbert space spanned by a Slater determinant reference $|\Phi\rangle$ and its particle-hole excitations $|\Phi_{h\ldots}^{p\ldots}\rangle$. Taken from Ref. [93].

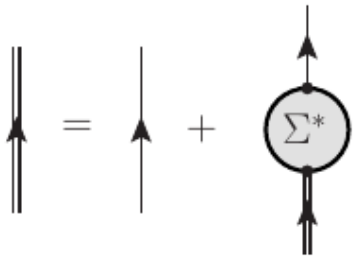

Figure 0.2. Diagrammatic representation of the Dyson equation. Single lines with an arrow represent the unperturbed propagator, double lines are the fully dressed propagator and Σ^* is the self-energy. Adapted from Ref. [94].

SCGF was the first *ab initio* method for middle-mass nuclei to be extended to open-shell nuclei through its Gorkov implementation (GSCGF) based on the use of particle-number-breaking HFB states [95, 96] and has become a standard method for semi-magic and neighboring nuclei [97], adressing radii [98, 99] as well as spectroscopic factors or nucleon separation energy [100, 101]. Despite the success of GSCGF, a proper particle-number projected formalism still remains to be designed. Indeed, results do carry contaminations associated to the particle-number breaking, whose importance depends on the nucleus and on the observable. A this point in time the error of *ab initio* many-body calculations of mid-mass nuclei are anyway dominated by the imperfections of currently available chiral EFT Hamiltonians.

0.2.3. Many-body methods and symmetry-breaking

Historically, many-body methods based on the expansion around an unperturbed product state, or mean field, have been introduced to overcome the computational difficulties associated with the computational cost of the Configuration Interaction (CI) approach [102, 103]. Such

methods have been able, based on realistic chiral Hamiltonians, to extend their reach up to $A \sim 130$ in the past decade [53], but remained for a long while limited to doubly-closed shell (or neighboring) nuclei. Going away from nuclear shell closures, the single-determinantal description becomes qualitatively wrong because several determinants contribute strongly to a CI expansion, requiring a proper treatment of *static correlations*. In order to overcome this drawback, more general reference states are required as already alluded to above.

A first option to overcome this difficulty is to rely on multi-reference (MR) methods, accounting for the different product states contributing substantially to the wave function. This idea has been followed to develop MR-IMSRG [89, 60, 88] in nuclear physics or MR-CC in quantum chemistry [68, 69, 72]. More recently this idea was employed in the context of MBPT by employing NCSM reference states [104]. Hybrid approaches, deriving effective interactions from IM-SRG, CC or MBPT and using them in CI numerical calculations have been proposed as well[105, 60, 88, 106, 107, 108].

A second option of present interest is to exploit the concept of spontaneous symmetry breaking, breaking e.g. $U(1)$ symmetry associated to the particle number conservation in order to capture the superfluid character of singly-open-shell nuclei. Doubly-open-shell nuclei can be addressed as well via the breaking of $SU(2)$ symmetry associated to the angular momentum conservation, allowing for nuclei to deform. Breaking $U(1)$ symmetry allows one to deal with Cooper pair's instability and capture the dominant effect of the infrared source of non-perturbativeness already at the level of the unperturbed states. Doing so, the degeneracy of an open-shell Slater determinant with respect to particle-hole excitations is lifted via the use of a more general Bogoliubov vacuum and commuted into a degeneracy with respect to symmetry transformations of the group. As a consequence, the ill-defined (i.e. singular) expansion of exact quantities around a Slater determinant is replaced by a well-behaved one.

Symmetry breaking has been used for decades in the Energy Density Functional (EDF) community [109, 110, 111, 112], i.e. at the mean field level. While pioneering work based on symmetry-broken reference states was achieved within the GSCGF framework [95, 113, 96], such an idea has scarcely been employed in *ab initio* calculations. One reason is that symmetry breaking cannot actually occur in finite quantum systems, hence the explicitly broken symmetry must eventually be restored, which has been a long-standing challenge already on a formal level. Still a similar formulation led to designing the Bogoliubov CC formalism, although only proof-of-principle calculations limited to small model spaces and two-body forces have actually been performed so far [77, 78].

Once the symmetry has been broken, a well-behaved expansion can be performed, and quantities computed. Still results carry a contamination associated with the contributions to the reference state of various particle numbers. The degeneracy with respect to transformations of the $U(1)$ group must thus be lifted by restoring the symmetry. While the design of a proper symmetry-restoration protocol remains yet to be formulated within the GSCGF framework, full-fledged symmetry-broken and -restored MBPT and CC formalisms have been recently designed to consistently restore the symmetry at any truncation order [76, 77]. The spin-projected CC version of this formalism [76] has been transferred and implemented successfully on the Hubbard model and on molecule dissociation [79].

0.2.4. Resurgence of many-body perturbation theory

Standard Many-Body Perturbation Theory (MBPT) [114, 115, 61] is the simplest method able to tackle medium-mass closed-shell nuclei[2]. The idea behind MBPT is to split the Hamiltonian in two parts as

$$H \equiv H_0 + H_1 \ , \tag{0.4}$$

with H_0 being simple enough for the Schrödinger equation for the reference state

$$H_0|\Phi\rangle = \mathrm{E}_0^{(0)}|\Phi\rangle \tag{0.5}$$

to be solved exactly. Then, the exact ground-state solution of the Schrödinger equation

$$H|\Psi\rangle = \mathrm{E}_0|\Psi\rangle \tag{0.6}$$

is obtained via an expansion around the solution for H_0 in powers of the residual part of the Hamiltonian H_1. Though MBPT is simple and computationally costless compared to the non-perturbative methods described in Sec. 0.2.2, it is neither variational nor guaranteed to converge. Especially, the hard-core character of the nuclear Hamiltonian made it impossible to use in practical applications in low-energy nuclear physics.

Only recently with the development of softer Hamiltonians generated through SRG transformations taming down the ultraviolet source of non-perturbativeness was it made possible again to use it [116, 117, 104]. Soon after, the concept of multi-determinantal reference states inspired the development of a MBPT variant based on a NCSM reference state in a small model space, yielding the perturbatively-improved no-core shell model (NCSM-PT). This method has allowed the first description of medium-mass nuclei with even and odd mass numbers on an equal footing [104]. In parallel, effective interactions were derived from MBPT to be used in shell model calculations [108].

As mentioned in Sec. 0.2.3, a symmetry-broken-and-restored many-body perturbation theory was recently proposed [76, 77]. The present work focuses on its particle-number-broken version which is coined as Bogoliubov many-body perturbation theory (BMBPT). The goal is to provide a full-fledged development of the formalism and propose the first numerical application dedicated to the systematic *ab initio* study of mid-mass nuclei. Though the symmetry is restored for BMBPT in the limit of an all-order resummation, finite truncations employed in a numerical calculations still carry such contaminations. The implementation of particle-number projected BMBPT (PNP-BMBPT), which restores exactly the particle number at each order [77] is thus necessary in the long run. It will however not be discussed in the present document.

0.3. On many-body diagrammatics

Diagrams have long been used in combination with formalisms, e.g., many-body perturbation theory (MBPT), self-consistent Green's function (SCGF) theory, coupled-cluster (CC) theory,

[2]Though standard MBPT is restricted to closed-shell systems in most cases, it is known from quantum chemistry that symmetry-restricted or -unrestricted MBPT approaches can be applied to high-spin open-shell systems using unrestricted Hartree-Fock (UHF) or restricted open-shell Hartree-Fock (ROHF) reference states [61].

etc., designed to solve the many-body Schrödinger equation, be it in nuclear physics, quantum chemistry, atomic physics or solid-state physics. Many-body diagrams belong to a series of tools introduced to compute the expectation value of products of (many) operators in a vacuum state in an incrementally faster, more flexible and less error-prone way. The first step in this series relied on the introduction of the second quantization formalism that makes algebraic manipulations much more efficient than within the first quantization formalism. The next step consisted in the elaboration of Wick's theorem [118], which is nothing but a procedure to capture the result in a condensed and systematic fashion. Still, the combinatorial associated with the application of Wick's theorem becomes quickly cumbersome whenever a long string of creation and annihilation operators is involved. Furthermore, many terms generated via the application of Wick's theorem happen to give identical contributions to the end results. Many-body diagrams were introduced next to provide a pictorial representation of the various contributions and, even more importantly, to capture at once all identical contributions generated via the straight application of Wick's theorem, thus reducing the combinatorial tremendously. The procedure results (i) in a set of *topological* rules to generate all valid diagrams and (ii) in a set of *algebraic* rules to evaluate their expressions, including a prefactor accounting for all identical contributions.

While diagrams have proven to be extremely useful, their number grows tremendously when applying, e.g., MBPT beyond the lowest orders, thus leading to yet another combinatorial challenge. This translates into the difficulty to both *generate* all allowed diagrams at a given order without missing any and to *evaluate* their expression in a quick and error-safe way. Consequently, yet another tool must be introduced to tackle this difficulty. As a matter of fact, there have been several attempts to generate MBPT diagrams automatically, e.g. see Refs. [119, 120, 121, 122, 123, 124]. However, it is of primer interest to also evaluate their algebraic expressions automatically [122, 123] in view of performing their numerical implementation. Such effort has already been made in the quantum chemistry community for CC and CI [125, 126].

It happens that the past decade has witnessed the development and/or the application of new formalisms to tackle the nuclear many-body problem [95, 76, 77, 127], some of which rely on original, i.e., more general, diagrammatics [76, 77]. This profusion of methods, along with the rapid progress of computational power allowing for high-order implementations, welcomes the development of a versatile code capable of both generating and evaluating diagrams. A large fraction of the present thesis is devoted to the development of such a tool within the context of BMBPT. This relies on formal breakthrough related to the generation and evaluation of diagrams that are eventually implemented numerically.

Many-body diagrams come in various forms and flavors. First, the diagrammatic framework depends on the nature of the reference state at play in the formalism. Second, most many-body methods can be designed within a time-dependent or a time-independent formalism, eventually leading to the same result[3]. While a time-independent formalism naturally translates into time-ordered diagrams, a time-dependent formulation can be represented by a time-unordered diagrammatic, i.e., by diagrams containing an explicit integration over time variables, thus, capturing different time orderings of the vertices at once.

[3]Dealing with static properties of an isolated system, the end results are obviously independent of time.

0.4. Outline

The present document is structured as follows: Chapter 1 discusses the necessary ingredients to formulate Bogoliubov many-body perturbation theory. Chapter 2 then details the perturbation theory formalism, provides diagrammatic and algebraic results at first and second order, and establishes connections with both closed-shell many-body perturbation theory and Bogoliubov coupled cluster theory. Chapter 3 presents the code ADG that automatically generates and evaluates BMBPT diagrams at arbitrary orders and the formal objects necessary to do so. Finally, first numerical results dedicated to the *ab initio* study of mid-mass nuclei are discussed and compared with non-perturbative state-of-the-art *ab initio* methods in Chapter 4. Useful matrix elements, analytical expressions, mathematical definitions and software documentation are provided in a set of appendices.

1. Basic ingredients

Let us first introduce ingredients that are necessary to the comprehension of standard, or *diagonal* Bogoliubov Many-Body Perturbation Theory. Although pedestrian, this chapter displays definitions and identities that are crucial to the building of the formalism later on.

1.1. Hamiltonian and particle number operator

Let the Hamiltonian $H = T + V$ of the system, with T being the kinetic energy and V the potential, be of the form[1]

$$H \equiv \frac{1}{(1!)^2}\sum_{pq} t_{pq} c_p^\dagger c_q + \frac{1}{(2!)^2}\sum_{pqrs} \bar{v}_{pqrs} c_p^\dagger c_q^\dagger c_s c_r + \frac{1}{(3!)^2}\sum_{pqrstu} \bar{w}_{pqrstu} c_p^\dagger c_q^\dagger c_r^\dagger c_u c_t c_s \ , \tag{1.1}$$

where antisymmetric matrix elements of the two- and three-body interaction are employed and where $\{c_p; c_p^\dagger\}$ denote particle annihilation and creation operators associated with an arbitrary orthonormal basis of the one-body Hilbert space $\mathcal{H}_1$. The particle-number operator $A = \sum_{n=1}^{\mathrm{A}} \mathbb{1}$ takes the second-quantized form

$$A = \sum_p c_p^\dagger c_p \ . \tag{1.2}$$

We further introduce a generic operator O commuting with A and H and containing one-, two- and three-body contributions[2]

$$O = \frac{1}{(1!)^2}\sum_{pq} o^{11}_{pq} c_p^\dagger c_q + \frac{1}{(2!)^2}\sum_{pqrs} \bar{o}^{22}_{pqrs} c_p^\dagger c_q^\dagger c_s c_r + \frac{1}{(3!)^2}\sum_{pqrstu} \bar{o}^{33}_{pqrstu} c_p^\dagger c_q^\dagger c_r^\dagger c_u c_t c_s \ , \tag{1.3}$$

to be used to develop the formalism and afterwards replaced by the operator of interest.

Each term o^{kk} of the particle-number conserving operator O is obviously characterized by the equal number k of particle-creation and annihilation operators. The class $o^{[2k]}$ is nothing but the term o^{kk} of k-body character. Matrix elements are fully antisymmetric, i.e.

$$o^{kk}_{p_1 \dots p_k p_{k+1} \dots p_{2k}} = (-1)^{\sigma(P)} o^{kk}_{P(p_1 \dots p_k | p_{k+1} \dots p_{2k})} \tag{1.4}$$

where $\sigma(P)$ refers to the signature of the permutation P. The notation $P(\dots|\dots)$ denotes a separation into the k particle-creation operators and the k particle-annihilation operators such that permutations are only considered between members of the same group.

[1] The formalism can be extended to a Hamiltonian containing four- and higher-body forces without running into any fundamental problem. Also, one subtracts the center of mass kinetic energy to the Hamiltonian in actual calculations of finite nuclei. As far as the present work is concerned, this simply leads to a redefinition of one-, two- and three-body matrix elements t_{pq}, $\bar{v}_{pqrs}$ and $\bar{w}_{pqrstu}$ in the Hamiltonian without changing any aspect of the many-body formalism that follows.

[2] Higher-body operators can be employed as well. From the formal point of view, it poses no fundamental difficulty but further increases the number of terms and complexifies the bookkeeping.

The definition of matrix elements and their (anti-)symmetry properties can be given explicitly. Direct-product matrix elements are defined through

$$o^{11}_{l_1 l_2} \equiv \langle 1:l_1|O^{11}|1:l_2\rangle \ , \tag{1.5a}$$
$$o^{22}_{l_1 l_2 l_3 l_4} \equiv \langle 1:l_1;2:l_2|O^{22}|1:l_3;2:l_4\rangle \ , \tag{1.5b}$$
$$o^{33}_{l_1 l_2 l_3 l_4 l_5 l_6} \equiv \langle 1:l_1;2:l_2;3:l_3|O^{33}|1:l_4;2:l_5;3:l_6\rangle \ , \tag{1.5c}$$

where particles are explicitly labeled 1, 2, 3. Because the interaction is symmetric under the renaming of any pair of particles, it follows that

$$o^{22}_{l_1 l_2 l_3 l_4} = o^{22}_{l_2 l_1 l_4 l_3} \ , \tag{1.6a}$$
$$o^{33}_{l_1 l_2 l_3 l_4 l_5 l_6} = o^{33}_{l_2 l_1 l_3 l_5 l_4 l_6} = o^{33}_{l_1 l_3 l_2 l_4 l_6 l_5} = o^{33}_{l_3 l_2 l_1 l_6 l_5 l_4} = o^{33}_{l_2 l_3 l_1 l_5 l_6 l_4} = o^{33}_{l_3 l_1 l_2 l_6 l_4 l_5} \ . \tag{1.6b}$$

From these direct-product matrix elements, matrix elements that are explicitly antisymmetrized to the right are introduced

$$\bar{o}^{22}_{l_1 l_2 l_3 l_4} \equiv o^{22}_{l_1 l_2 l_3 l_4} - o^{22}_{l_1 l_2 l_4 l_3} \ , \tag{1.7a}$$
$$\bar{o}^{33}_{l_1 l_2 l_3 l_4 l_5 l_6} \equiv o^{33}_{l_1 l_2 l_3 l_4 l_5 l_6} - o^{33}_{l_1 l_2 l_3 l_4 l_6 l_5} + o^{33}_{l_1 l_2 l_3 l_6 l_4 l_5} - o^{33}_{l_1 l_2 l_3 l_6 l_5 l_4} + o^{33}_{l_1 l_2 l_3 l_5 l_6 l_4} - o^{33}_{l_1 l_2 l_3 l_5 l_4 l_6} \ , \tag{1.7b}$$

such that

$$\bar{o}^{22}_{l_1 l_2 l_3 l_4} = -\bar{o}^{22}_{l_1 l_2 l_4 l_3} \ , \tag{1.8a}$$
$$\bar{o}^{33}_{l_1 l_2 l_3 l_4 l_5 l_6} = -\bar{o}^{33}_{l_1 l_2 l_3 l_4 l_6 l_5} = \bar{o}^{33}_{l_1 l_2 l_3 l_6 l_4 l_5} = -\bar{o}^{33}_{l_1 l_2 l_3 l_6 l_5 l_4} = \bar{o}^{33}_{l_1 l_2 l_3 l_5 l_6 l_4} = -\bar{o}^{33}_{l_1 l_2 l_3 l_5 l_4 l_6} \ . \tag{1.8b}$$

Combining the symmetry property under the exchange of any pair of particles with the explicit antisymmetrization with respect to right indices, antisymmetry is also obtained with respect to left indices, i.e.

$$\bar{o}^{22}_{l_1 l_2 l_3 l_4} = -\bar{o}^{22}_{l_2 l_1 l_3 l_4} \ , \tag{1.9a}$$
$$\bar{o}^{33}_{l_1 l_2 l_3 l_4 l_5 l_6} = -\bar{o}^{33}_{l_1 l_3 l_2 l_4 l_5 l_6} = \bar{o}^{33}_{l_3 l_1 l_2 l_4 l_5 l_6} = -\bar{o}^{33}_{l_3 l_2 l_1 l_4 l_5 l_6} = \bar{o}^{33}_{l_2 l_3 l_1 l_4 l_5 l_6} = -\bar{o}^{33}_{l_2 l_1 l_3 l_4 l_5 l_6} \ . \tag{1.9b}$$

1.2. $U(1)$ group

We consider the abelian compact Lie group $U(1) \equiv \{S(\varphi), \varphi \in [0, 2\pi]\}$ associated with the global rotation of an A-body fermion system in gauge space. As $U(1)$ is considered to be a symmetry group of H and O, commutation relations

$$[H, S(\varphi)] = [A, S(\varphi)] = [O, S(\varphi)] = 0 \ , \tag{1.10}$$

hold for any $\varphi \in [0, 2\pi]$.

We utilize the unitary representation of $U(1)$ on Fock space $\mathcal{F}$ given by

$$S(\varphi) = e^{iA\varphi} \ . \tag{1.11}$$

Irreducible representations (IRREPs) of $U(1)$ are given by

$$\langle \Psi^{\mathrm{A}}_{\mu}|S(\varphi)|\Psi^{\mathrm{A}'}_{\mu'}\rangle \equiv e^{i\mathrm{A}\varphi}\, \delta_{\mathrm{A}\mathrm{A}'}\, \delta_{\mu\mu'} \ , \tag{1.12}$$

where $|\Psi_\mu^{\mathrm{A}}\rangle$ is an eigenstate of A

$$A|\Psi_\mu^{\mathrm{A}}\rangle = \mathrm{A}|\Psi_\mu^{\mathrm{A}}\rangle \ , \tag{1.13}$$

and, as authorized by Eq. (1.10), of the Hamiltonian at the same time

$$H|\Psi_\mu^{\mathrm{A}}\rangle = \mathrm{E}_\mu^{\mathrm{A}}\,|\Psi_\mu^{\mathrm{A}}\rangle \ , \tag{1.14}$$

where $\mathrm{E}_\mu^{\mathrm{A}}$, with $\mu = 0, 1, 2\ldots$, orders increasing eigenenergies for a fixed A. From the group theory point of view, $\mathrm{A} \in \mathbb{Z}$ on the right-hand side of Eq. (1.12). Since A actually represents the number of fermions in the system, its value is constrained from the physics point of view to $\mathrm{A} \in \mathbb{N}$.

The volume of the group is

$$v_{U(1)} \equiv \int_0^{2\pi} \mathrm{d}\varphi = 2\pi \ , \tag{1.15}$$

and the orthogonality of IRREPs reads as

$$\frac{1}{v_{U(1)}} \int_0^{2\pi} \mathrm{d}\varphi\, e^{-i\mathrm{A}\varphi}\, e^{+i\mathrm{A}'\varphi} = \delta_{\mathrm{A}\mathrm{A}'} \ . \tag{1.16}$$

A tensor operator Q of rank[3] A and a state $|\Psi_\mu^{\mathrm{A}}\rangle$ transform under global gauge rotation according to

$$S(\varphi)\, Q\, S(\varphi)^{-1} = e^{i\mathrm{A}\varphi}\, Q \ , \tag{1.17a}$$

$$S(\varphi)\, |\Psi_\mu^{A}\rangle = e^{i\mathrm{A}\varphi}\, |\Psi_\mu^{\mathrm{A}}\rangle \ . \tag{1.17b}$$

A key feature for the following is that any integrable function $f(\varphi)$ defined on $[0, 2\pi]$ can be expanded over the IRREPs of the $U(1)$ group. This constitutes nothing but the Fourier decomposition of the function

$$f(\varphi) \equiv \sum_{\mathrm{A}\in\mathbb{Z}} f^{\mathrm{A}}\, e^{i\mathrm{A}\varphi} \ , \tag{1.18}$$

which defines the set of expansion coefficients $\{f^{\mathrm{A}}\}$. Last but not least, the IRREPs fulfill the first-order ordinary differential equation (ODE)

$$-\,i\frac{d}{d\varphi}e^{i\mathrm{A}\varphi} = \mathrm{A}\, e^{i\mathrm{A}\varphi} \ . \tag{1.19}$$

1.3. Bogoliubov algebra

The unitary and linear Bogoliubov transformation connects quasi-particle annihilation and creation operators $\{\beta_k; \beta_k^\dagger\}$ to particle ones through [109]

$$\beta_k = \sum_p U_{pk}^*\, c_p + V_{pk}^*\, c_p^\dagger \ , \tag{1.20a}$$

$$\beta_k^\dagger = \sum_p U_{pk}\, c_p^\dagger + V_{pk}\, c_p \ . \tag{1.20b}$$

[3] A tensor operator of rank A with respect to the $U(1)$ group is an operator that associates a state of the (N+A)-body Hilbert space $\mathcal{H}_{\mathrm{N+A}}$ to a state of the N-body Hilbert space $\mathcal{H}_{\mathrm{N}}$, i.e. which changes the number of particles by A units.

Both sets of fermionic operators obey anticommutation rules

$$\{c_p, c_q\} = 0 \quad ; \quad \{\beta_{k_1}, \beta_{k_2}\} = 0 \ , \tag{1.21a}$$
$$\{c_p^\dagger, c_q^\dagger\} = 0 \quad ; \quad \{\beta_{k_1}^\dagger, \beta_{k_2}^\dagger\} = 0 \ , \tag{1.21b}$$
$$\{c_p, c_q^\dagger\} = \delta_{pq} \ ; \ \{\beta_{k_1}, \beta_{k_2}^\dagger\} = \delta_{k_1 k_2} \ . \tag{1.21c}$$

The Bogoliubov transformation can be written in matrix form

$$\begin{pmatrix} \beta \\ \beta^\dagger \end{pmatrix} = W^\dagger \begin{pmatrix} c \\ c^\dagger \end{pmatrix} \ , \tag{1.22}$$

where

$$W \equiv \begin{pmatrix} U & V^* \\ V & U^* \end{pmatrix} \ . \tag{1.23}$$

One can further define the skew-symmetric matrix

$$Z \equiv V^* [U^*]^{-1} \tag{1.24}$$

in terms of which $|\Phi\rangle$ can be expressed by virtue of Thouless' theorem [128]. The anticommutation rules obeyed by the quasi-particle operators relate to the unitarity of W that leads to four relations

$$UU^\dagger + V^* V^T = 1 \ , \tag{1.25a}$$
$$VU^\dagger + U^* V^T = 0 \ , \tag{1.25b}$$
$$U^\dagger U + V^\dagger V = 1 \ , \tag{1.25c}$$
$$V^T U + U^T V = 0 \, , \tag{1.25d}$$

originating from $W^\dagger W = 1$ and four relations

$$UV^\dagger + V^* U^T = 0 \ , \tag{1.25e}$$
$$VV^\dagger + U^* U^T = 1 \ , \tag{1.25f}$$
$$U^\dagger V^* + V^\dagger U^* = 0 \ , \tag{1.25g}$$
$$V^T V^* + U^T U^* = 1 \ , \tag{1.25h}$$

originating from $WW^\dagger = 1$.

The Bogoliubov product state, which carries even number-parity as a quantum number, is defined as

$$|\Phi\rangle \equiv \mathcal{C} \prod_k \beta_k |0\rangle \ , \tag{1.26}$$

and is the vacuum of the quasiparticle operators, i.e. $\beta_k |\Phi\rangle = 0$ for all k. In Eq. (1.26), $\mathcal{C}$ is a complex normalization ensuring that $\langle\Phi|\Phi\rangle = 1$. As quasiparticle operators mix particle creation and annihilation operators (see Eq. (1.20)), the Bogoliubov vacuum breaks $U(1)$ symmetry associated with particle number conservation, i.e. $|\Phi\rangle$ is not an eigenstate of the particle-number operator A, except in the limit where it reduces to a Slater determinant.

The Bogoliubov state $|\Phi\rangle$ is fully characterized by the generalized density matrix [109]

$$\mathcal{R} \equiv \begin{pmatrix} \frac{\langle\Phi|c_p^\dagger c_q|\Phi\rangle}{\langle\Phi|\Phi\rangle} & \frac{\langle\Phi|c_p c_q|\Phi\rangle}{\langle\Phi|\Phi\rangle} \\ \frac{\langle\Phi|c_p^\dagger c_q^\dagger|\Phi\rangle}{\langle\Phi|\Phi\rangle} & \frac{\langle\Phi|c_p c_q^\dagger|\Phi\rangle}{\langle\Phi|\Phi\rangle} \end{pmatrix} \tag{1.27a}$$

$$\equiv \begin{pmatrix} +\rho_{qp} & +\kappa_{qp} \\ -\bar{\kappa}^*_{qp} & -\sigma^*_{qp} \end{pmatrix} , \tag{1.27b}$$

where ρ and κ denote the normal one-body density matrix and the anomalous density matrix (or pairing tensor), respectively, with

$$\rho = +V^* V^T , \tag{1.28a}$$
$$\kappa = +V^* U^T , \tag{1.28b}$$
$$\bar{\kappa}^* = -U^* V^T , \tag{1.28c}$$
$$\sigma^* = -U^* U^T . \tag{1.28d}$$

Using anticommutation rules of particle creation and annihilation operators (Eq. (1.21)), one demonstrates that

$$\rho_{qp} = +\rho^*_{pq} , \tag{1.29a}$$
$$\kappa_{qp} = -\kappa_{pq} , \tag{1.29b}$$
$$\sigma_{qp} = +\rho_{qp} - \delta_{qp} , \tag{1.29c}$$
$$\bar{\kappa}_{qp} = +\kappa_{qp} , \tag{1.29d}$$

meaning in particular that ρ is hermitian (i.e. $\rho^\dagger = \rho$) while κ is skew-symmetric (i.e. $\kappa^T = -\kappa$). Transforming the generalized density matrix to the quasi-particle basis via $\mathbf{R} \equiv W^\dagger \mathcal{R} W$ leads to

$$\mathbf{R} = \begin{pmatrix} \frac{\langle\Phi|\beta_p^\dagger \beta_q|\Phi\rangle}{\langle\Phi|\Phi\rangle} & \frac{\langle\Phi|\beta_p \beta_q|\Phi\rangle}{\langle\Phi|\Phi\rangle} \\ \frac{\langle\Phi|\beta_p^\dagger \beta_q^\dagger|\Phi\rangle}{\langle\Phi|\Phi\rangle} & \frac{\langle\Phi|\beta_p \beta_q^\dagger|\Phi\rangle}{\langle\Phi|\Phi\rangle} \end{pmatrix} \tag{1.30a}$$

$$\equiv \begin{pmatrix} R^{+-}_{pq} & R^{--}_{pq} \\ R^{++}_{pq} & R^{-+}_{pq} \end{pmatrix} \tag{1.30b}$$

$$= \begin{pmatrix} 0 & 0 \\ 0 & 1 \end{pmatrix} , \tag{1.30c}$$

where the result, trivially obtained by considering the action of quasi-particle operators on the vacuum, can also be recovered starting from Eq. (1.27) and making use of Eqs. (1.20) and (1.25).

1.4. Time-dependent state

The Bogoliubov reference state is not an eigenstate of the particle number operator A. The same is true of the perturbatively corrected state generated from it, unless the perturbative expansion

is resummed to all orders. Consequently, one must at least enforce that the expectation value of A matches the actual number of particles A of the targeted system. Correspondingly, the Hamiltonian H is to be replaced by the grand potential $\Omega \equiv H - \lambda A$ in the set up of the many-body formalism [77, 127], where λ denotes the chemical potential.

A Lagrange term is eventually required to constrain the particle number to the correct value on average. This leads to using the grand potential $\Omega \equiv H - \lambda A$ in place of H. Equations (1.13) and (1.14) trivially lead to

$$\Omega|\Psi_\mu^{\rm A}\rangle = \Omega_\mu^{\rm A}\,|\Psi_\mu^{\rm A}\rangle \ , \tag{1.31}$$

where $\Omega_\mu^{\rm A} \equiv {\rm E}_\mu^{\rm A} - \lambda {\rm A}$.

The many-body formalism displayed below is conveniently formulated within an imaginary-time framework. We thus introduce the evolution operator in imaginary time as[4]

$$\mathcal{U}(\tau) \equiv e^{-\tau\Omega} \ , \tag{1.32}$$

with τ real. A key quantity throughout the present study is the time-evolved many-body state defined as

$$\begin{aligned} |\Psi(\tau)\rangle &\equiv \mathcal{U}(\tau)|\Phi\rangle \\ &= \sum_{{\rm A}\in\mathbb{N}} \sum_\mu e^{-\tau\Omega_\mu^{\rm A}}\,|\Psi_\mu^{\rm A}\rangle\,\langle\Psi_\mu^{\rm A}|\Phi\rangle \ , \end{aligned} \tag{1.33}$$

where we have inserted a completeness relationship on Fock space under the form

$$\mathbb{1} = \sum_{{\rm A}\in\mathbb{N}} \sum_\mu |\Psi_\mu^{\rm A}\rangle\,\langle\Psi_\mu^{\rm A}| \ . \tag{1.34}$$

It is straightforward to demonstrate that $|\Psi(\tau)\rangle$ satisfies the time-dependent Schrödinger equation

$$\Omega\,|\Psi(\tau)\rangle = -\partial_\tau|\Psi(\tau)\rangle \ . \tag{1.35}$$

1.5. Large and infinite time limits

Below, we will be interested in first looking at the *large* τ limit of various quantities before eventually taking their *infinite* time limit. Although we utilize the same mathematical symbol ($\lim_{\tau\to\infty}$) in both cases for simplicity, the reader must not be confused by the fact that there remains a residual τ dependence in the first case, which typically disappears by considering ratios before actually promoting the time to infinity. The large τ limit is essentially defined as $\tau \gg \Delta E^{-1}$, where ΔE is the energy difference between the ground state and the first excited state of Ω. Depending on the system, the latter can be the first excited state in the IRREP (i.e. nucleus) of the ground state[5] or the lowest state of another IRREP (i.e. of a neighboring nucleus).

[4] The time is given in units of MeV^{-1}.

[5] To be more precise, in this case the first excited state belongs to a duplicate of the IRREP of the ground state labelled by other auxilliary quantum numbers.

1.6. Ground state

Taking the large τ limit provides the ground state of Ω under the form[6]

$$|\Psi_0^{A_0}\rangle \equiv \lim_{\tau\to\infty} |\Psi(\tau)\rangle \tag{1.36a}$$

$$= e^{-\tau\Omega_0^{A_0}} |\Psi_0^{A_0}\rangle \langle\Psi_0^{A_0}|\Phi\rangle \ . \tag{1.36b}$$

As will become clear below, the many-body scheme developed in the present work relies on choosing the Bogoliubov product state $|\Phi\rangle$ as the ground state of an unperturbed grand potential Ω_0 that breaks $U(1)$ symmetry. As such, $|\Phi\rangle$ mixes several IRREPs but is likely to contain a component belonging to the nucleus of interest given that it is typically chosen to have (close to) the number A_0 of particles in average. Eventually, one recovers from Eq. (1.35) that

$$\Omega|\Psi_0^{A_0}\rangle = \Omega_0^{A_0} |\Psi_0^{A_0}\rangle \ , \tag{1.37}$$

in the large τ limit.

1.7. Time-dependent kernels

We now introduce the time-dependent kernel of an operator[7] O through

$$O(\tau) \equiv \langle\Psi(\tau)|O|\Phi\rangle \ . \tag{1.38}$$

Doing so for the identity, the Hamiltonian, the particle number and the grand potential operators, defines the set of time-dependent kernels of interest

$$N(\tau) \equiv \langle\Psi(\tau)|\mathbb{1}|\Phi\rangle \ , \tag{1.39a}$$

$$H(\tau) \equiv \langle\Psi(\tau)|H|\Phi\rangle \ , \tag{1.39b}$$

$$A(\tau) \equiv \langle\Psi(\tau)|A|\Phi\rangle \ , \tag{1.39c}$$

$$\Omega(\tau) \equiv \langle\Psi(\tau)|\Omega|\Phi\rangle \ , \tag{1.39d}$$

where the first one denotes the time-dependent norm kernel and where the latter three are related through $\Omega(\tau) = H(\tau) - \lambda A(\tau)$.

Finally, use will often be made of the *reduced* kernel of an operator O defined through

$$\mathcal{O}(\tau) \equiv \frac{O(\tau)}{N(\tau)} \ , \tag{1.40}$$

which leads, for $O = \mathbb{1}$, to working with *intermediate normalization*, i.e. to having a norm kernel that satisfies $\mathcal{N}(\tau) \equiv 1$ for all τ.

[6] The chemical potential λ is fixed such that $\Omega_0^{A_0}$ for the targeted particle number A_0 is the lowest value of all Ω_μ^A over Fock space, i.e. it penalizes systems with larger number of particles such that $\Omega_0^{A_0} < \Omega_\mu^A$ for all $A > A_0$ while maintaining at the same time that $\Omega_0^{A_0} < \Omega_\mu^A$ for all $A < A_0$. This is achievable only if E_0^A is strictly convex in the neighborhood of A_0, which is generally but not always true for atomic nuclei.

[7] We are currently interested in operators that commute with Ω and that are scalars under transformations of the $U(1)$ group, i.e. that are of rank $A = 0$. Dealing with operators of rank $A \neq 0$ and with amplitudes between different many-body eigenstates of Ω requires an extension of the presently developed formalism.

1.8. Expansion of the time-dependent kernels

Inserting Eq. (1.34) into Eq. (1.39) while making use of Eqs. (1.13) and (1.14), one obtains the decomposition of the kernels

$$N(\tau) = \sum_{\mathrm{A}\in\mathbb{N}} \sum_{\mu} \quad e^{-\tau\Omega_\mu^{\mathrm{A}}} |\langle\Phi|\Psi_\mu^{\mathrm{A}}\rangle|^2 \ , \tag{1.41a}$$

$$H(\tau) = \sum_{\mathrm{A}\in\mathbb{N}} \sum_{\mu} \mathrm{E}_\mu^{\mathrm{A}} \ e^{-\tau\Omega_\mu^{\mathrm{A}}} |\langle\Phi|\Psi_\mu^{\mathrm{A}}\rangle|^2 \ , \tag{1.41b}$$

$$A(\tau) = \sum_{\mathrm{A}\in\mathbb{N}} \sum_{\mu} \mathrm{A} \ e^{-\tau\Omega_\mu^{\mathrm{A}}} |\langle\Phi|\Psi_\mu^{\mathrm{A}}\rangle|^2 \ , \tag{1.41c}$$

$$\Omega(\tau) = \sum_{\mathrm{A}\in\mathbb{N}} \sum_{\mu} \Omega_\mu^{\mathrm{A}} \ e^{-\tau\Omega_\mu^{\mathrm{A}}} |\langle\Phi|\Psi_\mu^{\mathrm{A}}\rangle|^2 \ , \tag{1.41d}$$

where one trivially notices that contributions associated with $\mathrm{A} < 0$ are zero.

1.9. Ground-state energy

Defining the large τ limit of a kernel via

$$O(\infty) \equiv \lim_{\tau\to\infty} O(\tau) \ , \tag{1.42}$$

one obtains

$$N(\infty) = \quad e^{-\tau\Omega_0^{\mathrm{A}_0}} |\langle\Phi|\Psi_0^{\mathrm{A}_0}\rangle|^2 \ , \tag{1.43a}$$

$$H(\infty) = \mathrm{E}_0^{\mathrm{A}_0} \ e^{-\tau\Omega_0^{\mathrm{A}_0}} |\langle\Phi|\Psi_0^{\mathrm{A}_0}\rangle|^2 \ , \tag{1.43b}$$

$$A(\infty) = \mathrm{A}_0 \ e^{-\tau\Omega_0^{\mathrm{A}_0}} |\langle\Phi|\Psi_0^{\mathrm{A}_0}\rangle|^2 \ , \tag{1.43c}$$

$$\Omega(\infty) = \Omega_0^{\mathrm{A}_0} \ e^{-\tau\Omega_0^{\mathrm{A}_0}} |\langle\Phi|\Psi_0^{\mathrm{A}_0}\rangle|^2 \ , \tag{1.43d}$$

where the residual time dependence typically disappears by eventually employing reduced kernels as defined in Eq. (1.40). Expressions (1.43) relate in the large-time limit operator kernels of interest to the norm kernel through eigenvalue-like equations

$$H(\infty) = \mathrm{E}_0^{\mathrm{A}_0} \, N(\infty) \ , \tag{1.44a}$$

$$A(\infty) = \mathrm{A}_0 \, N(\infty) \ , \tag{1.44b}$$

$$\Omega(\infty) = \Omega_0^{\mathrm{A}_0} \, N(\infty) \ , \tag{1.44c}$$

leading for reduced kernels to

$$\mathcal{H}(\infty) = \mathrm{E}_0^{\mathrm{A}_0} \ , \tag{1.45a}$$

$$\mathcal{A}(\infty) = \mathrm{A}_0 \ , \tag{1.45b}$$

$$\boldsymbol{\Omega}(\infty) = \Omega_0^{\mathrm{A}_0} \ . \tag{1.45c}$$

In Eq. (1.43c), the expansion coefficient in the particle-number operator kernel equates the expected value A_0, even though the kernel at finite time contains contributions associated with

$A \neq A_0$. While the latter property results from defining the kernels in terms of a Bogoliubov vacuum spanning several IRREPs of $U(1)$, the selection of the expected IRREP in the infinite time limit testifies that the exact ground-state $|\Psi_0^{\mathrm{A}_0}\rangle$ of Ω (and H) does carry good particle number A_0. Accordingly, Eqs. (1.44-1.45) demonstrate that the ratios of the various operator kernels to the norm kernel access eigenvalues that are in one-to-one relationship with the physical IRREP labelled by A_0.

Let us now consider the case of actual interest where the kernels defined in terms of a Bogoliubov vacuum breaking $U(1)$ symmetry are approximated. In this situation, kernels in the infinite time limit display the typical structure

$$N_{\mathrm{app}}(\infty) \equiv \sum_{\mathrm{A}\in\mathbb{Z}} \mathrm{N}^{\mathrm{A}}_{\mathrm{app}} \ , \tag{1.46a}$$

$$H_{\mathrm{app}}(\infty) \equiv \sum_{\mathrm{A}\in\mathbb{Z}} \mathrm{E}^{\mathrm{A}}_{\mathrm{app}}\, \mathrm{N}^{\mathrm{A}}_{\mathrm{app}} \ , \tag{1.46b}$$

$$A_{\mathrm{app}}(\infty) \equiv \sum_{\mathrm{A}\in\mathbb{Z}} \mathrm{A}^{\mathrm{A}}_{\mathrm{app}}\, \mathrm{N}^{\mathrm{A}}_{\mathrm{app}} \ , \tag{1.46c}$$

where the condition $N_{\mathrm{app}}(\infty) = \sum_{\mathrm{A}\in\mathbb{Z}} \mathrm{N}^{\mathrm{A}}_{\mathrm{app}} = 1$ characterizes intermediate normalization. In Eq. (1.46), the remaining sum over A signals the breaking of the symmetry induced by the approximation. In the expansion, the sum over the IRREPS still runs over $\mathbb{Z}$. If the many-body approximation scheme is well behaved from the physics standpoint, coefficients corresponding to $\mathrm{A} < 0$ must be zero, which acts as a check that the formalism is sensible [129, 112].

Except for going back to an exact computation of the kernels, such that all the expansion coefficients but the physical one are zero in Eq. (1.46), taking the straight ratio $H_{\mathrm{app}}(\infty)/N_{\mathrm{app}}(\infty)$ does not provide an approximate energy that is in one-to-one correspondence with the physical IRREP A_0. This materializes the contamination associated with the breaking of the symmetry.

1.10. Projective versus expectation value method

The formalism layed out in Secs. 1.7 to 1.9 has been designed in a projective way, as is historically the common approach for MBPT and CC: Eqs. (1.39) and following rely on a right-hand state that is the uncorrelated state $|\Phi\rangle$. Alternatively, one could have worked in an expectation-value fashion as is traditionally done in SCGF or Λ-CC, using fully-correlated states both on the right-hand and left-hand sides. Eq. (1.39) would then translate into

$$N(\tau) \equiv \langle\Psi(\tau)|\mathbb{1}|\Psi(\tau)\rangle \ , \tag{1.47a}$$

$$H(\tau) \equiv \langle\Psi(\tau)|H|\Psi(\tau)\rangle \ , \tag{1.47b}$$

$$A(\tau) \equiv \langle\Psi(\tau)|A|\Psi(\tau)\rangle \ , \tag{1.47c}$$

$$\Omega(\tau) \equiv \langle\Psi(\tau)|\Omega|\Psi(\tau)\rangle \ . \tag{1.47d}$$

Though the two approaches are equivalent in the exact limit, the truncation introduced in the perturbative series have them lay out different results. Especially, the projective approach needs additional consideration as its fundamentally asymmetric formulation introduces risks of obtaining non-real values for the observables once truncations are made. One thus needs to

consider both the projected form of the Schrödinger equation (Eq. (1.35)) and its complex-conjugated partner to obtain a real result, i.e. Eq. (1.45), that can be rewritten as

$$\mathrm{E}_0^{\mathrm{A}_0} = \lim_{\tau\to\infty} \frac{\langle\Psi(\tau)|H|\Phi\rangle}{\langle\Psi(\tau)|\Phi\rangle} \,, \tag{1.48a}$$

$$\mathrm{A}_0 = \lim_{\tau\to\infty} \frac{\langle\Psi(\tau)|A|\Phi\rangle}{\langle\Psi(\tau)|\Phi\rangle} \,, \tag{1.48b}$$

$$\Omega_0^{\mathrm{A}_0} = \lim_{\tau\to\infty} \frac{\langle\Psi(\tau)|\Omega|\Phi\rangle}{\langle\Psi(\tau)|\Phi\rangle} \,, \tag{1.48c}$$

thus needs to be replaced by

$$\mathrm{E}_0^{\mathrm{A}_0} \equiv \lim_{\tau\to\infty} \frac{1}{2}\left(\frac{\langle\Psi(\tau)|H|\Phi\rangle}{\langle\Psi(\tau)|\Phi\rangle} + \frac{\langle\Phi|H|\Psi(\tau)\rangle}{\langle\Phi|\Psi(\tau)\rangle} \right) \,, \tag{1.49a}$$

$$\mathrm{A}_0 \equiv \lim_{\tau\to\infty} \frac{1}{2}\left(\frac{\langle\Psi(\tau)|A|\Phi\rangle}{\langle\Psi(\tau)|\Phi\rangle} + \frac{\langle\Phi|A|\Psi(\tau)\rangle}{\langle\Phi|\Psi(\tau)\rangle} \right) \,, \tag{1.49b}$$

$$\Omega_0^{\mathrm{A}_0} \equiv \lim_{\tau\to\infty} \frac{1}{2}\left(\frac{\langle\Psi(\tau)|\Omega|\Phi\rangle}{\langle\Psi(\tau)|\Phi\rangle} + \frac{\langle\Phi|\Omega|\Psi(\tau)\rangle}{\langle\Phi|\Psi(\tau)\rangle} \right) \,. \tag{1.49c}$$

Indeed, as will appear later on, while the asymmetric formulation of Eq. 1.48 does provide real results for the grand potential $\Omega_0^{\mathrm{A}_0}$, it is a priori not the case[8] for the energy $\mathrm{E}_0^{\mathrm{A}_0}$ or for the the particle number A_0 that require the symmetric formulation of Eq. 1.49. Eventually, the practical approach consists of working with the first term of Eq. (1.49) and taking eventually the real part of the results, as will be done implicitly in the rest of the document. This choice is somewhat unconventional, as practitioners traditionally work with the second. Both choices are eventually equivalent, as they relate through a simple conjugation.

1.11. Normal ordering

The present formalism is best formulated in the quasiparticle basis introduced in Eq. (1.20) by normal ordering all operators at play with respect to $|\Phi\rangle$ on the basis of Wick's theorem [118]. Taking O as an example, and as extensively discussed in Ref. [78], its normal-ordered form expressed in terms of fully antisymmetric matrix elements[9] reads as

[8] The problem does not manifest in standard MBPT as will be discussed in Sec. 2.11.

[9] Explicit expressions of $O^{ij}_{k_1\ldots k_i k_{i+1}\ldots k_{i+j}}$ in terms of matrix elements o^{1N}_{pq}, $\bar{o}^{2N}_{pqrs}$ and $\bar{o}^{3N}_{pqrstu}$ as well as matrix elements of (U, V) are provided in App. C.1.

$$O \equiv O^{[0]} + O^{[2]} + O^{[4]} + O^{[6]} \tag{1.50a}$$

$$\equiv O^{00} + \Big[O^{11} + \{O^{20} + O^{02}\}\Big] + \Big[O^{22} + \{O^{31} + O^{13}\} + \{O^{40} + O^{04}\}\Big] \tag{1.50b}$$

$$+ \Big[O^{33} + \{O^{42} + O^{24}\} + \{O^{51} + O^{15}\} + \{O^{60} + O^{06}\}\Big] \tag{1.50c}$$

$$= O^{00} \tag{1.50d}$$

$$+ \frac{1}{1!}\sum_{k_1k_2} O^{11}_{k_1k_2}\beta^\dagger_{k_1}\beta_{k_2} + \frac{1}{2!}\sum_{k_1k_2}\Big\{O^{20}_{k_1k_2}\beta^\dagger_{k_1}\beta^\dagger_{k_2} + O^{02}_{k_1k_2}\beta_{k_2}\beta_{k_1}\Big\} \tag{1.50e}$$

$$+ \frac{1}{(2!)^2}\sum_{k_1k_2k_3k_4} O^{22}_{k_1k_2k_3k_4}\beta^\dagger_{k_1}\beta^\dagger_{k_2}\beta_{k_4}\beta_{k_3} \tag{1.50f}$$

$$+ \frac{1}{3!}\sum_{k_1k_2k_3k_4}\Big\{O^{31}_{k_1k_2k_3k_4}\beta^\dagger_{k_1}\beta^\dagger_{k_2}\beta^\dagger_{k_3}\beta_{k_4} + O^{13}_{k_1k_2k_3k_4}\beta^\dagger_{k_1}\beta_{k_4}\beta_{k_3}\beta_{k_2}\Big\} \tag{1.50g}$$

$$+ \frac{1}{4!}\sum_{k_1k_2k_3k_4}\Big\{O^{40}_{k_1k_2k_3k_4}\beta^\dagger_{k_1}\beta^\dagger_{k_2}\beta^\dagger_{k_3}\beta^\dagger_{k_4} + O^{04}_{k_1k_2k_3k_4}\beta_{k_4}\beta_{k_3}\beta_{k_2}\beta_{k_1}\Big\} \tag{1.50h}$$

$$+ \frac{1}{(3!)^2}\sum_{k_1k_2k_3k_4k_5k_6} O^{33}_{k_1k_2k_3k_4k_5k_6}\beta^\dagger_{k_1}\beta^\dagger_{k_2}\beta^\dagger_{k_3}\beta_{k_6}\beta_{k_5}\beta_{k_4} \tag{1.50i}$$

$$+ \frac{1}{2!\,4!}\sum_{k_1k_2k_3k_4k_5k_6}\Big\{O^{42}_{k_1k_2k_3k_4k_5k_6}\beta^\dagger_{k_1}\beta^\dagger_{k_2}\beta^\dagger_{k_3}\beta^\dagger_{k_4}\beta_{k_6}\beta_{k_5} + O^{24}_{k_1k_2k_3k_4k_5k_6}\beta^\dagger_{k_1}\beta^\dagger_{k_2}\beta_{k_6}\beta_{k_5}\beta_{k_4}\beta_{k_3}\Big\} \tag{1.50j}$$

$$+ \frac{1}{5!}\sum_{k_1k_2k_3k_4k_5k_6}\Big\{O^{51}_{k_1k_2k_3k_4k_5k_6}\beta^\dagger_{k_1}\beta^\dagger_{k_2}\beta^\dagger_{k_3}\beta^\dagger_{k_4}\beta^\dagger_{k_5}\beta_{k_6} + O^{15}_{k_1k_2k_3k_4k_5k_6}\beta^\dagger_{k_1}\beta_{k_6}\beta_{k_5}\beta_{k_4}\beta_{k_3}\beta_{k_2}\Big\} \tag{1.50k}$$

$$+ \frac{1}{6!}\sum_{k_1k_2k_3k_4k_5k_6}\Big\{O^{60}_{k_1k_2k_3k_4k_5k_6}\beta^\dagger_{k_1}\beta^\dagger_{k_2}\beta^\dagger_{k_3}\beta^\dagger_{k_4}\beta^\dagger_{k_5}\beta^\dagger_{k_6} + O^{06}_{k_1k_2k_3k_4k_5k_6}\beta_{k_6}\beta_{k_5}\beta_{k_4}\beta_{k_3}\beta_{k_2}\beta_{k_1}\Big\}\,, \tag{1.50l}$$

where

1. Each term O^{ij} is characterized by its number i (j) of quasiparticle creation (annihilation) operators. Because O has been normal-ordered with respect to $|\Phi\rangle$, all quasiparticle creation operators (if any) are located to the left of all quasiparticle annihilation operators (if any). The class $O^{[2k]}$ groups all the terms O^{ij} of *effective* k-body character, i.e., with $i + j = 2k$. The first contribution

$$O^{[0]} = O^{00} = \frac{\langle\Phi|O|\Phi\rangle}{\langle\Phi|\Phi\rangle} \tag{1.51}$$

   denotes the fully contracted part of O and is nothing but a (real) number.

2. The subscripts of the matrix elements $O^{ij}_{k_1\ldots k_i k_{i+1}\ldots k_{i+j}}$ are ordered sequentially, independently of the creation or annihilation character of the operators the indices refer to. While quasiparticle creation operators themselves also follow sequential order, quasiparticle

annihilation operators follow inverse sequential order. In Eq. (1.50f), for example, the two creation operators are ordered $\beta^\dagger_{k_1}\beta^\dagger_{k_2}$ while the two annihilation operators are ordered $\beta_{k_4}\beta_{k_3}$.

3. Matrix elements are fully antisymmetric, i.e.

$$O^{ij}_{k_1\ldots k_i k_{i+1}\ldots k_{i+j}} = (-1)^{\sigma(P)} O^{ij}_{P(k_1\ldots k_i|k_{i+1}\ldots k_{i+j})} \ , \tag{1.52}$$

where $\sigma(P)$ refers to the signature of the permutation P. The notation $P(\ldots|\ldots)$ denotes a separation into the i quasiparticle creation operators and the j quasiparticle annihilation operators such that permutations are only considered between members of the same group.

4. As each $O^{[k]}$ component is hermitian, matrix elements exhibit the following behavior under hermitian conjugation

$$O^{11}_{k_1k_2} = O^{11*}_{k_2k_1} \ , \tag{1.53a}$$
$$O^{20}_{k_1k_2} = O^{02*}_{k_1k_2} \ , \tag{1.53b}$$
$$O^{22}_{k_1k_2k_3k_4} = O^{22*}_{k_3k_4k_1k_2} \ , \tag{1.53c}$$
$$O^{31}_{k_1k_2k_3k_4} = O^{13*}_{k_4k_1k_2k_3} \ , \tag{1.53d}$$
$$O^{40}_{k_1k_2k_3k_4} = O^{04*}_{k_1k_2k_3k_4} \ , \tag{1.53e}$$
$$O^{33}_{k_1k_2k_3k_4k_5k_6} = O^{33*}_{k_4k_5k_6k_1k_2k_3} \ , \tag{1.53f}$$
$$O^{42}_{k_1k_2k_3k_4k_5k_6} = O^{24*}_{k_5k_6k_1k_2k_3k_4} \ , \tag{1.53g}$$
$$O^{51}_{k_1k_2k_3k_4k_5k_6} = O^{15*}_{k_6k_1k_2k_3k_4k_5} \ , \tag{1.53h}$$
$$O^{60}_{k_1k_2k_3k_4k_5k_6} = O^{06*}_{k_1k_2k_3k_4k_5k_6} \ . \tag{1.53i}$$

The normal-ordered form of each operator of interest, i.e. H, Ω, A or A^2, is obtained in this way.[10]

The operator kernel can be split into various contributions associated with its normal-ordered components, i.e.

$$O(\tau) \equiv O^{00}(\tau) \tag{1.54a}$$
$$+ O^{20}(\tau) + O^{11}(\tau) + O^{02}(\tau) \tag{1.54b}$$
$$+ O^{40}(\tau) + O^{31}(\tau) + O^{22}(\tau) + O^{13}(\tau) + O^{04}(\tau) \tag{1.54c}$$
$$+ O^{60}(\tau) + O^{51}(\tau) + O^{42}(\tau) + O^{33}(\tau) + O^{24}(\tau) + O^{15}(\tau) + O^{06}(\tau) \ , \tag{1.54d}$$

having trivially that $O^{00}(\tau) = O^{00}\, N(\tau)$.

1.12. Diagrammatic representation of an operator

Normal-ordered operators in the Schrödinger representation can be displayed diagrammatically. Taking a generic operator, the grand potential and the particle-number operators as typical

[10] Explicit expressions of the different operators are provided in App. C.

cases of interest, canonical diagrams representing their normal-ordered contributions O^{ij}, Ω^{ij} and A^{ij} are shown in Figs. 1.1, 1.2 and 1.3, respectively. Such a representation based on fully-antisymetrized vertices compacted into a point characterizes so-called Hugenholtz diagrams. Focusing on O as an example, the various diagrams contributing to it must be understood in the following way.

1. The factor $O^{ij}_{k_1 \dots k_i k_{i+1} \dots k_{i+j}}$ must be associated to the dot vertex, where i denotes the number of lines traveling out of the vertex and representing quasiparticle creation operators while j denotes the number of lines traveling into the vertex and representing quasiparticle annihilation operators.

2. A factor $1/[i!j!]$ must multiply $O^{ij}_{k_1 \dots k_i k_{i+1} \dots k_{i+j}}$ given that the corresponding diagram contains j equivalent ingoing lines and i equivalent outgoing lines.

3. In the canonical representation used in Figs. 1.1, 1.2 and 1.3, all oriented lines go up, i.e. lines representing quasiparticle creation (annihilation) operators appear above (below) the vertex. Accordingly, indices $k_1 \dots k_i$ must be assigned consecutively from the leftmost to the rightmost line above the vertex, while $k_{i+1} \dots k_{i+j}$ must be similarly assigned consecutively for lines below the vertex.

4. In the diagrammatic representation at play in the many-body formalism designed below, it is possible for a line to propagate downwards. This can be obtained unambiguously starting from the canonical representation given in Figs. 1.1, 1.2 and 1.3 at the price of adding a specific rule. As illustrated in Fig. 1.4 for the diagram representing O^{22}, lines must only be rotated through the right of the diagram, i.e. going through the dashed line, while it is forbidden to rotate them through the full line. Additionally, a minus sign must be added to the amplitude $O^{ij}_{k_1 \dots k_i k_{i+1} \dots k_{i+j}}$ associated with the canonical diagram each time two lines cross as illustrated in Fig. 1.4.

Now that the necessary ingredients have been carefully introduced, one can derive the specific formulation of the norm and energy kernel in the framework of Bogoliubov many-body perturbation theory.

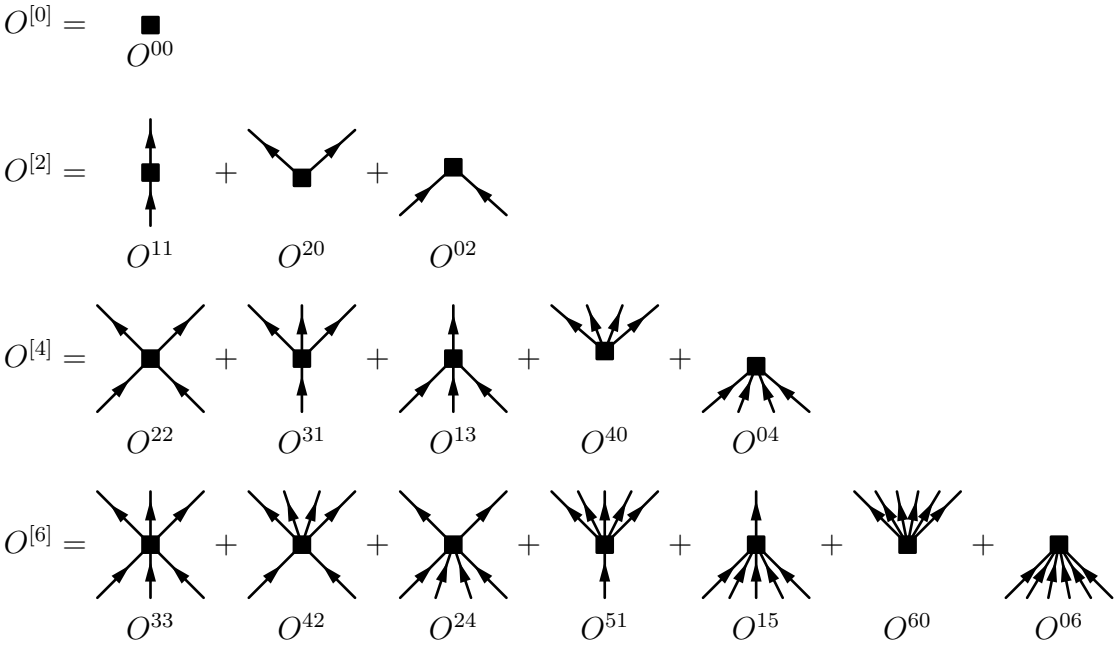

Figure 1.1. Canonical diagrammatic representation of normal-ordered contributions to the operator O in the Schrödinger representation.

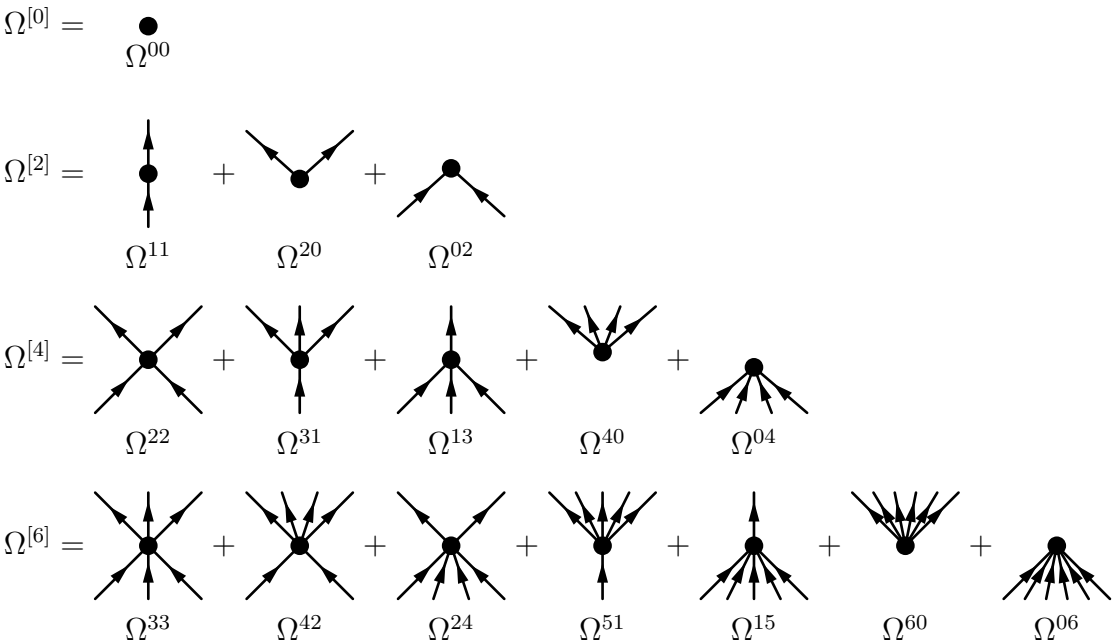

Figure 1.2. Canonical diagrammatic representation of normal-ordered contributions to the grand potential operator Ω in the Schrödinger representation.

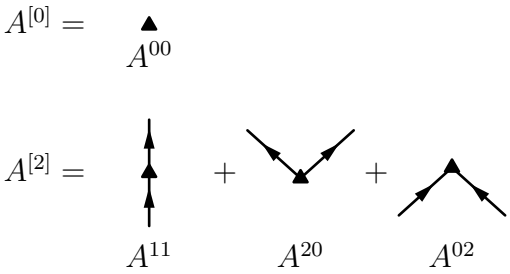

Figure 1.3. Canonical diagrammatic representation of the normal-ordered contributions to the particle-number operator A in the Schrödinger representation.

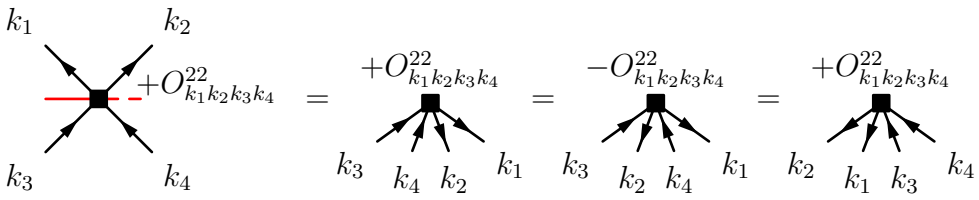

Figure 1.4. Rules to apply when departing from the canonical diagrammatic representation of a normal-ordered operator. Oriented lines can be rotated through the dashed line but not through the full line.

2. Perturbation theory

The necessary ingredients having been introduced in Chap. 1, the present chapter presents the Bogoliubov many-body perturbation theory formalism. Diagrammatic and algebraic contributions are derived up to second order, and connections with closed-shell many-body perturbation theory and Bogoliubov coupled cluster are discussed.

2.1. Unperturbed system

2.1.1. Splitting of the grand potential

The grand potential is split into an unperturbed part Ω_0 and a residual part Ω_1

$$\Omega = \Omega_0 + \Omega_1 \ , \tag{2.1}$$

such that

$$\Omega_0 \equiv \Omega^{00} + \bar{\Omega}^{11} \ , \tag{2.2a}$$

$$\begin{aligned}\Omega_1 \equiv{}& \Omega^{20} + \breve{\Omega}^{11} + \Omega^{02} \\ &+ \Omega^{40} + \Omega^{31} + \Omega^{22} + \Omega^{13} + \Omega^{04} \\ &+ \Omega^{60} + \Omega^{51} + \Omega^{42} + \Omega^{33} + \Omega^{24} + \Omega^{15} + \Omega^{06} \ ,\end{aligned} \tag{2.2b}$$

where $\breve{\Omega}^{11} \equiv \Omega^{11} - \bar{\Omega}^{11}$. The term $\bar{\Omega}^{11}$ has the same formal structure as Ω^{11} and remains to be specified.

We decided in the present chapter as well as in Chap. 4 to follow the typical procedure in the nuclear physics community, that consists of truncating the normal-ordered Hamiltonian by excluding $\Omega^{[6]}$ such that the dominant effect of the three-nucleon interaction is taken into account through its contribution to $\Omega^{[p]}$ with $p \leq 4$. Such a truncation is justified by the high computational cost of treating the three-body interaction in full. This procedure is shown to work well in mid-mass closed-shell nuclei, and the quality of the approximation has been the topic of a few studies [130, 131].

For a given number of interacting fermions, the key is to choose Ω_0 with a low-enough symmetry for its ground state $|\Phi\rangle$ to be non-degenerate with respect to elementary excitations. For open-shell superfluid nuclei, this leads to choosing an operator Ω_0 that breaks particle number conservation, i.e. while Ω commutes with $U(1)$ transformations, we are interested in the case where Ω_0, and thus Ω_1, do *not* commute with $S(\varphi)$, i.e.

$$[\Omega_0, S(\varphi)] \neq 0 \ , \tag{2.3a}$$

$$[\Omega_1, S(\varphi)] \neq 0 \ . \tag{2.3b}$$

In this context, the vacuum $|\Phi\rangle$ is a Bogoliubov state; i.e. a *deformed* product state in gauge space that is not an eigenstate of A and thus it spans several IRREPs of $U(1)$.

2.1.2. Eigenbasis of Ω_0

The operator Ω_0 is written in diagonal form in terms of its one quasi-particle eigenstates

$$\Omega_0 \equiv \Omega^{00} + \sum_k E_k \beta_k^\dagger \beta_k \ , \tag{2.4}$$

with $E_k > 0$ for all k. Introducing many-body states generated via all possible combinations of quasi-particle excitations[1] of the vacuum

$$|\Phi^{k_1 k_2 \cdots}\rangle \equiv \beta_{k_1}^\dagger \, \beta_{k_2}^\dagger \, \ldots |\Phi\rangle \ , \tag{2.5}$$

the unperturbed system is fully characterized over Fock space by its complete set of eigenstates

$$\Omega_0 \, |\Phi\rangle = \Omega^{00} \, |\Phi\rangle \ , \tag{2.6a}$$

$$\Omega_0 \, |\Phi^{k_1 k_2 \cdots}\rangle = \left[\Omega^{00} + E_{k_1} + E_{k_2} + \ldots\right] |\Phi^{k_1 k_2 \cdots}\rangle \ . \tag{2.6b}$$

Equation (2.6) is indeed obtained via

$$\begin{aligned} \Omega_0 \, |\Phi\rangle &= \Omega^{00} \, |\Phi\rangle + \sum_k E_k \beta_k^\dagger \beta_k |\Phi\rangle \\ &= \Omega^{00} \, |\Phi\rangle \end{aligned}$$

as β_k annihilate the vacuum, and similarly via

$$\begin{aligned} \Omega_0 |\Phi^{k_1 k_2 \cdots}\rangle &= \Omega^{00} |\Phi^{k_1 k_2 \cdots}\rangle + \sum_k E_k \beta_k^\dagger \beta_k |\Phi^{k_1 k_2 \cdots}\rangle \\ &= \Omega^{00} |\Phi^{k_1 k_2 \cdots}\rangle + \sum_k E_k \beta_k^\dagger \beta_k \beta_{k_1}^\dagger \beta_{k_2}^\dagger \ldots |\Phi\rangle \\ &= \Omega^{00} |\Phi^{k_1 k_2 \cdots}\rangle + \sum_k E_k \left(\sum_{k_i} \delta_{k k_i} \right) |\Phi^{k_1 k_2 \cdots}\rangle \\ &= \left[\Omega^{00} + E_{k_1} + E_{k_2} + \ldots\right] |\Phi^{k_1 k_2 \cdots}\rangle \ . \end{aligned}$$

As mentioned above, the Bogoliubov vacuum $|\Phi\rangle$ necessarily possesses a *closed-shell* character with respect to elementary (i.e. quasi-particle) excitations. This means that there exists a finite energy gap between the vacuum state and the lowest two quasi-particle excitations, i.e. $E_{k_1} + E_{k_2} \geq 2\Delta_{\mathrm{F}} > 0$ for all (k_1, k_2), where $\Delta_{\mathrm{F}} \equiv \min_{k_1,k_2} \left(E_{k_1} + E_{k_2}\right)/2$ is traditionally characterized as the pairing gap. The strict positivity of unperturbed excitations $E_{k_1 k_2 \ldots} \equiv E_{k_1} + E_{k_2} + \ldots$ characterizes the lifting of the particle-hole degeneracy authorized by the spontaneous breaking of $U(1)$ symmetry in open-shell nuclei at the mean-field level.

Although Bogoliubov states do not carry a definite particle number, it is still useful to discuss the spectroscopic content associated with $|\Phi\rangle$. Let us consider states with a given number

[1] The present many-body formalism only requires to consider Bogoliubov states with a given, i.e. odd or even, number parity. As such, Bogoliubov states involved necessarily differ from one another by an *even* number of quasi-particle excitations.

of quasi-particles $|\Phi^{k_1k_2\cdots}\rangle$, and prove that only one-quasi-particle states can have non-zero spectroscopic factors associated with one-nucleon addition or removal processes

$$\begin{aligned}
\mathfrak{F}^{+}_{k_1k_2\ldots} &= \sum_p \langle\Phi|c_p|\Phi^{k_1k_2\cdots}\rangle\langle\Phi^{k_1k_2\cdots}|c_p^\dagger|\Phi\rangle \\
&= \sum_p \langle\Phi|c_p\beta^\dagger_{k_1}\,\beta^\dagger_{k_2}\,\ldots|\Phi\rangle\langle\Phi|\ldots\,\beta_{k_2}\,\beta_{k_1}c_p^\dagger|\Phi\rangle \\
&= \sum_p \langle\Phi|\sum_k\left(U_{pk}\beta_k + V^*_{pk}\beta^\dagger_k\right)\beta^\dagger_{k_1}\,\beta^\dagger_{k_2}\,\ldots|\Phi\rangle\langle\Phi|\ldots\,\beta_{k_2}\,\beta_{k_1}\sum_{k'}\left(V_{pk'}\beta_{k'} + U^*_{pk'}\beta^\dagger_{k'}\right)|\Phi\rangle \\
&= \sum_p \left[\sum_k U_{pk}\langle\Phi|\beta_k\beta^\dagger_{k_1}\,\beta^\dagger_{k_2}\,\ldots|\Phi\rangle\right]\left[\sum_{k'} U^*_{pk'}\langle\Phi|\ldots\,\beta_{k_2}\,\beta_{k_1}\beta^\dagger_{k'}|\Phi\rangle\right] \\
&= \sum_p \left[\sum_k U_{pk}\sum_{k_j}\delta_{kk_j}\langle\Phi|\prod_{k_i\neq k_j}\beta^\dagger_{k_i}|\Phi\rangle\right]\left[\sum_{k'} U^*_{pk'}\sum_{k_j}\delta_{k'k_j}\langle\Phi|\prod_{k_i\neq k_j}\beta_{k_i}|\Phi\rangle\right] .
\end{aligned}$$

One notices that the previous expression vanishes, unless $k, k' \in \{k_1, k_2, ...\}$. Furthermore, if the set of quasi-particle excitations does not reduce to one-quasi-particle states, i.e. if the set of $k_i \neq k_j$ contains a least one element, the associated β_i (respectively $\beta_i^\dagger$) annihilates the vacuum to its right (respectively to its left). Hence the only non-zero spectroscopic factors correspond to one-quasi-particle states, and the previous expression reduces to

$$\begin{aligned}
\mathfrak{F}^{+}_{k_j} &= \sum_p \left[\sum_k U_{pk}\delta_{kk_j}\langle\Phi|\Phi\rangle\right]\left[\sum_{k'} U^*_{pk'}\delta_{k'k_j}\langle\Phi|\Phi\rangle\right] \\
&= \sum_p \left|U_{pk_j}\right|^2 .
\end{aligned}$$

A similar result is obtained for $\mathfrak{F}^{-}_{k_1k_2\ldots}$. Spectroscopic factors for the addition (removal) of a nucleon are denoted by $\mathfrak{F}^{+}_{k}(\mathfrak{F}^{-}_{k})$ and thus read as [132]

$$\mathfrak{F}^{+}_{k} \equiv \sum_p \langle\Phi|c_p|\Phi^k\rangle\langle\Phi^k|c_p^\dagger|\Phi\rangle = \sum_p |U_{pk}|^2 , \tag{2.7a}$$

$$\mathfrak{F}^{-}_{k} \equiv \sum_p \langle\Phi|c_p^\dagger|\Phi^k\rangle\langle\Phi^k|c_p|\Phi\rangle = \sum_p |V_{pk}|^2 , \tag{2.7b}$$

where the odd number-parity states $|\Phi^k\rangle \equiv \beta_k^\dagger|\Phi\rangle$ describe the A $\pm$ 1 systems.

The total binding energy $\mathcal{E}_0$ is obtained through the normal ordering of Ω with respect to $|\Phi\rangle$ given that $\Omega^{00} = H^{00} - \lambda A^{00} = \mathcal{E}_0 - \lambda$A (see Eqs. (C.2a) and (C.5)). The energy can also be computed from the Galitskii-Koltun sum rule at play in self-consistent Gorkov-Green's function theory [95]. This alternative formulation provides a check for consistency and convergence in the solution of the Bogoliubov equations, and can be written under the form of a trace over the one-body Hilbert space $\mathcal{H}_1$, i.e.

$$\Omega^{00} = +\frac{1}{4\pi i}\int_C \mathrm{d}\omega\ \sum_{pq}\left\{G^{11(0)}_{qp}(\omega)\left[T_{pq} - \lambda\delta_{pq} + \omega\delta_{pq}\right]\right\} - \frac{1}{6}\sum_{pq}\left\{\Gamma^{3N}_{qp}\rho_{pq} + \Delta^{3N}_{qp}\kappa^*_{pq}\right\} , \tag{2.8}$$

where $G^{11(0)}(\omega)$ denotes the Bogoliubov approximation to the normal Gorkov propagator[2] [95], while the second term represents the explicit correction to the standard Galitskii-Koltun sum

[2]This propagator must not be confused with the soon-to-be-introduced unperturbed propagator used in the BMBPT formalism.

rule due to the presence of three-nucleon forces [56]. The explicit expressions of the Hartree-Fock Γ^{3N} and Bogoliubov Δ^{3N} fields associated with the three-nucleon force contribution are provided in App. C.2. Writing $G^{11(0)}(\omega)$ in its Lehmann representation

$$G^{11(0)}_{pq}(\omega) = \sum_k \frac{U_{pk}U^*_{qk}}{\omega - E_k + i\eta} + \frac{V^*_{pk}V_{qk}}{\omega + E_k - i\eta} \,, \tag{2.9}$$

where η is an infinitesimally small positive parameter, the contour integral in Eq. (2.8) is effected over the upper-half plan to obtain

$$\mathcal{E}_0 = +\frac{1}{2}\sum_{pq} t_{pq}\,\rho_{qp} - \frac{1}{2}\sum_k (E_k - \lambda)\;\mathfrak{F}^-_k - \frac{1}{6}\sum_{pq}\left[\Gamma^{3N}_{pq}\,\rho_{qp} + \Delta^{3N}_{pq}\,\kappa^*_{qp}\right] . \tag{2.10}$$

2.1.3. Hartree-Fock-Bogoliubov reference state

The expressions thus far have been formulated for an arbitrary Bogoliubov vacuum (Eq. (1.26)). In practical applications, one must specify how the quasi-particle operators $\{\beta_k; \beta^\dagger_k\}$ and energies $\{E_k\}$ entering Eq. (2.4) are determined. This corresponds to fixing the Bogoliubov transformation W (Eq. (1.23)), and thus $|\Phi\rangle$, along with $\bar{\Omega}^{11}$. Several choices are possible for $|\Phi\rangle$: a Brueckner reference state which maximizes the overlap with the true ground state [133], a simple BCS state, or the solution of the variational problem, i.e. the Bogoliubov vacuum $|\Phi_{\mathrm{HFB}}\rangle$ that solves self-consistent Hartree-Fock-Bogoliubov (HFB) equations [109] under a set of symmetry requirements so that $|\Phi_{\mathrm{HFB}}\rangle$ minimizes Ω^{00}. We focus here on the last option.

The HFB approach invokes Ritz' variational principle to minimize the energy under the constraint that $\langle\Phi|A|\Phi\rangle = A_0$ via

$$\delta\frac{\langle\Phi|\Omega|\Phi\rangle}{\langle\Phi|\Phi\rangle} = 0 \,, \tag{2.11}$$

where small variations of the wavefunction $|\delta\Phi\rangle$ are considered under the constraint that the state remains a Bogoliubov product state. Since the chosen wavefunction $|\Phi'\rangle = |\Phi\rangle + |\delta\Phi\rangle$ is non-orthogonal to $|\Phi\rangle$, Thouless' theorem [128] states that $|\Phi'\rangle$ can be expressed under the form

$$|\Phi'\rangle = \langle\Phi|\Phi'\rangle \exp\!\left(\frac{1}{2}\sum_{kk'} Z_{kk'}\beta^\dagger_k\beta^\dagger_{k'}\right)|\Phi\rangle \,, \tag{2.12}$$

where Z is a skew-symmetric matrix whose independent matrix elements constitute the variational parameters. Employing Eqs. (2.11) and (2.12) and truncating to second order in the expansion leads to

$$\begin{aligned}\frac{\langle\Phi'|\Omega|\Phi'\rangle}{\langle\Phi'|\Phi'\rangle} = \Omega^{00} &+ \frac{1}{2}\sum_{k_1k_2}\left(\Omega^{20}_{k_1k_2}Z^*_{k_1k_2} + \Omega^{02}_{k_1k_2}Z_{k_1k_2}\right) \\ &+ \frac{1}{8}\sum_{k_1k_2k_3k_4}\left(\Omega^{40}_{k_1k_2k_3k_4}Z^*_{k_1k_2}Z^*_{k_3k_4} + \Omega^{04}_{k_1k_2k_3k_4}Z_{k_1k_2}Z_{k_3k_4} + 2\Omega^{22}_{k_1k_2k_3k_4}Z^*_{k_1k_2}Z_{k_3k_4}\right) .\end{aligned} \tag{2.13}$$

The variation with respect to $Z^*_{k_1k_2}$ yields, for all (k_1, k_2),

$$\frac{\partial}{\partial Z^*_{k_1k_2}}\frac{\langle\Phi'|\Omega|\Phi'\rangle}{\langle\Phi'|\Phi'\rangle}\bigg|_{Z=0} = \Omega^{20}_{k_1k_2} = 0 \,, \tag{2.14}$$

with a complementary equation for the variation with respect to $Z_{k_1k_2}$ to produce

$$\Omega^{02}_{k_1k_2} = 0 \ . \tag{2.15}$$

The requirements $\Omega^{20}_{k_1k_2} = \Omega^{02}_{k_1k_2} = 0$ do not constrain the form of $\Omega^{11}_{k_1k_2}$. However, the additional requirement to make Ω^{11} diagonal such that $\Omega^{11}_{k_1k_2} = \delta_{k_1k_2} E_{k_1}$ allows one to find the variational solution via the diagonalization of the matrix

$$\mathfrak{H}_{qp} \equiv \begin{pmatrix} \Omega^{11} & \Omega^{20} \\ -\Omega^{02} & -\Omega^{11} \end{pmatrix} \ . \tag{2.16}$$

Transforming back to the single-particle basis of Eq. (1.20) provides the usual form of the HFB Hamiltonian matrix

$$H_{\mathrm{HFB}} = \mathcal{W}\mathfrak{H}_{qp}\mathcal{W}^\dagger = \begin{pmatrix} h-\lambda & \Delta \\ -\Delta^* & -(h-\lambda)^* \end{pmatrix} \ , \tag{2.17}$$

where h and Δ are defined in Eq. (C.5), such that finding the variational minimum amounts to solving the so-called HFB eigenvalue equation [109]

$$\begin{pmatrix} h-\lambda & \Delta \\ -\Delta^* & -(h-\lambda)^* \end{pmatrix} \begin{pmatrix} U_k \\ V_k \end{pmatrix} = E_k \begin{pmatrix} U_k \\ V_k \end{pmatrix} \ , \tag{2.18}$$

where columns (U_k, V_k) of the U and V matrices determine the quasiparticle operators $\{\beta_k; \beta_k^\dagger\}$ of Eq. (1.20).

In practical applications, the HFB solution will be utilized as the Bogoliubov vacuum. This corresponds to working within a Møller-Plesset scheme. While this choice conveniently leads to canceling Ω^{20} and Ω^{02} in Ω while setting $\bar{\Omega}^{11} = \Omega^{11}$ so that $\breve{\Omega}^{11} = 0$, we do not impose this choice a priori in order to design the formalism in its general Rayleigh-Schrödinger form. Therefore, a general Bogoliubov vacuum is used to derive Bogoliubov MBPT equations. Eventually, the Møller-Plesset scheme can be obtained by imposing the above choice for Ω^{20}, Ω^{02}, $\bar{\Omega}^{11}$ and $\breve{\Omega}^{11}$.

The careful reader of Eq. (2.18) will have noticed that the HFB equation returns $2n$ eigenvalues E_k, with n the dimension of the one-body Hilbert space $\mathcal{H}_1$. However, those eigenvalues come in pairs, with n positive eigenvalues $+E_k$ and their n negative counterparts $-E_k$ [134]. The lowest HFB solution of even number parity is actually obtained by only conserving positive eigenvalues $+E_k$ and their associated (U_k, V_k) vector when building the density matrices ρ and κ as well as the fields h and Δ.

2.2. Unperturbed propagator

Quasi-particle creation and annihilation operators read in the interaction representation as

$$\beta_k(\tau) \equiv e^{+\tau\Omega_0}\, \beta_k\, e^{-\tau\Omega_0} = e^{-\tau E_k}\, \beta_k \ , \tag{2.19a}$$

$$\beta_k^\dagger(\tau) \equiv e^{+\tau\Omega_0}\, \beta_k^\dagger\, e^{-\tau\Omega_0} = e^{+\tau E_k}\, \beta_k^\dagger \ . \tag{2.19b}$$

The generalized unperturbed one-body propagator is introduced as a 2×2 matrix in Bogoliubov space

$$\mathbf{G}^0 \equiv \begin{pmatrix} G^{+-(0)} & G^{--(0)} \\ G^{++(0)} & G^{-+(0)} \end{pmatrix} \ , \tag{2.20}$$

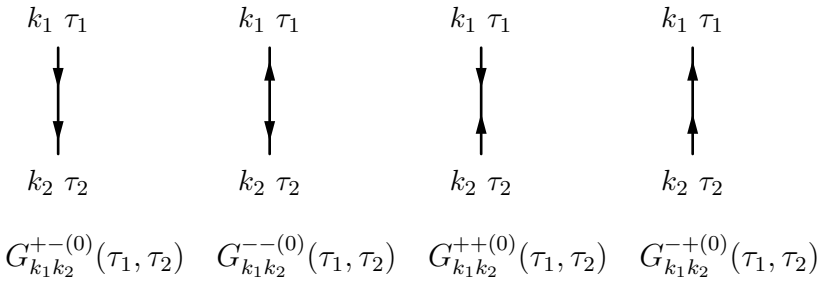

Figure 2.1. Diagrammatic representation of the four unperturbed elementary one-body propagators $G^{gg'(0)}$. The association between the propagators and their diagrammatic representation is presently obtained by reading the diagram from top to bottom.

whose four components are defined through their matrix elements in the quasi-particle basis $\{\beta_k;\beta_k^\dagger\}$ according to

$$G^{+-(0)}_{k_1k_2}(\tau_1,\tau_2) \equiv \frac{\langle\Phi|\mathrm{T}[\beta^\dagger_{k_1}(\tau_1)\beta_{k_2}(\tau_2)]|\Phi\rangle}{\langle\Phi|\Phi\rangle} \ , \tag{2.21a}$$

$$G^{--(0)}_{k_1k_2}(\tau_1,\tau_2) \equiv \frac{\langle\Phi|\mathrm{T}[\beta_{k_1}(\tau_1)\beta_{k_2}(\tau_2)]|\Phi\rangle}{\langle\Phi|\Phi\rangle} \ , \tag{2.21b}$$

$$G^{++(0)}_{k_1k_2}(\tau_1,\tau_2) \equiv \frac{\langle\Phi|\mathrm{T}[\beta^\dagger_{k_1}(\tau_1)\beta^\dagger_{k_2}(\tau_2)]|\Phi\rangle}{\langle\Phi|\Phi\rangle} \ , \tag{2.21c}$$

$$G^{-+(0)}_{k_1k_2}(\tau_1,\tau_2) \equiv \frac{\langle\Phi|\mathrm{T}[\beta_{k_1}(\tau_1)\beta^\dagger_{k_2}(\tau_2)]|\Phi\rangle}{\langle\Phi|\Phi\rangle} \ , \tag{2.21d}$$

where T denotes the time-ordering operator, i.e. it orders a product of operators depending on their time labels in decreasing order (larger times to the left) and multiplies it with the signature of the permutation used to achieve the corresponding reordering. For example, considering two time-dependent operators $A(t)$ and $B(t)$, one has

$$\mathrm{T}\left[A(t_1)B(t_2)\right] = \theta(t_1-t_2)A(t_1)B(t_2) - \theta(t_2-t_1)B(t_2)A(t_1) \ . \tag{2.22}$$

The diagrammatic representation of the four elementary propagators $G^{gg'(0)}$, with $g \equiv \pm$ and $g' \equiv \pm$, is provided in Fig. 2.1. The two propagators with $g = g'$ are said to be *anomalous* as they involve two quasi-particle operators of the same kind, i.e. two creation or two annihilation operators. Contrarily, the two propagators with $g \neq g'$ are said to be *normal*. The above definition of propagators implies the relations

$$G^{+-(0)}_{k_1k_2}(\tau_1,\tau_2) = -G^{-+(0)}_{k_2k_1}(\tau_2,\tau_1) \ , \tag{2.23a}$$

$$G^{--(0)}_{k_1k_2}(\tau_1,\tau_2) = -G^{--(0)}_{k_2k_1}(\tau_2,\tau_1) \ , \tag{2.23b}$$

$$G^{++(0)}_{k_1k_2}(\tau_1,\tau_2) = -G^{++(0)}_{k_2k_1}(\tau_2,\tau_1) \ . \tag{2.23c}$$

It is to be noted that, as Eq. (2.23a) translates an antisymmetry relation between $G^{+-(0)}$ and $G^{-+(0)}$, it allows to eventually consider only one of the two normal propagators in diagrammatic representations, once the reading direction has been fixed at the price of introducing minus signs.

Combining Eqs. (1.30) and (2.19), together with the vacuum character of $|\Phi\rangle$, one obtains

$$\begin{aligned}
G^{+-(0)}_{k_1k_2}(\tau_1,\tau_2) &= \frac{\langle\Phi|\mathrm{T}[\beta^\dagger_{k_1}(\tau_1)\beta_{k_2}(\tau_2)]|\Phi\rangle}{\langle\Phi|\Phi\rangle} \\
&= +\theta(\tau_1-\tau_2)\frac{\langle\Phi|\beta^\dagger_{k_1}(\tau_1)\beta_{k_2}(\tau_2)|\Phi\rangle}{\langle\Phi|\Phi\rangle} - \theta(\tau_2-\tau_1)\frac{\langle\Phi|\beta_{k_2}(\tau_2)\beta^\dagger_{k_1}(\tau_1)|\Phi\rangle}{\langle\Phi|\Phi\rangle} \\
&= +\theta(\tau_1-\tau_2)e^{\tau_1 E_{k_1}}e^{-\tau_2 E_{k_2}}\frac{\langle\Phi|\beta^\dagger_{k_1}\beta_{k_2}|\Phi\rangle}{\langle\Phi|\Phi\rangle} - \theta(\tau_2-\tau_1)e^{\tau_1 E_{k_1}}e^{-\tau_2 E_{k_2}}\frac{\langle\Phi|\beta_{k_2}\beta^\dagger_{k_1}|\Phi\rangle}{\langle\Phi|\Phi\rangle} \\
&= +\theta(\tau_1-\tau_2)e^{\tau_1 E_{k_1}}e^{-\tau_2 E_{k_2}}R^{+-}_{k_1k_2} - \theta(\tau_2-\tau_1)e^{\tau_1 E_{k_1}}e^{-\tau_2 E_{k_2}}R^{-+}_{k_2k_1} \\
&= -\theta(\tau_2-\tau_1)e^{\tau_1 E_{k_1}}e^{-\tau_2 E_{k_2}}\delta_{k_2k_1} \\
&= -\theta(\tau_2-\tau_1)e^{-(\tau_2-\tau_1)E_{k_1}}\delta_{k_1k_2} \ .
\end{aligned}$$

Proceeding similarly for the other propagators, one finally obtains

$$G^{+-(0)}_{k_1k_2}(\tau_1,\tau_2) = -e^{-(\tau_2-\tau_1)E_{k_1}}\theta(\tau_2-\tau_1)\delta_{k_1k_2} \ , \tag{2.24a}$$

$$G^{--(0)}_{k_1k_2}(\tau_1,\tau_2) = 0 \ , \tag{2.24b}$$

$$G^{++(0)}_{k_1k_2}(\tau_1,\tau_2) = 0 \ , \tag{2.24c}$$

$$G^{-+(0)}_{k_1k_2}(\tau_1,\tau_2) = +e^{-(\tau_1-\tau_2)E_{k_1}}\theta(\tau_1-\tau_2)\delta_{k_1k_2} \ , \tag{2.24d}$$

in agreement with Eq. (2.23a). We observe the important fact that BMBPT worked out in the quasi-particle basis does not involve anomalous propagators.

The equal-time unperturbed propagator deserves special attention. Equal-time propagators will solely arise from contracting two quasi-particle operators belonging to the same normal-ordered operator displaying creation operators to the left of annihilation ones. In both $G^{+-(0)}_{k_1k_2}(\tau,\tau)$ and $G^{-+(0)}_{k_1k_2}(\tau,\tau)$, this necessarily leads to selecting a contraction associated with R^{+-} that is identically zero. As a result, no equal-time contraction, and thus no contraction of an interaction vertex onto itself, can occur.

2.3. Expansion of the evolution operator

The imaginary-time evolution operator $\mathcal{U}(\tau)$ defined in Eq. (1.32) can be expanded in powers of Ω_1. Taking τ real, one writes

$$\mathcal{U}(\tau) \equiv e^{-\tau\Omega_0}\,\mathcal{U}_1(\tau) \tag{2.25}$$

such that

$$\mathcal{U}_1(\tau) = e^{\tau\Omega_0}\,e^{-\tau(\Omega_0+\Omega_1)} \ , \tag{2.26}$$

and thus

$$\partial_\tau\mathcal{U}_1(\tau) = -e^{\tau\Omega_0}\,\Omega_1\,e^{-\tau\Omega_0}\,\mathcal{U}_1(\tau) \ . \tag{2.27}$$

The formal solution to Eq. (2.27) reads

$$\mathcal{U}_1(\tau) = \mathrm{T}e^{-\int_0^\tau \mathrm{d}t\Omega_1(t)} \ , \tag{2.28}$$

with the initial condition that $\mathcal{U}_1(0) = \mathcal{U}(0) = \mathbb{1}$ and where $\Omega_1(\tau)$ defines the perturbation in the interaction representation[3]

$$\Omega_1(\tau) \equiv e^{\tau\Omega_0}\,\Omega_1\,e^{-\tau\Omega_0}\ . \tag{2.29}$$

Eventually, the full solution reads as

$$\mathcal{U}(\tau) = e^{-\tau\Omega_0}\,\mathrm{T}e^{-\int_0^\tau \mathrm{d}\tau\Omega_1(\tau)}\ . \tag{2.30}$$

2.4. Norm kernel

2.4.1. Perturbative expansion

Expressing Ω_1 in the eigenbasis of Ω_0 and expanding the exponential in Eq. (2.30) in power series, one obtains the perturbative expansion of the time-dependent norm kernel

$$\begin{aligned}
N(\tau) &= \langle\Phi|\mathcal{U}(\tau)|\Phi\rangle \\
&= \langle\Phi|e^{-\tau\Omega_0}\mathcal{U}_1(t)|\Phi\rangle \\
&= e^{-\tau\Omega_{00}}\langle\Phi|\mathrm{T}e^{-\int_0^\tau \mathrm{d}t\Omega_1(t)}|\Phi\rangle \\
&= e^{-\tau\Omega^{00}}\langle\Phi|\left\{1 - \int_0^\tau \mathrm{d}\tau_1\Omega_1\left(\tau_1\right) + \frac{1}{2!}\int_0^\tau \mathrm{d}\tau_1\mathrm{d}\tau_2\mathrm{T}\left[\Omega_1\left(\tau_1\right)\Omega_1\left(\tau_2\right)\right] + ...\right\}|\Phi\rangle \\
&= e^{-\tau\Omega^{00}}\left\{\sum_{p=0}^{\infty}\frac{(-1)^p}{p!}\sum_{\substack{i_1+j_1=2,4\\ \vdots \\ i_p+j_p=2,4}}\int_0^\tau \mathrm{d}\tau_1\ldots\mathrm{d}\tau_p\sum_{\substack{k_1\ldots k_{i_1}\\ k_{i_1+1}\ldots k_{i_1+j_1}\\ \vdots \\ l_1\ldots l_{i_p}\\ l_{i_p+1}\ldots l_{i_p+j_p}}}\frac{\Omega^{i_1j_1}_{k_1\ldots k_{i_1}k_{i_1+1}\ldots k_{i_1+j_1}}}{(i_1)!(j_1)!}\ldots\frac{\Omega^{i_pj_p}_{l_1\ldots l_{i_p}l_{i_p+1}\ldots l_{i_p+j_p}}}{(i_p)!(j_p)!}\right. \\
&\quad\times\langle\Phi|\mathrm{T}\left[\beta^\dagger_{k_1}\left(\tau_1\right)\ldots\beta^\dagger_{k_{i_1}}\left(\tau_1\right)\beta_{k_{i_1+j_1}}\left(\tau_1\right)\ldots\beta_{k_{i_1+1}}\left(\tau_1\right)\ldots\right. \\
&\qquad\left.\left.\ldots\beta^\dagger_{l_1}\left(\tau_p\right)\ldots\beta^\dagger_{l_{i_p}}\left(\tau_p\right)\beta_{l_{i_p+j_p}}\left(\tau_p\right)\ldots\beta_{l_{i_p+1}}\left(\tau_p\right)\right]|\Phi\rangle\right\}\ ,
\end{aligned} \tag{2.31}$$

where $\breve{\Omega}^{11}$ must be understood in place of Ω^{11} whenever necessary.

Thanks to time-dependent Wick's theorem [118], each matrix element of products of time-dependent field operators appearing in Eq. (2.31) can be expressed as the sum of all possible systems of products of elementary contractions $G^{gg'(0)}_{k_1k_2}(\tau_1,\tau_2)$ (Eqs. (2.21-2.24)), eventually multiplied by the unperturbed norm kernel $\langle\Phi|\Phi\rangle$. As discussed at length in the following, the corresponding set of algebraic contributions can be put in full correspondence with a diagrammatic representation.

[3] A time-dependent *operator* $O(\tau) = \mathcal{U}_0^{-1}(\tau)O\mathcal{U}_0(\tau)$ in the interaction representation, with $\mathcal{U}(\tau) = \mathcal{U}_0(\tau)\mathcal{U}_1(\tau)$, should not be confused with the time-dependent *kernel* $O(\tau) = \langle\Phi|\mathcal{U}(\tau)O|\Phi\rangle$ of that operator as defined in Eq. (1.38). In general, the situation is transparent enough to avoid the confusion.

2.4.2. Extraction of the diagrammatic rules

As discussed in the introduction, the pedestrian application of Wick's theorem becomes quickly cumbersome as the order p increases. Furthermore, it leads to computing independently many contributions that are in fact identical. By identifying the corresponding pattern, one can design a diagrammatic representation of the various contributions and evaluate their algebraic expressions such that a single diagram captures all identical contributions at once. In order to achieve this goal, one must first introduce the diagrammatic representation of the building blocks.

Let us now derive simple contributions to the norm kernel (Eq. 2.31) to infer some of the diagrammatic rules that are eventually needed to determine all contributions systematically.

First order One first focuses on first-order contributions, i.e. terms characterized by $p = 1$ in Eq. ((2.31)). Expanding Ω_1 in terms of its normal-ordered contributions (Eq. (2.2b)) and applying Wick's theorem leads to[4]

$$
\begin{aligned}
N^{(1)}(\tau) &= -\int_0^\tau \mathrm{d}\tau_1 \langle\Phi|\Omega_1(\tau_1)|\Phi\rangle \\
&= -\int_0^\tau \mathrm{d}\tau_1 \Bigg\{ \sum_{k_1k_2} \frac{\breve{\Omega}^{11}_{k_1k_2}}{1!\,1!} \langle\Phi|\mathrm{T}\left[\beta^\dagger_{k_1}(\tau_1)\beta_{k_2}(\tau_1)\right]|\Phi\rangle \\
&\qquad + \sum_{k_1k_2} \frac{\Omega^{20}_{k_1k_2}}{2!\,0!} \langle\Phi|\mathrm{T}\left[\beta^\dagger_{k_1}(\tau_1)\beta^\dagger_{k_2}(\tau_1)\right]|\Phi\rangle + \sum_{k_1k_2} \frac{\Omega^{02}_{k_1k_2}}{0!\,2!} \langle\Phi|\mathrm{T}\left[\beta_{k_2}(\tau_1)\beta_{k_1}(\tau_1)\right]|\Phi\rangle \\
&\qquad + \sum_{k_1k_2k_3k_4} \frac{\Omega^{22}_{k_1k_2k_3k_4}}{2!\,2!} \langle\Phi|\mathrm{T}\left[\beta^\dagger_{k_1}(\tau_1)\beta^\dagger_{k_2}(\tau_1)\beta_{k_4}(\tau_1)\beta_{k_3}(\tau_1)\right]|\Phi\rangle \\
&\qquad + \sum_{k_1k_2k_3k_4} \frac{\Omega^{31}_{k_1k_2k_3k_4}}{3!\,1!} \langle\Phi|\mathrm{T}\left[\beta^\dagger_{k_1}(\tau_1)\beta^\dagger_{k_2}(\tau_1)\beta^\dagger_{k_3}(\tau_1)\beta_{k_4}(\tau_1)\right]|\Phi\rangle \\
&\qquad + \sum_{k_1k_2k_3k_4} \frac{\Omega^{13}_{k_1k_2k_3k_4}}{1!\,3!} \langle\Phi|\mathrm{T}\left[\beta^\dagger_{k_1}(\tau_1)\beta_{k_4}(\tau_1)\beta_{k_3}(\tau_1)\beta_{k_2}(\tau_1)\right]|\Phi\rangle \\
&\qquad + \sum_{k_1k_2k_3k_4} \frac{\Omega^{40}_{k_1k_2k_3k_4}}{4!\,0!} \langle\Phi|\mathrm{T}\left[\beta^\dagger_{k_1}(\tau_1)\beta^\dagger_{k_2}(\tau_1)\beta^\dagger_{k_3}(\tau_1)\beta^\dagger_{k_4}(\tau_1)\right]|\Phi\rangle \\
&\qquad + \sum_{k_1k_2k_3k_4} \frac{\Omega^{04}_{k_1k_2k_3k_4}}{0!\,4!} \langle\Phi|\mathrm{T}\left[\beta_{k_4}(\tau_1)\beta_{k_3}(\tau_1)\beta_{k_2}(\tau_1)\beta_{k_1}(\tau_1)\right]|\Phi\rangle \Bigg\}
\end{aligned}
$$

[4] We omit here and in similar developments the factor $e^{-\tau\Omega^{00}}$ (see Eq. (2.31)), which will be brought back later.

$$
\begin{aligned}
= -\int_0^\tau \mathrm{d}\tau_1 \Bigg\{ & \sum_{k_1 k_2} \breve{\Omega}^{11}_{k_1 k_2} G^{+-(0)}_{k_1 k_2}(\tau_1,\tau_1) \\
& + \frac{1}{2}\sum_{k_1 k_2} \Omega^{20}_{k_1 k_2} G^{++(0)}_{k_1 k_2}(\tau_1,\tau_1) + \frac{1}{2}\sum_{k_1 k_2} \Omega^{02}_{k_1 k_2} G^{--(0)}_{k_2 k_1}(\tau_1,\tau_1) \\
& + \frac{1}{4}\sum_{k_1 k_2 k_3 k_4} \Omega^{22}_{k_1 k_2 k_3 k_4} \Big(G^{++(0)}_{k_1 k_2}(\tau_1,\tau_1) G^{--(0)}_{k_4 k_3}(\tau_1,\tau_1) \\
& \qquad - G^{+-(0)}_{k_1 k_4}(\tau_1,\tau_1) G^{+-(0)}_{k_2 k_3}(\tau_1,\tau_1) \\
& \qquad + G^{+-(0)}_{k_1 k_3}(\tau_1,\tau_1) G^{+-(0)}_{k_2 k_4}(\tau_1,\tau_1) \Big) \\
& + \frac{1}{3!}\sum_{k_1 k_2 k_3 k_4} \Omega^{31}_{k_1 k_2 k_3 k_4} \Big(G^{++(0)}_{k_1 k_2}(\tau_1,\tau_1) G^{+-(0)}_{k_3 k_4}(\tau_1,\tau_1) \\
& \qquad - G^{++(0)}_{k_1 k_3}(\tau_1,\tau_1) G^{+-(0)}_{k_2 k_4}(\tau_1,\tau_1) \\
& \qquad + G^{+-(0)}_{k_1 k_4}(\tau_1,\tau_1) G^{++(0)}_{k_2 k_3}(\tau_1,\tau_1) \Big) \\
& + \frac{1}{3!}\sum_{k_1 k_2 k_3 k_4} \Omega^{13}_{k_1 k_2 k_3 k_4} \Big(G^{+-(0)}_{k_1 k_4}(\tau_1,\tau_1) G^{--(0)}_{k_3 k_2}(\tau_1,\tau_1) \\
& \qquad - G^{+-(0)}_{k_1 k_3}(\tau_1,\tau_1) G^{--(0)}_{k_4 k_2}(\tau_1,\tau_1) \\
& \qquad + G^{+-(0)}_{k_1 k_2}(\tau_1,\tau_1) G^{--(0)}_{k_4 k_3}(\tau_1,\tau_1) \Big) \\
& + \frac{1}{4!}\sum_{k_1 k_2 k_3 k_4} \Omega^{40}_{k_1 k_2 k_3 k_4} \Big(G^{++(0)}_{k_1 k_2}(\tau_1,\tau_1) G^{++(0)}_{k_3 k_4}(\tau_1,\tau_1) \\
& \qquad - G^{++(0)}_{k_1 k_3}(\tau_1,\tau_1) G^{++(0)}_{k_2 k_4}(\tau_1,\tau_1) \\
& \qquad + G^{++(0)}_{k_1 k_4}(\tau_1,\tau_1) G^{++(0)}_{k_2 k_3}(\tau_1,\tau_1) \Big) \\
& + \frac{1}{4!}\sum_{k_1 k_2 k_3 k_4} \Omega^{04}_{k_1 k_2 k_3 k_4} \Big(G^{++(0)}_{k_4 k_3}(\tau_1,\tau_1) G^{++(0)}_{k_2 k_1}(\tau_1,\tau_1) \\
& \qquad - G^{++(0)}_{k_4 k_2}(\tau_1,\tau_1) G^{++(0)}_{k_3 k_1}(\tau_1,\tau_1) \\
& \qquad + G^{++(0)}_{k_4 k_1}(\tau_1,\tau_1) G^{++(0)}_{k_3 k_2}(\tau_1,\tau_1) \Big) \Bigg\} \\
= 0 \ , &
\end{aligned}
\tag{2.32}
$$

as equal-time propagators are identically zero. One recovers the results of Eq. (2.24), i.e. normal-ordered operator vertices cannot form contractions with themselves, and thus, the first-order contribution to the norm kernel is zero.

Second order Let us now consider the second-order contribution to the norm kernel, i.e. $p = 1, 2$ in Eq. (2.31). Applying Wick's theorem leads to

$$
\begin{aligned}
N^{(2)}(\tau) &= N^{(1)}(\tau) + \frac{1}{2!}\int_0^\tau \mathrm{d}\tau_1 \mathrm{d}\tau_2 \langle\Phi|\mathrm{T}\left[\Omega_1(\tau_1)\Omega_1(\tau_2)\right]|\Phi\rangle \\
&= \frac{1}{2!}\int_0^\tau \mathrm{d}\tau_1 \mathrm{d}\tau_2 \Bigg\{ \sum_{k_1k_2l_1l_2} \frac{\breve{\Omega}^{11}_{k_1k_2}}{1!\,1!}\frac{\breve{\Omega}^{11}_{l_1l_2}}{1!\,1!}\langle\Phi|\mathrm{T}\left[\beta^\dagger_{k_1}(\tau_1)\beta_{k_2}(\tau_1)\beta^\dagger_{l_1}(\tau_2)\beta_{l_2}(\tau_2)\right]|\Phi\rangle \\
&\quad + \sum_{k_1k_2l_1l_2} \frac{\Omega^{02}_{k_1k_2}}{0!\,2!}\frac{\Omega^{20}_{l_1l_2}}{2!\,0!}\langle\Phi|\mathrm{T}\left[\beta_{k_2}(\tau_1)\beta_{k_1}(\tau_1)\beta^\dagger_{l_1}(\tau_2)\beta^\dagger_{l_2}(\tau_2)\right]|\Phi\rangle \\
&\quad + \sum_{k_1k_2l_1l_2} \frac{\Omega^{20}_{k_1k_2}}{2!\,0!}\frac{\Omega^{02}_{l_1l_2}}{0!\,2!}\langle\Phi|\mathrm{T}\left[\beta^\dagger_{k_1}(\tau_1)\beta^\dagger_{k_2}(\tau_1)\beta_{l_2}(\tau_2)\beta_{l_1}(\tau_2)\right]|\Phi\rangle \\
&\quad + \sum_{k_1k_2l_1l_2} \frac{\breve{\Omega}^{11}_{k_1k_2}}{1!\,1!}\frac{\Omega^{02}_{l_1l_2}}{0!\,2!}\langle\Phi|\mathrm{T}\left[\beta^\dagger_{k_1}(\tau_1)\beta_{k_2}(\tau_1)\beta_{l_2}(\tau_2)\beta_{l_1}(\tau_2)\right]|\Phi\rangle \\
&\quad + \sum_{k_1k_2l_1l_2} \frac{\breve{\Omega}^{11}_{k_1k_2}}{1!\,1!}\frac{\Omega^{20}_{l_1l_2}}{2!\,0!}\langle\Phi|\mathrm{T}\left[\beta^\dagger_{k_1}(\tau_1)\beta_{k_2}(\tau_1)\beta^\dagger_{l_1}(\tau_2)\beta^\dagger_{l_2}(\tau_2)\right]|\Phi\rangle \\
&\quad + \sum_{k_1k_2l_1l_2} \frac{\Omega^{20}_{k_1k_2}}{2!\,0!}\frac{\breve{\Omega}^{11}_{l_1l_2}}{1!\,1!}\langle\Phi|\mathrm{T}\left[\beta^\dagger_{k_1}(\tau_1)\beta^\dagger_{k_2}(\tau_1)\beta^\dagger_{l_1}(\tau_2)\beta_{l_2}(\tau_2)\right]|\Phi\rangle \\
&\quad + \sum_{k_1k_2l_1l_2} \frac{\Omega^{02}_{k_1k_2}}{0!\,2!}\frac{\breve{\Omega}^{11}_{l_1l_2}}{1!\,1!}\langle\Phi|\mathrm{T}\left[\beta_{k_2}(\tau_1)\beta_{k_1}(\tau_1)\beta^\dagger_{l_1}(\tau_2)\beta_{l_2}(\tau_2)\right]|\Phi\rangle \\
&\quad + \sum_{k_1k_2l_1l_2} \frac{\Omega^{02}_{k_1k_2}}{0!\,2!}\frac{\Omega^{02}_{l_1l_2}}{0!\,2!}\langle\Phi|\mathrm{T}\left[\beta_{k_2}(\tau_1)\beta_{k_1}(\tau_1)\beta_{l_2}(\tau_2)\beta_{l_1}(\tau_2)\right]|\Phi\rangle \\
&\quad + \sum_{k_1k_2l_1l_2} \frac{\Omega^{20}_{k_1k_2}}{2!\,0!}\frac{\Omega^{20}_{l_1l_2}}{2!\,0!}\langle\Phi|\mathrm{T}\left[\beta^\dagger_{k_1}(\tau_1)\beta^\dagger_{k_2}(\tau_1)\beta^\dagger_{l_1}(\tau_2)\beta^\dagger_{l_2}(\tau_2)\right]|\Phi\rangle \\
&\quad + \quad \dots \Bigg\} \,,
\end{aligned}
\tag{2.33}
$$

where dots indicate remaining terms originating from the expansion of both $\Omega_1(\tau_1)$ and $\Omega_1(\tau_2)$ according to Eq. (2.2b).

We only wish to calculate few of the second-order contributions, and extrapolate diagrammatic rules out of them. Let us first calculate the $\Omega^{02}\Omega^{20}$ term. We have to consider all contractions

allowed by Wick's theorem

$$
\begin{aligned}
N^{(2)}_{02.20}(\tau) &\equiv \frac{1}{2!}\int_0^\tau \mathrm{d}\tau_1\mathrm{d}\tau_2 \sum_{k_1k_2l_1l_2} \frac{\Omega^{02}_{k_1k_2}}{0!\,2!}\frac{\Omega^{20}_{l_1l_2}}{2!\,0!}\langle\Phi|\mathrm{T}\left[\beta_{k_2}(\tau_1)\beta_{k_1}(\tau_1)\beta^\dagger_{l_1}(\tau_2)\beta^\dagger_{l_2}(\tau_2)\right]|\Phi\rangle \\
&= \frac{1}{8}\int_0^\tau \mathrm{d}\tau_1\mathrm{d}\tau_2 \sum_{k_1k_2l_1l_2} \Omega^{02}_{k_1k_2}\Omega^{20}_{l_1l_2}\Big\{G^{--(0)}_{k_2k_1}(\tau_1,\tau_1)G^{++(0)}_{l_1l_2}(\tau_2,\tau_2) \\
&\qquad\qquad -G^{-+(0)}_{k_2l_1}(\tau_1,\tau_2)G^{-+(0)}_{k_1l_2}(\tau_1,\tau_2) + G^{-+(0)}_{k_2l_2}(\tau_1,\tau_2)G^{-+(0)}_{k_1l_1}(\tau_1,\tau_2)\Big\} \\
&= \frac{1}{8}\int_0^\tau \mathrm{d}\tau_1\mathrm{d}\tau_2 \sum_{k_1k_2l_1l_2} \Omega^{02}_{k_1k_2}\Omega^{20}_{l_1l_2}\Big\{-G^{-+(0)}_{k_2l_1}(\tau_1,\tau_2)G^{-+(0)}_{k_1l_2}(\tau_1,\tau_2) \\
&\qquad\qquad +G^{-+(0)}_{k_2l_2}(\tau_1,\tau_2)G^{-+(0)}_{k_1l_1}(\tau_1,\tau_2)\Big\} \\
&= \frac{1}{8}\sum_{k_1k_2l_1l_2} \Omega^{02}_{k_1k_2}\Omega^{20}_{l_1l_2}\int_0^\tau \mathrm{d}\tau_1\mathrm{d}\tau_2\Big\{-\theta(\tau_1-\tau_2)\delta_{k_2l_1}\delta_{k_1l_2}e^{-(\tau_1-\tau_2)(E_{k_1}+E_{k_2})} \\
&\qquad\qquad +\theta(\tau_1-\tau_2)\delta_{k_2l_2}\delta_{k_1l_1}e^{-(\tau_1-\tau_2)(E_{k_1}+E_{k_2})}\Big\} \\
&= \frac{1}{8}\sum_{k_1k_2l_1l_2} \Omega^{02}_{k_1k_2}\Omega^{20}_{l_1l_2}\left(-\delta_{k_2l_1}\delta_{k_1l_2}+\delta_{k_2l_2}\delta_{k_1l_1}\right)\int_0^\tau \mathrm{d}\tau_1\mathrm{d}\tau_2\theta(\tau_1-\tau_2)e^{-(\tau_1-\tau_2)(E_{k_1}+E_{k_2})} \\
&= \frac{1}{8}\sum_{k_1k_2}\left(-\Omega^{02}_{k_1k_2}\Omega^{20}_{k_2k_1}+\Omega^{02}_{k_1k_2}\Omega^{20}_{k_1k_2}\right)\left[\frac{\tau}{E_{k_1}+E_{k_2}}+\frac{e^{-\tau(E_{k_1}+E_{k_2})}-1}{(E_{k_1}+E_{k_2})^2}\right] \\
&= \frac{1}{4}\sum_{k_1k_2}\frac{\Omega^{02}_{k_1k_2}\Omega^{20}_{k_1k_2}}{E_{k_1}+E_{k_2}}\left[\tau-\frac{1-e^{-\tau(E_{k_1}+E_{k_2})}}{E_{k_1}+E_{k_2}}\right],
\end{aligned}
\tag{2.34}
$$

where Eqs. (2.24d) and (A.1b) have been used along with the antisymmetry of $\Omega^{20}_{k_1k_2}$.

The $\Omega^{20}\Omega^{02}$ term reads similarly as

$$
\begin{aligned}
N^{(2)}_{20.02}(\tau) &\equiv \frac{1}{2!}\int_0^\tau \mathrm{d}\tau_1\mathrm{d}\tau_2 \sum_{k_1k_2l_1l_2} \frac{\Omega^{20}_{k_1k_2}}{2!\,0!}\frac{\Omega^{02}_{l_1l_2}}{0!\,2!}\langle\Phi|\mathrm{T}\left[\beta^\dagger_{k_1}(\tau_1)\beta^\dagger_{k_2}(\tau_1)\beta_{l_2}(\tau_2)\beta_{l_1}(\tau_2)\right]|\Phi\rangle \\
&= \frac{1}{8}\int_0^\tau \mathrm{d}\tau_1\mathrm{d}\tau_2 \sum_{k_1k_2l_1l_2} \Omega^{20}_{k_1k_2}\Omega^{02}_{l_1l_2}\Big\{G^{++(0)}_{k_1k_2}(\tau_1,\tau_1)G^{--(0)}_{l_2l_1}(\tau_2,\tau_2) \\
&\qquad\qquad -G^{+-(0)}_{k_1l_2}(\tau_1,\tau_2)G^{+-(0)}_{k_2l_1}(\tau_1,\tau_2) + G^{+-(0)}_{k_1l_1}(\tau_1,\tau_2)G^{+-(0)}_{k_2l_2}(\tau_1,\tau_2)\Big\} \\
&= \frac{1}{8}\sum_{k_1k_2l_1l_2} \Omega^{20}_{k_1k_2}\Omega^{02}_{l_1l_2}\left(-\delta_{k_2l_1}\delta_{k_1l_2}+\delta_{k_2l_2}\delta_{k_1l_1}\right)\int_0^\tau \mathrm{d}\tau_1\mathrm{d}\tau_2\theta(\tau_2-\tau_1)e^{-(\tau_2-\tau_1)(E_{k_1}+E_{k_2})} \\
&= \frac{1}{4}\sum_{k_1k_2}\frac{\Omega^{20}_{k_1k_2}\Omega^{02}_{k_1k_2}}{E_{k_1}+E_{k_2}}\left[\tau-\frac{1-e^{-\tau(E_{k_1}+E_{k_2})}}{E_{k_1}+E_{k_2}}\right].
\end{aligned}
\tag{2.35}
$$

One notices that the two previous contributions are strictly equal. Actually, trying to represent both of them diagrammatically would produce two time-unlabelled diagrams that are topologically identical. Such a so-called faithful diagrammatic representation, associating each contribution with one diagram, brings however no real simplification. Diagrams must resum identical algebraic contributions in one unique diagram. Thus, contributions derived in Eqs. (2.34) and (2.35) are summarized as one diagram in the diagrammatic representation of the norm kernel in Fig. 2.4, labelled PN2.1. The factor associated with so-called equivalent

lines and with the symmetry under the exchange of time labels in the diagrammatic rules provided below is designed to produce the appropriate net coefficient (i.e. 1/2) obtained when summing both algebraic contributions.

Focusing on the $\breve{\Omega}^{11}\Omega^{02}$ term, one obtains

$$\begin{aligned} N^{(2)}_{11.02}(\tau) &\equiv \frac{1}{2!}\int_0^\tau \mathrm{d}\tau_1\mathrm{d}\tau_2 \sum_{k_1k_2l_1l_2} \frac{\breve{\Omega}^{11}_{k_1k_2}}{1!\,1!}\frac{\Omega^{02}_{l_1l_2}}{0!\,2!}\langle\Phi|\mathrm{T}\left[\beta^\dagger_{k_1}(\tau_1)\beta_{k_2}(\tau_1)\beta_{l_2}(\tau_2)\beta_{l_1}(\tau_2)\right]|\Phi\rangle \\ &= \frac{1}{4}\int_0^\tau \mathrm{d}\tau_1\mathrm{d}\tau_2 \sum_{k_1k_2l_1l_2} \breve{\Omega}^{11}_{k_1k_2}\Omega^{02}_{l_1l_2}\Big\{G^{+-(0)}_{k_1k_2}(\tau_1,\tau_1)G^{--(0)}_{l_1l_2}(\tau_2,\tau_2) \\ &\qquad -G^{+-(0)}_{k_1l_2}(\tau_1,\tau_2)G^{--(0)}_{k_2l_1}(\tau_1,\tau_2) + G^{+-(0)}_{k_1l_1}(\tau_1,\tau_2)G^{--(0)}_{k_2l_2}(\tau_1,\tau_2)\Big\} \\ &= 0\ , \end{aligned} \tag{2.36}$$

as $G^{--(0)}$ is identically zero. In fact, a diagram is identically zero anytime a contraction between two creation or two annihilation operators is considered. Therefore, one can exclude from the start every contribution associated with a combination of operators that bring in total a different number of creation and annihilation operators, as it necessary leads to anomalous contractions.

We now derive the $\breve{\Omega}^{11}\breve{\Omega}^{11}$ term

$$\begin{aligned} N^{(2)}_{11.11}(\tau) &\equiv \frac{1}{2!}\int_0^\tau \mathrm{d}\tau_1\mathrm{d}\tau_2 \sum_{k_1k_2l_1l_2} \frac{\breve{\Omega}^{11}_{k_1k_2}}{1!\,1!}\frac{\breve{\Omega}^{11}_{l_1l_2}}{1!\,1!}\langle\Phi|\mathrm{T}\left[\beta^\dagger_{k_1}(\tau_1)\beta_{k_2}(\tau_1)\beta^\dagger_{l_1}(\tau_2)\beta_{l_2}(\tau_2)\right]|\Phi\rangle \\ &= \frac{1}{2!}\int_0^\tau \mathrm{d}\tau_1\mathrm{d}\tau_2 \sum_{k_1k_2l_1l_2} \breve{\Omega}^{11}_{k_1k_2}\breve{\Omega}^{11}_{l_1l_2}\Big\{G^{+-(0)}_{k_1k_2}(\tau_1,\tau_1)G^{+-(0)}_{l_1l_2}(\tau_2,\tau_2) \\ &\qquad -G^{++(0)}_{k_1l_1}(\tau_1,\tau_2)G^{--(0)}_{k_2l_2}(\tau_1,\tau_2) + G^{+-(0)}_{k_1l_2}(\tau_1,\tau_2)G^{-+(0)}_{k_2l_1}(\tau_1,\tau_2)\Big\} \\ &= -\frac{1}{2!}\sum_{k_1k_2l_1l_2} \breve{\Omega}^{11}_{k_1k_2}\breve{\Omega}^{11}_{l_1l_2}\delta_{k_1l_2}\delta_{k_2l_2}\int_0^\tau \mathrm{d}\tau_1\mathrm{d}\tau_2\theta(\tau_2-\tau_1)\theta(\tau_1-\tau_2)e^{-(\tau_2-\tau_1)(E_{k_1}-E_{k_2})} \\ &= 0\ , \end{aligned} \tag{2.37}$$

as $\theta(\tau_2-\tau_1)\theta(\tau_1-\tau_2)=0$. Hence, normal propagators linking two vertices with different time labels must propagate in the same direction, as could have been inferred from Eqs. (2.24a) and (2.24d), i.e. to be non-zero a contribution must only involve normal propagators of the same type (either $G^{+-(0)}$ or $G^{-+(0)}$) when the latter connect the same two vertices.

Such a rule can be generalized to larger sets of vertices, as a set of propagators running between them in a circular way would introduce a step function loop of the type $\theta(\tau_\alpha-\tau_\beta)\ldots\theta(\tau_\omega-\tau_\alpha)$, hence constraining all the time labels to be equal and resulting in a set of time-equal propagators. Hence, no oriented loop between a set of two or more vertices is possible.

2.4.3. Diagram generation

Equation (2.31) for $N(\tau)$ can be translated into an infinite set of vacuum-to-vacuum diagrams. The topological Feynman rules to build those diagrams are now detailed.

1. A vacuum-to-vacuum, i.e. closed, Feynman diagram of order p consists of p vertices $\Omega^{ij}(\tau_k)$ connected by fermionic quasi-particle lines, i.e. elementary propagators $G^{gg'(0)}$, forming a set of closed loops.

2. Each vertex is labeled by a time variable while each line is labeled by two quasi-particle indices and two time labels at its ends, the latter being associated with the two vertices the line is attached to. Each vertex contributes a factor $\Omega^{ij}_{k_1\dots k_i k_{i+1}\dots k_{i+j}}$ with the sign convention detailed in Sec. 1.12. Each line contributes a factor $G^{gg'(0)}_{k_1k_2}(\tau_k,\tau_{k'})$, where $g=\pm$ and $g'=\pm$ characterize the type of elementary propagator the line corresponds to.

3. The contributions to $N(\tau)$ arising at order p are generated by drawing all possible vacuum-to-vacuum diagrams involving p operators $\Omega_1(\tau_k)$. This is done by contracting the quasi-particle lines attached to the vertices in all possible ways. Eventually, the set of diagrams must be limited to *topologically distinct* time-unlabelled diagrams, i.e. time-unlabelled diagrams that cannot be obtained from one another via a mere displacement, i.e. translation, of the vertices. This rule is illustrated in Fig. 2.2.

As each operator $\Omega_1(\tau)$ actually contains eight normal-ordered operators $\Omega^{ij}(\tau)$, with $i+j=2$ or 4, one may be worried about the proliferation of diagrams. Several "selection rules" can be identified by virtue of Eq. (2.24), and as examplified in Sec. 2.4.2, that limit drastically the number of non-zero diagrams. Let us detail those additional rules.

1. Anomalous propagators are zero and thus do not need to be considered. Whenever a string of operators contains different numbers of creation and annihilation operators, the result is necessarily zero, i.e. for an arbitrary matrix element $\langle\Phi|\Omega^{i_1j_1}(\tau_1)\Omega^{i_2j_2}(\tau_2)\dots\Omega^{i_pj_p}(\tau_p)|\Phi\rangle$ to give non-zero contributions (diagrams), it is mandatory that $n_a\equiv\sum_{k=1}^{p}(j_k-i_k)=0$.

2. Normal lines linking a set of vertices must not form an oriented loop. For a set of two given vertices $\Omega^{i_kj_k}(\tau_k)$ and $\Omega^{i_{k'}j_{k'}}(\tau_{k'})$, it means that normal lines must propagate in the same direction.

3. As stipulated after Eq. (2.24), propagators starting and ending at the same vertex correspond to equal-time propagators and are thus zero. Hence, no contraction of a vertex on itself is to be considered.

Finally, it is to be noted that Ω_1 has the same diagrammatic representation as Ω except that Ω^{00} must be omitted and Ω^{11} replaced by $\breve{\Omega}^{11}$, which requires to use a different symbol for that particular vertex[5].

2.4.4. Diagram evaluation

Once the diagrams have been generated using the topological rules listed in Sec. 2.4.3, the algebraic rules to express the diagrams analytically are now detailed.

1. Each vertex is labeled by a time variable while each line is labeled by two quasi-particle indices and two time labels at its ends, the latter being associated with the two vertices the line is attached to. Each vertex contributes a factor $\Omega^{ij}_{k_1\dots k_i k_{i+1}\dots k_{i+j}}$ with the sign

[5] We omit to use a different symbol for $\breve{\Omega}^{11}$ in the following although it must be clear that the vertex with one line coming in and one line coming out does represent $\breve{\Omega}^{11}$ whenever it originates from the perturbative expansion of the evolution operator. This may be confusing whenever $O=\Omega$ since in this case there can also be a vertex Ω^{11} at fixed time $t=0$.

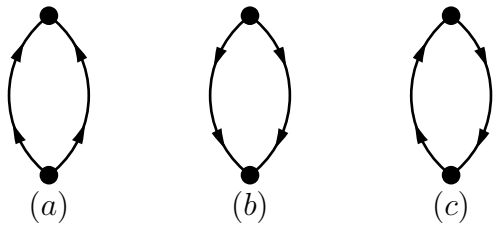

Figure 2.2. Examples of time-unlabelled diagrams: (a) and (b) are topologically identical, whereas (c) is topologically distinct from (a) and (b).

convention detailed in Sec. 1.12. Each line contributes a factor $G^{gg'(0)}_{k_1k_2}(\tau_k, \tau_{k'})$, where $g = \pm$ and $g' = \pm$ characterize the type of elementary propagator the line corresponds to.

2. A normal line can be interpreted as $G^{-+(0)}$ or $G^{+-(0)}$ depending on the ascendant or descendant reading of the diagram. Similarly, the ordering of quasi-particle and time labels of a propagator depends on the ascendant or descendant reading of the diagram. *All* the lines involved in a given diagram must be interpreted in the *same* way, i.e. sticking to an ascendant or descendant way of reading the diagram all throughout. By default the diagrams are intended to be read in a descendant fashion[6].

3. All quasi-particle labels must be summed over while all time variables must be integrated over from 0 to τ.

4. A sign factor $(-1)^{p+n_c}$, where p denotes the order of the diagram and n_c denotes the number of crossing lines in the diagram, must be considered. The overall sign results from multiplying this factor with the sign associated with each factor $\Omega^{ij}_{k_1\ldots k_i k_{i+1}\ldots k_{i+j}}$ and the sign factor associated with the direction in which the diagram is read as discussed in rule 3 above.

5. Each diagram comes with a numerical prefactor obtained from the following combination
   - A factor $1/(n_e)!$ must be considered for *each* group of n_e equivalent lines. Equivalent lines must all begin and end at the same vertices, and must correspond to the same type of contractions, i.e. they must all correspond to propagators characterized by the same superscripts g and g' in addition to having identical time labels.
   - A symmetry factor $1/n_s$ must be considered in connection with exchanging the time labels of the vertices in all possible ways, counting the identity as one. The factor n_s corresponds to the number of ways exchanging the time labels provides a time-labelled diagram that is topologically equivalent to the original one. This rule is illustrated in Fig. 2.3.

2.4.5. Exponentiation of connected diagrams

Diagrams representing the time-dependent norm kernel $N(\tau)$ are vacuum-to-vacuum diagrams, i.e. diagrams with no incoming or outgoing external lines. In general, a diagram consists of

[6] Reading them in an ascendant one is possible but requires an additional factor $(-1)^{n_p}$, with n_p the number of propagators in the diagram.

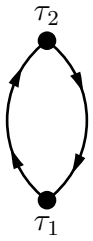

Figure 2.3. Determination of the n_s symmetry factor: here $n_s = 2$ as exchanging the time labels leads to a topologically equivalent diagram.

disconnected parts which are joined neither by vertices nor by propagators. Consider a diagram $\Gamma(\tau)$ contributing to Eq. (2.31) and consisting of n_1 identical connected parts $\Gamma_1^c(\tau)$, of n_2 identical connected parts $\Gamma_2^c(\tau)$, and so on.

For a given diagram, the times corresponding to the different vertices are ordered in a specific way. As a diagram contains various connected parts, one is able to form a family of similar diagrams, only differing by the time-ordering of the different connected parts' vertices. Summing the contributions of all diagrams belonging to this family, only the vertices inside a given connected part remain time-ordered. Hence, the sum of the contributions writes as the product

$$\Gamma(\tau) \propto \Gamma_1^c(\tau)^{n_1} \Gamma_2^c(\tau)^{n_2} \dots \ . \tag{2.38}$$

Let us further process such a family of diagrams for which several connected parts are identical. In fact, members of the family are not all different from each other. When exchanging two of those identical parts, no new diagram is created. Thus, if a family contains n times a connected part, $n!$ identical diagrams are produced by permuting the time labels of the identical connected parts in all possible ways. Including the corresponding symmetry factor, the overall contribution eventually reads as

$$\Gamma(\tau) = \frac{\Gamma_1^c(\tau)^{n_1}}{n_1!} \frac{\Gamma_2^c(\tau)^{n_2}}{n_2!} \dots \ . \tag{2.39}$$

It follows that the sum of all vacuum-to-vacuum diagrams is equal to the exponential of the sum of *connected* vacuum-to-vacuum diagrams [135], i.e.

$$\begin{aligned} \langle \Phi | \mathcal{U}_1(\tau) | \Phi \rangle &= \sum_{\Gamma} \Gamma(\tau) \\ &= \sum_{n_1 n_2 \dots} \frac{\Gamma_1^c(\tau)^{n_1}}{n_1!} \frac{\Gamma_2^c(\tau)^{n_2}}{n_2!} \cdots \\ &= e^{\Gamma_1^c(\tau) + \Gamma_2^c(\tau) + \dots} \ . \end{aligned} \tag{2.40}$$

Let us note that the diagram containing only one vertex and no propagator, and corresponding to Ω^{00}, is conventionnally not a connected diagram. The norm can thus be written, *prior* to proceeding to any truncation, as

$$N(\tau) = e^{-\tau \Omega^{00} + n(\tau)} \langle \Phi | \Phi \rangle \ , \tag{2.41}$$

where $n(\tau) \equiv \sum_{n=1}^{\infty} n^{(n)}(\tau)$, with $n^{(n)}(\tau)$ the sum of all time-dependent connected Feynman vacuum-to-vacuum diagrams of order n. By virtue of Eqs. (2.40-2.41), only connected diagrams have to be eventually considered in practice.

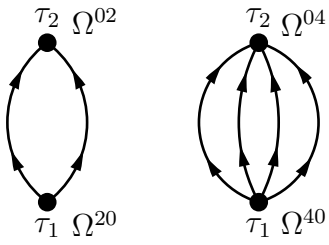

Figure 2.4. Second-order connected Feynman diagrams contributing to $n(\tau)$.

2.4.6. Dependence on τ

Matching Eq. (1.43a) with Eq. (2.41) in the large τ limit allows one to write

$$\lim_{\tau\to\infty} n(\tau) \equiv -\tau\Delta\Omega_0^{\mathrm{A}_0} + \ln|\langle\Phi|\Psi_0^{\mathrm{A}_0}\rangle|^2 \ . \tag{2.42}$$

Equation (2.42) relates to the known result applicable to the logarithm of the norm kernel whose part proportional to τ provides the correction to the unperturbed ground-state eigenvalue of Ω

$$\begin{aligned}\Delta\Omega_0^{\mathrm{A}_0} &\equiv \Omega_0^{\mathrm{A}_0} - \Omega^{00} \\ &= \langle\Phi|\Omega_1 \sum_{k=1}^{\infty} \left(\frac{1}{\Omega^{00}-\Omega_0}\Omega_1\right)^{k-1} |\Phi\rangle_c \ ,\end{aligned} \tag{2.43}$$

given under the form of Goldstone's formula [114], which is here computed relative to the superfluid (i.e. Bogoliubov) reference state $|\Phi\rangle$ breaking global gauge symmetry. Relation (2.42) recalls that, in the large τ limit, $n(\tau)$ gathers a term independent of τ and a term linear in τ. This characteristic behavior at large imaginary time can be proven for any arbitrary order by trivially adapting the proof given in App. B.7 of Ref. [76].

In Eq. (2.42), the contribution that does not depend on τ provides the overlap between the unperturbed state and the correlated ground-state. This overlap is not equal to 1, which underlines that the expansion of $N(\tau)$ does not rely on intermediate normalization.

2.4.7. Second-order BMBPT diagrams

We recall, in agreement with Eq. (2.32), that first-order contributions are zero. Following the topological rules listed in Sec. 2.4.3, the only two non-zero second-order connected vacuum-to-vacuum diagrams contributing to $n(\tau)$ are displayed in Fig. 2.4. When applying Møller-Plesset BMBPT, i.e. using a vacuum that is solution of the HFB equations, PN2.1 vanishes and only PN2.2 is left as non-zero second-order contribution.

While the analytic expression of both diagrams is provided in App. D.1, we presently detail the calculation of one of them for illustration. The second-order diagram labeled as PN 2.2 in Fig. 2.4 is displayed in full details in Fig. 2.5. It contains one Ω^{40} vertex and one Ω^{04} vertex. The diagram contains two vertices and no crossing lines ($(-1)^{p+n_c} = +1$), four equivalent lines of normal type propagating in the same direction ($n_e = 4$), and a symmetry factor $n_s = 1$ as exchanging the time labels of the two vertices gives topologically distinct time-labelled

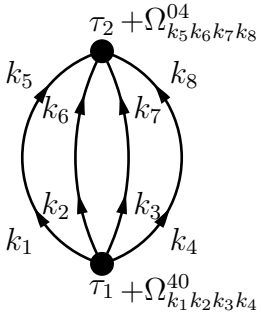

Figure 2.5. Example of a fully-labelled BMBPT diagram contributing to $n(\tau)$, i.e. the second-order diagram labelled PN2.2 in Fig. 2.4.

diagrams. Last but not least, the sign convention for the vertices requires to associate the factors $+\Omega^{40}_{k_1k_2k_3k_4}$ and $+\Omega^{04}_{k_5k_6k_7k_8}$ to the vertices as they appear on the diagram drawn in Fig. 2.5. Eventually, diagram PN2.2 reads as

$$\begin{aligned}
\mathrm{PN2.2} &= +\frac{1}{4!}\sum_{\substack{k_1k_2k_3k_4\\k_5k_6k_7k_8}}\Omega^{40}_{k_1k_2k_3k_4}\Omega^{04}_{k_5k_6k_7k_8}\\
&\qquad\times\int_0^\tau \mathrm{d}\tau_1\mathrm{d}\tau_2 G^{-+(0)}_{k_5k_1}(\tau_2,\tau_1)G^{-+(0)}_{k_6k_2}(\tau_2,\tau_1)G^{-+(0)}_{k_7k_3}(\tau_2,\tau_1)G^{-+(0)}_{k_8k_4}(\tau_2,\tau_1)\\
&= +\frac{1}{4!}\sum_{\substack{k_1k_2k_3k_4\\k_5k_6k_7k_8}}\Omega^{40}_{k_1k_2k_3k_4}\Omega^{04}_{k_5k_6k_7k_8}\delta_{k_1k_5}\delta_{k_2k_6}\delta_{k_3k_7}\delta_{k_4k_8}\\
&\qquad\times\int_0^\tau \mathrm{d}\tau_1\mathrm{d}\tau_2\,\theta(\tau_2-\tau_1)e^{-(\tau_2-\tau_1)(E_{k_1}+E_{k_2}+E_{k_3}+E_{k_4})}\\
&= +\frac{1}{4!}\sum_{k_1k_2k_3k_4}\frac{\Omega^{40}_{k_1k_2k_3k_4}\Omega^{04}_{k_1k_2k_3k_4}}{E_{k_1}+E_{k_2}+E_{k_3}+E_{k_4}}\left[\tau-\frac{1-e^{-\tau(E_{k_1}+E_{k_2}+E_{k_3}+E_{k_4})}}{E_{k_1}+E_{k_2}+E_{k_3}+E_{k_4}}\right], \qquad (2.44)
\end{aligned}$$

where use was made of the identities provided in App. A. In the large τ limit, the result reduces to

$$\mathrm{PN2.2} = +\frac{1}{4!}\sum_{k_1k_2k_3k_4}\frac{\Omega^{40}_{k_1k_2k_3k_4}\Omega^{04}_{k_1k_2k_3k_4}}{E_{k_1}+E_{k_2}+E_{k_3}+E_{k_4}}\left[\tau-\frac{1}{E_{k_1}+E_{k_2}+E_{k_3}+E_{k_4}}\right]. \qquad (2.45)$$

2.5. Generic operator kernel

2.5.1. Perturbative expansion

One develops here the perturbative expansion of a generic operator kernel, with the sole restriction that it must commute with H and A. Having developed the complete formalism, one can eventually substitute operator O with any operator of actual interest, e.g. Ω, H or A. Proceeding similarly to $N(\tau)$, one obtains the perturbative expansion of an operator kernel

according to

$$O(\tau) = \langle\Phi|e^{-\tau\Omega_0}\,\mathrm{T}e^{-\int_0^\tau \mathrm{d}t\Omega_1(t)}O|\Phi\rangle \tag{2.46a}$$

$$= e^{-\tau\Omega^{00}}\langle\Phi|\Big\{O(0) - \int_0^\tau \mathrm{d}\tau_1 \mathrm{T}\left[\Omega_1\left(\tau_1\right)O(0)\right] + \frac{1}{2!}\int_0^\tau \mathrm{d}\tau_1\mathrm{d}\tau_2\mathrm{T}\left[\Omega_1\left(\tau_1\right)\Omega_1\left(\tau_2\right)O(0)\right] + ...\Big\}|\Phi\rangle\ , \tag{2.46b}$$

where each term in the matrix element can be fully expanded as done for the norm kernel in Eq. (2.31). The one key difference with the norm kernel relates to the presence of the extra time-independent operator O to which the fixed time $t = 0$ is attributed in order to insert it inside the time ordering at no cost.

As for $N(\tau)$, $O(\tau)$ can be expressed diagrammatically according to

$$O(\tau) \equiv e^{-\tau\Omega^{00}} \sum_{i+j=0,2,4} \sum_{n=0}^{\infty} O^{ij\,(n)}(\tau)\langle\Phi|\Phi\rangle\ , \tag{2.47}$$

where $O^{ij\,(n)}(\tau)$ denotes the sum of all vacuum-to-vacuum diagrams of order n including the operator O^{ij} at fixed time $t = 0$. The convention is that the zero-order diagram $O^{ij\,(0)}(\tau)$ solely contains the fixed-time operator $O^{ij}(0)$, i.e. the latter must not be considered when counting the order of the diagram to apply the diagrammatic rules listed in Sec. 2.4.3.[7]

2.5.2. Factorization of linked/connected diagrams

Any diagram $O^{ij\,(n)}(\tau)$ consists of a part that is *linked* to the operator O^{ij} at time 0, i.e. that results from contractions involving the creation and annihilation operators of O^{ij}, and parts that are disconnected. In the infinite series of diagrams obtained via the BMBPT expansion of $O^{ij}(\tau)$, each vacuum-to-vacuum diagram linked to O^{ij} effectively multiplies the complete set of vacuum-to-vacuum diagrams making up $N(\tau)$. Gathering those infinite sets of diagrams accordingly leads to the remarkable factorization

$$O^{ij}(\tau) \equiv o^{ij}(\tau)\,N(\tau)\ , \tag{2.48}$$

such that

$$\mathcal{O}^{ij}(\tau) = o^{ij}(\tau)\ , \tag{2.49}$$

where

$$o^{ij}(\tau) \equiv \sum_{n=0}^{\infty} o^{ij\,(n)}(\tau) \tag{2.50}$$

sums all connected vacuum-to-vacuum diagrams of order n *linked* to O^{ij}.

The fact that the (reduced) kernel $O(\tau)$ ($\mathcal{O}(\tau)$) of any operator O factorizes into its linked/connected part $o(\tau)$ times the (reduced) norm kernel $N(\tau)$ ($\mathcal{N}(\tau)$) is a fundamental result of BMBPT that is now exploited to access the actual ground state observables of interest.

[7] As explained earlier, this corresponds to shifting by one unit the definition of the order of a diagram compared to the commonly accepted definition. This is a price to pay to have diagrammatic rules that are consistent with the ones introduced for the norm kernel.

2.6. Expansion of the observable

2.6.1. Perturbative expansion

According to Eq. (1.48) and to Eq. (2.48), the ground-state observable of interest is eventually accessed through [77, 127]

$$\begin{aligned}
\mathrm{O}_0^{\mathrm{A}} &\equiv \lim_{\tau\to\infty} \frac{\langle\Phi|\mathcal{U}(\tau)O|\Phi\rangle}{\langle\Phi|\mathcal{U}(\tau)|\Phi\rangle} \\
&= \lim_{\tau\to\infty} \langle\Phi|\mathrm{T}e^{-\int_0^\tau dt\Omega_1(t)}O|\Phi\rangle_c \\
&= \langle\Phi|O|\Phi\rangle \\
&\quad - \frac{1}{1!}\int_0^{+\infty} d\tau_1 \langle\Phi|\mathrm{T}\left[\Omega_1\left(\tau_1\right)O(0)\right]|\Phi\rangle_c \\
&\quad + \frac{1}{2!}\int_0^{+\infty} d\tau_1 d\tau_2 \langle\Phi|\mathrm{T}\left[\Omega_1\left(\tau_1\right)\Omega_1\left(\tau_2\right)O(0)\right]|\Phi\rangle_c \\
&\quad - \ldots ,
\end{aligned} \tag{2.51}$$

where the lower index c refers to the restriction to connected diagrams, thus, yielding a size-extensive many-body framework that properly scales with system size.

Gathering all terms up to order p in perturbation theory, the observable $\mathrm{O}_0^{\mathrm{A}}$ sums matrix elements of products of up to $p+1$ time-dependent operators. The running time variables are integrated over from 0 to $\tau \to +\infty$ whereas the time label attributed to the operator O itself remains fixed at $t = 0$, i.e., contributions of order p contain a p-tuple time integral that needs to be performed to generate the end result under the required form.

2.6.2. Diagram generation

Using the building blocks introduced in Secs. 1.12 and 2.2, BMBPT Feynman diagrams representing the contributions to $\mathrm{O}_0^{\mathrm{A}}$ are generated by assembling them according to the following set of topological rules [77, 127]

1. A Feynman diagram of order p consists of p vertices $\Omega^{i_k j_k}(\tau_k)$, $i_k + j_k = 2$ or 4, along with one vertex $O^{mn}(0)$, $m+n = 0, 2$ or 4, that are connected by fermionic quasi-particle lines, i.e., via non-zero propagators $G^{+-(0)}$ or $G^{-+(0)}$.

2. Each vertex is labelled by a time variable while each line is labelled by two quasi-particle indices and two time labels at its ends, the latter being associated with the two vertices the line is attached to.

3. Generating all contributions to Eq. (2.51) requires to form all possible diagrams, i.e., contract quasi-particle lines attached to the vertices in all possible ways while fulfilling the following restrictions.

   a) Forbid equal-time propagators starting and ending at the same vertex as they are zero, i.e., no contraction of a vertex onto itself is to be considered.

b) Restrict the set to *connected* diagrams, i.e., omit diagrams containing parts that are not connected to each other by either propagators or vertices. This implies in particular that the vertex O^{00} with no line can only appear at order $p = 0$[8].

c) The generic operator O at fixed time 0 is necessarily at the bottom of the diagram. Its contributing vertices $O^{mn}(0)$ can only have propagators going out. Indeed, a line going in would necessarily be associated with a propagator $G^{+-(0)}$ carrying a step function contradicting the fact that all the running times are positive (see Eq. 2.24a). Consequently, contributing vertices are restricted to $O^{m0}(0)$, $m = 0, 2$ or 4.

d) Because of the time-ordering relations carried by the propagators (see Eq. 2.24), lines linking any set of vertices may not form an oriented loop, has it would lead to equal-time propagators.

e) Restrict the set to *vacuum-to-vacuum* diagrams forming a set of closed undirected loops with no external, i.e., unpaired, lines. This condition strongly constrains which normal-ordered parts $\Omega^{i_k j_k}(\tau_k)$ and $O^{m0}(0)$ of the $p+1$ involved operators can be combined, i.e., the condition

$$n_a \equiv \sum_{k=1}^{p} (j_k - i_k) - m = 0\,,$$

must be fulfilled.

f) Restrict the set to *topologically distinct* time-unlabelled diagrams, i.e., time-unlabelled diagrams that cannot be obtained from one another via a mere displacement, i.e., translation, of the vertices.

2.6.3. Diagram evaluation

The way to translate BMBPT diagrams into their mathematical expressions follows the set of algebraic rules

1. Each of the $p+1$ vertices contributes a factor, e.g., $\Omega^{ij}_{k_1 \ldots k_i k_{i+1} \ldots k_{i+j}}$ with the sign convention detailed in Sec. 1.12.

2. Each of the
$$n_b \equiv \frac{1}{2}\left(\sum_{k=1}^{p} (j_k + i_k) + m\right)\,,$$
lines contributes a factor $G^{gg'(0)}_{k_1 k_2}(\tau_k, \tau_{k'})$, where $g = \pm = -g'$ characterize the type of elementary propagator the line corresponds to in agreement with the convention of Fig. 2.1. According to Eq. (2.24), each of the n_b propagators carries an exponential function and a step function of the time labels associated with the two vertices it connects.

[8] It is the only vertex appearing at order 0 given that the vacuum expectation value of all the other terms is zero by virtue of their normal-ordered character. This is a particular occurrence of the rule stipulating that no contraction of a vertex onto itself is to be considered.

3. All quasi-particle labels must be summed over while all running time variables must be integrated over from 0 to $\tau \to +\infty$.

4. A sign factor $(-1)^{p+n_c}$, where p denotes the order of the diagram and n_c denotes the number of crossing lines in the diagram, must be considered. The overall sign results from multiplying this factor with the sign associated with each matrix element.

5. Each diagram comes with a numerical prefactor obtained from the following combination
   a) A factor $1/(n_e)!$ must be considered for *each* group of n_e equivalent lines. Equivalent lines begin and end at the same vertices.
   b) A symmetry factor $1/n_s$ must be considered in connection with exchanging the time labels of the vertices in all possible ways, counting the identity as one. The factor n_s corresponds to the number of ways exchanging the time labels provides a time-labelled diagram that is topologically equivalent to the original one.

2.6.4. Zero- and first-order BMBPT diagrams

Applying the diagrammatic rules detailed in Sec. 2.6.2, the three connected/linked zero- and first-order diagrams contributing to $\mathrm{O}_0^{\mathrm{A}}$ obtained are displayed on the top and middle lines of Fig. 2.6. When working with Møller-Plesset BMBPT, i.e. with a reference state that solves the HFB equation, PO1.1 vanishes and only two diagrams remain. Given that first-order diagrams involve $\Omega_1(\tau_1)$ and $O(0)$ with the constraint that $\tau_1 > 0$, normal lines not only propagate in the same direction but are also limited to propagating upward.

While the analytic expression of the three diagrams is provided in App. D.2, we presently detail the calculation of one of them for illustration by applying the diagrammatic rules detailed in Sec. 2.6.3. The first-order connected/linked diagram labeled as PO1.2 in Fig. 2.6 and displayed in full details in Fig. 2.7 contains one Ω^{04} vertex at running time τ_1 coming from the perturbative expansion of the evolution operator and one vertex O^{40} at fixed time 0. The diagram contains one vertex and no crossing line ($(-1)^{p+n_c} = -1$), four equivalent lines ($n_e = 4$), and a symmetry factor $n_s = 1$ as only one vertex carries a running time and thus cannot be exchanged with any other. Last but not least, the sign convention requires to associate the factors $+\Omega^{04}_{k_5k_6k_7k_8}$ and $+O^{40}_{k_1k_2k_3k_4}$ to the vertices as they appear in Fig 2.7. Eventually, diagram PO1.2 reads as

$$\begin{aligned}
\mathrm{PO1.2} &= \lim_{\tau\to\infty}(-1)^1\frac{1}{4!}\sum_{\substack{k_1k_2k_3k_4\\k_5k_6k_7k_8}} O^{40}_{k_1k_2k_3k_4}\Omega^{04}_{k_5k_6k_7k_8} \\
&\qquad\qquad \times\int_0^\tau \mathrm{d}\tau_1 G^{-+(0)}_{k_5k_1}(\tau_1,0)G^{-+(0)}_{k_6k_2}(\tau_1,0)G^{-+(0)}_{k_7k_3}(\tau_1,0)G^{-+(0)}_{k_8k_4}(\tau_1,0) \\
&= \lim_{\tau\to\infty} -\frac{1}{4!}\sum_{\substack{k_1k_2k_3k_4\\k_5k_6k_7k_8}} O^{40}_{k_1k_2k_3k_4}\Omega^{04}_{k_5k_6k_7k_8}\delta_{k_5k_1}\delta_{k_6k_2}\delta_{k_7k_3}\delta_{k_8k_4}\int_0^\tau \mathrm{d}\tau_1\theta(\tau_1)e^{-\tau_1(E_{k_1}+E_{k_2}+E_{k_3}+E_{k_4})} \\
&= \lim_{\tau\to\infty} -\frac{1}{4!}\sum_{k_1k_2k_3k_4}\frac{O^{40}_{k_1k_2k_3k_4}\Omega^{04}_{k_1k_2k_3k_4}}{E_{k_1}+E_{k_2}+E_{k_3}+E_{k_4}}\left[1-e^{-\tau(E_{k_1}+E_{k_2}+E_{k_3}+E_{k_4})}\right] ,
\end{aligned} \tag{2.52}$$

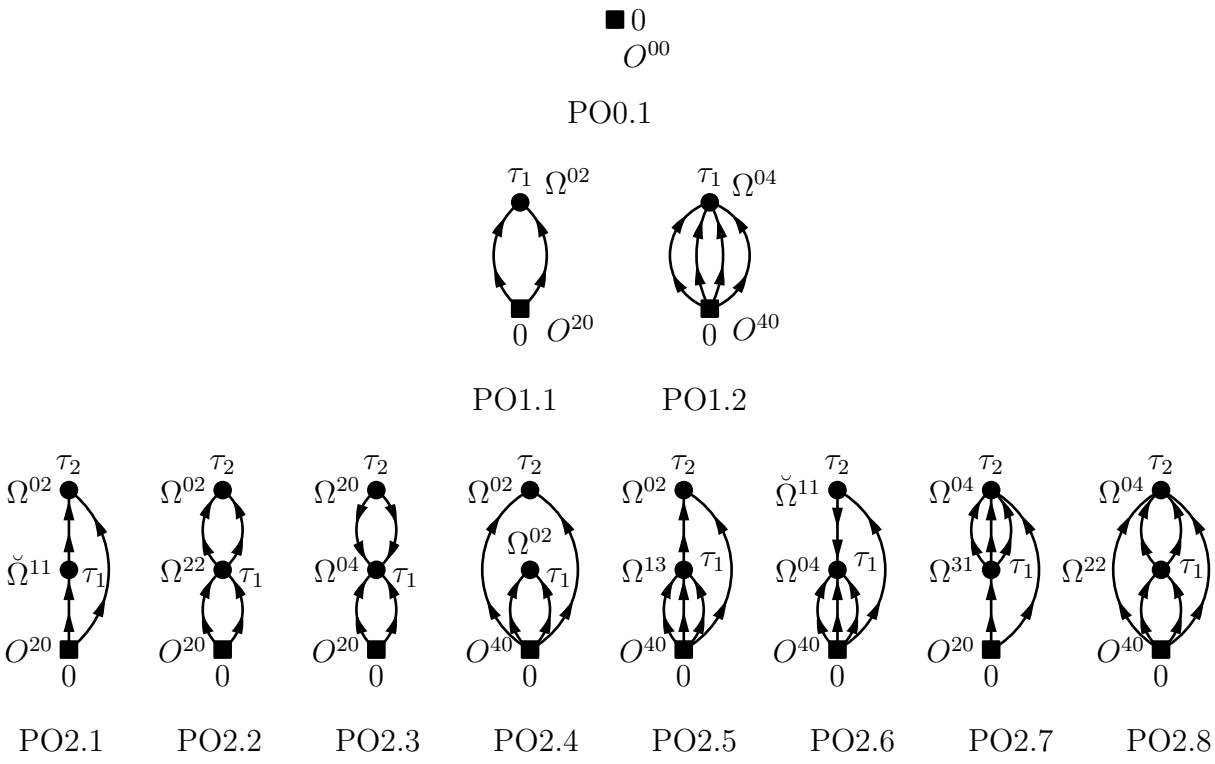

Figure 2.6. Zero-, first- and second-order Feynman BMBPT diagrams contributing to $\mathrm{O}_0^{\mathrm{A}}$ generated from operator vertices of two-body character at most, i.e. $\Omega = \Omega^{[0]} + \Omega^{[2]} + \Omega^{[4]}$ and $O = O^{[0]} + O^{[2]} + O^{[4]}$.

where use was made of the identities provided in App. A. Performing the infinite τ limit, Eq. (2.52) provides the contribution to $\mathrm{O}_0^{\mathrm{A}_0}$ under the form

$$\mathrm{PO1.2} = -\frac{1}{4!} \sum_{k_1 k_2 k_3 k_4} \frac{O^{40}_{k_1 k_2 k_3 k_4} \Omega^{04}_{k_1 k_2 k_3 k_4}}{E_{k_1} + E_{k_2} + E_{k_3} + E_{k_4}} \ . \tag{2.53}$$

2.6.5. Second-order BMBPT diagrams

Applying the rules described in Sec. 2.6.2, one obtains eight connected/linked second-order diagrams contributing to $\mathrm{O}_0^{\mathrm{A}}$, displayed in the bottom line of Fig. 2.6. When employing Møller-Plesset BMBPT, six of them vanish and only PO2.7 and PO2.8 remain. Furthermore, if the operator of interest is the grand-canonical potential, PΩ2.7 vanishes as well. Hence, the only second-order grand potential diagram is PΩ2.8 in this case.

While the analytic expression of the eight diagrams is provided in App. D.2, we presently detail the calculation of one of them for illustration by applying the diagrammatic rules detailed in Sec. 2.6.3. The second-order connected/linked diagram labeled as PO2.6 in Fig. 2.6 and displayed in full details in Fig. 2.8 contains one Ω^{04} vertex at running time τ_1 and one Ω^{11} vertex at running time τ_2 coming from the perturbative expansion of the evolution operator

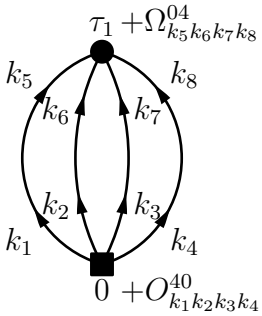

Figure 2.7. Example of first-order fully-labelled Feynman BMBPT diagram contributing to $\mathrm{O}_0^{\mathrm{A}}$, i.e. the diagram labelled PO1.2 in Fig. 2.6.

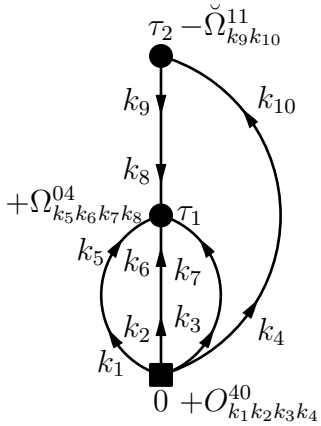

Figure 2.8. Example of second-order fully-labelled Feynman BMBPT diagram contributing to $\mathrm{O}_0^{\mathrm{A}}$, i.e. the diagram labelled PO2.6 in Fig. 2.6.

along with one vertex O^{40} at fixed time 0. The diagram contains two Ω vertices and no crossing line ($(-1)^{p+n_c} = 1$), three equivalent lines ($n_e = 3$), and a symmetry factor $n_s = 1$ as the two vertices carrying time labels are different and thus cannot be exchanged. Last but not least, the sign convention requires to associate the factors $+\Omega^{04}_{k_5k_6k_7k_8}$, $-\Omega^{11}_{k_9k_{10}}$ and $+O^{40}_{k_1k_2k_3k_4}$ to the

vertices as they appear in Fig 2.8. Eventually, diagram PO2.6 reads as

$$\begin{aligned}
\mathrm{PO2.6} &= \lim_{\tau\to\infty} -(-1)^2\frac{1}{3!}\sum_{\substack{k_1k_2k_3k_4k_5\\k_6k_7k_8k_9k_{10}}} O^{40}_{k_1k_2k_3k_4}\Omega^{04}_{k_5k_6k_7k_8}\breve{\Omega}^{11}_{k_9k_{10}} \\
&\quad\times\int_0^\tau \mathrm{d}\tau_1\mathrm{d}\tau_2 G^{-+}_{k_5k_1}(\tau_1,0)G^{-+}_{k_6k_2}(\tau_1,0)G^{-+}_{k_7k_3}(\tau_1,0)G^{-+}_{k_{10}k_4}(\tau_2,0)G^{+-}_{k_9k_8}(\tau_2,\tau_1) \\
&= \lim_{\tau\to\infty} -\frac{1}{6}\sum_{\substack{k_1k_2k_3k_4k_5\\k_6k_7k_8k_9k_{10}}} O^{40}_{k_1k_2k_3k_4}\Omega^{04}_{k_5k_6k_7k_8}\breve{\Omega}^{11}_{k_9k_{10}}\delta_{k_5k_1}\delta_{k_6k_2}\delta_{k_7k_3}\delta_{k_{10}k_4}\delta_{k_9k_8} \\
&\quad\times\int_0^\tau \mathrm{d}\tau_1\mathrm{d}\tau_2\theta(\tau_1-\tau_2)e^{-\tau_1\left(E_{k_1}+E_{k_2}+E_{k_3}\right)}e^{-\tau_2E_{k_4}}e^{-(\tau_1-\tau_2)E_{k_8}} \\
&= \lim_{\tau\to\infty} -\frac{1}{6}\sum_{k_1k_2k_3k_4k_8} O^{40}_{k_1k_2k_3k_4}\Omega^{04}_{k_1k_2k_3k_8}\breve{\Omega}^{11}_{k_8k_4} \\
&\quad\times\int_0^\tau \mathrm{d}\tau_1\mathrm{d}\tau_2\theta(\tau_1-\tau_2)e^{-\tau_1\left(E_{k_1}+E_{k_2}+E_{k_3}+E_{k_8}\right)}e^{\tau_2\left(E_{k_8}-E_{k_4}\right)} \\
&= \lim_{\tau\to\infty} -\frac{1}{6}\sum_{k_1k_2k_3k_4k_5} \frac{O^{40}_{k_1k_2k_3k_4}\Omega^{04}_{k_1k_2k_3k_5}\breve{\Omega}^{11}_{k_5k_4}}{E_{k_5}-E_{k_4}} \\
&\quad\times\left[\frac{1-e^{-\tau\left(E_{k_1}+E_{k_2}+E_{k_3}+E_{k_4}\right)}}{E_{k_1}+E_{k_2}+E_{k_3}+E_{k_4}} - \frac{1-e^{-\tau\left(E_{k_1}+E_{k_2}+E_{k_3}+E_{k_5}\right)}}{E_{k_1}+E_{k_2}+E_{k_3}+E_{k_5}}\right] ,
\end{aligned} \tag{2.54}$$

where use was made of the identities provided in App. A, and label k_8 was renamed k_5 in the last line. Performing the infinite τ limit, Eq. (2.54) provides the contribution to $\mathrm{O}_0^{\mathrm{A}_0}$ under the form

$$\mathrm{PO2.6} = -\frac{1}{6}\sum_{k_1k_2k_3k_4k_5} \frac{O^{40}_{k_1k_2k_3k_4}\Omega^{04}_{k_1k_2k_3k_5}\breve{\Omega}^{11}_{k_5k_4}}{\left(E_{k_1}+E_{k_2}+E_{k_3}+E_{k_4}\right)\left(E_{k_1}+E_{k_2}+E_{k_3}+E_{k_5}\right)} . \tag{2.55}$$

2.6.6. Towards higher orders

In order to illustrate the typical expression of a higher-order BMBPT diagram and confronting arising difficulties, let us write it for the third-order diagram displayed in Fig. 2.9, i.e.,

$$\begin{aligned}
D &= \lim_{\tau\to\infty}\frac{(-1)^3}{2(2!)^4}\sum_{k_i} O^{40}_{k_1k_2k_3k_4}\Omega^{40}_{k_5k_6k_7k_8}\Omega^{04}_{k_5k_6k_1k_2}\Omega^{04}_{k_7k_8k_3k_4} \\
&\quad\times\int_0^\tau \mathrm{d}\tau_1\mathrm{d}\tau_2\mathrm{d}\tau_3\,\theta(\tau_2-\tau_1)\theta(\tau_3-\tau_1)e^{-\tau_1\epsilon^{k_5k_6k_7k_8}}e^{-\tau_2\epsilon_{k_1k_2k_5k_6}}e^{-\tau_3\epsilon_{k_3k_4k_7k_8}}
\end{aligned} \tag{2.56}$$

where the notation

$$\epsilon^{k_ak_b\cdots}_{k_ik_j\cdots} \equiv E_{k_i}+E_{k_j}+\ldots-E_{k_a}-E_{k_b}-\ldots , \tag{2.57}$$

was introduced. The sign, the combinatorial factors and the four matrix elements directly reflect Feynman's algebraic rules listed above and are easy to interpret. The final form of the integrand originates from expliciting the $n_b = 8$ propagators $G^{-+(0)}$ and displays a typical structure that needs to be scrutinized for the following.

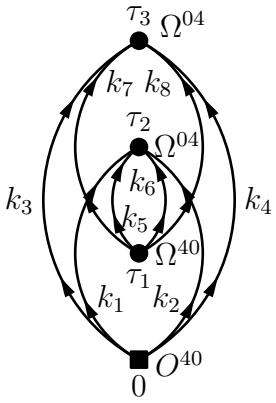

Figure 2.9. A third-order BMBPT diagram.

- While the vertex O^{40} is at fixed time 0, the Ω^{40} vertex is at running time τ_1 and the two Ω^{04} vertices are at running times τ_2 and τ_3. The two step functions characterize the time ordering between Ω^{40} and each of the two Ω^{04} vertices it is directly connected to via propagators. Contrarily, the two Ω^{04} vertices are not connected via propagators and do not belong to a linear sequence of connected vertices such that their time labels are not ordered with respect to one another. Eventually, the fact that the three running variables are positive is directly encoded into the boundary of the triple integral.
- Grouping appropriately the exponential functions coming from the 8 propagators, the integrand displays one exponential factor per running time, i.e., per $\Omega^{i_k j_k}(\tau_k)$ vertex. The relevant energy factor $\epsilon^{k_a k_b \cdots}_{k_i k_j \cdots}$ multiplying the variable τ_k in this exponential function denotes nothing but the sum/difference of quasi-particle energies associated with the lines entering/leaving the corresponding vertex.

The two above points characterizing (a) the steps functions associated with the links between the vertices and (b) the exponential function associated with each vertex can be viewed as an optimal rephrasing of the algebraic rule 2 stipulated above.

Eventually, the complexity of the BMBPT diagrams expressions grows significantly with the perturbative order. Especially, more complex topologies with respect to the time labels associated to vertices may appear. As such, being able to generate and even more evaluate BMBPT diagrams becomes more and more challenging. The design and application of automated tools to generate and evaluate BMBPT diagrams at higher order is discussed extensively in Chap. 3.

2.7. Complex versus real character of the diagrams

An important check to perform once the diagrams have been derived is that at each order, the sum of diagrams contributing to a given observable produces a real result. Indeed, the ground state energy or the particle number of the nucleus are real quantities. In standard MBPT, each of the Goldstone diagrams either have a complex conjugate partner or is self-conjugate [61], such that the sum of diagrams indeed produces a real energy.

In the case of BMBPT, and as previously alluded to in Sec. 1.10, the complex or real status of the diagrams depend on the actual observable of interest, knowing that one is bound from

Self-conjugate diagrams	 PΩ0.1	 PΩ1.1	 PΩ1.2	 PΩ2.1	 PΩ2.2	 PΩ2.6	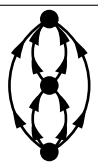 PΩ2.8
Diagrams with conjugate partners	 PΩ2.3 ⇔	 PΩ2.4	 PΩ2.5 ⇔	 PΩ2.7			

Table 2.1. Grand potential BMBPT Feynman diagrams up to second order and their real (top) or complex (bottom) character.

the outset to compute the grand potential, the energy and the particle number to actually implement the formalism. In the case of a general operator O, it appears clearly from diagrams expressions in App. D.2 or from their diagrammatic representation in Fig. 2.6 that the diagrams cannot be either self-conjugate or complex-conjugate-partners, and thus it is necessary to consider only the real part of the diagrams' contribution[9]. Contrarily, if the observable of interest is the grand potential $\Omega_0^{\mathrm{A}_0}$, O is replaced by Ω and the corresponding expressions in this particular case are displayed in App. D.3. Using Eq. 1.53, one can show that diagrams are indeed self-conjugate or have a complex-conjugate partner, as is represented diagrammatically in Tab. 2.1.

Let us illustrate this by taking the Hermitian conjugate of the diagram labelled as PΩ1.2 in Tab. 2.1

$$\begin{aligned} \mathrm{P}\Omega 1.2^* &= -\frac{1}{4!}\sum_{k_1k_2k_3k_4}\frac{\Omega^{40*}_{k_1k_2k_3k_4}\Omega^{04*}_{k_1k_2k_3k_4}}{E_{k_1}+E_{k_2}+E_{k_3}+E_{k_4}} \\ &= -\frac{1}{4!}\sum_{k_1k_2k_3k_4}\frac{\Omega^{04}_{k_1k_2k_3k_4}\Omega^{40}_{k_1k_2k_3k_4}}{E_{k_1}+E_{k_2}+E_{k_3}+E_{k_4}} \ , \end{aligned} \tag{2.58}$$

which is nothing but PΩ1.2 itself. PΩ1.2 is thus self-conjugate. Let us contrarily focus on the diagram labelled as PΩ2.5 in Tab. 2.1. Its Hermitian conjugate reads as

$$\begin{aligned} \mathrm{P}\Omega 2.5^* &= +\frac{1}{6}\sum_{k_1k_2k_3k_4k_5}\frac{\Omega^{40*}_{k_1k_2k_3k_4}\Omega^{13*}_{k_5k_1k_2k_3}\Omega^{02*}_{k_5k_4}}{(E_{k_1}+E_{k_2}+E_{k_3}+E_{k_4})\,(E_{k_4}+E_{k_5})} \\ &= +\frac{1}{6}\sum_{k_1k_2k_3k_4k_5}\frac{\Omega^{40}_{k_1k_2k_3k_4}\Omega^{31}_{k_1k_2k_3k_5}\Omega^{20}_{k_5k_4}}{(E_{k_1}+E_{k_2}+E_{k_3}+E_{k_4})\,(E_{k_4}+E_{k_5})} \\ &= +\frac{1}{6}\sum_{k_1k_2k_3k_4k_5}\frac{\Omega^{40}_{k_1k_2k_3k_4}\Omega^{31}_{k_1k_2k_3k_5}\Omega^{20}_{k_1k_2}}{(E_{k_2}+E_{k_3}+E_{k_4}+E_{k_5})\,(E_{k_1}+E_{k_2})} \end{aligned} \tag{2.59}$$

[9] Actually, in the particular case where the Hamiltonian used for numerical applications is real, the contribution associated with each and every diagram is real.

where k_4 and k_2 as well as k_5 and k_1 labels have been exchanged and some permutations effected at the last line. The result corresponds to the diagram labelled as PΩ2.7. Diagrams PΩ2.5 and PΩ2.7 are thus conjugate partners. If the bottom vertex is anything but Ω, i.e. H or A, the above derivations do not hold, such that th result at a given order is indeed complex and its real part must eventually be taken.

2.8. Perturbative Bogoliubov coupled-cluster theory

One observes that the number of BMBPT diagrams grows significantly as the perturbative order increases, i.e. there are three diagrams up to first order, and already eleven up to second order. It is interesting to recast all contributions using Bogoliubov coupled cluster (BCC) amplitudes. While coupled-cluster (CC) theory is out of the scope of this work (a better introduction can be found in Ref. [61], and in Ref. [77] for its open-shell counterpart), such an operation reduces drastically the number of diagrams by introducing intermediate quantities and allows a connection with BCC theory. Furthermore, such a rewriting could prove handy when extending the present work to PNP-BMBPT [77] in the future.

2.8.1. Definitions

We introduce the n-tuple (i.e. $2n$-quasiparticle) Bogoliubov cluster operator through

$$\mathcal{T}_n^\dagger(\tau) = \frac{1}{(2n)!} \sum_{k_1 \dots k_{2n}} \int_0^\tau \mathrm{d}\tau_1 \dots \mathrm{d}\tau_{2n} \mathcal{T}^\dagger_{k_1 \dots k_{2n}}(\tau_1 \dots \tau_{2n}) \mathrm{T}\Big[\beta_{k_{2n}}(\tau_{2n}) \dots \beta_{k_1}(\tau_1)\Big] \ , \tag{2.60}$$

where the Feynman amplitude $\mathcal{T}^\dagger_{k_1 \dots k_{2n}}(\tau_1 \dots \tau_{2n})$ is antisymmetric under the exchange of (k_i, τ_i) and (k_j, τ_j) for any $(i, j) \in \{1, \dots 2n\}^2$. Because we unconventionally proceed through the first term of Eq. (1.49) rather than through the second, the operator introduced in Eq. (2.60) is the *hermitian conjugate* of the cluster operator entering in BCC theory [78] that is most naturally developed from the second term in Eq. (1.49).

By definition, the time-dependent (i.e. Feynman) single cluster amplitude $\mathcal{T}^\dagger_{k_1 k_2}(\tau_1 \tau_2)$ denotes the *complete* sum of connected BMBPT diagrams with one line entering at an arbitrary time τ_1 and another line entering at an arbitrary time τ_2. The double cluster amplitude $\mathcal{T}^\dagger_{k_1 k_2 k_3 k_4}(\tau_1 \tau_2 \tau_3 \tau_4)$ represents the *complete* sum of connected BMBPT diagrams with four lines entering at arbitrary times τ_1, τ_2, τ_3 and τ_4. This definition can be extended to any n-tuple Bogoliubov cluster amplitude.

The time-integrated (i.e. Goldstone) single cluster amplitude is defined through

$$\mathcal{T}^\dagger_{k_1 k_2}(\tau) \equiv \int_0^\tau \mathrm{d}\tau_1 \mathrm{d}\tau_2 \mathcal{T}^\dagger_{k_1 k_2}(\tau_1 \tau_2) e^{-E_{k_1}\tau_1} e^{-E_{k_2}\tau_2} \ , \tag{2.61}$$

such that

$$\mathcal{T}_1^\dagger(\tau) = \frac{1}{2!} \sum_{k_1 k_2} \mathcal{T}^\dagger_{k_1 k_2}(\tau)\, \beta_{k_2}\, \beta_{k_1} \ . \tag{2.62}$$

Similarly, the time-integrated double cluster amplitude reads as

$$\mathcal{T}^{\dagger}_{k_1k_2k_3k_4}(\tau) \equiv \int_0^{\tau} \mathrm{d}\tau_1\mathrm{d}\tau_2\mathrm{d}\tau_3\mathrm{d}\tau_4 \mathcal{T}^{\dagger}_{k_1k_2k_3k_4}(\tau_1\tau_2\tau_3\tau_4) e^{-E_{k_1}\tau_1} e^{-E_{k_2}\tau_2} e^{-E_{k_3}\tau_3} e^{-E_{k_4}\tau_4} \ , \tag{2.63}$$

such that

$$\mathcal{T}^{\dagger}_2(\tau) = \frac{1}{4!} \sum_{k_1k_2k_3k_4} \mathcal{T}^{\dagger}_{k_1k_2k_3k_4}(\tau)\, \beta_{k_4}\, \beta_{k_3}\, \beta_{k_2}\, \beta_{k_1} \ . \tag{2.64}$$

2.8.2. Operator kernel

The topology of the complete set of BMBPT diagrams is such that, in the exact limit, the connected/linked operator kernel is fully captured by four distinct terms according to

$$o(\tau) = O^{00} \tag{2.65a}$$
$$+ \frac{1}{2} \sum_{k_1k_2} \mathcal{T}^{\dagger}_{k_1k_2}(\tau)\, O^{20}_{k_1k_2} \tag{2.65b}$$
$$+ \frac{1}{8} \sum_{k_1k_2k_3k_4} \mathcal{T}^{\dagger}_{k_1k_2}(\tau) \mathcal{T}^{\dagger}_{k_3k_4}(\tau)\, O^{40}_{k_1k_2k_3k_4} \tag{2.65c}$$
$$+ \frac{1}{4!} \sum_{k_1k_2k_3k_4} \mathcal{T}^{\dagger}_{k_1k_2k_3k_4}(\tau)\, O^{40}_{k_1k_2k_3k_4} \ . \tag{2.65d}$$

Equation (2.65) is valid when resumming all contributions and in standard approximations of BCC theory. It can also be exploited at each finite order in perturbation theory, at the price of paying attention to the counting of perturbative orders. Topological and algebraic rules to do so are detailed in the following.

In the perturbative account of BCC theory, the amplitude equations cannot be solved given that the cluster amplitudes are computed in perturbation theory. Consequently, only single and double cluster amplitudes are required for the computation of the operator kernel.

Feynman topological rules to generate all perturbative contributions to single and double cluster amplitudes are given by

1. For contributions arising at order p, consider all sets of p vertices Ω^{ij} with $\sum_{k=1}^{p}(i_k - j_k) = -2$ for the single cluster amplitude, and $\sum_{k=1}^{p}(i_k - j_k) = -4$ for the double cluster amplitude.

2. For a given set of vertices, draw all possible sets of propagators, knowing that no oriented loop is allowed among a set of vertices. One must be left with two entering external legs for contributions to the single amplitude, and with four entering external legs for contributions to the double amplitude.

3. Exclude disconnected diagrams.

4. Check for possible topologically equivalent diagrams. External legs are equivalent if and only if they connect to the same vertex.

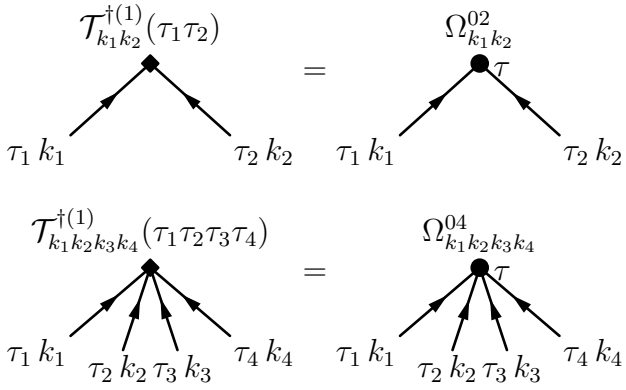

Figure 2.10. Feynman single (left) and double (right) cluster amplitudes at first order in BMBPT.

2.8.3. Diagram evaluation

The algebraic diagrammatic rules needed to translate Feynman diagrams into analytical expressions of the cluster amplitudes are given below.

1. To derive Feynman cluster amplitudes
   a) Label external legs k_i, τ_i from left to right.
   b) Label internal lines (follow BMBPT rules for kernels detailed in Sec. 2.6.3).
   c) Associate time labels to all vertices.
   d) Associate propagator expression to each internal line.
   e) Associate to each vertex connected to an external leg a delta function over their time labels.
   f) Antisymmetrize the diagram under the exchange of external legs by adding the appropriate permutation operator, acting on labels of inequivalent external lines, i.e. external lines that connect different vertices. Take note that external legs connected to the same vertex are equivalent lines. As such, they are already antisymmetrized with respect to one another.
   g) Sum over all internal lines.
   h) Integrate over all internal time labels from 0 to τ.

2. To derive Goldstone amplitudes
   a) Start from the Feynman amplitude.
   b) Associate a factor $e^{-E_{k_i}\tau_i}$ to each external leg.
   c) Integrate over all external time labels from 0 to τ.

2.8.4. First- and second-order Bogoliubov cluster amplitudes

The topological rules detailed in Sec. 2.8.2 applied at first-order generate the diagram contributing to the single Feynman amplitude and the diagram contributing to the double Feynman amplitude displayed in Fig. 2.10. Their expressions are detailed in App. E, along with the expressions of the needed permutation operators.

Focusing on the diagram for the single amplitude displayed in Fig. 2.10 and applying the algebraic rules detailed in Sec. 2.8.3, one obtains th Feynman amplitude

$$\begin{aligned}\mathcal{T}^{\dagger(1)}_{k_1k_2}(\tau_1\tau_2) &= -\Omega^{02}_{k_1k_2}\int_0^\tau \mathrm{d}\tau'\delta(\tau'-\tau_1)\delta(\tau'-\tau_2)\\ &= -\Omega^{02}_{k_1k_2}\delta(\tau_1-\tau_2)\ ,\end{aligned} \tag{2.66}$$

and its Goldstone counterpart

$$\begin{aligned}\mathcal{T}^{\dagger(1)}_{k_1k_2}(\tau) &= -\Omega^{02}_{k_1k_2}\int_0^\tau \mathrm{d}\tau_1\mathrm{d}\tau_2\delta(\tau_1-\tau_2)e^{-E_{k_1}\tau_1}e^{-E_{k_2}\tau_2}\\ &= -\Omega^{02}_{k_1k_2}\int_0^\tau \mathrm{d}\tau_1 e^{-\tau_1\left(E_{k_1}+E_{k_2}\right)}\\ &= -\frac{\Omega^{02}_{k_1k_2}}{E_{k_1}+E_{k_2}}\left[1-e^{-\tau\left(E_{k_1}+E_{k_2}\right)}\right]\ .\end{aligned} \tag{2.67}$$

Performing the infinite time limit, the Goldstone amplitude reduces to

$$\mathcal{T}^{\dagger(1)}_{k_1k_2}(\infty) = -\frac{\Omega^{02}_{k_1k_2}}{E_{k_1}+E_{k_2}}\ . \tag{2.68}$$

The topological rules detailed in Sec. 2.8.2 applied at second order generate the four (three) additional diagrams contributing to the single (double) Feynman amplitude displayed in Fig. 2.11. Their expressions are detailed in App. E, along with the expressions of the needed permutation operators.

Focusing on the contribution to the second-order double cluster amplitude associated to the first corresponding diagram appearing in Fig. 2.11 and displayed in details in Fig. 2.12, the algebraic rules detailed in Sec. 2.8.3 can be applied to obtain the associated expression. Let us first note that the Ω^{13} vertex is linked to three external lines associated with times τ_1, τ_2 and τ_3. We thus associate the vertex with the time label τ and the external lines with corresponding delta functions. The Ω^{02} vertex is associated with one external line with the time label τ_4, and is thus itself straightforwardly associated with τ_4. There is no crossing line and two vertices, hence $(-1)^{p+n_c}=1$, no equivalent internal lines ($n_e=1$), and a symmetry factor $n_s=1$ as the two vertices carrying time labels are different and thus cannot be exchanged. Last but not least, the sign convention requires to associate the factors $+\Omega^{13}_{k_5k_1k_2k_3}$ and $+O^{20}_{k_6k_4}$ to the vertices as they appear in Fig 2.12. Finally, the lines associated with k_1, k_2 and k_3 are equivalent to one another, but the one associated with k_4 is inequivalent to any other line, i.e. one needs to

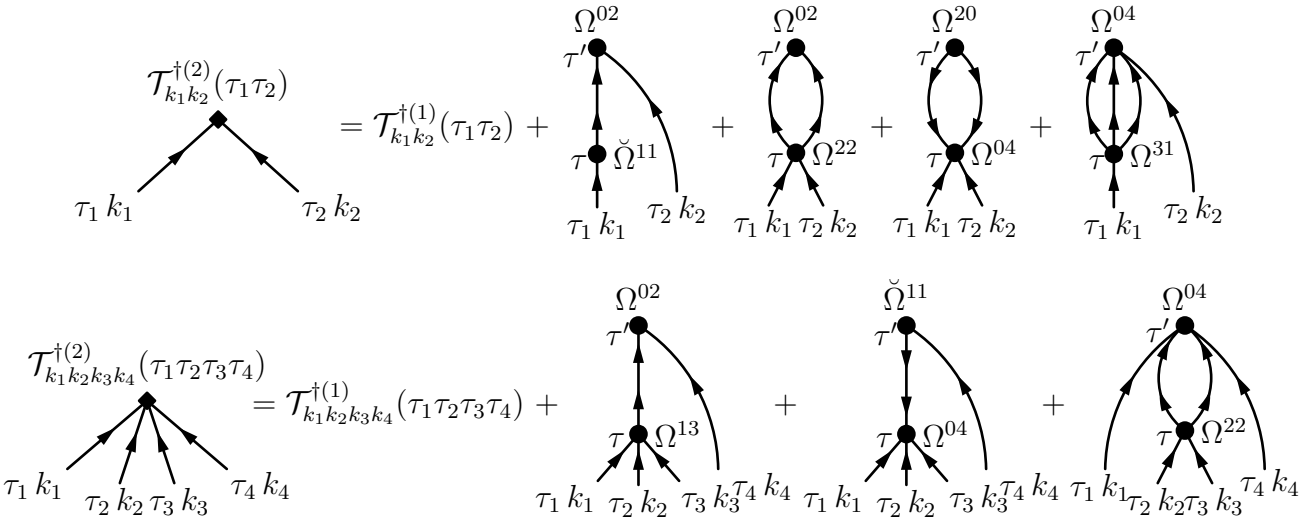

Figure 2.11. Feynman single (first line) and double (second line) cluster amplitudes at second order in BMBPT.

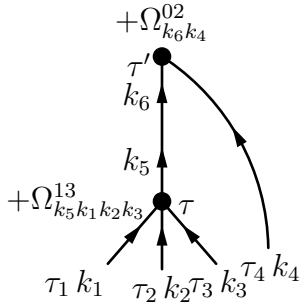

Figure 2.12. Feynman coupled-cluster-like diagram for the $\mathcal{T}^{\dagger(2).1}_{k_1k_2k_3k_4}(\tau)$ component of the cluster amplitude $\mathcal{T}^{\dagger(2)}_2(\tau)$ contributing to $o^{(2)}(\tau)$.

apply the permutation operator $P(k_1k_2k_3/k_4)$. Eventually, the Feynman amplitude reads as

$$\begin{aligned}\mathcal{T}^{\dagger(2).1}_{k_1k_2k_3k_4}(\tau_1\tau_2\tau_3\tau_4) &= (-1)^2 P(k_1k_2k_3/k_4)\sum_{k_5k_6}\Omega^{13}_{k_5k_1k_2k_3}\Omega^{02}_{k_6k_4}\int_0^\tau \mathrm{d}\tau'\mathrm{d}\tau'' G^{-+}_{k_6k_5}(\tau'',\tau') \\ &\qquad\times \delta(\tau'-\tau_1)\delta(\tau'-\tau_2)\delta(\tau'-\tau_3)\delta(\tau''-\tau_4) \\ &= +P(k_1k_2k_3/k_4)\sum_{k_5k_6}\Omega^{13}_{k_5k_1k_2k_3}\Omega^{02}_{k_6k_4}G^{-+}_{k_6k_5}(\tau_4,\tau_1)\delta(\tau_1-\tau_2)\delta(\tau_1-\tau_3)\ ,\end{aligned} \tag{2.69}$$

from which the Goldstone amplitude is obtained through

$$\begin{aligned}
\mathcal{T}^{\dagger(2).1}_{k_1k_2k_3k_4}(\tau) &= +P(k_1k_2k_3/k_4)\sum_{k_5k_6}\Omega^{13}_{k_5k_1k_2k_3}\Omega^{02}_{k_6k_4}\int_0^\tau \mathrm{d}\tau_1\mathrm{d}\tau_2\mathrm{d}\tau_3\mathrm{d}\tau_4 G^{-+}_{k_6k_5}(\tau_4,\tau_1) \\
&\qquad \times \delta(\tau_1-\tau_2)\delta(\tau_1-\tau_3)e^{-E_{k_1}\tau_1}e^{-E_{k_2}\tau_2}e^{-E_{k_3}\tau_3}e^{-E_{k_4}\tau_4} \\
&= +P(k_1k_2k_3/k_4)\sum_{k_5k_6}\Omega^{13}_{k_5k_1k_2k_3}\Omega^{02}_{k_6k_4}\int_0^\tau \mathrm{d}\tau_1\mathrm{d}\tau_4\delta_{k_5k_6}\theta(\tau_4-\tau_1) \\
&\qquad \times e^{-(\tau_1-\tau_4)E_{k_5}}e^{-\tau_1\left(E_{k_1}+E_{k_2}+E_{k_3}\right)}e^{-E_{k_4}\tau_4} \\
&= +P(k_1k_2k_3/k_4)\sum_{k_5}\frac{\Omega^{13}_{k_5k_1k_2k_3}\Omega^{02}_{k_5k_4}}{E_{k_5}-E_{k_1}-E_{k_2}-E_{k_3}} \\
&\qquad \times\left[\frac{1-e^{-\tau\left(E_{k_1}+E_{k_2}+E_{k_3}+E_{k_4}\right)}}{E_{k_1}+E_{k_2}+E_{k_3}+E_{k_4}}-\frac{1-e^{-\tau\left(E_{k_5}-E_{k_4}\right)}}{E_{k_4}+E_{k_5}}\right] . \qquad (2.70)
\end{aligned}$$

Performing the infinite time limit, the Goldstone amplitude eventually reduces to

$$\mathcal{T}^{\dagger(2).1}_{k_1k_2k_3k_4}(\infty) = +P(k_1k_2k_3/k_4)\sum_{k_5}\frac{\Omega^{13}_{k_5k_1k_2k_3}\Omega^{02}_{k_5k_4}}{\left(E_{k_1}+E_{k_2}+E_{k_3}+E_{k_4}\right)\left(E_{k_4}+E_{k_5}\right)} . \qquad (2.71)$$

2.8.5. Contributions to the observables

Eventually, all first-order contributions to $o(\tau)$ provided in App. D.2 are captured through

$$\begin{aligned}
o^{(1)}(\tau) &= O^{00} && (2.72a)\\
&+ \frac{1}{2}\sum_{k_1k_2}\mathcal{T}^{\dagger(1)}_{k_1k_2}(\tau)\,O^{20}_{k_1k_2} && (2.72b)\\
&+ \frac{1}{4!}\sum_{k_1k_2k_3k_4}\mathcal{T}^{\dagger(1)}_{k_1k_2k_3k_4}(\tau)\,O^{40}_{k_1k_2k_3k_4} , && (2.72c)
\end{aligned}$$

where $\mathcal{T}^{\dagger(1)}_{k_1k_2}(\tau)$ denotes the first-order approximation to $\mathcal{T}^{\dagger}_{k_1k_2}(\tau)$ while $\mathcal{T}^{\dagger(1)}_{k_1k_2k_3k_4}(\tau)$ represents the first-order approximation to $\mathcal{T}^{\dagger}_{k_1k_2k_3k_4}(\tau)$. The Goldstone Bogoliubov coupled-cluster amplitudes used to build the three diagrams contributing to $o^{(1)}(\tau)$ are displayed in Fig. 2.13.

Similarly, all contributions to $o(\tau)$ up to second order given in App. D.2 are captured through

$$\begin{aligned}
o^{(2)}(\tau) &= O^{00} && (2.73a)\\
&+ \frac{1}{2}\sum_{k_1k_2}\mathcal{T}^{\dagger(2)}_{k_1k_2}(\tau)\,O^{20}_{k_1k_2} && (2.73b)\\
&+ \frac{1}{8}\sum_{k_1k_2k_3k_4}\mathcal{T}^{\dagger(1)}_{k_1k_2}(\tau)\mathcal{T}^{\dagger(1)}_{k_3k_4}(\tau)\,O^{40}_{k_1k_2k_3k_4} && (2.73c)\\
&+ \frac{1}{4!}\sum_{k_1k_2k_3k_4}\mathcal{T}^{\dagger(2)}_{k_1k_2k_3k_4}(\tau)\,O^{40}_{k_1k_2k_3k_4} , && (2.73d)
\end{aligned}$$

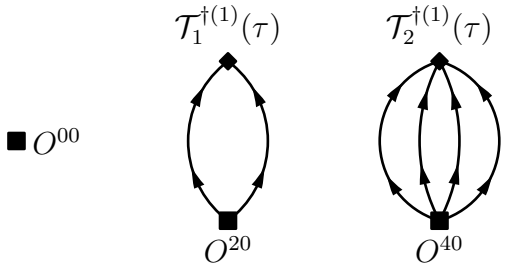

Figure 2.13. Goldstone Bogoliubov coupled cluster diagrams contributing to $o^{(1)}(\tau)$.

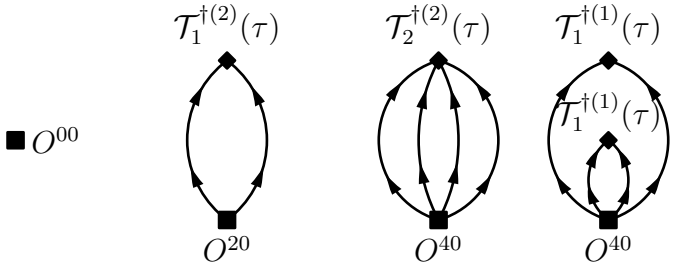

Figure 2.14. Goldstone Bogoliubov coupled cluster diagrams contributing to $o^{(2)}(\tau)$.

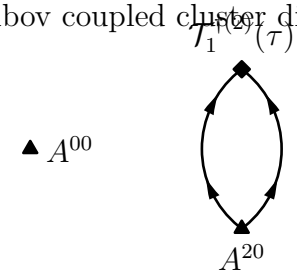

Figure 2.15. Goldstone Bogoliubov coupled cluster diagrams contributing to $a^{(2)}(\tau)$.

where $\mathcal{T}^{\dagger(2)}_{k_1k_2}(\tau)$ denotes the second-order approximation to $\mathcal{T}^{\dagger}_{k_1k_2}(\tau)$ while $\mathcal{T}^{\dagger(2)}_{k_1k_2k_3k_4}(\tau)$ represents the second-order approximation to $\mathcal{T}^{\dagger}_{k_1k_2k_3k_4}(\tau)$. Their Goldstone Bogoliubov coupled cluster amplitudes used to build the four diagrams contributing to $o^{(2)}(\tau)$ are displayed in Fig. 2.14.

2.9. Constraint on particle number

As discussed in Sec. 1.4, the extraction of the binding energy at a given order n requires the subtraction of the Lagrange term computed at the same order. Computing $\mathrm{A}_0^{(n)}$ using Eq. 2.51 and the matrix elements in App. C.4 is done straightforwardly using the diagrams expressions in App. D.4. Such diagrams are displayed in the coupled-cluster amplitude fashion in Fig. 2.15. In practice, of course, this must be done separately for both the neutron number N and the proton number Z. In this formal presentation, A stands for either of them. As the reference state is constrained to have the correct particle number on average, it implies that $\mathrm{A}_0^{(0)} = \mathrm{A}_0$. The constraint is nevertheless not carried over to the perturbed state, and thus to particle number computed beyond zeroth-order. Eventually, the expectation value of A in the reference state must be constrained to a value $\mathrm{A}_{\mathrm{aux}} \neq \mathrm{A}_0$ in order for the constraint to be satisfied for A_0 at the order one is working.

Working with a HFB reference state, it can be shown that $\mathrm{A}_0^{(1)} = 0$ due to the fact that $\Omega^{20} = \Omega^{02} = 0$ (cf. Sec. 2.1.3). Consequently, the first correction to the average particle number

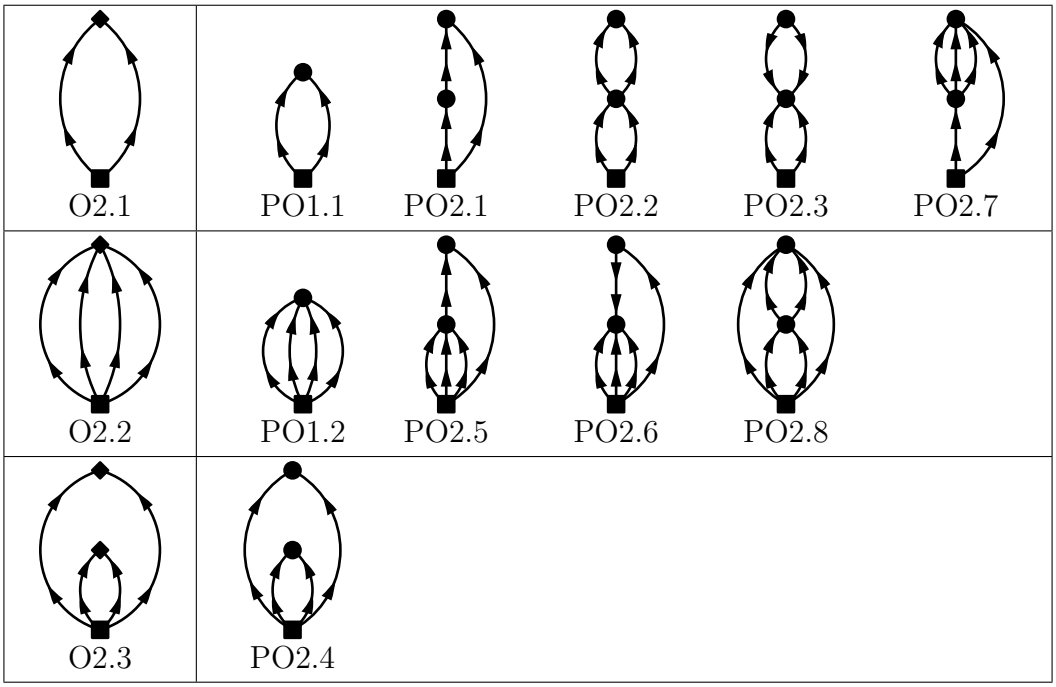

Table 2.2. Observable BCC diagrams versus Feynman BMBPT diagrams contributing to them up to second-order.

appears at second order such that it becomes $\mathrm{A}_0 + \mathrm{A}_0^{(2)} \neq \mathrm{A}_0$. This feature requires an iterative BMBPT scheme in order for the particle number to be correct at order $n \geq 2$. To do so, one needs to rerun the HFB calculation with a shifted chemical potential such that, through a series of iterations, one eventually obtains, e.g., $\mathrm{A}_0^{(0)} + \mathrm{A}_0^{(2)} = \mathrm{A}_0$.

2.10. Particle number variance

In addition to constraining the average particle number, it is of interest to monitor the breaking of $U(1)$ symmetry by computing the variance associated with the operator A. From operators A and A^2, the particle-number variance $\Delta\mathrm{A}^2$ is obtained via

$$\Delta\mathrm{A}^2 \equiv a^2(\infty) - a(\infty)^2 \ . \tag{2.74}$$

To proceed, one needs to write opertator A^2 carefully. By definition, one has

$$\begin{aligned} A^2 &= \left(\sum_{pq} \delta_{pq} c_p^\dagger c_q\right)\left(\sum_{rs} \delta_{rs} c_r^\dagger c_s\right) \\ &= \sum_{pqrs} \delta_{pq}\delta_{rs} c_p^\dagger c_q c_r^\dagger c_s \\ &= \sum_{pqrs} \delta_{pq}\delta_{rs}\left(-c_p^\dagger c_r^\dagger c_q c_s + \delta_{qr} c_p^\dagger c_s\right) \\ &= \sum_{ps} \delta_{ps} c_p^\dagger c_s + \sum_{pqrs} \delta_{pr}\delta_{qs} c_p^\dagger c_q^\dagger c_s c_r \\ &= \sum_{pq} \delta_{pq} c_p^\dagger c_q + \frac{1}{2}\sum_{pqrs} \left(2\delta_{pr}\delta_{qs}\right) c_p^\dagger c_q^\dagger c_s c_r \\ &\equiv \sum_{pq} a_{pq}^{(1)} c_p^\dagger c_q + \frac{1}{2}\sum_{pqrs} a_{pqrs}^{(2)} c_p^\dagger c_q^\dagger c_s c_r \end{aligned} \tag{2.75}$$

where multiple indices substitution were used, along with the anti-commutation relations of creation and annihilation operators (Eq. (1.21)). One notices that A^2 has the structure of a two-body operator, with its one-body component being equal to A itself.

One now introduces the fully antisymmetrized matrix elements of the two-body part of A^2

$$\begin{aligned} \bar{a}_{pqrs}^{(2)} &\equiv a_{pqrs}^{(2)} - a_{pqsr}^{(2)} \\ &= 2\delta_{pr}\delta_{qs} - 2\delta_{ps}\delta_{qr} \\ &= 2(\delta_{pr}\delta_{qs} - \delta_{ps}\delta_{qr}) \ , \end{aligned} \tag{2.76}$$

such that

$$A^2 = \sum_{pq} a_{pq}^{(1)} c_p^\dagger c_q + \frac{1}{4}\sum_{pqrs} \bar{a}_{pqrs}^{(2)} c_p^\dagger c_q^\dagger c_s c_r \ . \tag{2.77}$$

With this at hand, one can apply the results of Sec. 2.5 on general two-body operators with the matrix elements displayed in App. C.5.

2.11. Connection to closed-shell MBPT

Having derived all BMBPT diagrams up to second order, it is of interest to perform their Slater determinant limit that correspond to working with a symmetry-conserving reference state, i.e. to recover standard MBPT. Especially, it provides a stringent test of our derivations, as the MBPT diagrams should match at each order those computed within the frame of closed-shell MBPT [61].

2.11.1. Slater determinant limit

Starting from the diagrams previously derived and represented in Fig. 2.6, significantly simpler expressions are obtained when the Bogoliubov vacuum defined in Eq. (1.26) and satisfying Eq. (2.6a) reduces to a Slater determinant

$$|\Phi\rangle = \prod_{i=1}^{\mathrm{A}_0} c_i^\dagger |0\rangle, \tag{2.78}$$

where indices $i, j, k \ldots$ denote occupied (hole) single-particle states while indices $a, b, c \ldots$ characterize unoccupied (particle) ones. Such a reference vacuum is typically appropriate for doubly closed-(sub)shell nuclei.

With a Slater determinant as the vacuum, the Bogoliubov transformation (Eq. (1.20)) simplifies to[10]

$$a > \mathrm{A}_0 : \qquad \beta_a = c_a, \quad \beta_a^\dagger = c_a^\dagger, \tag{2.79a}$$
$$i \leq \mathrm{A}_0 : \qquad \beta_i^\dagger = c_i, \quad \beta_i = c_i^\dagger. \tag{2.79b}$$

In connection to Eq. (1.20), Eq. (2.79) is equivalent to saying that matrix elements of $\mathcal{W}$ are either 0 or 1, i.e. U and V matrix elements are

$$a > \mathrm{A}_0 : \qquad V_{ak} = 0, \quad U_{ak} = \delta_{ak}, \tag{2.80a}$$
$$i \leq \mathrm{A}_0 : \qquad V_{ik} = \delta_{ik}, \quad U_{ik} = 0. \tag{2.80b}$$

From Eq. (1.28), Eq. (2.80) leads to

$$a > \mathrm{A}_0 : \qquad \rho_{ap} = 0, \quad \kappa_{ap} = 0, \tag{2.81a}$$
$$i \leq \mathrm{A}_0 : \qquad \rho_{ip} = \delta_{ip}, \quad \kappa_{ip} = 0, \tag{2.81b}$$

while Eq. (C.5e) further provides that $\Delta = 0$.

In order to obtain the appropriate form of Ω_0, let us now express $\beta_k^\dagger \beta_k$ in the Slater determinant limit

$$\begin{aligned} \beta_k^\dagger \beta_k &= \left(c_a^\dagger \delta_{ka} + c_i \delta_{ki}\right)\left(c_a \delta_{ka} + c_i^\dagger \delta_{ki}\right) \\ &= \begin{cases} c_a^\dagger c_a & \text{if } k = a \ , \\ c_i c_i^\dagger & \text{if } k = i \ . \end{cases} \end{aligned} \tag{2.82}$$

One obtains two different contributions starting from one quasiparticle term. This will actually be the case for most matrix elements, which is one of the reasons why BMBPT encapsulates the results of standard MBPT while using much fewer diagrams as is shown below.

Generally speaking, quasi-particle energies E_k associated with quasi-particle eigenstates defined in Eq. (2.6) and entering the definition of Ω_0 are arbitrary, with the restriction that $E_k > 0$. In the present context, it is useful to reparametrize them as

$$E_k \equiv |\epsilon_k - \lambda| \ , \tag{2.83}$$

where the ordering of ϵ_k and λ depends on the hole or particle nature of the single-particle state associated to the quasi-particle state, i.e.

$$E_k = \begin{cases} \epsilon_a - \lambda & \text{if } k = a > \mathrm{A}_0 \ , \\ \lambda - \epsilon_i & \text{if } k = i < \mathrm{A}_0 \ , \end{cases} \tag{2.84}$$

[10] In practice the single-particle basis can be different from the one initially introduced to represent the operator, as the Slater determinant can be built from creation operators associated with the HF basis. However, one can go from one basis to the other with the help of a trivial unitary transformation, that we spare here for the sake of concision.

hence maintaining $E_k > 0$.

As a result, Ω_0 reads as[11]

$$\Omega_0 = \Omega^{00} + \sum_a (\epsilon_a - \lambda)\, c_a^+ c_a + \sum_i (\lambda - \epsilon_i)\, c_i c_i^+ \ , \tag{2.85}$$

where Eqs. (2.82) and (2.84) were applied to Eq. (2.4). Excited eigenstates of Ω_0 become nothing but particle-hole excitations of $|\Phi\rangle$

$$|\Phi_{ij\ldots}^{ab\ldots}\rangle = c_a^\dagger c_i c_b^\dagger c_j \ldots |\Phi\rangle \ , \tag{2.86}$$

with the eigenenergies

$$\Omega_0|\Phi\rangle = \epsilon_0|\Phi\rangle \ , \tag{2.87a}$$

$$\Omega_0|\Phi_{ij\ldots}^{ab\ldots}\rangle = \left[\epsilon_0 + \epsilon_{ij\ldots}^{ab\ldots}\right] |\Phi_{ij\ldots}^{ab\ldots}\rangle \ , \tag{2.87b}$$

where

$$\epsilon_0 \equiv \Omega^{00} \ , \tag{2.88a}$$

$$\epsilon_{ij\ldots}^{ab\ldots} \equiv \epsilon_a + \epsilon_b + \cdots - \epsilon_i - \epsilon_j - \ldots \ . \tag{2.88b}$$

In the particular case where $|\Phi\rangle$ is the Hartree-Fock Slater determinant, the one-body states defining Ω_0 are obtained as solutions of the Hartree-Fock equations, i.e. they are solution of Eq. (2.18) in the Slater determinant limit that reads as

$$\begin{pmatrix} h - \lambda & 0 \\ 0 & -(h-\lambda)^* \end{pmatrix} \begin{pmatrix} U_k \\ V_k \end{pmatrix} = E_k \begin{pmatrix} U_k \\ V_k \end{pmatrix} \ . \tag{2.89}$$

Inserting Eq. (2.84), the first (second) line of Eq. (2.89) provides the HF eigenvalue equation for particle (hole) states

$$h\, U_a = \epsilon_a U_a \ , \tag{2.90a}$$

$$h\, V_i^* = \epsilon_i V_i^* \ , \tag{2.90b}$$

such that ϵ_a (ϵ_i) are the eigenvalues of the HF equation and U_a (V_i^*) are the corresponding eigenfunctions.

2.11.2. Limit of BMBPT diagrams

The expressions of all BMBPT diagrams for a generic operator in the Slater determinant limit up to second order are provided in App. F. The corresponding relation between BMBPT grand potential diagrams and MBPT energy diagrams is displayed in Tab. 2.3. This relation can be established starting either from the BMBPT grand potential or energy diagrams, except for the diagrams labelled as PΩ0.1 and PH0.1. Indeed all A^{ij} matrix elements are zero in the Slater determinant limit except for A^{00} and A^{11}, such that the particle number diatgrams contributing above zeroth order and displayed in App. D.4 for first and second order vanish, as expected in

[11] The limit associated with Eq. (2.79) has to be applied to Ω^{00} in the following.

a symmetry-conserving formalism. Consequently, the particle number contributions associated to the grand potential diagrams vanish and the contributions associated to the energy diagrams are recovered eventually.

For illustration, let us derive below the Slater determinant limit of the diagram labelled as PO2.1 in Fig. 2.6, where the considered operator is the grand canonical potential Ω, thus giving the grand potential diagram PΩ2.1. The Slater determinant limit of each matrix element is computed by applying relations (2.80) to its expression as displayed in App. C, with $\breve{\Omega}^{11} = \Omega^{11} - \bar{\Omega}^{11}$. Note that Eq. (2.81) further implies that Υ and Ξ matrices are identically zero, and that matrix Λ displays a far simpler form. One obtains

$$\begin{aligned}
\mathrm{P}\Omega 2.1 &= -\sum_{k_1k_2k_3} \frac{\Omega^{20}_{k_1k_2}\breve{\Omega}^{11}_{k_3k_1}\Omega^{02}_{k_3k_2}}{(E_{k_1}+E_{k_2})(E_{k_2}+E_{k_3})} \\
&= -\sum_{k_1k_2k_3} \frac{1}{(E_{k_1}+E_{k_2})(E_{k_2}+E_{k_3})} \Big(\Lambda_{k_1k_2}\delta_{k_1a}\delta_{k_2i} - \Lambda^T_{k_1k_2}\delta_{k_1i}\delta_{k_2a}\Big) \\
&\quad \times \Big(\Lambda_{k_3k_1}\delta_{k_3b}\delta_{k_1a} - \Lambda^T_{k_3k_1}\delta_{k_3j}\delta_{k_1i} - (\epsilon_a-\lambda)\delta_{k_1a}\delta_{k_3b}\delta_{ab} + (\lambda-\epsilon_i)\delta_{k_1i}\delta_{k_3j}\delta_{ij}\Big) \\
&\quad \times \Big(-\Lambda_{k_3k_2}\delta_{k_3j}\delta_{k_2a} + \Lambda^T_{k_3k_2}\delta_{k_3b}\delta_{k_2i}\Big) \\
&= \sum_{aij} \frac{h_{ai}\,(h_{ij}-\epsilon_i\delta_{ij})\,h_{ja}}{(\epsilon_a-\lambda-\epsilon_i+\lambda)(\epsilon_a-\lambda-\epsilon_j+\lambda)} - \sum_{abi} \frac{h_{ai}\,(h_{ba}-\epsilon_a\delta_{ab})\,h_{ib}}{(\epsilon_a-\lambda-\epsilon_i+\lambda)(\epsilon_b-\lambda-\epsilon_i+\lambda)} \\
&= \sum_{aij} \frac{h'_{ai}h'_{ij}h'_{ja}}{\epsilon^a_i\epsilon^a_j} - \sum_{abi} \frac{h'_{ai}h'_{ba}h'_{ib}}{\epsilon^a_i\epsilon^b_i} \ ,
\end{aligned} \tag{2.91}$$

where $h'_{pq} \equiv h_{pq} - \epsilon_p\delta_{pq}$. Two terms are thus recovered, i.e. two MBPT diagrams, starting from one BMBPT diagram. The diagram denoted as PΩ2.1 actually recasts diagrams 13 and 14 displayed on page 133 of Ref. [61], where operator f' correponds to h' here.

2.11.3. Discussion

Taking the Slater determinant limit, which corresponds to dealing with closed-shell systems, the eleven Feynman BMBPT diagrams contributing to $\mathrm{E}_0^{\mathrm{A}_0}$ strictly reduce to the corresponding 14 standard Goldstone MBPT diagrams generated from two-body forces [61] as displayed in Tab. 2.3. Their exact expressions are detailed in App. F. Some BMBPT diagrams encompasses several MBPT diagrams, e.g. PΩ2.1, PΩ2.5, PΩ2.6, PΩ2.7 and PΩ2.8. The reduction of the number of diagrams at any given order n when going from MBPT to BMBPT is a consequence of working in a quasi-particle representation that does not distinguish particle and hole states. Conversely, all summations over quasi-particle labels run over the entire dimension of the one-body Hilbert space.

In the specific case where the reference state $|\Phi\rangle$ is solution of the Hartree-Fock equation, i.e. when working within a Møller-Plesset scheme, all MBPT diagrams but those labelled as 1, 2 and 3 in Tab. 2.3 and displayed in Fig. 2.16 vanish, such that *canonical HF-MBPT* diagrams are recovered. They correspond to BMBPT diagrams PΩ0.1, PΩ1.2 and PΩ2.8, that respectively match Eq. (5.7) of p.131 and Eq. (5.8) of p.132 in Ref. [61]. It is equivalent to working with an HFB vacuum in the BMBPT framework.

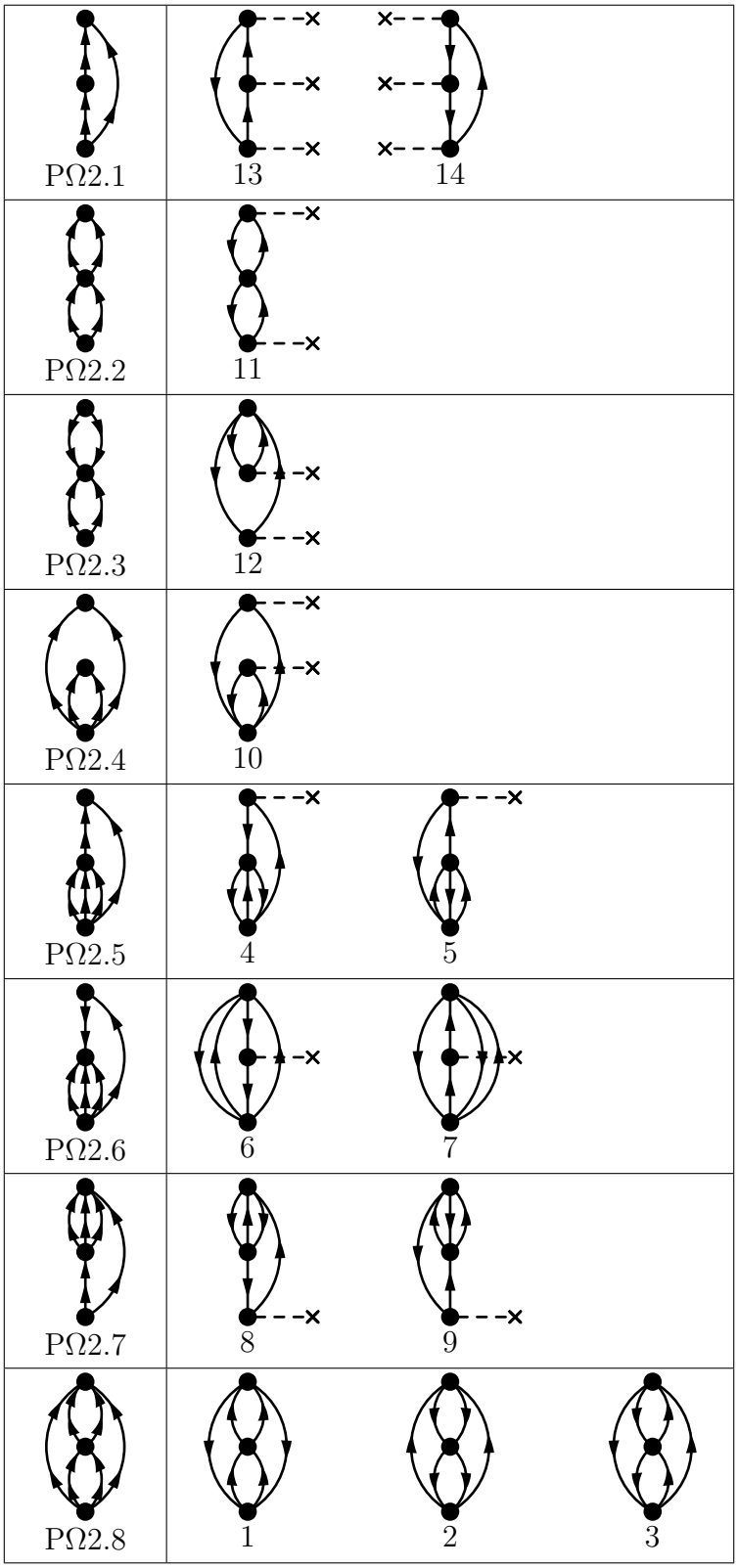

Table 2.3. BMBPT Feynman diagrams appearing at second order and their associated MBPT Goldstone diagrams. The numbering of the MBPT diagrams is the one used on page 133 of Ref. [61].

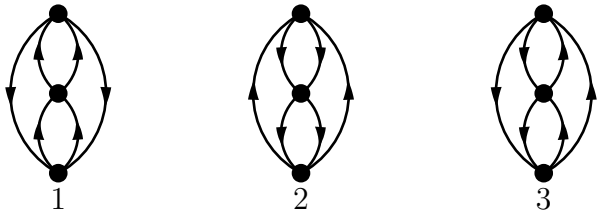

Figure 2.16. Canonical MBPT diagrams, as displayed and numbered on page 133 of Ref. [61] and obtained from the BMBPT diagram PO2.8 in Fig. 2.6.

2.12. Implementation algorithm

Let us eventually synthesize the steps that must be followed to implement the Bogoliubov MBPT formalism. In order to facilitate back-and-forth reading with the rest of the document, the equation numbers displayed here are the original ones.

1. Solve, e.g., Hartree-Fock-Bogoliubov equations in the single-particle basis of interest,

$$\begin{pmatrix} h-\lambda & \Delta \\ -\Delta^* & -(h-\lambda)^* \end{pmatrix} \begin{pmatrix} U_k \\ V_k \end{pmatrix} = E_k \begin{pmatrix} U_k \\ V_k \end{pmatrix} \ , \tag{2.18}$$

   where the h and Δ fields are defined in Eq. (C.5). This fixes the reference state $|\Phi\rangle$ and Ω_0, i.e. it delivers the set of $\{U_k, V_k, E_k \geq 0\}$. One proceeds to the computation under the constraint $\langle\Phi|A|\Phi\rangle = A^{00} = \mathrm{A}_{\mathrm{aux}}$. Starting by imposing $\mathrm{A}_{\mathrm{aux}} = \mathrm{A}_0$ produces a first guess for the Lagrange parameter λ.

   From there, one can compute ρ, κ, κ^* and σ matrices according to

$$\rho = +V^* V^T \ , \tag{1.28a}$$
$$\kappa = +V^* U^T \ , \tag{1.28b}$$
$$\bar{\kappa}^* = -U^* V^T \ , \tag{1.28c}$$
$$\sigma^* = -U^* U^T \ , \tag{1.28d}$$

   using solutions $(U, V)_k$ of Eq. (2.18) corresponding to positive quasi-particle energies $E_k \geq 0$.

2. Build matrix elements $\Omega^{ij}_{k_1\ldots k_i k_{i+1}}$, $A^{ij}_{k_1\ldots k_i k_{i+1}}$, $H^{ij}_{k_1\ldots k_i k_{i+1}}$, $A^{2.ij}_{k_1\ldots k_i k_{i+1}}$ according to App. C.

3. Observables of interest must be computed on the basis of

$$\mathrm{O}_0^{\mathrm{A}_0} = o(\infty) \ ,$$

   at order n in BMBPT according to

$$o^{(n)}(\infty) = \sum_{i,j=0,2,4} \sum_{l=0}^{n} o^{ij\,(l)}(\infty) \ .$$

With zero-, first-, and second-order diagrams taken from App. D.2 and displayed in Fig. 2.6, one has

$$\begin{aligned} o^{(2)} = O^{00} & \\ & + \frac{1}{2} \sum_{k_1 k_2} O^{20}_{k_1 k_2} \mathcal{T}^{\dagger(2)}_{k_1 k_2}(\infty) \\ & + \frac{1}{8} \sum_{k_1 k_2 k_3 k_4} O^{40}_{k_1 k_2 k_3 k_4} \mathcal{T}^{\dagger(1)}_{k_1 k_2}(\infty) \mathcal{T}^{\dagger(1)}_{k_3 k_4}(\infty) \\ & + \frac{1}{4!} \sum_{k_1 k_2 k_3 k_4} O^{40}_{k_1 k_2 k_3 k_4} \mathcal{T}^{\dagger(2)}_{k_1 k_2 k_3 k_4}(\infty) \ , \end{aligned}$$

where the definition of the amplitudes in terms of the matrix elements of App. C is given in Eq. (E.1). $\omega(\infty)$, $a(\infty)$, $a^2(\infty)$ and $h(\infty) = \omega(\infty) + \lambda a(\infty)$ can be computed using the previous expressions and replacing matrix elements of O by those of the appropriate operator (see App. C).

Be reminded that choosing the reference state $|\Phi\rangle$ to be the solution of HFB equations amounts to setting $\breve{\Omega}^{11} = \Omega^{20} = \Omega^{02} = 0$ such that diagrams PN2.1, PO1.1, PO2.1, PO2.2, PO2.3, PO2.4, PO2.5 and PO2.6 are zero in the Møller-Plesset scheme, i.e. the set reduces from two non-zero diagrams to one non-zero diagram for the norm at second order, and from eleven to four non-zero diagrams for other operators at second order. For the coupled-cluster-like amplitudes, it corresponds to $\mathcal{T}_1^\dagger$ being zero at first order, and having only one contribution arising at second order. The number of contributions to $\mathcal{T}_2^\dagger$ arising at second order reduces coincidently from three to one. For kernels of one-body operators like the particle number A, it implies that corrections first appear only at second order in perturbation theory. For two- and many-body operators like the grand canonical potential Ω, only $\mathcal{T}_2^\dagger$ contributes at first order, and the expression of the contributions at second-order are somewhat simplified.

4. Compute the expectation value $a(\infty)$ of the particle number operator A with the goal that

$$\mathrm{A}_0 = a(\infty) \ . \tag{1.45b}$$

If $a(\infty) \neq \mathrm{A}_0$, adjust λ by going back to step 1. If $a(\infty) > \mathrm{A}_0$ ($a(\infty) < \mathrm{A}_0$), solve step 1 such that $\langle\Phi|A|\Phi\rangle = A^{00} = \mathrm{A}_{\mathrm{aux}} < \mathrm{A}_0$ ($\mathrm{A}_{\mathrm{aux}} > \mathrm{A}_0$). This will deliver a new set of $\{U_k, V_k, E_k > 0\}$. Repeat until Eq. (1.45b) is satisfied.

5. At convergence, compute observables $\omega(\infty)$, $a(\infty)$, $a^2(\infty)$ and $h(\infty)$, and determine the particle-number variance through

$$\Delta\mathrm{A}^2 = a^2(\infty) - a(\infty)^2 \ . \tag{2.74}$$

3. Systematic generation and evaluation of BMBPT diagrams

3.1. Introduction

Having carefully detailed Bogoliubov many-body perturbation theory in Chapter 2, and having genereated and derived its diagrams at first and second order, the next step is to do so at higher orders. The problem is however to do it in a safe and efficient way, as both the number of diagrams and their topological complexity rises rapidly in many-body perturbation theory. Different attempts have been made in the past to generate automatically MBPT diagrams [119, 120, 121, 122, 123, 124], and even to evaluate their expressions [122, 123]. A similar effort has been made in the quantum chemistry community for CC and CI [125, 126]. Recently, Monte Carlo methods have been used to generate and compute diagrammatic contributions for the Fermi gas [136, 137].

In the present chapter, the focus is on the automated generation and evaluation of BMBPT diagrams. Related formal difficulties are detailed and a method to overcome them is introduced, leading to the identification of a novel diagrammatic rule generalizing the standard resolvent rule. The numerical code ADG that relies on this breakthrough is eventually introduced.

3.1.1. Time-integrated expression

Let us first remind the expression associated to the third-order BMBPT diagram displayed in Fig. 2.9 as already stated in Eq. (2.56),

$$D = \lim_{\tau\to\infty} \frac{(-1)^3}{2(2!)^4} \sum_{k_i} O^{40}_{k_1k_2k_3k_4} \Omega^{40}_{k_5k_6k_7k_8} \Omega^{04}_{k_5k_6k_1k_2} \Omega^{04}_{k_7k_8k_3k_4} \times \int_0^\tau \mathrm{d}\tau_1 \mathrm{d}\tau_2 \mathrm{d}\tau_3 \, \theta(\tau_2-\tau_1)\theta(\tau_3-\tau_1) e^{-\tau_1\epsilon^{k_5k_6k_7k_8}} e^{-\tau_2\epsilon_{k_1k_2k_5k_6}} e^{-\tau_3\epsilon_{k_3k_4k_7k_8}} \ .$$

The expression obtained via the application of Feynman's algebraic rules does not yet constitute the form needed for the numerical implementation of the formalism. While the sign, the combinatorial factor and the matrix elements will remain untouched, the p-tuple time integral must be performed in order to obtain the needed expression. Generically denoting the energy factor multiplying the time label τ_k in the integrand as a_k, the integral associated with our

example of Fig. 2.9 can be worked out in the following fashion

$$\begin{aligned} T &= \lim_{\tau\to\infty} \int_0^\tau d\tau_1 d\tau_2 d\tau_3 \theta(\tau_2-\tau_1)\theta(\tau_3-\tau_1) e^{-a_1\tau_1-a_2\tau_2-a_3\tau_3} \\ &= \lim_{\tau\to\infty} \int_0^\tau d\tau_1\, e^{-a_1\tau_1} \int_{\tau_1}^\tau d\tau_2\, e^{-a_2\tau_2} \int_{\tau_1}^\tau d\tau_3\, e^{-a_3\tau_3} \\ &= \lim_{\tau\to\infty} \int_0^\tau d\tau_1\, e^{-a_1\tau_1} \frac{e^{-a_2\tau}-e^{-a_2\tau_1}}{a_2} \frac{e^{-a_3\tau}-e^{-a_3\tau_1}}{a_3} \\ &= \frac{1}{(a_1+a_2+a_3)a_2a_3}\,. \end{aligned} \tag{3.1}$$

Two important lessons can be learned from this particular example.

- Exploiting the time-ordering relations imposed by the step functions, one performs the p integrals following a specific sequence, i.e., one starts with the greatest time label whose corresponding integral is written in the right-most position before proceeding to integrals over smaller times, i.e., moving in steps towards the leftmost integral. In doing so, we see that the integrals over τ_2 and τ_3 are in fact independent as the two time variables are not ordered with respect to each other and only entertain a causal relation with respect to a common variable, i.e., τ_1, corresponding to an *earlier* time. The integral over τ_1 does depend on the result of the integrals over τ_2 and τ_3 and is thus performed last.

- While the energy variables entering the time integrand are a_1, a_2 and a_3, the end result takes the form of a fraction whose non-trivial factors appear in the denominator and are specific combinations of these original energy variables. Expressing a_1, a_2 and a_3 back in terms of quasi-particle energies, these combinations read as

$$\begin{aligned} a_1+a_2+a_3 &= \epsilon_{k_1k_2k_3k_4}\,, \\ a_2 &= \epsilon_{k_1k_2k_5k_6}\,, \\ a_3 &= \epsilon_{k_3k_4k_7k_8}\,, \end{aligned} \tag{3.2}$$

  and thus correspond to positive sums of quasi-particle energies. We will identify later on what these specific combinations of quasi-particle energies actually correspond to.

Combining Eqs. (3.1) and (3.2) and inserting the result back into Eq. (2.56) provides the time-integrated expression of the diagram under the needed form

$$D = \frac{(-1)^3}{2(2!)^4} \sum_{k_i} \frac{O^{40}_{k_1k_2k_3k_4}\Omega^{40}_{k_5k_6k_7k_8}\Omega^{04}_{k_5k_6k_1k_2}\Omega^{04}_{k_7k_8k_3k_4}}{\epsilon_{k_1k_2k_3k_4}\ \epsilon_{k_1k_2k_5k_6}\ \epsilon_{k_3k_4k_7k_8}}\,.$$

3.1.2. Towards higher orders

BMBPT diagrams of order $p = 0, 1$, and 2 have been generated and evaluated manually within the NO2B approximation, i.e., excluding operators $O^{[k]}$ with $k > 4$. The eleven corresponding diagrams have been displayed in Fig. 2.6. They have been recently implemented numerically to perform *ab initio* nuclear structure calculations of mid- and heavy-mass open-shell nuclei [138]. Results will be discussed in Chap. 4.

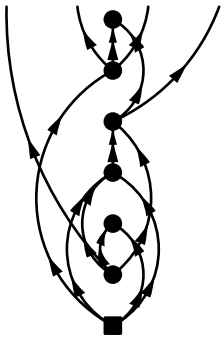

Figure 3.1. Lower-part of a possible arbitrary-order BMBPT diagram.

When going to higher orders and/or using vertices with more legs, the number of vertices and propagators grows out of proportion, as schematically illustrated in Fig. 3.1, with diagrams potentially displaying very involved topologies. The associated combinatorial makes generating all diagrams more difficult, cumbersome and prone to omissions. Algebraically, while the high order directly translates into the rise of the dimensionality of the time integral, the potentially complex topology of the diagram translates into the intricate structure of the time integrand dictated by the many step functions at play. The development of automated tools to produce and evaluate high-order diagrams generated from vertices containing more, e.g., six, legs becomes thus essential.

Eventually, the expression of a generic diagram of order p obtained from the application of Feynman's algebraic rules typically reads as

$$D = \lim_{\tau\to\infty} \frac{(-1)^a}{2^b 3^c 4^d 5^e 6^f} \sum_{k_i} \Omega^{i_1 j_1}_{k\dots k} \dots \Omega^{i_p j_p}_{k\dots k} O^{m0}_{k\dots k} \int_0^\tau d\tau_1 \dots d\tau_p \, \theta(\tau_q - \tau_r) \dots \theta(\tau_u - \tau_v) e^{-a_1\tau_1} \dots e^{-a_p\tau_p} \,, \tag{3.3}$$

where $(a, b, c, \dots)$ are integer numbers characterizing the topology of the diagram, $(q, r, \dots u, v)$ are integers between 1 and p and $(a_1, \dots, a_p)$ denote the sum/difference of quasi-particle energies associated with the lines entering/leaving each of the p $\Omega^{ij}(\tau_k)$ vertices. Quasiparticle indices k_i have been stripped of their labels in the matrix elements for the sake of concision.

In the following, we detail the strategy, the algorithm and the code to automatically *generate* and *evaluate* all BMBPT diagrams appearing at an arbitrary order p.

3.2. Automatic generation of BMBPT diagrams

The automated generation of BMBPT Feynman diagrams is based on the use of graph theory, which is the domain of mathematics that focuses on studying graphs. Definitions and properties of quantities of interest, i.e., graph, walk and path on a graph, cycle, tree graph, adjacency matrix etc. are detailed in App. B. Here, we limit ourselves to a brief and qualitative description of these notions and refer to the appendix for a more rigourous account.

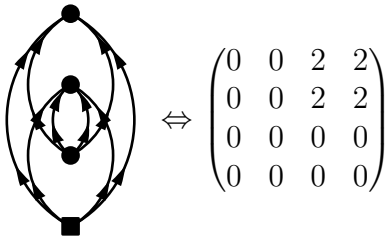

$$\Leftrightarrow \begin{pmatrix} 0 & 0 & 2 & 2 \\ 0 & 0 & 2 & 2 \\ 0 & 0 & 0 & 0 \\ 0 & 0 & 0 & 0 \end{pmatrix}$$

Figure 3.2. A BMBPT diagram and its associated adjacency matrix.

3.2.1. Basic elements

The main notions of interest are

- A graph G denotes a set of nodes and a set of edges, each edge being attached to a node or a pair of nodes.
- A walk on a graph is an alternating sequence of nodes and edges connecting them. A walk is closed (open) if the first and last nodes are (not) the same. The length of a walk corresponds to its number of edges.
- A path is a walk whose nodes are all distinct.
- A cycle is a closed walk where the initial/final node and the internal nodes are distinct.
- A graph is connex if, for any pair of nodes, there exists a path connecting them.
- A tree graph is a connex graph without cycle.
- The oriented adjacency matrix $\tilde{A}(G)$ associated to a graph G with labelled nodes $v_1 ... v_n$ is the matrix whose elements $\tilde{a}_{ij}$ indicate the number of edges going from node v_i to node v_j.

3.2.2. Oriented adjacency matrix and BMBPT diagram

A BMBPT diagram being a connected graph with oriented edges, one can extract its oriented adjacency matrix, as exemplified in Fig. 3.2. Feynman's topological rules characterizing valid BMBPT diagrams constrain the form of their oriented adjacency matrices.

1. A BMBPT diagram of order p, i.e., containing $p+1$ vertices, is associated to a $(p+1)\times(p+1)$ adjacency matrix.
2. As a BMBPT diagram is connected, its associated adjacency matrix cannot be recast into block-diagonal form through permutation of its rows and columns.
3. As each vertex Ω^{ij} involved has either an effective one-, two- or three-body character, thus exhibiting $i + j = 2, 4$ or 6, each matrix index k fulfils the identity

$$\sum_l (\tilde{a}_{kl} + \tilde{a}_{lk}) = 2, 4 \text{ or } 6\,. \tag{3.4}$$

4. As only $O^{m0}(0)$ vertices with propagators going out contribute to BMBPT diagrams, the corresponding, e.g. first, column of a valid adjacency matrix is necessarily zero.

5. As no contraction of a vertex onto itself is possible, all diagonal elements $\tilde{a}_{ii}$ of a valid adjacency matrix are zero.

6. As no loop between two vertices is possible, matrix elements $\tilde{a}_{ij}$ and $\tilde{a}_{ji}$ of a valid adjacency matrix cannot be non-zero simultaneously.

Producing the complete set of $(p+1) \times (p+1)$ matrices satisfying the above rules, one is sure to generate all possible BMBPT diagrams of order p. One must, however, further discard topologically equivalent diagrams. This can be done by performing simultaneous permutations of rows and columns and by comparing the result with other matrices in the set. However, as the generic operator O is at fixed time 0, it must not be considered in the process, i.e., its column and row must not be permuted with any other.

3.2.3. Pedestrian generation of adjacency matrices

A simple way to generate all $(p+1) \times (p+1)$ adjacency matrices for a maximal vertex degree equal to `deg_max`[1] (i.e., 4 or 6 depending on the two- or three-body character of the operators) is to start with a set of matrices containing only one matrix fully initialized to zero and proceed as follows

1. Consider a matrix element,
   a) Consider a matrix in the set,
      i. Save the matrix,
      ii. Save copies of the matrix with the matrix element changed to every possible value from 1 to `deg_max`,
   b) Go back to (a) until all matrices in the set are exhausted,
2. Go back to 1. until all matrix elements are exhausted.

With this method, detailed in a pseudocode fashion in Alg. 1, all possible BMBPT adjacency matrices are necessarily produced[2]. One must, however, apply the set of tests necessary to only retain adjacency matrices that conform with the rules listed in Sec. 3.2.2.

[1] Though the code allows to distinguish between `deg_max` for the observable and `deg_max` for the Hamiltonian, for the sake of clarity the same `deg_max` is used for both in the following.

[2] In particular, the rule regarding $n_a = 0$ is respected by construction, as the matrices are generated on a propagator-by-propagator basis, with no external leg. The burden is thus transferred on making sure only vertices with the appropriate one-, two- or three-body character are produced. A generalization of the process authorizing $n_a \geq 0$ thus has to be considered for off-diagonal BMBPT.

Algorithm 1 Generation of adjacency matrices

```
1: function GenAdjMat
2:     MatList = {}
3:     set_zero(A)
4:     d ∈ {0, 2, ..., deg_max}
5:     for i = 0, ..., p + 1 do
6:         for j = 0, ..., p + 1 do
7:             a_ij = d
8:     if (CheckProperties(A) = True) then
9:         append A to MatList
```

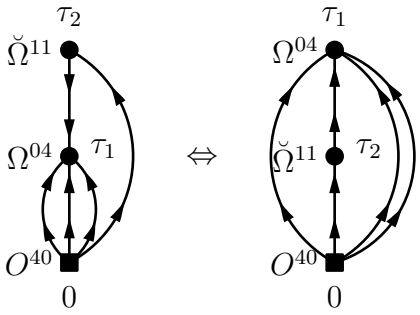

Figure 3.3. A BMBPT diagram drawn with some propagators going downwards (left) can be turned into an equivalent diagram with all its propagators going upwards (right) by moving the second vertex above the third one.

3.2.4. Optimized generation of adjacency matrices

The pedestrian method detailed in Sec. 3.2.3 is time and memory consuming from a numerical viewpoint. It is thus beneficial to integrate as many of the selection rules as possible into the very production process of the matrices. Doing so, time and memory are saved as less matrices are actually produced while the tests enforcing the selection rules become superfluous. This is particularly beneficial regarding the restriction to topologically distinct diagrams as the corresponding test scales factorially with the number of matrices in the set.

The first obvious improvement is to avoid producing any matrix with a non-zero diagonal element. Second, the fact that BMBPT diagrams do not display oriented loops between any given number of vertices makes always possible, by moving vertices within the plane of the graph, to recast any BMBPT diagram as an equivalent diagram with all propagators moving upwards, as is exemplified in Fig. 3.3. Accordingly, one limits the generation to upper-triangular matrices, thus reducing their number drastically and discarding at the same time a whole set of topologically equivalent diagrams.

The number of considered matrices can be further reduced by checking the k-body character of the vertices on-the-fly. As the matrix elements are updated row by row, and thus vertex by vertex given that only upper-triangular matrices are considered, one can check directly after filling a row that the corresponding vertex has indeed a one-, two- or three-body character, i.e., that it satisfies Eq. (3.4). If it is not the case, the matrix is rejected on-the-fly along with all

matrices that would have spawn from it. For example, the adjacency matrix

$$\begin{pmatrix} 0 & 2 & 2 & 1 \\ 0 & 0 & 0 & 0 \\ 0 & 0 & 0 & 0 \\ 0 & 0 & 0 & 0 \end{pmatrix} \tag{3.5}$$

can be discarded right after filling the first row given that the sum of its matrix elements differ from 2, 4 or 6.

A similar reasoning applies to the disconnected character of the diagrams. For matrices associated to diagrams of order $p > 0$, it is possible to test after the second (or any further) row is filled if the matrix is bound to span a disconnected diagram in the end. For example, the adjacency matrix

$$\begin{pmatrix} 0 & 2 & 0 & 0 \\ 0 & 0 & 0 & 0 \\ 0 & 0 & 0 & 0 \\ 0 & 0 & 0 & 0 \end{pmatrix}, \tag{3.6}$$

if already filled on its two first rows, would result in vertices 1 and 2 being disconnected from vertices 3 and 4. One can thus eliminate the matrix on the fly, along with all matrices that would have spawn from it.

3.2.5. Drawing associated BMBPT diagrams

Once all allowed $(p+1) \times (p+1)$ adjacency matrices have been produced, the corresponding BMBPT diagrams can be drawn by simply reading the matrices, as each matrix element encodes the number of propagators going from one vertex to another. As the number of generated diagrams quickly increases with p, it is of interest to design a program to do it automatically. The program reads the content of the matrix and writes in a text file the appropriate drawing instructions for *FeynMF* [139], a LaTeX package designed to draw Feynman diagrams.

Although adjacency matrices are sufficient to draw the diagrams, one may want to perform operations on the diagrams. We thus chose to make use of a graph theory package for Python called *NetworkX* [140]. The package takes adjacency matrices as input and produces graph objects on which different operations can be performed. For example, the check for topologically equivalent diagrams is performed using the built-in *NetworkX* function `is_isomorphic` and its related interfaces. Combining the `MultiDiGraph` object from NetworkX and object-oriented programming, it was possible to implement this test in a time-savy way, first checking that two graphs share basic structures properties (degree of the different nodes, two-body only or three-body operators character, etc.) before performing the costly permutations eventually needed to check if they are indeed topologically equivalent.

With topologically distinct *NetworkX* BMBPT diagrams at hand, we could adapt the program running through adjacency matrices to make it iterate through the nodes of the graph and obtain the FeynMP instructions accordingly. As an example, the output displaying the drawing instructions of the BMBPT diagram displayed in Fig. 2.9 is given in Fig. 3.4.

```
\begin{fmffile}{diag10}
\begin{fmfgraph*}(80,80)
\fmfcmd{style_def prop_pm expr p =
draw_plain p;
shrink(.7);
cfill (marrow (p, .25));
cfill (marrow (p, .75))
endshrink;
enddef;}
\fmftop{v3}\fmfbottom{v0}
\fmf{phantom}{v0,v1}
\fmfv{d.shape=square,d.filled=full,d.size=3thick}{v0}
\fmf{phantom}{v1,v2}
\fmfv{d.shape=circle,d.filled=full,d.size=3thick}{v1}
\fmf{phantom}{v2,v3}
\fmfv{d.shape=circle,d.filled=full,d.size=3thick}{v2}
\fmfv{d.shape=circle,d.filled=full,d.size=3thick}{v3}
\fmffreeze
\fmf{prop_pm,left=0.6}{v0,v2}
\fmf{prop_pm,right=0.6}{v0,v2}
\fmf{prop_pm,left=0.6}{v0,v3}
\fmf{prop_pm,right=0.6}{v0,v3}
\fmf{prop_pm,left=0.5}{v1,v2}
\fmf{prop_pm,right=0.5}{v1,v2}
\fmf{prop_pm,left=0.6}{v1,v3}
\fmf{prop_pm,right=0.6}{v1,v3}
\end{fmfgraph*}
\end{fmffile}
```

Figure 3.4. *FeynMF* instructions to draw the BMBPT diagram displayed in Fig. 2.9.

3.3. Automatic evaluation of BMBPT diagrams

Having the capacity to generate all BMBPT Feynman diagrams of order p, the next challenge is to systematically derive their expression. Doing so on the basis of Feynman's algebraic rules is rather straightforward. However, it leaves the p-tuple time integral to perform in order to obtain the time-integrated expression of interest. Finding an algorithm to do so without prior knowledge of the perturbative order or of the topology of the diagram constitutes an unsolved challenge to our knowledge. In the present section, we introduce a method to achieve this goal, eventually leading to the identification of a novel diagrammatic rule.

3.3.1. Time-structure diagram

In a BMBPT Feynman diagram, a time label is attached to each vertex. Given any two vertices, their time labels are ordered with respect to each other as soon as a propagator connects the vertices directly by virtue of the step function it carries (see Eq. 2.24). The time labels may also be ordered in a less obvious way if the two vertices are connected through a set of

intermediate vertices and propagators.

Eventually, a BMBPT Feynman diagram exhibits an underlying time structure that translates into the specific form of the integrand of the p-tuple integral to be performed. This specific form is characterized by a string of step functions ordering a subset of the time variables that must be integrated over. In order to characterize the typical structure of the integrand and compute the corresponding integral, we choose to represent it diagrammatically by introducing the so-called time-structure diagram (TSD) of a given BMBPT diagram. As we shall see below, the algorithm to perform the time-integral strongly depends on the *topology* of the TSD that happens to play a fundamental role. Consequently, we now introduce and characterize TSDs.

1. The TSD associated to a BMBPT diagram of order p is made out of the following building blocks
   a) $p+1$ vertices representing operators in the interaction representation. While their positive time labels $(0, \tau_1, \ldots, \tau_p)$ are left implicit, vertices but the bottom one carry explicit energy factors $(a_1, \ldots, a_p)$.
   b) oriented links representing ordering relations, i.e., step functions, between pairs of vertices. A link is oriented from the vertex carrying the smaller time to the vertex carrying the larger time. Only the minimal set of links necessary to describe the time structure of the diagram is to be drawn, i.e. if several paths exist, only the ones comprising at least two links are to be represented[3].
   c) BMBPT diagrams being connected, TSDs are necessarily connex.
2. The expression of a TSD of order p is extracted in the following way
   a) each vertex a_q, $q = 1, \ldots, p$, contributes a factor $e^{-a_q \tau_q}$,
   b) each link[4] oriented from vertex a_u to vertex a_v contributes the step function $\theta(\tau_v - \tau_u)$,
   c) the p time labels $\tau_1, \ldots, \tau_p$ are integrated over from 0 to $\tau \to +\infty$,

   and thus typically reads as
   $$T = \lim_{\tau \to \infty} \int_0^\tau d\tau_1 \ldots d\tau_p \, \theta(\tau_q - \tau_r) \ldots \theta(\tau_u - \tau_v) e^{-a_1 \tau_1} \ldots e^{-a_p \tau_p} \ , \tag{3.7}$$
   where $(q, r, \ldots u, v)$ are integers between 1 and p.
3. The TSD associated to a BMBPT diagram can be obtained from the latter through the following steps
   a) copy the BMBPT diagram,
   b) replace propagators by links,
   c) add a link between the bottom vertex at time 0 and every other vertex if such a link does not exist[5],

[3] This corresponds to omitting a step function $\theta(\tau_i - \tau_j)$ whenever a string of step functions $\theta(\tau_i - \tau_\alpha) \ldots \theta(\tau_\omega - \tau_j)$ carrying the same information already appears.

[4] Links originating from the bottom vertex do not contribute an explicit step function given that the positivity of the running time labels is encoded into the boundary of the integral; see rule 2.(c).

[5] The operator vertex O at time 0 entertains an ordering relation with every other vertex.

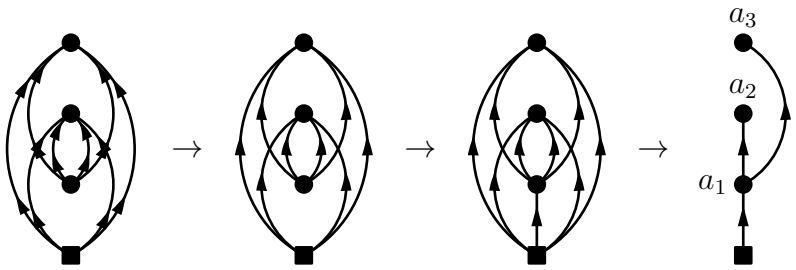

Figure 3.5. Production of the TSD associated with the third-order BMBPT diagram displayed in Fig. 2.9.

d) for each pair of vertices, consider all possible pathes linking them and discard the ones comprising only one link if longer paths exist,

e) match a_q to the sum/difference of quasi-particle energies associated with the lines entering/leaving the corresponding vertex in the BMBPT diagram.

The procedure is illustrated in Fig. 3.5 for the BMBPT diagram originally displayed in Fig. 2.9. Cleared of other informations, the TSD transparently characterizes the time-ordering structure underlying the BMBPT diagram, i.e., the three Ω^{ij} vertices are at higher times than O^{40} such that the two Ω^{04} vertices are at higher times than Ω^{40} without being ordered with respect to one another. From the graph theory viewpoint, the corresponding TSD is a tree, i.e., it contains no cycle, with two branches such that the vertices on the two branches are not ordered with respect to one another.

3.3.2. Discussion

It is mandatory to generate the TSDs *from* the underlying BMBPT diagrams. Indeed, only in the latter can the maximum degree `deg_max` of the operators at play be employed to constrain the topology of the diagrams, eventually dictating the topology of allowed TSDs. With this in mind and following the above rules, the 1/1/2/5/15 TSDs of order 0/1/2/3/4 corresponding to BMBPT diagrams generated from operators with `deg_max` = 6, i.e., containing effective three-body terms, have been produced and systematically displayed in Figs. 3.6 and 3.7. One notices that the first TSD containing a cycle is the third-order TSD labelled as T3.5 in Fig. 3.6, i.e., all TSDs up to order 2 (3) are trees (but one). At order 4, seven out of fourteen TSDs contain cycles. Obviously, the higher the order, the more complex the topology can be.

In the end, *different* BMBPT diagrams of order p can have the *same* TSD, i.e., the same underlying time structure. For instance, the eleven BMBPT diagrams of orders 0, 1 and 2 displayed in Fig. 2.6 translate into only four TSDs in Fig. 3.6. However, the time integral eventually turns into a different result for each associated BMBPT diagram given that the energy labels in terms of which the result is expressed have a different meaning in each case. Back to our example of Fig. 3.5, the full labelling of the BMBPT diagram provided in Fig. 3.8

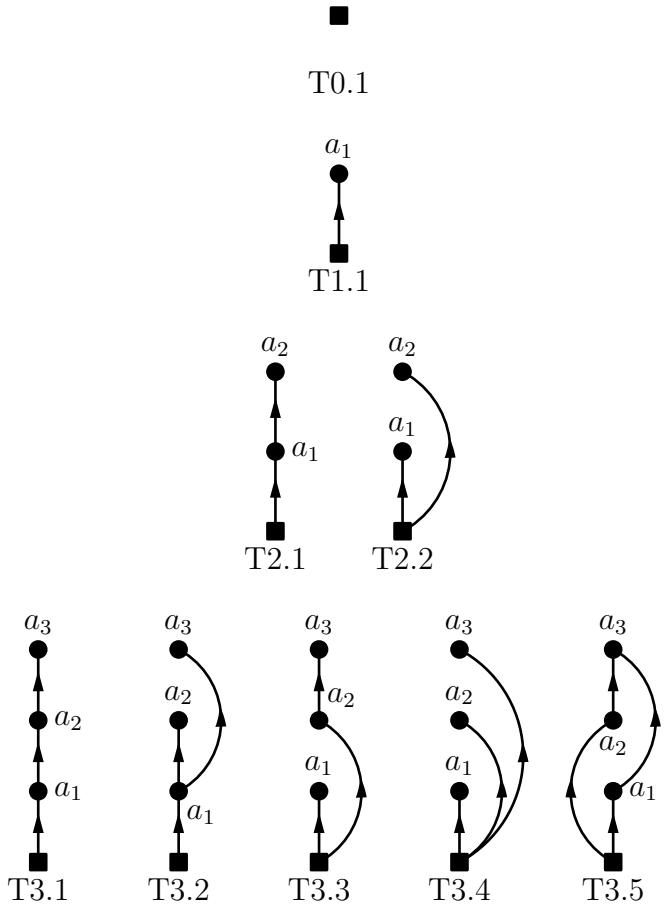

Figure 3.6. Zero-, first-, second- and third-order TSDs corresponding to BMBPT diagrams generated from operators containing six legs at most, i.e., with `deg_max` = 6.

allows us to identify the actual expression of the vertex labels

$$a_1 = \epsilon^{k_5 k_6 k_7 k_8} \ ,$$
$$a_2 = \epsilon_{k_1 k_2 k_5 k_6} \ ,$$
$$a_3 = \epsilon_{k_3 k_4 k_7 k_8} \ ,$$

to be used in the final outcome of the TSD. Another fourth-order diagram with the same TSD would associate other combinations of quasi-particle energies to the energy labels a_1, a_2 and a_3.

3.3.3. Calculation of tree TSDs

Tree TSDs happen to play an instrumental role in the present context. Indeed, they constitute the category for which a direct algorithm can be found to evaluate the corresponding p-tuple time integral. Building on it, non-tree TSDs (i.e., starting with order $p = 3$) will be treated by re-expressing them as a sum of tree TSDs.

The identification of the rule to compute a tree TSD relies on a recursive procedure, i.e., starting from a tree TSD of order p, whose expression is considered to be known, a vertex Ω

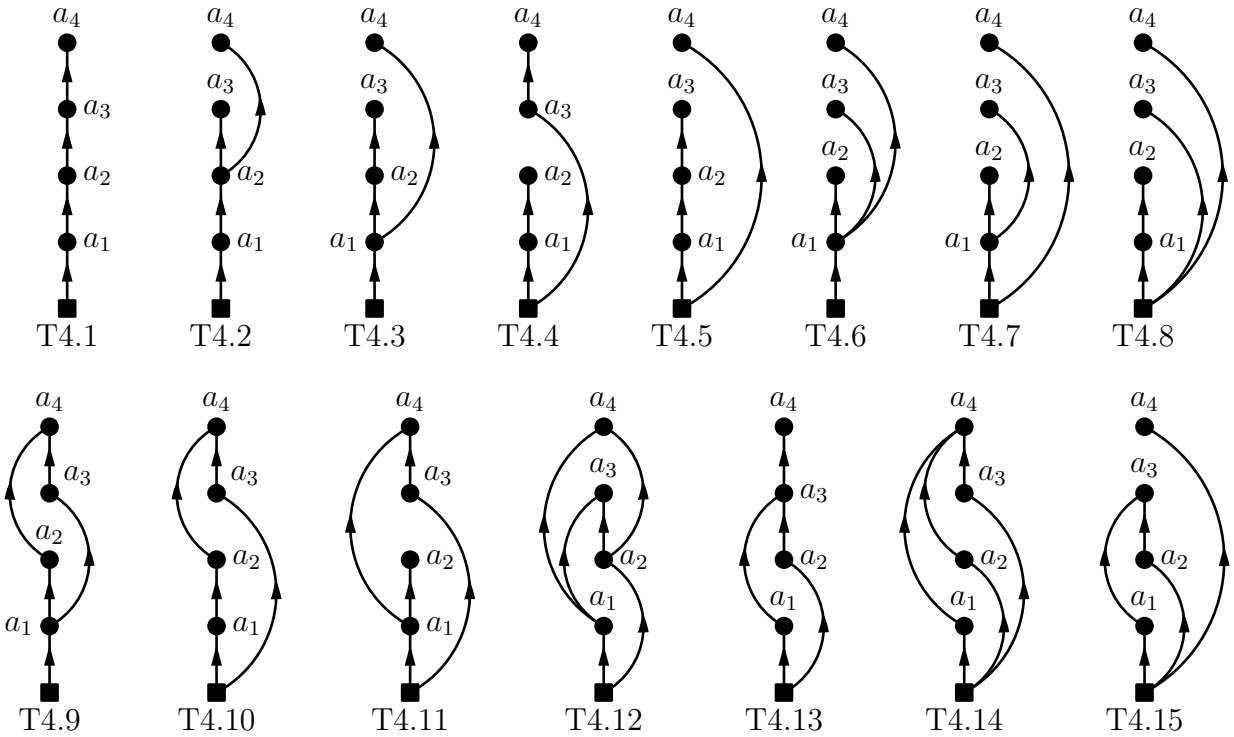

Figure 3.7. Fourth-order TSDs corresponding to BMBPT diagrams generated from operators containing six legs at most, i.e., with `deg_max` $= 6$.

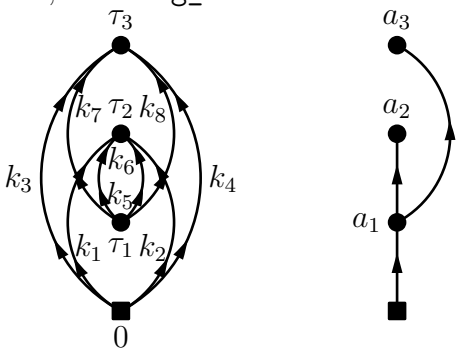

Figure 3.8. Fully-labelled third-order BMBPT diagram displayed in Fig. 2.9 and its associated TSD.

carrying label a_{p+1} is added by connecting it to one of the vertices of the original TSD. Having generated a new TSD of order $p+1$, its expression is obtained.

Minimal tree TSD

One starts with the minimal tree TSD, i.e., the single TSD of order 0 denoted as T0.1 in Fig. 3.6. It is built from the sole vertex representing the operator O and does not carry any running time label. It looks like

■

and its expression is nothing but

$$\mathrm{T0.1} = 1 \ .$$

First-order TSD

The single first-order TSD, denoted as T1.1 in Fig. 3.6, is generated from the minimal tree graph by connecting one Ω vertex carrying label a_1 to the vertex O

The expression of this TSD is given by the single integral

$$\begin{aligned} \mathrm{T1.1} &= \lim_{\tau\to\infty} \int_0^\tau d\tau_1 \, e^{-a_1\tau_1} \\ &= \frac{1}{a_1} \ , \end{aligned}$$

such that the end denominator is simply equal to the energy factor a_1[6]. One trivially observes that the end result could have been obtained directly by adding the factor a_1 associated to the new vertex to the denominator of the minimal tree TSD.

Second-order TSDs

As is visible in Fig. 3.6, two second-order TSDs denoted as T2.1 and T2.2 can be built from the first-order TSD. The first one is obtained by connecting the new vertex to the one labelled by a_1. It provides the *linear* tree TSD

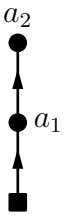

in which all vertices belong to the same branch and are thus sequentially ordered in time. As a result, the double time integral displays two nested integrals, the one over the earlier time

[6]The finiteness of the result relies on the fact that the energy factor a_1 is taken to be positive. In the following, all prefactors contributing to a given integral will be assumed to be positive, which will eventually be justified for BMBPT diagrams in Sec. 3.3.3.

depending on the result of the one over the later time that is thus performed first, i.e.

$$\begin{aligned}
\text{T2.1} &= \lim_{\tau\to\infty} \int_0^\tau d\tau_1 d\tau_2\, \theta(\tau_2-\tau_1) e^{-a_1\tau_1} e^{-a_2\tau_2} \\
&= \lim_{\tau\to\infty} \int_0^\tau d\tau_1 e^{-a_1\tau_1} \int_{\tau_1}^\tau d\tau_2 e^{-a_2\tau_2} \\
&= \lim_{\tau\to\infty} -\frac{1}{a_2} \int_0^\tau d\tau_1 e^{-a_1\tau_1} \left(e^{-a_2\tau} - e^{-a_2\tau_1}\right) \\
&= \lim_{\tau\to\infty} \frac{1}{a_2} \left(\int_0^\tau d\tau_1 e^{-(a_1+a_2)\tau_1} - e^{-a_2\tau} \int_0^\tau d\tau_1 e^{-a_1\tau_1}\right) \\
&= \frac{1}{a_2(a_1+a_2)} \,.
\end{aligned}$$

One observes that the end result could have been obtained directly by adding the factor a_2 associated to the new vertex to the denominator of T1.1 and by further replacing a_1 by a_1+a_2. This is because the first integration over τ_2 trivially brings the factor a_2 to the denominator and makes at the same time the variable a_1+a_2 become the factor in front of τ_1 in the part of the subsequent integration that eventually remains in the limit $\tau\to+\infty$.

The alternative way to generate a second-order TSD from the first-order one is to connect the new vertex to the bottom vertex. This gives a tree TSD with two branches

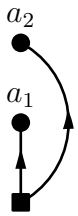

such that the vertices in the two branches are not time ordered with respect to each other. Consequently, the double time integral reduces to the product of two independent single integrals, i.e.

$$\begin{aligned}
\text{T2.2} &= \lim_{\tau\to\infty} \int_0^\tau d\tau_1 d\tau_2\, e^{-a_1\tau_1} e^{-a_2\tau_2} \\
&= \lim_{\tau\to\infty} \left(\int_0^\tau d\tau_1 e^{-a_1\tau_1}\right) \left(\int_0^\tau d\tau_2 e^{-a_2\tau_2}\right) \\
&= \lim_{\tau\to\infty} \frac{1}{a_1 a_2} \left(e^{-a_1\tau} - 1\right) \left(e^{-a_2\tau} - 1\right) \\
&= \frac{1}{a_1 a_2} \,.
\end{aligned}$$

One observes that the end result could have been obtained directly by adding the factor a_2 associated to the new vertex to the denominator of T1.1, leaving a_1 unaffected. Indeed, while the first integration over τ_2 trivially brings the factor a_2 to the denominator, it leaves the second integration unaffected as the two are independent.

Order-p TSDs

The procedure described above can be extended to compute any tree TSD of order $p > 0$ in terms of a reference TSD of order $p-1$. Indeed, any tree TSD of order $p > 0$ can be obtained via the addition of a vertex a_p to a reference TSD of order $p-1$. The only three options to do so are to add vertex a_p (i) through a link originating from a pre-existing vertex a_q, $q = 1, \dots p-1$, such that a_q (i1) continues an existing branch or (i2) initiates a new branch containing a single vertex (i.e., itself), or (ii) through a link originating from the bottom vertex at fixed time 0. In all three cases, the integral over τ_p trivially brings the factor a_p to the final denominator. In cases (i1) and (i2), the prefactor a_q in the integration over τ_q in the reference TSD is replaced by the factor $a_q + a_p$ in the part of the integral that eventually remains in the limit $\tau \to +\infty$. Contrarily, all factors a_q, $q = 1, \dots, p-1$, involved in the subsequent integrations are left unaffected in case (ii). As a result, the denominator of the TSD of interest can be calculated through the following steps

1. start from the denominator expression of the reference TSD of order $p-1$,
2. add the factor a_p,
3. replace every occurrence of a_q by $a_q + a_p$ except if the new vertex is linked to the bottom vertex.

Algorithm

Given a general tree TSD of order p, the above procedure can be used iteratively to calculate its expression, i.e., the end denominator. Starting from the vertices located at the very end of each branch of the tree, one can indeed iterate the above algorithm to remove them one by one back to the minimal tree TSD. In doing so, the merging of branches is naturally handled. Each step of the way, the most external vertex of a branch is treated as if it had been added to a tree TSD of one order less. Applying the above algorithm, one elementary step results into (i) chopping off the treated vertex, (ii) storing a contribution to the end denominator equal to the effective label carried by the removed vertex and (iii) adding the effective label of the removed vertex to the label of the vertex it was linked to, except if the latter is the bottom vertex, in which case the procedure associated to that branch stops. The end expression of the denominator contains p factors resulting from the p steps necessary to iterate through all the vertices. Eventually, the iterative procedure induces the rule to be employed to generate the denominator of any tree TSD of order p, i.e.

1. Consider a vertex a_q, $q = 1, \dots, p$, in the TSD,
   a) find all its *descendants*, i.e., all the vertices that are reachable from a_q by following links upward,
   b) sum label a_q to the labels of all its descendants,
   c) add the corresponding factor to the denominator expression,
2. Go back to 1. until all vertices have been exhausted.

Let us illustrate the diagrammatic rule for tree TSDs by computing the denominator associated with the third-order TSD displayed in Fig. 3.8

1. Starting with vertex a_1, vertices a_2 and a_3 are reached by following two different sets of links upward[7] corresponding to the two branches of the tree TSD. Consequently, the factor $a_1 + a_2 + a_3$ is associated to vertex a_1.

2. Moving to vertex a_2, no other vertex is reachable from it. Thus, the plain factor a_2 is associated to it.

3. Similarly, the plain factor a_3 must be associated to vertex a_3.

4. Eventually, the denominator is formed by the product of the factors associated with vertices a_1, a_2 and a_3; i.e., it is equal to $(a_1 + a_2 + a_3)a_2a_3$. One correctly recovers the result derived in Sec. 3.1.1 via the explicit integration of the corresponding triple time integral.

We, thus, have a rule at hand to compute the time-integrated expression of *any* tree TSD, independently of its perturbative order and of its topology. Although TSDs including at least one cycle are excluded at this point, a tree TSD of arbitrary order p may already correspond to a complex BMBPT diagram displaying any number of branches and sub-branches of arbitrary lengths.

Output of the *ADG* program

A typical output for a tree TSD looks like

Time-structure diagram T1:

$$\mathrm{T1} = \frac{1}{(a_1 + a_2)a_2}$$

Related Feynman diagrams: 8, 6, 5, 4, 3, 2, 1.

The TSD is displayed along with its associated expression and the labels of all the BMBPT diagrams it corresponds to.

[7] In the present example, each path followed contains only one link.

From a tree TSD back to BMBPT diagrams

Once the expression of a tree TSD of order p has been obtained, the goal is to generate the actual time-integrated expression of the BMBPT diagrams associated to it. One obvious way consists of replacing the factors a_q, $q = 1, \ldots, p$, by their expressions for each BMBPT diagram. However, while these factors constitute the natural variables to write the integrand associated with the Feynman diagram, the time-integrated expression rather depends on specific combinations of them that eventually lead to remarkable cancellations between the terms. It is, thus, more satisfactory to identify what these combinations actually correspond to and formulate the final rule directly in terms of them.

To do so, we introduce the notion of subdiagram, or subgraph, of a diagram as a diagram composed by a subset of vertices plus the propagators that are exchanged between them. As each vertex label a_q in a TSD eventually stands for the sum/difference of quasi-particle energies associated with the lines entering/leaving the *vertex* in the associated BMBPT diagram, a combination of these labels denotes the sum/difference of quasi-particle energies associated with the lines entering/leaving the *subdiagram* grouping the corresponding vertices.

Let us illustrate this notion by coming back to the BMBPT diagram displayed in Fig. 3.8. The expression of the associated TSD denominator includes a factor $a_1 + a_2 + a_3 = \epsilon_{k_1 k_2 k_3 k_4}$. Considering the subdiagram grouping vertices a_1, a_2 and a_3, one observes that this factor indeed corresponds to the sum/difference of quasi-particle energies associated with the lines entering/leaving it, which in the present case reduces to the sum of E_{k_1}, E_{k_2}, E_{k_3} and E_{k_4} corresponding to the four entering lines, i.e., there is no line leaving the subdiagram.

The above example underlines a fundamental point. Because each effective factor entering the end denominator sums the label of a given vertex with the labels of all its descendants, the corresponding BMBPT subdiagram only displays entering lines. This results into the effective factors being positive sums of quasi-particle energies. This key feature is responsible for the finiteness of all the encountered time integrals in the limit $\tau \to +\infty$, as alluded to in footnote 13.

Eventually, the energy denominator of a BMBPT diagram associated with a tree TSD is obtained in the following way

1. Consider a vertex but the lowest one in the BMBPT diagram,
   a) determine all its descendants using the TSD,
   b) form a subdiagram using the vertex and its descendants,
   c) sum the quasi-particle energies corresponding to the lines entering the subdiagram,
   d) add the corresponding factor to the denominator expression,
2. Go back to 1. until all vertices have been exhausted.

Let us illustrate the final diagrammatic rule by coming back to the BMBPT diagram displayed in Fig. 3.8.

1. The vertex at time τ_1 in the BMBPT diagram corresponds to vertex a_1 in the TSD. Its descendants are vertices a_2 and a_3 corresponding to BMBPT vertices at times τ_2 and τ_3, respectively. The sum of quasi-particle energies associated to the lines entering the

subgraph grouping the three vertices is $\epsilon_{k_1k_2k_3k_4}$, thus, providing the first factor entering the denominator.

2. The vertex at time τ_2 in the BMBPT diagram correspond to vertex a_2 in the TSD. It has no descendant such that the corresponding subgraph reduces to itself. The sum of quasi-particle energies associated to the lines entering the subgraph is $\epsilon_{k_1k_2k_5k_6}$, thus. providing the second factor entering the denominator.

3. The vertex at time τ_3 in the BMBPT diagram correspond to vertex a_3 in the TSD. It has no descendant such that the corresponding subgraph reduces to itself. The sum of quasi-particle energies associated to the lines entering the subgraph is $\epsilon_{k_3k_4k_7k_8}$, thus, providing the last factor entering the denominator.

4. Eventually, the complete denominator reads as

$$\epsilon_{k_1k_2k_3k_4}\,\epsilon_{k_1k_2k_5k_6}\,\epsilon_{k_3k_4k_7k_8}\ ,$$

where each factor corresponds to a positive sum of quasi-particle energies.

The result does indeed match the one obtained in Sec. 3.1.1.

3.3.4. Calculation of non-tree TSDs

Having a direct method at hand to compute the time-integrated form of any BMBPT diagram associated with a tree TSD, one is left with the important task to find an algorithm to tackle diagrams corresponding to non-tree TSDs, i.e., to TSDs containing at least one cycle. As no direct rule applies to them, the strategy consists of commuting any non-tree TSD into a sum of tree TSDs to which the above diagrammatic rule applies.

Minimal non-tree TSD

To familiarize ourselves with non-tree TSDs, let us focus on the simplest of them, the third-order TSD denoted as T3.5 in Fig. 3.6

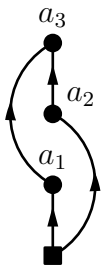

One first notices that vertices a_1 and a_2 are not time ordered with respect to each other. While this could be dealt with if the two vertices were situated on different branches of a tree TSD, the fact that they are time ordered with respect to a_3, i.e., that their time labels run from 0 to τ_3 and not from 0 to $\tau \to +\infty$, prevents a direct treatment. In the following, we use the

term *cycle*[8] to describe structures where some vertices are not time ordered with respect to one another while being time ordered with respect to a vertex or a set of vertices at higher times. Calculating the triple time integral associated to the TSD leads to

$$\begin{aligned}\text{T3.5} &= \lim_{\tau\to\infty}\int_0^\tau d\tau_1 d\tau_2 d\tau_3\,\theta(\tau_3-\tau_1)\,\theta(\tau_3-\tau_2)e^{-a_1\tau_1}e^{-a_2\tau_2}e^{-a_3\tau_3}\\ &= \frac{1}{(a_1+a_3)(a_2+a_3)}\left[\frac{1}{a_3}+\frac{1}{a_1+a_2+a_3}\right]\\ &= \frac{1}{a_3(a_1+a_2+a_3)}\left[\frac{1}{a_1+a_3}+\frac{1}{a_2+a_3}\right]\,. \end{aligned} \tag{3.8}$$

Because the lines inside a cycle do not constitute separate branches, the corresponding time integrals are not independent from one another. It implies that the vertices inside a cycle need to be ordered explicitly in all possible ways. It is what is actually behind the two terms appearing in Eq. 3.8 that were generated via the time partitioning $1=\theta(\tau_1-\tau_2)+\theta(\tau_2-\tau_1)$ in the integrals over τ_1 and τ_2 thus producing the two ways of ordering a_1 and a_2.

Diagrammatically, employing such a partitioning for two vertices inside a cycle corresponds to generating the sum of two TSDs through the following steps

1. Select the two internal vertices that are not connected by a link.
2. Connect them via an oriented link and only keep the maximal length paths between each pair of vertices in the graph. This generates a first new graph.
3. Proceeding similarly but with the added link pointing in the opposite direction generates a second new graph.

In the minimal non-tree graph, the two vertices to be ordered are a_1 and a_2. Applying the ordering procedure leads to

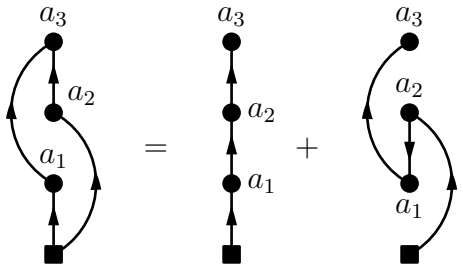

such that the non-tree graph T3.5 is nothing but the sum of twice the linear tree graph T3.1 with the order of a_1 and a_2 exchanged[9].

Applying the algorithm detailed in Sec. 3.3.3 to each of the two resulting tree TSDs provides

$$\begin{aligned}\text{T3.5} &= \frac{1}{a_3(a_2+a_3)(a_1+a_2+a_3)}+\frac{1}{a_3(a_1+a_3)(a_1+a_2+a_3)}\\ &= \frac{1}{a_3(a_1+a_2+a_3)}\left[\frac{1}{a_1+a_3}+\frac{1}{a_2+a_3}\right]\,, \end{aligned} \tag{3.9}$$

which is indeed the result of Eq. 3.8.

[8] It actually corresponds to an undirected cycle as defined in B.

[9] It is obviously necessary to move a_1 above a_2 into the second tree graph to realize that it also displays the topology of T3.1.

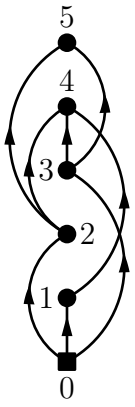

Figure 3.9. A fifth-order non-tree TSD

Cycles identification

In order to treat non-tree TSDs, one must first identify all the cycles, i.e., the end nodes of the cycles, possibly contained in a given TSD. Exploiting the *NetworkX* graph, it is done by applying the following algorithm

1. Consider `node_a` with `out_degree` ≥ 2,
   a) Consider `node_b` different from `node_a`,
      - Check for paths going from `node_a` to `node_b`,
      - If `in_degree(node_b)` ≥ 2 and `nb_paths` ≥ 2, `node_a` and `node_b` are end nodes of a cycle,
      - Check that the two paths share only their end nodes,
   b) Go back to (a) until all nodes are exhausted,
2. Go back to 1. until all nodes are exhausted,

where the `in_degree` (`out_degree`) of a node, or vertex, denotes the number of incoming (outgoing) lines.

Let us illustrate the algorithm by applying it to the fifth-order non-tree TSD displayed in Fig. 3.9.

1. `node_0` has `out_degree` ≥ 2.
   - `node_1`, `node_2` and `node_3` have `in_degree` $= 1$.
   - `node_4` has `in_degree` $= 3$ and `nb_paths` $= 3$, so `node_0` and `node_4` are end nodes of a cycle, since the paths do not share other nodes.
   - `node_5` has `in_degree` $= 2$ and `nb_paths` $= 2$, so `node_0` and `node_5` are end nodes of a cycle, since the paths do not share other nodes.
2. `node_1` has `out_degree` $= 1$.
3. `node_2` has `out_degree` ≥ 2.
   - `node_4` has only one path coming from `node_2`.

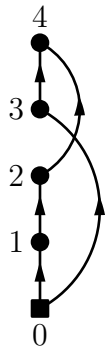

Figure 3.10. A fourth order non-tree TSD.

- `node_5` has only one path coming from `node_2`.

4. `node_3` has `out_degree` ≥ 2.
   - `node_4` has only one path coming from `node_3`.
   - `node_5` has only one path coming from `node_3`.

Eventually, the TSD comprises two cycles, one with end nodes `node_0` and `node_4`, and one with end nodes `node_0` and `node_5`.

Cycles treatment

Once the cycles of a TSD have been identified, they must be traded for a sum of tree TSDs via the systematic ordering of their internal vertices. Starting from the *NetworkX* diagram, the two end nodes of the cycle, and the two paths connecting the end nodes, one applies the following algorithm

1. Set `node_to_insert` as the first node of `path_1` after start node.
2. For each `daughter_node` in `path_2` but the starting node
   a) Make a copy of the graph,
   b) Add a link from `node_to_insert` to `daughter_node`,
   c) Set `mother_node` as the node preceding `daughter_node` in `path_2`,
   d) Add a link from `mother_node` to `daughter_node`,
   e) Remove the links carrying unnecessary information.

Let us illustrate the previous algorithm by applying it to the fourth-order TSD displayed in Fig. 3.10. One chooses here to set `path_1` as $\{0, 3, 4\}$ and `path_2` as $\{0, 1, 2, 4\}$.

1. Set `node_to_insert` to `node_3`,
2. Set `daughter_node` to `node_1`
   a) Copy the graph,
   b) Add a link from `node_3` to `node_1`,

c) Set `mother_node` to `node_0`,

d) Add a link from `node_0` to `node_3`,

e) Remove the links from `node_0` to `node_1` and from `node_3` to `node_4`,

3. Set `daughter_node` to `node_2`

a) Copy the graph,

b) Add a link from `node_3` to `node_2`,

c) Set `mother_node` to `node_1`,

d) Add a link from `node_1` to `node_3`,

e) Remove the links from `node_1` to `node_2` and from `node_3` to `node_4`,

4. Set `daughter_node` to `node_4`

a) Copy the graph,

b) Add a link from `node_3` to `node_4`,

c) Set `mother_node` to `node_2`,

d) Add a link from `node_2` to `node_3`,

e) Remove the links from `node_0` to `node_3` and one of the links from `node_3` to `node_4`.

The tree TSDs thus generated are displayed in Fig. 3.11. In the present case, they all correspond to the linear tree TSD of order 4, denoted as T4.1 in Fig. 3.7, with different orderings of vertices a_1, a_2 and a_3.

Though applying once the algorithm exemplified above does not guarantee to obtain only tree TSDs, the three diagrams obtained presently are indeed tree TSDs. Whenever it is not the case, one must repeatedly apply the cycle (identification and treatment) algorithms to the TSDs generated at each step until only tree TSDs are obtained. In the above example, initially inverting `path_1` and `path_2` would have required more than one step.

All tree TSDs corresponding to an initial non-tree TSD being generated, the algorithm detailed in Sec. 3.3.3 can be applied to each of them. The expression of the non-tree TSD is nothing but the sum of the individual contributions thus obtained.

Output of the *ADG* program

A typical output of ADG for a non-tree TSD looks like

Time-structure diagram T4:

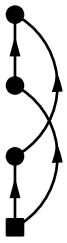

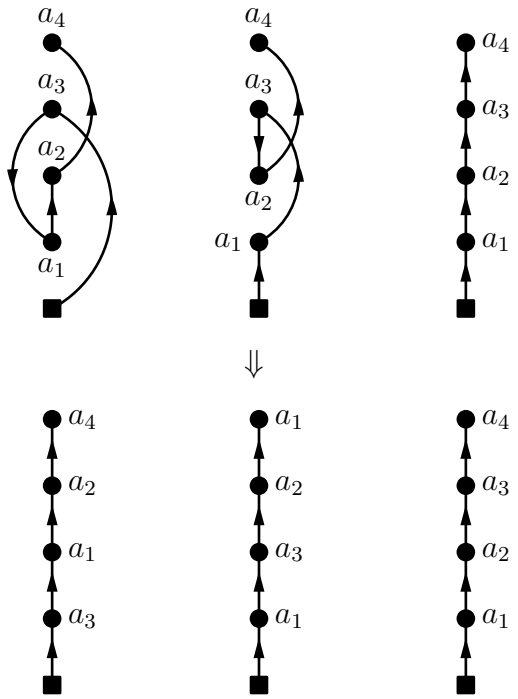

Figure 3.11. Tree TSDs generated by applying the cycle treatment algorithm to the non-tree TSD displayed in Fig. 3.10 with the choice of setting `daughter_node` to 1, 2 and 4, drawn with the original vertex ordering (top) or after reordering the vertices ascendantly (bottom).

$$\mathrm{T4} = \frac{1}{(a_1 + a_3)(a_2 + a_1 + a_3)a_3} + \frac{1}{(a_1 + a_2 + a_3)(a_2 + a_3)a_3}$$

Equivalent tree diagrams: T1, T1.

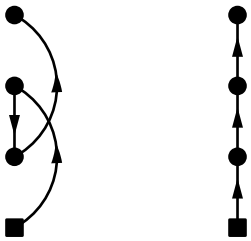

Related Feynman diagrams: 6, 9, 20, 27, 31, 39, 40, 43, 48, 50.

The TSD is displayed along with its expression and a graphical representation of the tree TSDs obtained by disentangling its cycles. The list of associated BMBPT Feynman diagrams is also provided.

3.3.5. Final ouput of the ADG program

Exploiting the findings detailed in the previous sections, we are now in position to provide the typical output of the ADG program. For a BMBPT diagram associated with a tree TSD, the output looks like

Diagram 1:

$$\begin{aligned}\mathrm{PO3.1} &= \lim_{\tau\to\infty}\frac{(-1)^2}{(2!)^3}\sum_{k_i} O^{40}_{k_1k_2k_3k_4}\Omega^{22}_{k_5k_6k_1k_2}\Omega^{04}_{k_5k_6k_3k_4}\int_0^\tau \mathrm{d}\tau_1\mathrm{d}\tau_2\theta(\tau_2-\tau_1)e^{-\tau_1\epsilon^{k_5k_6}_{k_1k_2}}e^{-\tau_2\epsilon_{k_3k_4k_5k_6}} \\ &= \frac{(-1)^2}{(2!)^3}\sum_{k_i}\frac{O^{40}_{k_1k_2k_3k_4}\Omega^{22}_{k_5k_6k_1k_2}\Omega^{04}_{k_5k_6k_3k_4}}{\epsilon_{k_1k_2k_3k_4}\ \epsilon_{k_3k_4k_5k_6}}\end{aligned}$$

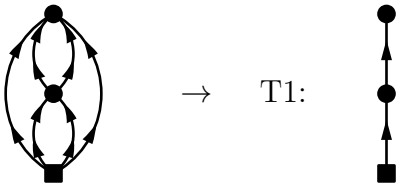

$$\mathrm{T1} = \frac{1}{(a_1+a_2)a_2}$$

$$\begin{aligned}a_1 &= \epsilon^{k_5k_6}_{k_1k_2} \\ a_2 &= \epsilon_{k_3k_4k_5k_6}\end{aligned}$$

whereas for a BMBPT diagram associated with a non-tree TSD, it looks like

Diagram 6:

$$\begin{aligned}\mathrm{PO4.6} &= \lim_{\tau\to\infty}\frac{-(-1)^3}{(3!)^2}\sum_{k_i} O^{40}_{k_1k_2k_3k_4}\Omega^{31}_{k_5k_6k_7k_1}\Omega^{13}_{k_8k_2k_3k_4}\Omega^{04}_{k_8k_5k_6k_7} \\ &\quad\times\int_0^\tau \mathrm{d}\tau_1\mathrm{d}\tau_2\mathrm{d}\tau_3\theta(\tau_3-\tau_1)\theta(\tau_3-\tau_2)e^{-\tau_1\epsilon^{k_5k_6k_7}_{k_1}}e^{-\tau_2\epsilon^{k_8}_{k_2k_3k_4}}e^{-\tau_3\epsilon_{k_5k_6k_7k_8}} \\ &= \frac{-(-1)^3}{(3!)^2}\sum_{k_i} O^{40}_{k_1k_2k_3k_4}\Omega^{31}_{k_5k_6k_7k_1}\Omega^{13}_{k_8k_2k_3k_4}\Omega^{04}_{k_8k_5k_6k_7} \\ &\quad\times\left[\frac{1}{\epsilon_{k_1k_8}\ \epsilon_{k_1k_2k_3k_4}\ \epsilon_{k_5k_6k_7k_8}}+\frac{1}{\epsilon_{k_1k_2k_3k_4}\ \epsilon_{k_2k_3k_4k_5k_6k_7}\ \epsilon_{k_5k_6k_7k_8}}\right]\end{aligned}$$

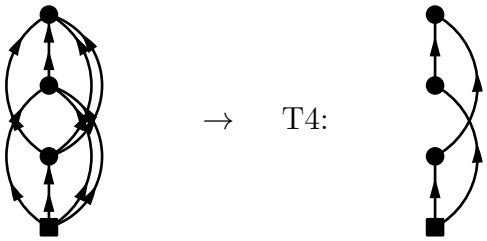

$$\mathrm{T4} = \frac{1}{(a_1+a_3)(a_2+a_1+a_3)a_3}+\frac{1}{(a_1+a_2+a_3)(a_2+a_3)a_3}$$

$$\begin{aligned}a_1 &= \epsilon^{k_5k_6k_7}_{k_1} \\ a_2 &= \epsilon^{k_8}_{k_2k_3k_4} \\ a_3 &= \epsilon_{k_5k_6k_7k_8}\end{aligned}$$

The BMBPT diagram and its associated TSD are displayed. The original Feynman expression, its time-integrated expression and the expression of the TSD it derives from are added before listing the correspondence between the vertex labels in the TSD and the sum of quasiparticle energies in the BMBPT diagram.

3.4. Connection to time-ordered diagrammatics

The formal and numerical developments presented in this work rely on the time-dependent formulation of (B)MBPT. It is, however, more customary to design MBPT on the basis of a time-independent formalism [61]. While the end result is necessarily the same, the partitioning[10] of the complete order-p contribution to the observable $\mathrm{O}_0^{\mathrm{A}}$ differs in both approaches.

3.4.1. Combinatorics

The main characteristic of the time-dependent formalism is to authorize each diagram to capture as many different time orderings of the vertices as possible. While the contractions linking the vertices explicitly order a subset of the vertices, some vertices are left unordered in the integrand such that the diagram eventually seizes, i.e., sums, all remaining orderings at once. The combinatorics of these remaining orderings depends on the diagram and relates to the topology of the associated TSD.

1. Vertices belonging to the *linear* tree TSD of order p are fully ordered in time such that no further reordering is possible.

2. A *non-linear* tree TSD contains several branches. The vertices on a given branch are fully ordered with respect to each other and with respect to the vertices located on the trunk the branch emerges from. However, the vertices on a branch are not ordered with respect to those belonging to another branch. Correspondingly, one can define the combinatorics "n_{branches}" as the total number of ways to order the vertices on the various branches. This corresponds to the number of fully time-ordered diagrams (i.e. linear tree TSDs) the Feynman diagram captures.

3. A *non-tree* TSD further contains cycles. The vertices on a branch inside a cycle are fully ordered with respect to each other and with respect to the vertices located below (above) the starting (end) node of the cycle. However, the vertices on the various branches of the cycle are not ordered with respect to each others. The combinatorics "n_{cycle}" relates to ordering the vertices on the various branches of the cycle in all possible ways. The corresponding algorithm was discussed at length in Sec. 3.3.4. Performing this ordering for all cycles in a given non-tree TSD generates a set of tree TSDs.

Contrarily, the main characteristic of the time-independent formalism is to operate with fully time-ordered diagrams from the outset, i.e., to associate one diagram per possible time ordering

[10] A valid partitioning relates to splitting the complete order p in a sum of terms that are individually proportional to a fraction of the form $1/(\epsilon_{k_i\dots k_j}\dots\epsilon_{k_u\dots k_v})$ with p energy factors in the denominator. Any other form does not constitute a valid partioning in the present context.

Order		0	1	2	3	4
`deg_max` $= 4$	TSD	1	1	2	4	14
	BMBPT	1	2	8	59	568
`deg_max` $= 6$	TSD	1	1	2	5	15
	BMBPT	1	3	23	396	10 716

Table 3.1. Number of *time-unordered* diagrams generated from operators containing at most four (`deg_max` $= 4$) or six (`deg_max` $= 6$) legs.

Order		0	1	2	3	4
`deg_max` $= 4$	TSD	1	1	1	1	1
	BMBPT	1	2	9	87	1 377
`deg_max` $= 6$	TSD	1	1	1	1	1
	BMBPT	1	3	25	551	21 814

Table 3.2. Number of *time-ordered* diagrams generated from operators containing at most four (`deg_max` $= 4$) or six (`deg_max` $= 6$) legs.

of all the vertices. Correspondingly, there is no point invoking TSDs in this diagrammatics given that each time-ordered diagram of order p trivially relates to the linear tree TSD of order p.

Obviously, the main difference between both diagrammatics relates to the number of diagrams partitioning the complete order p. The number of time-unordered[11] (time-ordered) BMBPT diagrams and associated TSDs generated from operators containing at most four or six legs are provided in Tab. 3.1 (Tab. 3.2) for perturbative orders $p = 0, 1, 2, 3$ and 4. While the difference is not significant at low-order and/or for low `deg_max`, it obviously increases with p and `deg_max`.

A key interest of the present work is to demonstrate that (i) a direct and systematic calculation of any Feynman BMBPT diagram associated with a tree TSD is possible and that (ii) the treatment of diagrams associated with non-tree TSD does require an explicit reordering of the vertices inside a given cycle. On the one hand, point (ii) underlines that the smaller number of time-unordered diagrams is partially illusory given that some explicit ordering (with combinatorial factor "n_{cycle}") of the vertices is actually mandatory to compute the diagrams. On the other, point (i) stresses that the large combinatorics of the fully-time-ordered diagrammatic is an overkill that can be avoided given that explicitly ordering the vertices on the various branches of tree diagrams (with combinatorial factor "n_{branches}") is superfluous.

As a result of the above, the optimal, i.e., minimal, number of BMBPT diagrams and associated TSDs one must eventually handle after ordering the vertices inside cycles is given in Tab. 3.3. This corresponds to what can be denoted as the *partially-time-ordered* diagrammatic whose combinatorics is obviously in between those appearing in Tabs. 3.1 and 3.2. The number

[11] As explained above, *time-unordered* diagrams do contain a certain degree of time ordering among a subset of vertices but this degree is *minimal*. One could thus better refer to the *minimally-ordered* diagrammatic.

Order		0	1	2	3	4
`deg_max` $= 4$	TSD	1	1	2	3	7
	BMBPT	1	2	8	69	866
`deg_max` $= 6$	TSD	1	1	2	4	8
	BMBPT	1	3	23	449	15 250

Table 3.3. Number of *partially-time-ordered* diagrams generated from operators containing at most four (`deg_max` $= 4$) or six (`deg_max` $= 6$) legs.

Order	0		1		2		3		4	
	TSD	BMBPT	TSD	BMBPT	TSD	BMBPT	TSD	BMBPT	TSD	BMBPT
Linear tree	1	1	1	2	1	7	1	35	1	205
Non-linear tree	0	0	0	0	1	1	2	14	6	147
Non-tree	0	0	0	0	0	0	1	10	7	216

Table 3.4. Number of TSDs and BMBPT diagrams per topological category generated from operators containing at most four legs (`deg_max` $= 4$).

Order	0		1		2		3		4	
	TSD	BMBPT	TSD	BMBPT	TSD	BMBPT	TSD	BMBPT	TSD	BMBPT
Linear tree	1	1	1	3	1	21	1	267	1	4970
Non-linear tree	0	0	0	0	1	2	3	76	7	2311
Non-tree	0	0	0	0	0	0	1	53	7	3435

Table 3.5. Number of TSDs and BMBPT diagrams per topological category generated from operators containing at most six legs (`deg_max` $= 6$).

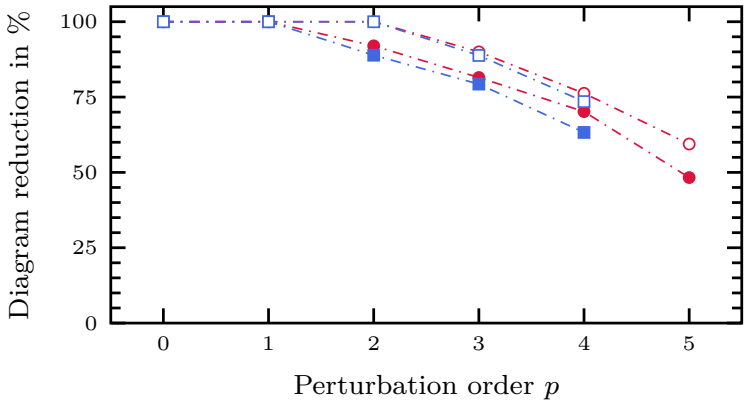

Figure 3.12. Resummation efficiency expressed as the number of time-unordered BMBPT diagrams with respect to fully-ordered BMBPT diagrams. Red dots (blue squares) correspond to using vertices with four (six) legs at most. Empty symbols correspond to canonical diagrams only.

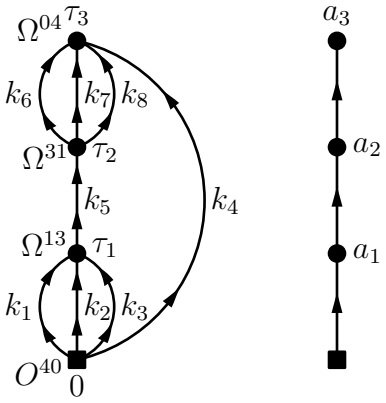

Figure 3.13. A third-order BMBPT diagram and its associated linear tree TSD.

of diagrams typically is comprised between 40% and 90% of those at play in the fully-time-ordered diagrammatic as illustrated in Fig. 3.12, and reduces with growing perturbative order. This minimal number of diagrams that must effectively be dealt with is of course dictated by how many of the original time-unordered diagrams relates to (i) a linear tree, (ii) a non-linear tree or (iii) a non-tree TSD. Indeed, how many of the original diagrams are in fact already fully time-ordered limits how much one can take advantage of not fully ordering the other ones. For orientation, this partitioning of the diagrams is given in Tabs. 3.4 and 3.5 for perturbative orders $p = 0, 1, 2, 3$ and 4. Beyond the lowest orders, the number of BMBPT Feynman diagrams that are not fully time-ordered to begin with grows radiply with both p and `deg_max`.

3.4.2. Resolvent rule

In the time-independent formulation of MBPT, the expression of each time-ordered diagram is derived via the application of the so-called resolvent rule [61]. It is of interest to realize that the diagrammatic rule presently identified to compute any generic tree TSD in the time-unordered

diagrammatic reduces to the resolvent rule for linear trees, i.e., for TSDs corresponding to BMBPT diagrams that are in fact fully time ordered.

Let us illustrate this feature on the basis of the third-order BMBPT diagram and its associated linear tree TSD displayed in Fig. 3.13. The expression of the diagram reads, via the application of our diagrammatic rule based on the identification of the subdiagram associated to each vertex and its descendants, as

$$D = \frac{(-1)^3}{(3!)^2} \sum_{k_i} \frac{O^{40}_{k_1k_2k_3k_4} \Omega^{13}_{k_5k_1k_2k_3} \Omega^{31}_{k_6k_7k_8k_5} \Omega^{04}_{k_6k_7k_8k_4}}{\epsilon_{k_1k_2k_3k_4}\, \epsilon_{k_4k_5}\, \epsilon_{k_4k_6k_7k_8}} \,. \tag{3.10}$$

While keeping all other elements unchanged, let us work out the denominator via the resolvent rule

1. drawing a line between the two lowest vertices, four lines carrying quasi-particle indices k_1, k_2, k_3 and k_4 are crossed. As a result, the resolvent rule contributes a factor $\epsilon_{k_1k_2k_3k_4}$ to the denominator.

2. Repeating the procedure for the resolvent located between second and third (third and fourth) vertices, a factor $\epsilon_{k_4k_5}$ ($\epsilon_{k_4k_6k_7k_8}$) is found to contribute to the denominator.

The overall denominator is thus the same as in Eq. 3.10. This result is easily understandable given that the lines between any two successive vertices of a linear tree are nothing but those entering the subdiagram formed by the second vertex and all its descendants.

3.4.3. Diagrammatic resummation

As mentioned in Sec. 3.4.1, the minimally-ordered BMBPT diagrammatics allows for a certain resummation of *linear tree* TSDs into a more *general tree* TSD associated to a combinatorial factor n_{branches}. Indeed the diagrammatic rule identified in Sec. 3.3.3 permits to sum at once, i.e., from a single BMBPT Feynman diagram associated to a tree TSD, the whole class of fully-time-ordered diagrams that derive from it, leading to a significant compactification of the computation. The number of fully-time-ordered diagrams generated from a tree TSD of order p denoted as Tp.k is

$$n_{\text{branches}}(\text{Tp.k}) = \frac{p!}{\prod_{i=1}^{p} p_i} \,, \tag{3.11}$$

where p_i denotes the effective order of the subdiagram associated with vertex i, i.e. the number of vertices in the subgraph made out of vertex i and all its descendants. The product in the denominator accounts for all the combinations that are *not* summed into the tree TSD due to the vertices being partially ordered to begin with. The degree of resummation is maximal for a tree TSD in which all perturbative vertices are unordered with respect to each other, i.e. for a TSD containing p independent branches associated with p vertices directly connected to the bottom vertex. Indeed, $p_i = 1$ for $i = 1, \ldots, p$ in this case such that $n_{\text{branches}}(\text{Tp.k}) = p!$. Contrarily, all vertices belonging to the same branch in a linear tree, the successive p_i coefficients are equal to $1, 2, \ldots, p$ as one runs through the branch from top to bottom such that $n_{\text{branches}}(\text{Tp.k}) = 1$ as expected.

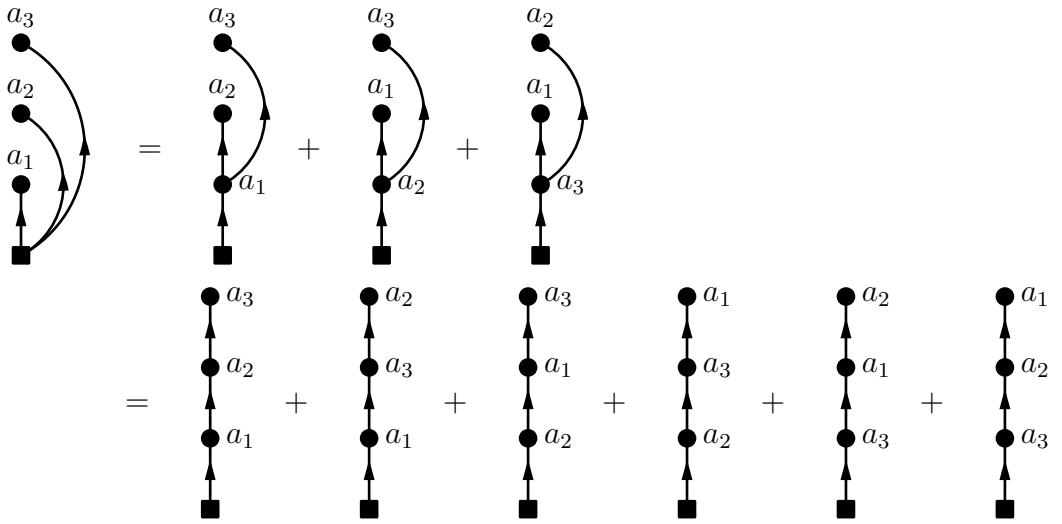

Figure 3.14. Decomposition of T3.4 into a sum of linear tree TSDs.

Order	0	1	2	3	4	5	6	7
`deg_max` = 4	1	1	2	3	8	30	90	420
`deg_max` = 6	1	1	2	6	12	40	180	1 008
$p!$	1	1	2	6	24	120	720	5 040

Table 3.6. Maximal degree of resummation of tree TSDs associated with BMBPT diagrams generated from operators containing at most four (`deg_max` = 4) or six (`deg_max` = 6) legs. Factorial values are also provided for comparison.

Let us illustrate the above for the two third-order tree TSDs denoted as T3.3 and T3.4 in Fig. 3.6. Their decomposition into fully-time-ordered linear trees is displayed in Figs. 3.14 and 3.15, respectively. The number of fully-time-ordered diagrams resummed into T3.4 is $n_{\text{branches}}(\text{T3.4}) = 3!$. It corresponds to a maximal degree of resummation as T3.4 is made out of three independent vertices directly connected to the bottom vertex. Proceeding similarly with T3.3, the number of resummed fully-time-ordered diagrams is not maximal and equal to $n_{\text{branches}}(\text{T3.3}) = 3!/2 = 3$ in this case. This relates to the fact that two vertices are ordered with respect to each other to begin with.

The maximal degree of resummation of tree TSDs of order p generated from vertices containing at most four (`deg_max` = 4) or six (`deg_max` = 6) legs is given in Tab. 3.6. It is compared to the hypothetical maximal value of $p!$. The reason why the maximal degree becomes systematically smaller than the ideal value $p!$ as p increases is that the number of independent branches authorized at a given order p is drastically constrained by the value of `deg_max`.

The capacity of tree TSDs to resum large classes of fully-time-ordered diagrams translates algebraically into the remarkable fact that the sum of associated fractions factorizes into a single fraction whose factors in the denominator are obtained by invoking a specific set

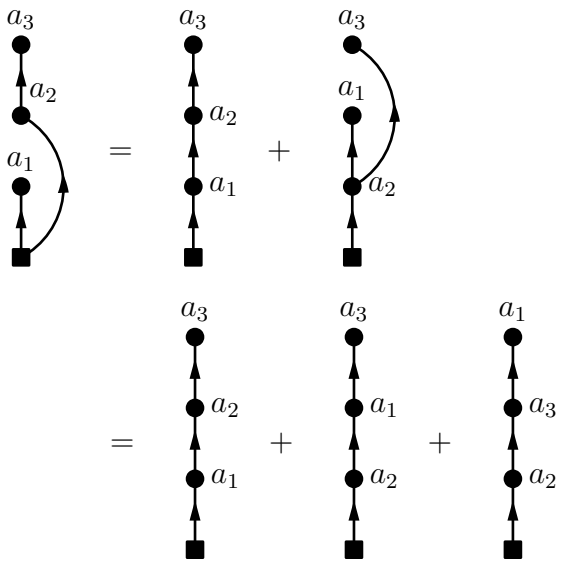

Figure 3.15. Decomposition of T3.3 into a sum of linear tree TSDs.

of subdiagrams. Starting with T3.4, and following[12] the diagrammatic process displayed in Fig. 3.14, its expression is decomposed by steps into a sum of fractions corresponding to partially- and eventually fully-time-ordered, i.e. linear, trees

$$
\begin{aligned}
\mathrm{T3.4} &= \frac{1}{a_1 a_2 a_3} \\
&= \frac{1}{a_1+a_2+a_3}\left[\frac{1}{a_2 a_3}+\frac{1}{a_1 a_3}+\frac{1}{a_1 a_2}\right] \\
&= \frac{1}{a_1+a_2+a_3}\left[\frac{1}{a_2+a_3}\left(\frac{1}{a_3}+\frac{1}{a_2}\right)+\frac{1}{a_1+a_3}\left(\frac{1}{a_3}+\frac{1}{a_1}\right)+\frac{1}{a_1+a_2}\left(\frac{1}{a_2}+\frac{1}{a_1}\right)\right] \\
&= \frac{1}{(a_1+a_2+a_3)(a_2+a_3)a_3}+\frac{1}{(a_1+a_2+a_3)(a_2+a_3)a_2}+\frac{1}{(a_1+a_2+a_3)(a_1+a_3)a_3} \\
&\quad +\frac{1}{(a_1+a_2+a_3)(a_1+a_3)a_1}+\frac{1}{(a_1+a_2+a_3)(a_1+a_2)a_2}+\frac{1}{(a_1+a_2+a_3)(a_1+a_2)a_1}\,.
\end{aligned}
$$

Proceeding similarly with T3.3, the decomposition of the fraction operates as

$$
\begin{aligned}
\mathrm{T3.3} &= \frac{1}{a_1(a_2+a_3)a_3} \\
&= \frac{1}{(a_1+a_2+a_3)a_3}\left[\frac{1}{a_2+a_3}+\frac{1}{a_1}\right] \\
&= \frac{1}{a_1+a_2+a_3}\left[\frac{1}{(a_2+a_3)a_3}+\frac{1}{a_1+a_3}\left(\frac{1}{a_3}+\frac{1}{a_1}\right)\right] \\
&= \frac{1}{(a_1+a_2+a_3)(a_2+a_3)a_3}+\frac{1}{(a_1+a_2+a_3)(a_1+a_3)a_3}+\frac{1}{(a_1+a_2+a_3)(a_1+a_3)a_1}\,.
\end{aligned}
$$

[12]The second equality provides an extra intermediate step to better visualize how the decomposition (factorization) operates between the first and last step.

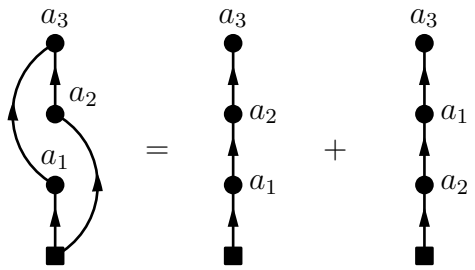

Figure 3.16. Decomposition of T3.5 into a sum of linear tree TSDs.

In order to illustrate why a given set of fractions associated with linear trees may or may not be resummed into a single fraction, we now compare T3.3 with T3.5 whose decomposition into linear tree TSDs is displayed in Fig. 3.16 and whose expression was already given in Eq. 3.9. The non-tree TSD T3.5 sums one less linear tree than T3.3 whose associated fraction is necessary to factorize and cancel the longest factor $(a_1 + a_2 + a_3)$ appearing in all third-order linear trees to eventually obtain a single term. The linear tree in question corresponds to a_1 being at higher times than both a_2 and a_3. It is missing from T3.5 because a_1 and a_2 belong to a cycle and are thus unordered with respect to each other while being both ordered with respect to a_3 that is at a higher time. This situation corresponding to non-tree TSDs typically lead to missing terms that are necessary for the complete factorization to occur.

Eventually, the resummation of $n_{\text{branches}}(\text{Tp.k})$ fully-time-ordered TSDs (fractions) into a single time-unordered TSD (fraction) can be generically written as

$$\sum_{i=1}^{n_{\text{branches}}(\text{Tp.k})} \frac{1}{(a_{i1}\dots a_{ip})(a_{i2}\dots a_{ip})\dots a_{ip}} = \frac{1}{\prod_{j=1}^{p}(a_{j1}+\dots+a_{jp_j})}\,, \tag{3.12}$$

where $a_{i1},\dots,a_{ip}$ label the p vertices from bottom to top in each of the $i = 1,\dots,n_{\text{branches}}(\text{Tp.k})$ summed linear tree TSDs, whereas $a_{j1},\dots,a_{jp_j}$ label the p_j vertices in the subgraph of Tp.k made out of vertex j and all its descendants.

3.5. Use of the *ADG* program

3.5.1. System requirements

ADG has been designed to work on any computer with a Python2.7 distribution, and successfully tested on recent GNU/Linux distributions and on MacOS. Additionally to Python, *setuptools* and *distutils* packages must already be installed, which is the case on most standard recent distributions. Having *pip* installed eases the process but is not technically required. The *NumPy*, *NetworkX* and *SciPy* libraries are automatically downloaded during the install process. Additionally, one needs a LaTeX distribution installed with the PDFLaTeX compiler for ADG to produce the pdf file associated to the output if desired.

3.5.2. Installation

From the Python Package Index

The easiest way to install ADG is to obtain it from the Python Package Index[13] by entering the following command

```
pip2 install adg
```

Provided *setuptools* is already installed, *pip* takes care of downloading and installing ADG as well as *NumPy* and *NetworkX*. Once a new version of ADG is released, one can install it by entering the command

```
pip2 install --upgrade adg
```

From the source files

Once the ADG source files are downloaded from the GitHub repository[14], one must enter the project folder and either run

```
pip2 install .
```

or

```
python2 setup.py install
```

With this method, *pip*[15] also takes care of downloading and installing ADG, *NumPy*, *NetworkX* and *SciPy*.

3.5.3. Run the program

Batch mode

The most convenient way to use ADG is to run it in batch mode with the appropriate flags. For example, to run the program and generate BMBPT diagrams at order 4 for example, one can use

```
adg -o 4 -t BMBPT -d -c
```

where the `-o` flag is for the order, `-t` for the type of theory, `-d` indicates that the diagrams must be drawn and `-c` that ADG must compile the LaTeX output. A complete list of the program's options can be obtained via the program's documentation (see Sec. 3.5.5) or through

```
adg -h
```

[13] https://pypi.org/project/adg/
[14] https://github.com/adgproject/adg
[15] Depending on the system, it might be necessary either to use the "–user" flag to install it only for a specific user or to run the previous command with "sudo -H" to install it system-wide.

Currently, ADG can be run either in relation to MBPT by using `-t MBPT` or to BMBPT by using `-t BMBPT`. Though the algorithms described in the previous sections can be used regardless of the diagrams' orders, ADG has been arbitrarily restricted to order 10 or lower to avoid major overloads of the system. Future users are nevertheless advised to first launch calculations at low orders (2, 3 or 4 typically) as the time and memory needed for computations rise rapidly with the perturbative order.

Interactive mode

As an alternative to the batch mode, ADG can be run on a terminal by entering the command

```
adg -i
```

A set of questions must be answered using the keyboard to configure and launch the calculation. The interactive mode then proceeds identically to the batch mode.

3.5.4. Steps of a program run

Let us briefly recapitulate the different steps of a typical ADG run

- Run options are set either by using the command-line flags entered by the user or during the interactive session via keyboard input.
- ADG creates a list of adjacency matrices for the appropriate theory and perturbative order, and via *NumPy*, feeds them to *NetworkX* that creates *MultiDiGraph* objects.
- Checks are performed on the list of graphs to remove topologically equivalent or anomalous graphs.
- The list of topologically unique graphs is used to produce *Diagram* objects that store the graph as well as some of its associated properties depending on the theory (HF status, excitation level, etc.). The expression associated to the graphs are extracted.
- The program then prints on the terminal the number of diagrams per category and writes the LaTeX output file, the details of which depend on the options selected by the user, as well as a list of adjacency matrices associated to the diagrams. Other output files may be produced, depending on the theory and the user's input.
- If asked by the user, the program performs the PDFLaTeX compilation.
- Unnecessary temporary files are removed and the programs exits.

3.5.5. Documentation

Local documentation

Once the source files have been downloaded, a quick start guide is available in the `README.md` file. Once ADG is installed, it is possible to read its manpages through

```
man adg
```

or a brief description of the program and its options through

```
adg -h
```

A more detailed HTML documentation can be generated directly from the source files by going into the `docs` directory and run

```
make html
```

The documentation is then stored in `docs/build/html`, with the main file being `index.html`. A list of other possible types of documentation format is available by running

```
make help
```

Online documentation

The full HTML documentation is available online under https://adg.readthedocs.io/, and help with eventual bugs of the program can be obtained by opening issues on the GitHub repository at https://github.com/adgproject/adg.

4. Numerical implementation and results

4.1. Introduction

Having derived BMBPT diagrams manually in Chap. 2 and being now able to generate and evaluate all diagrams at an arbitrary order as detailed in Chap. 3, the next step consists in implementing it numerically and compare the obtained results with both experimental values and other *ab initio* methods[1]. Eventually, predictions can be performed on large sets of nuclei, and can be used to test newly produced families of chiral Hamiltonians in the future.

The first full-fledged implementation of BMBPT in large model spaces with an approximate inclusion of three-body forces via normal-ordering techniques is presented[2] in this chapter. Ground-state energies are investigated along complete medium-mass isotopic chains with further emphasis on two-neutron separation energies to monitor footprints of nuclear shell closures. Whenever possible, BMBPT calculations are benchmarked against well-established non-perturbative IT-NCSM, GSCGF, and MR-IMSRG results for the same input Hamiltonian.

4.2. Hamiltonian

Though the formalism exposed in the previous chapters is agnostic with respect to the employed Hamiltonian, the first calculations detailed below are focusing on an *ab initio* perspective, i.e. calculations are done using a realistic Hamiltonian derived from chiral Effective Field Theory (EFT) and evolved via Similarity Renormalization Group (SRG) technique.

4.2.1. Chiral Effective Field Theory

Chiral EFT [141, 142, 143, 144, 145] has been developed over the past few decades and is partly responsible for the rapid development of *ab initio* methods in nuclear physics lately. Introduced as a way to circumvent the impossibility to assess a theoretical error to phenomenological potentials, chiral EFT relies on the separation of scale between the typical momentum q of processes involved in the description of nuclear structure, ranging from a few MeV to roughly 100 MeV, and a large momentum scale Λ characterized by the chiral symmetry breaking scale as well as the nucleon mass, all close to 1 GeV. Such a separation allows for a description

[1] The work detailed in this chapter was led by A. Tichai. The author contribution consisted in coding all non-canonical diagrams that are however not contributing to the present results given that the calculations are based on an HFB reference state.

[2] These results being also presented in Ref. [138], the reader is advised that the perturbative orders listed there correspond to the historical MBPT convention, i.e. are shifted up by one compared to the present document.

of the internucleonic Lagrangian as a power series in q/Λ respecting the symmetries of the underlying Field Theory, i.e. QCD [146].

A power counting has to be assessed based on, e.g., dimensional analysis, to attribute to each operator the order at which it enters the power series. The lowest order is called Leading Order (LO), each subsequent order being denoted as Next-to-Leading Order (NLO), Next-to-Next-to-Leading Order (N2LO), etc. Such a construction allows for a systematic and consistent incorporation of the three- and higher-body forces [147].

These characteristics have established Hamiltonians [148, 147] derived from chiral EFT as the standard choice for *ab initio* applications, with the past years showing both further developments [149, 150, 151, 152] and a diversification of approaches [153, 154, 155, 156].

4.2.2. Similarity Renormalization group

Though now the golden standard of *ab initio* methods, chiral EFT Hamiltonians are not perturbative enough for MBPT methods because of their hard-core character, and are thus reserved to more involved methods resumming infinite classes of diagrams such as CC or SCGF. To circumvent the difficulties associated with the strong low-to-high momentum coupling, various methods were developed [157, 158], the most prominent of them being the Similarity Renormalization Group (SRG) [81, 82, 83, 84, 85, 86, 87]. Especially, SRG-evolved Hamiltonian were proved to be soft enough to be used in MBPT for closed-shell nuclei [159, 116].

The idea behind SRG is to use the renormalization flow equation

$$\frac{\mathrm{d}H_\alpha}{\mathrm{d}\alpha} = [\eta_\alpha\,, H_\alpha] \ , \tag{4.1}$$

where α is the flow parameter and H_α the evolved Hamiltonian with $H_0 = H$ to pre-diagonalize the Hamiltonian through a continuous, unitary transformation. Low- and high-momentum components are thus decoupled and the convergence of many-body calculations is accelerated while observables remains unchanged. The SRG-transformation however produces higher-body forces, which are eventually discarded. The transformation must therefore remain under control to avoid producing sizable higher-body forces, which, once omitted, compromise the unitarity of the transformation in the A-body Hilbert space.

4.2.3. Hamiltonian used for the calculations

The chiral EFT Hamiltonian used in this work combines a chiral two-nucleon (2N) interaction at next-to-next-to-next-to leading order with a cutoff of $\Lambda_{2N} = 500\,\mathrm{MeV}$ [148] with a three-nucleon (3N) interaction[3] at next-to-next-to leading order with a local regulator based on a cutoff of $\Lambda_{3N} = 400\,\mathrm{MeV}$ [147, 130].

The Hamiltonian is further softened using a SRG transformation with a flow parameter $\alpha = 0.08\,\mathrm{fm}^4$. This transformation induces many-nucleon forces that are included consistently up to the 3N level, i.e. chiral and induced many-body forces beyond that level are neglected. Working in the normal-ordered two-body approximation (NO2B) [160, 130, 131, 161] in the

[3] We still use the original value of c_D, although it was recently found that this does not reproduce the triton half-life. This interaction still provides a valuable starting point for the comparison of many-body approaches.

quasi-particle representation[4], the residual three-body part $\Omega^{[6]}$ is presently discarded. Details on the normal-ordering procedure as well as expressions of the matrix elements of each operator Ω^{ij} in terms of the original matrix elements of the Hamiltonian and of the (U, V) matrices can be found in App. C.

All calculations are performed using the eigenbasis of a spherical harmonic oscillator with frequency $\hbar\Omega = 20$ MeV[5]. One- and two-body operators are represented using all states up to $e_{\max} = (2n + l)_{\max} = 12$. Three-body matrix elements on the other hand only use a subset of the triplets built from the truncated basis such that their corresponding excitations are limited to $E_{3\max} = 14$. For the Hamiltonian employed here, this has proven sufficient up to heavy nickel isotopes [53].

Calculations are presently restricted to even-even semi-magic nuclear ground states characterized by $J^\Pi = 0^+$. This enables the use of angular-momentum coupling techniques to solve the HFB equations and compute the perturbative corrections. Furthermore, perturbative corrections displayed above are recast into traces over matrix products that can be evaluated economically using BLAS routines. This allows a very efficient evaluation of low-order BMBPT corrections. More details, including the J-scheme expressions for the normal-ordered grand potential and of the perturbative corrections will be presented in a future publication [127].

As discussed in Sec. 2.9, the extraction of the binding energy requires an iterative BMBPT scheme with a shifted chemical potential in order for the particle number to be correct at order $n \geq 2$, e.g., at second order, $\mathrm{A}_0^{(0)} + \mathrm{A}_0^{(2)} = \mathrm{A}_0$. Such an iterative procedure has not been implemented yet in the second-order results shown below, hence they contain an associated contamination $\Delta\mathrm{E}_0^{(2)}$.

4.3. Low-order results in mid-mass nuclei

4.3.1. Isotopic chains calculations

Figure 4.1 provides systematic results of zeroth- (HFB), first- and (preliminary) second-order BMBPT calculations along O, Ca, and Ni isotopic chains. The top panel displaying absolute binding energies demonstrates that the bulk of dynamic correlations is obtained at first order [116, 104]. In closed-shell, sub-closed or slightly paired open-shell nuclei, the second-order contribution is consistently suppressed compared to first order and indicates a gentle behavior of low-order BMBPT corrections. The computation of third-order contributions will help us to further assess the convergence behavior of low-order BMBPT contributions based on SRG-transformed Hamiltonians in the future.

While being informative, our preliminary second-order calculations are clearly contaminated in open-shell nuclei for which the correction to the particle number is significant, e.g., in $^{42-46}$Ca and $^{50-54}$Ni. We observe that the spurious arches in the binding energy directly reflect the behavior of $A_0^{(2)}$ displayed in panel (d) of Fig. 4.1. It is consistent with the fact that the

[4] We emphasize that the NO2B approximation does not break particle number itself, i.e., the truncated grand potential does commute with A.

[5] The chosen value was confirmed to be close to the variational minimum from IMSRG calculations. A systematic study of variations of the oscillator frequency in the BMBPT framework is postponed to a future publication [127].

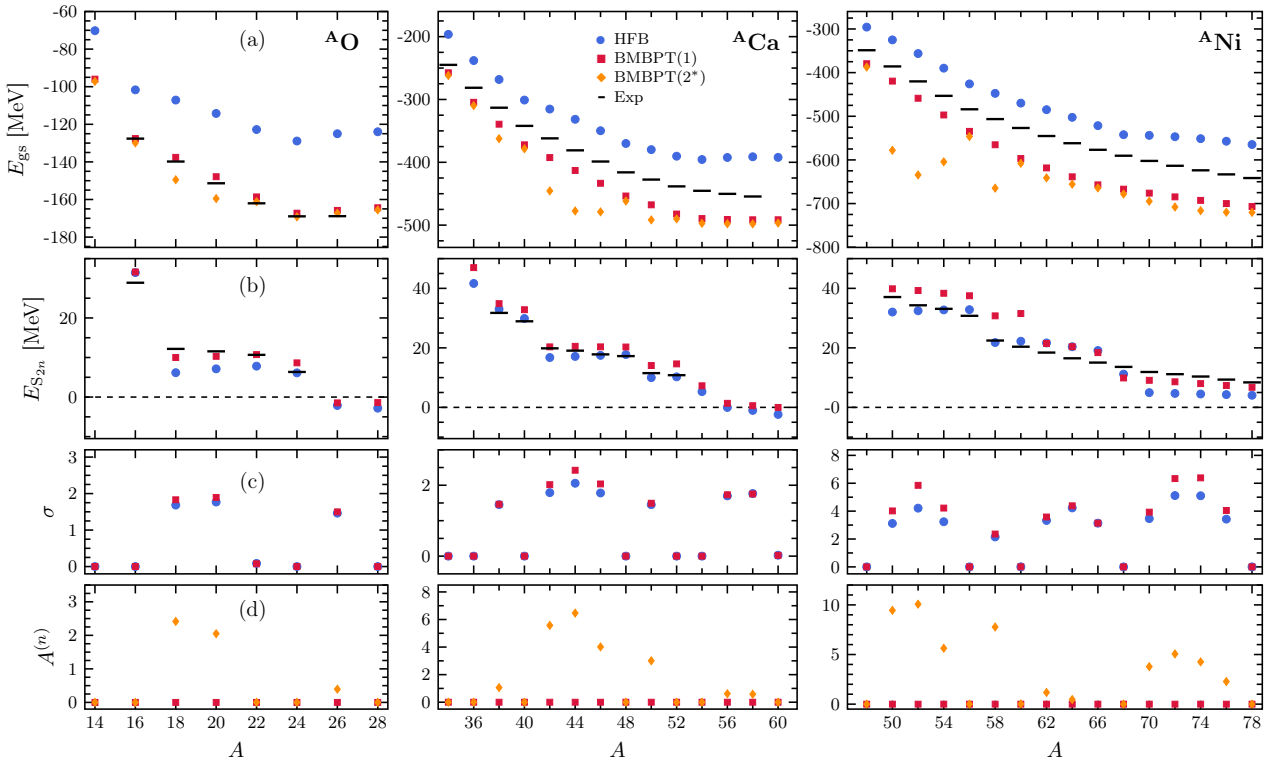

Figure 4.1. Systematics along O, Ca and Ni isotopic chains: (a) absolute binding energy, (b) two-neutron separation energy, (c) neutron-number dispersion, (d) perturbative correction to the average neutron number. Plot markers correspond to HFB (●), first-order BMBPT (■) and second-order BMBPT (◆). Experimental values are shown as black bars [162].

contaminating term is nothing but $\Delta \mathrm{E}_0^{(2)} \equiv \lambda \mathrm{A}_0^{(3)}$, leading to an overbinding whenever $\mathrm{A}_0^{(2)}$ leads to an excess of particles as it is systematically the case here. The contamination $\Delta \mathrm{E}_0^{(2)}$ is exaggerated by the fact that the employed Hamiltonian overbinds mid-mass nuclei [53], thus making the neutron chemical potential artificially large and negative. In any case, the iterative readjustment of the average particle number at the working order n will eventually eliminate the spurious arches in the binding energy.

Panel (b) of Fig. 4.1 displays two-neutron separation energies. While results are already qualitatively correct at zeroth order, first-order corrections are non-negligible and tend to shrink magic gaps. The behaviour is overall very satisfactory. Panel (c) shows the neutron-number dispersion $\sigma \equiv \sqrt{\langle A^2 \rangle - \langle A \rangle^2}$, which overall grows with the nuclear mass. While the dispersion is bound to go to zero in the limit of an all-order resummation, the first-order contribution does not decrease it compared to HFB. This indicates the merit of exactly restoring $U(1)$ symmetry to complement low-order dynamic correlations with non-perturbative static ones, as in projected Bogoliubov CC [77] or MR-IMSRG [88, 93]. Because the dispersion changes abruptly at (sub-)shell closures, restoring good particle number will mostly affect differential quantities, e.g., two-neutron separation energies, around (sub-)shell closures.

4.3.2. Comparisons with state-of-the-art *ab initio* methods

Figure 4.2 benchmarks first-order BMPBT results against well-established many-body approaches that are partially or fully non-perturbative. The Hamiltonian is the same in all calculations and numerical details associated with the basis size and the treatment of three-body forces are identical whenever possible or at least consistent. The most advanced reference, only available for O isotopes, is the importance-truncated no-core shell model (IT-NCSM) using a natural-orbital single-particle basis [163]. Results from the NCSM-PT to second order are also available along the O isotopic chain [104]. Covering the same range of mid-mass nuclei as BMBPT, MR-IMSRG and GSCGF calculations are systematically displayed. While the IMSRG flow is truncated at the two-body level, i.e., yielding the IMSRG(2) approximation [57, 60, 88], GSCGF includes self-energy diagrams up to second order, i.e., yielding the so-called ADC(2) approximation [164, 95]. Finally, closed-shell CC calculations performed at the CR-CC(2,3) level [165, 53] are added whenever available. Each of these many-body methods systematically incorporates large classes of perturbation theory diagrams beyond first-order BMBPT.

We find that first-order BMBPT ground-state energies are in very good agreement with the more sophisticated methods for all systems under consideration, i.e., the relative deviation does not exceed 2%. In particular all methods are similar and in good agreement with IT-NCSM in O isotopes. MR-IMSRG(2) and NCSM-PT (when available) do provide a stronger binding compared to first-order BMBPT. On the other hand, GSCGF-ADC(2) results are very comparable to first-order BMBPT while being often slightly less bound. Of course, it will be of great interest to perform this comparison again once proper second-order and/or particle-number-restored BMBPT are systematically available. The consistency of the absolute binding energies and two-neutron separation energies provided by all the many-body methods further confirms that discrepancies with experimental data, e.g., the systematic overbinding in Ca and Ni isotopes or the incorrect behavior of S_{2N} around ^{56}Ni, reflect the shortcomings of the employed chiral Hamiltonian. CR-CC(2,3) calculations further incorporates the effect of triple excitations that are absent from MR-IMSRG(2), GSCGF-ADC(2) or first- and second-order BMBPT. Corresponding results demonstrate that a highly-accurate description of mid-mass systems requires the incorporation of triples, i.e., six-quasi-particle excitations in the language of BMBPT. The leading contributions of this type appear at the third order of the BMBPT expansion. In addition, one should consider the explicit inclusion of the 3N interaction without resorting to the NO2B approximation, as demonstrated in the CC context [131, 161].

4.3.3. Numerical scaling

Figure 4.3 provides the computational runtime in CPU hours of first- and second-order BMBPT calculations for several isotopic chains. The tin isotopic chain is included here for the record even though the corresponding results were not displayed in Figs. 4.1 and 4.2 due to the poor performance of the chiral Hamiltonian and to the lack of convergence of the calculation with respect to the $E_{3\max}$ truncation in this mass region at $E_{3\max} = 14$. BMBPT calculations were performed on an Intel Xeon X5650 computing node with 12 cores at 2.67 GHz. The runtime is essentially independent of the mass number of the system for fixed values of $e_{\max}$ and $E_{3\max}$. A typical run requires only up to 15 CPUh for open-shell nuclei and as little as 6 CPUh in closed-shell nuclei. The reduction in the closed-shell case is achieved by exploiting that the

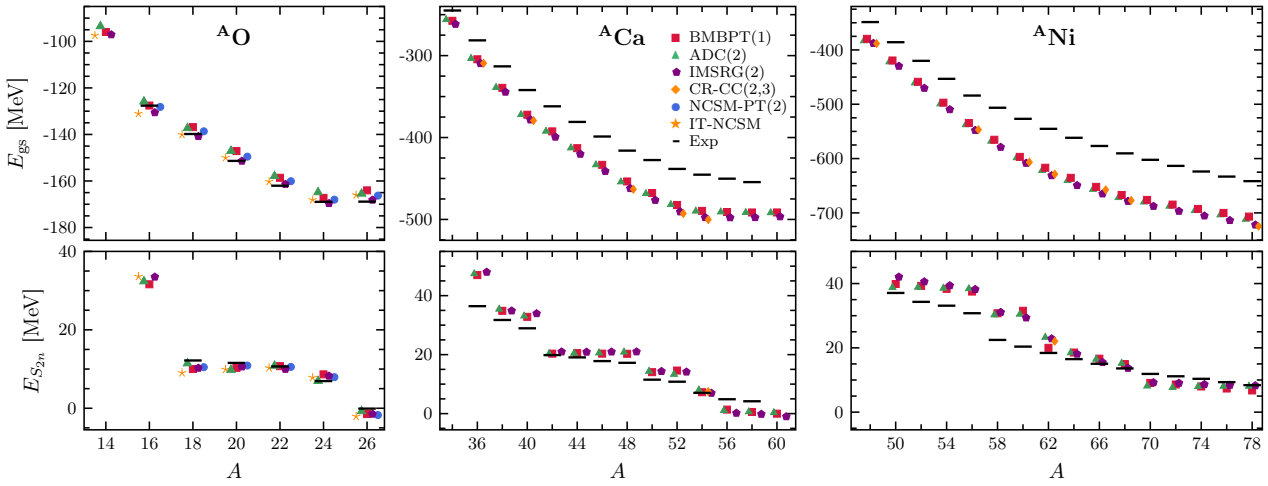

Figure 4.2. Absolute ground-state binding energies (top) and two-neutron separation energies (bottom) along O, Ca and Ni isotopic chains. Results are displayed for first-order BMBPT (■), second-order NCSM-PT (●), large-scale IT-NCSM (★), GSCGF-ADC(2) (▲), MR-IMSRG(2) (⬟) and CR-CC(2,3) (◆). Experimental value are shown as black bars [162].

Bogoliubov matrix V (U) becomes zero for particle (hole) states when the grand potential is normal ordered, i.e., one recovers the benefit of an explicit partition between particle and hole states. In principle, we could also take advantage of the block structure of the Hamiltonian matrix with respect to isospin that disappears when normal ordering the grand potential with respect to a Bogoliubov state [78]. This would lead to an additional reduction by a factor of about 5, thus, making BMBPT calculations of open-shell nuclei about 10 times more expensive than genuine MBPT calculations of closed-shell systems.

Of course, BMBPT does strictly reduce to standard MBPT in a closed-shell system. Conversely, all summations over quasi-particle labels run over the entire dimension of the one-body Hilbert space, which significantly increases the computational scaling compared to standard MBPT. In any case, low-order BMBPT corrections only induce low polynomial cost with respect to quasi-particle summation and do not suffer from the storage of large tensors as more sophisticated all-order many-body approaches such as CC or IMSRG.

Most importantly, Fig. 4.3 demonstrates that second-order BMBPT calculations generate results similar to state-of-the-art medium-mass approaches at a computational cost that is about two orders of magnitude smaller, e.g., MR-IMSRG(2) requires roughly 2000 CPUh per run when applied to a open-shell system. The computational advantage of low-order BMBPT calculations over non-perturbative approaches could make BMBPT a particularly useful tool in the future to provide relatively cheap systematic tests of newly generated chiral EFT Hamiltonians over a wide range of nuclei.

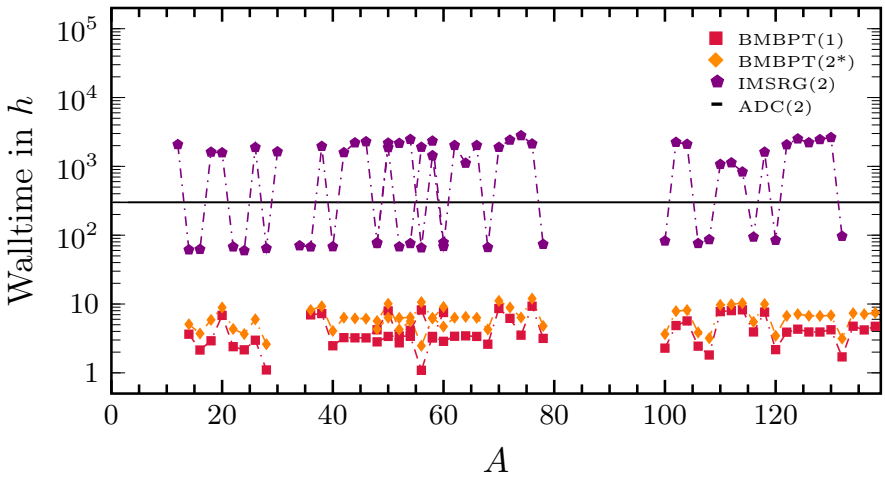

Figure 4.3. Computational runtime versus mass number for BMBPT(1) (■), BMBPT(2*) (◆), MR-IMSRG(2) (⬟) and ADC(2).

Conclusion

Ab initio many-body methods [116, 49, 50, 51, 52, 54, 56, 57, 58, 60] have been established in the past decades as a prominent and fastly-evolving domain of nuclear structure theory. The simultaneous development of chiral EFT Hamiltonians [141, 142, 143, 144, 145] rooted in Quantum Chromodynamics and of many-body methods, both formally and numerically, supported by a rapid growth in computing power, have extended the reach of *ab initio* calculations to the mid-mass region of the nuclear chart up to $A \sim 130$ [53].

The diagrammatic translation of certain of those methods, e.g. many-body perturbation theory [114, 115, 61, 116, 117, 104], self-consistent Green's function theory [54, 55, 56, 95, 96], coupled cluster theory [49, 50, 51, 52, 53, 78] etc, is used to build an intuition about the systematic contributions to a physical observable and to derive the corresponding algebraic expressions at minimal cost. However, (1) the need in nuclear physics to tackle three-nucleon interactions, i.e., six-leg vertices, (2) the development of novel many-body methods based on generalized diagrammatics [76, 77] and (3) the implementation of high-order contributions authorized by the rapid progress of computational power, welcome the development of a versatile code capable of both generating and evaluating many-body diagrams automatically.

The present work has focused on the recently formulated Bogoliubov many-body perturbation theory (BMBPT) [77, 127] to tackle (near) degenerate Fermi systems, e.g. open-shell nuclei displaying a superfluid character. This many-body method perturbatively expands the exact solution of the Schrödinger equation around a so-called Bogoliubov reference state, i.e., a general product state breaking $U(1)$ global-gauge symmetry associated with the conservation of good particle-number in the system. Chap. 1 presented the necessary ingredients to develop the perturbation theory. Chap. 2 detailed the perturbative expansion of the norm kernel and of the observable from an analytical and a diagrammatic point of view, the results at first and second order in BMBPT, and established connections with closed-shell many-body perturbation theory as well as perturbative Bogoliubov coupled-cluster.

The first version (v1.00) of the code ADG that generates all valid BMBPT diagrams and evaluates their algebraic expression to be implemented in a numerical application has been extensively described in Chap. 3. This is realized at an arbitrary order p for a Hamiltonian containing both two-body (four-legs) and three-body (six-legs) interactions (vertices). The automated generation of BMBPT diagrams of order p is achieved by producing all oriented adjacency matrices of size $(p+1) \times (p+1)$ satisfying topological Feynman's rules. The automated evaluation of all BMBPT diagrams of order p relies both on the application of algebraic Feynman's rules and on the design of a systematic method to perform the remaining p-tuple time integral. This method provides a novel diagrammatic rule allowing for the straight summation of large classes of time-ordered diagrams at play in the time-independent formulation of BMBPT. The standard resolvent rule employed to compute time-ordered diagrams one by one happens to be a particular case of the general rule presently identified. The code ADG is written in *Python2.7* and uses the graph manipulation package *NetworkX*. A publication containing

all formal and numerical developments associated with ADG has been submitted [166]. It is made flexible enough to be expanded throughout the years to tackle the diagrammatics at play in various many-body formalisms that either already exist or are yet to be formulated.

The first full-fledged *ab initio* application of Bogoliubov many-body perturbation theory to finite nuclei has been presented in Chap. 4. A corresponding publication has been published [138]. Expanding the exact solution around a particle-number-broken Hartree-Fock-Bogoliubov reference state, this single-reference many-body perturbation theory is systematically applicable to genuine mid- and heavy-mass open-shell nuclei. As a first proof-of-principle investigation, systematic ground-state energies along complete isotopic chains from oxygen up to tin have been computed using a standard chiral effective field theory Hamiltonian. Low-order BMBPT with a soft interaction was found to agree at the level of 2% with state-of-the-art non-perturbative many-body methods at a small fraction of the computational cost. As a matter of fact, the approach is applicable beyond the tin region without becoming computationally infeasible. For now, it is the (in)accuracy of modern Hamiltonians in heavy systems and the handling of three-body matrix elements necessary to reach model-space convergence that prevent us from performing meaningful studies on nuclei far above mass number $A \approx 100$. Furthermore, the onset of nuclear deformations for $A > 100$ requires the additional breaking of $SU(2)$ symmetry. Incidently, the low computational cost exhibited by BMBPT establish it as a test-method of interest for newly produced chiral EFT Hamiltonians in the future.

Our goal is to expand BMBPT in several directions in the future. The immediate next step consists of implementing the consistent adjustment of particle-number corrections at second order, which requires an iterative evaluation of the HFB equations, of the quasi-particle normal-ordering and of the perturbative corrections. A detailed investigation of this, together with a sensitivity analysis of BMBPT results with respect to model space parameters and the similarity renormalization group transformation of the Hamiltonian, will be the content of an upcoming publication. Next, the third-order correction will be evaluated for high-accuracy calculations and to further probe the convergence pattern of the BMBPT expansion. In that respect, it is also of interest to test Bogoliubov reference states that are *not* optimized by solving the HFB equations, which involves so-called non-canonical diagrams. While the first application was limited to ground-state energies, the underlying formalism is currently being extended to other observables, e.g., charge radii, as well as to low-lying excitation energies and electromagnetic transitions. Given our capacity to automatically generate and evaluate all diagrams appearing at an arbitrary order n on the basis of 2N and 3N interactions using ADG, it is also of interest to test the validity of the normal-ordered two-body approximation to the full 3N interaction.

As a mid-term goal, we plan to implement the particle-number-restored BMBPT [77]. It requires both a full developmentof the formalism and an explicit extension of the ADG code. PNP-BMBPT will be applied to investigate the impact of the symmetry contaminations on various systems/observables. In parallel, the non-perturbative Bogoliubov CC extension of BMBPT will be implemented along the line of Ref. [77] in order to achieve realistic applications. ADG will prove to be a critical tool for this extension as well. On the longer term, it is of interest to implement a many-body perturbation theory that consistently breaks (and restores) both $SU(2)$ and $U(1)$ symmetries to tackle doubly open-shell nuclei [76, 77]. Along with its extension to PNP-BMBPT, the ADG code will be extended as well to develop GSCGF at the ADC(3) level [167].

A. Useful identities

$$\int_0^\tau \mathrm{d}\tau_1\, e^{a\tau_1} = \frac{1}{a}\Big(e^{\tau a} - 1\Big)\,, \tag{A.1a}$$

$$\begin{aligned}\int_0^\tau \mathrm{d}\tau_1 \mathrm{d}\tau_2\, \theta\left(\tau_1 - \tau_2\right) e^{a(\tau_1-\tau_2)} &= \int_0^\tau \mathrm{d}\tau_1\, e^{a\tau_1} \int_0^{\tau_1} \mathrm{d}\tau_2\, e^{-a\tau_2} \\ &= -\frac{\tau}{a} + \frac{1}{a^2}\Big(e^{\tau a} - 1\Big)\,, \end{aligned} \tag{A.1b}$$

$$\begin{aligned}\int_0^\tau d\tau_1 d\tau_2\, \theta\left(\tau_1 - \tau_2\right) e^{a\tau_1+b\tau_2} &= \int_0^\tau \mathrm{d}\tau_1\, e^{a\tau_1} \int_0^{\tau_1} \mathrm{d}\tau_2\, e^{b\tau_2} \\ &= \frac{1}{b\,(a+b)}\Big(e^{\tau(a+b)} - 1\Big) - \frac{1}{ab}\Big(e^{\tau a} - 1\Big)\,. \end{aligned} \tag{A.1c}$$

Given that such integrals only appear in the theory with $a < 0$ and $a + b < 0$, one obtains

$$\lim_{\tau\to\infty} \int_0^\tau \mathrm{d}\tau\, e^{a\tau} = -\frac{1}{a}\,, \tag{A.2a}$$

$$\lim_{\tau\to\infty} \int_0^\tau \mathrm{d}\tau_1 \mathrm{d}\tau_2\, \theta\left(\tau_1 - \tau_2\right) e^{a(\tau_1-\tau_2)} = -\frac{\tau}{a} - \frac{1}{a^2}\,, \tag{A.2b}$$

$$\lim_{\tau\to\infty} \int_0^\tau \mathrm{d}\tau_1 \mathrm{d}\tau_2\, \theta\left(\tau_1 - \tau_2\right) e^{a\tau_1+b\tau_2} = \frac{1}{a(a+b)}\,, \tag{A.2c}$$

where the first and third results are necessarily positive.

B. Basic elements of graph theory

Graph theory is a domain of discrete mathematics focusing on the study of graphs and their properties. In this section one introduces basic notation and terminology required for reformulating aspects of many-body theory in terms of graph-theory language. For an extensive discussion see, e.g., the classical textbook [168].

Definition A *graph* is a triplet $G = (V, E, \psi)$ consisting of a set V whose elements are called *vertices* and a set E whose elements are called *edges* together with an incidence relation ψ. Let further $E' \subset E$, $V' \subset V$ and $\psi|_{E'}$ be the restriction of ψ to E' then the triplet $G' = (E', V', \psi|_{E'})$ is called a *subgraph* of G. We call a graph *oriented* if every edge has a fixed direction.

Note that the finiteness of either V or E is not assumed. In applications for BMBPT diagrams, however, both sets will always be finite for any perturbative order. Two nodes v_1, v_2 are further called *adjacent* if there exists an edge e connecting v_1 with v_2. An edge that starts and end at the same vertex is called a *loop*. If an edge $e \in E$ starts or ends at a vertex $v \in V$ then e is called *incident* to e. The number of incident edges of a vertex is called *degree* and denoted as $\deg(v)$.

Definition Let $G = (V, E, \psi)$ be a graph with $v_i \in V$ and $e_i \in E$. The sequence

$$v_0 e_1 v_1 e_1 .... e_n v_n \tag{B.1}$$

is called a *walk*. The walk is *closed* if $v_0 = v_n$. Furthermore, the *length* of a walk is the number of edges $|\{e_0, ..., e_n\}|$.

The first node v_0 and last node v_n are called *initial* and *terminal* nodes, respectively. If all nodes in a walk are distinct, it is a *path*. Of particular importance is the case where the initial and terminal node coincide, which is called a *cycle*.

Definition A graph $G = (V, E, \psi)$ is *connected* if for any pair of nodes there is a path connecting them.

The definition of connectedness of graphs is crucial since it directly relates to physical properties of the many-body expansion. A connected graph without a cycle is called *tree*.

For now, graphs have been treated as abstract objects. For computational purposes it is convenient to have a representation of graphs.

Definition Let $G = (V, E, \psi)$ be a graph. The *incidence matrix* $M(g)$ is the $|V| \times |E|$ matrix with entries

$$m_{ij} = \begin{cases} 1, & \text{if } e_j \text{ is incident to } v_i \\ 0, & \text{otherwise} \end{cases} . \tag{B.2}$$

The notation of incidence matrices is an edge-based representation of the graph. However, for our applications the use of a vertex-based description is more useful.

Definition Let $G = (V, E, \psi)$ be a graph. The *adjacency matrix* $A(g)$ is the $|V| \times |V|$ matrix with entries

$$a_{ij} = \Big|\{e_k \in E \,:\, e_k \,\text{connects}\, v_i, v_j\}\Big| \,. \tag{B.3}$$

For oriented graphs the definition night to be slightly extended:

Definition Let $G = (V, E, \psi)$ be an oriented graph. The *oriented adjacency matrix* $\tilde{A}(g)$ is the $|V| \times |V|$ matrix with entries

$$\tilde{a}_{ij} = \Big|\{e_k \in E \,:\, e_k \,\text{goes from}\, v_i \text{to}\, v_j\}\Big| \,. \tag{B.4}$$

We emphasize that the (oriented) adjacency matrix of a graph G encodes all relevant structural information.

Proposition. *Let $G = (V, E, \psi)$ be a graph with $|V| = n$ $|E| = m$ then the following are equivalent*

(*i*) *G is connected and contains no cycle.*

(*ii*) *G has no cycle and $m = n - 1$.*

(*iii*) *G is connected and $m = n - 1$.*

(*iv*) *G is connected but would not be if any of its edges were suppressed.*[1]

(*v*) *G contains no cycle and adding a new edge to it creates a unique cycle.*

(*vi*) *For any pair of nodes v_i and v_j, there exists a single path from v_i to v_j.*

[1] This notion corresponds to one-line irreducible diagrams in physics.

C. Normal-ordered matrix elements

C.1. Generic operator O

As the $O^{[6]}$ terms are not considered for practical applications at this point, the matrix elements $O^{ij}_{k_1k_2k_3k_4k_5k_6}$, with $i+j=6$, are excluded for brevity. The generic operator O of Eq. (1.3), up to and including $O^{[4]}$

$$O \equiv O^{[0]} + O^{[2]} + O^{[4]} \tag{C.1a}$$

$$\equiv O^{00} + \Big[O^{11} + \{O^{20} + O^{02}\}\Big] + \Big[O^{22} + \{O^{31} + O^{13}\} + \{O^{40} + O^{04}\}\Big] \,, \tag{C.1b}$$

displays fully antisymmetrized matrix elements, whose explicit expressions in terms of antisymmetrized matrix elements of O^{1N}, O^{2N} and O^{3N}, as well as of U and V matrices defining the reference Bogoliubov state, are

$$O^{00} = \sum_{l_1 l_2} \Big[\Lambda^{1N}_{l_1 l_2}\rho_{l_2 l_1} + \frac{1}{2}\Lambda^{2N}_{l_1 l_2}\rho_{l_2 l_1} + \frac{1}{3}\Lambda^{3N}_{l_1 l_2}\rho_{l_2 l_1} - \frac{1}{2}\Upsilon^{2N}_{l_1 l_2}\kappa^*_{l_2 l_1} + \frac{1}{3}\Upsilon^{3N}_{l_1 l_2}\kappa^*_{l_2 l_1}\Big] \,, \tag{C.2a}$$

$$O^{11}_{k_1 k_2} = \sum_{l_1 l_2} \Big[U^\dagger_{k_1 l_1}\Lambda_{l_1 l_2}U_{l_2 k_2} - V^\dagger_{k_1 l_1}\Lambda^T_{l_1 l_2}V_{l_2 k_2} + U^\dagger_{k_1 l_1}\Upsilon_{l_1 l_2}V_{l_2 k_2} - V^\dagger_{k_1 l_1}\Upsilon^*_{l_1 l_2}U_{l_2 k_2}\Big] \,, \tag{C.2b}$$

$$O^{20}_{k_1 k_2} = \sum_{l_1 l_2} \Big[U^\dagger_{k_1 l_1}\Lambda_{l_1 l_2}V^*_{l_2 k_2} - V^\dagger_{k_1 l_1}\Lambda^T_{l_1 l_2}U^*_{l_2 k_2} + U^\dagger_{k_1 l_1}\Upsilon_{l_1 l_2}U^*_{l_2 k_2} - V^\dagger_{k_1 l_1}\Upsilon^*_{l_1 l_2}V^*_{l_2 k_2}\Big] \,, \tag{C.2c}$$

$$O^{02}_{k_1 k_2} = \sum_{l_1 l_2} \Big[- V^T_{k_1 l_1}\Lambda_{l_1 l_2}U_{l_2 k_2} + U^T_{k_1 l_1}\Lambda^T_{l_1 l_2}V_{l_2 k_2} - V^T_{k_1 l_1}\Upsilon_{l_1 l_2}V_{l_2 k_2} + U^T_{k_1 l_1}\Upsilon^*_{l_1 l_2}U_{l_2 k_2}\Big] \,, \tag{C.2d}$$

$$\begin{aligned} O^{22}_{k_1 k_2 k_3 k_4} = \sum_{l_1 l_2 l_3 l_4} \Big[& \Theta_{l_1 l_2 l_3 l_4}\Big(U^*_{l_1 k_1}U^*_{l_2 k_2}U_{l_3 k_3}U_{l_4 k_4} + V^*_{l_3 k_1}V^*_{l_4 k_2}V_{l_1 k_3}V_{l_2 k_4} + U^*_{l_1 k_1}V^*_{l_4 k_2}V_{l_2 k_3}U_{l_3 k_4} \\ & - V^*_{l_4 k_1}U^*_{l_1 k_2}V_{l_2 k_3}U_{l_3 k_4} - U^*_{l_1 k_1}V^*_{l_4 k_2}U_{l_3 k_3}V_{l_2 k_4} + V^*_{l_4 k_1}U^*_{l_1 k_2}U_{l_3 k_3}V_{l_2 k_4}\Big) \\ & + \Xi_{l_1 l_2 l_3 l_4}\Big(U^*_{l_1 k_1}U^*_{l_2 k_2}U_{l_4 k_3}V_{l_3 k_4} + U^*_{l_1 k_1}V^*_{l_4 k_2}V_{l_3 k_3}V_{l_2 k_4} \\ & - U^*_{l_1 k_1}U^*_{l_2 k_2}V_{l_3 k_3}U_{l_4 k_4} - V^*_{l_4 k_1}U^*_{l_1 k_2}V_{l_3 k_3}V_{l_2 k_4}\Big) \\ & - \Xi^*_{l_1 l_2 l_3 l_4}\Big(V^*_{l_3 k_1}U^*_{l_4 k_2}U_{l_1 k_3}U_{l_2 k_4} + V^*_{l_3 k_1}V^*_{l_2 k_2}V_{l_4 k_3}U_{l_1 k_4} \\ & - U^*_{l_4 k_1}V^*_{l_3 k_2}U_{l_1 k_3}U_{l_2 k_4} - V^*_{l_3 k_1}V^*_{l_2 k_2}V_{l_4 k_4}U_{l_1 k_3}\Big)\Big] \,, \end{aligned} \tag{C.2e}$$

$$
\begin{aligned}
O^{31}_{k_1k_2k_3k_4} = \sum_{l_1l_2l_3l_4} \Big[& \Theta_{l_1l_2l_3l_4} \Big(U^*_{l_1k_1} V^*_{l_4k_2} V^*_{l_3k_3} V_{l_2k_4} - V^*_{l_4k_1} U^*_{l_1k_2} V^*_{l_3k_3} V_{l_2k_4} - V^*_{l_3k_1} V^*_{l_4k_2} U^*_{l_1k_3} V_{l_2k_4} \\
& \quad + V^*_{l_3k_1} U^*_{l_2k_2} U^*_{l_1k_3} U_{l_4k_4} - U^*_{l_2k_1} V^*_{l_3k_2} U^*_{l_1k_3} U_{l_4k_4} - U^*_{l_1k_1} U^*_{l_2k_2} V^*_{l_3k_3} U_{l_4k_4} \Big) \\
& + \Xi_{l_1l_2l_3l_4} \Big(U^*_{l_1k_1} U^*_{l_2k_2} U^*_{l_3k_3} U_{l_4k_4} + V^*_{l_4k_1} U^*_{l_2k_2} U^*_{l_1k_3} V_{l_3k_4} \\
& \quad - U^*_{l_2k_1} V^*_{l_4k_2} U^*_{l_1k_3} V_{l_3k_4} + U^*_{l_2k_1} U^*_{l_1k_2} V^*_{l_4k_3} V_{l_3k_4} \Big) \\
& + \Xi^*_{l_1l_2l_3l_4} \Big(U^*_{l_4k_1} V^*_{l_3k_2} V^*_{l_2k_3} U_{l_1k_4} - V^*_{l_3k_1} U^*_{l_4k_2} V^*_{l_2k_3} U_{l_1k_4} \\
& \quad + V^*_{l_3k_1} V^*_{l_2k_2} U^*_{l_4k_3} U_{l_1k_4} - V^*_{l_3k_1} V^*_{l_2k_2} V^*_{l_1k_3} V_{l_4k_4} \Big) \Big] \,, \qquad \text{(C.2f)} \\
O^{13}_{k_1k_2k_3k_4} = \sum_{l_1l_2l_3l_4} \Big[& \Theta_{l_1l_2l_3l_4} \Big(V^*_{l_4k_1} U_{l_3k_2} V_{l_2k_3} V_{l_1k_4} - V^*_{l_4k_1} V_{l_2k_2} U_{l_3k_3} V_{l_1k_4} - V^*_{l_4k_1} V_{l_1k_2} V_{l_2k_3} U_{l_3k_4} \\
& \quad + U^*_{l_1k_1} V_{l_2k_2} U_{l_3k_3} U_{l_4k_4} - U^*_{l_1k_1} U_{l_3k_2} V_{l_2k_3} U_{l_4k_4} + U^*_{l_1k_1} U_{l_3k_2} U_{l_4k_3} V_{l_2k_4} \Big) \\
& + \Xi_{l_1l_2l_3l_4} \Big(U^*_{l_1k_1} V_{l_2k_2} V_{l_3k_3} U_{l_4k_4} - V^*_{l_4k_1} V_{l_1k_2} V_{l_2k_3} V_{l_3k_4} \\
& \quad + U^*_{l_1k_1} U_{l_4k_2} V_{l_2k_3} V_{l_3k_4} - U^*_{l_1k_1} V_{l_2k_2} U_{l_4k_3} V_{l_3k_4} \Big) \\
& + \Xi^*_{l_1l_2l_3l_4} \Big(V^*_{l_3k_1} V_{l_4k_2} U_{l_1k_3} U_{l_2k_4} - V^*_{l_3k_1} U_{l_1k_2} V_{l_4k_3} U_{l_2k_4} \\
& \quad + V^*_{l_3k_1} U_{l_1k_2} U_{l_2k_3} V_{l_4k_4} - U^*_{l_4k_1} U_{l_1k_2} U_{l_2k_3} U_{l_3k_4} \Big) \Big] \,, \qquad \text{(C.2g)} \\
O^{40}_{k_1k_2k_3k_4} = \sum_{l_1l_2l_3l_4} \Big[& \Theta_{l_1l_2l_3l_4} \Big(U^*_{l_1k_1} U^*_{l_2k_2} V^*_{l_4k_3} V^*_{l_3k_4} - U^*_{l_1k_1} V^*_{l_4k_2} U^*_{l_2k_3} V^*_{l_3k_4} - V^*_{l_4k_1} U^*_{l_2k_2} U^*_{l_1k_3} V^*_{l_3k_4} \\
& \quad + U^*_{l_1k_1} V^*_{l_4k_2} V^*_{l_3k_3} U^*_{l_2k_4} + V^*_{l_4k_1} U^*_{l_2k_2} V^*_{l_3k_3} U^*_{l_1k_4} + V^*_{l_4k_1} V^*_{l_3k_2} U^*_{l_1k_3} U^*_{l_2k_4} \Big) \\
& + \Xi_{l_1l_2l_3l_4} \Big(U^*_{l_1k_1} U^*_{l_2k_2} U^*_{l_3k_3} V^*_{l_4k_4} - U^*_{l_1k_1} U^*_{l_2k_2} V^*_{l_4k_3} U^*_{l_3k_4} \\
& \quad + U^*_{l_1k_1} V^*_{l_4k_2} U^*_{l_2k_3} U^*_{l_3k_4} - V^*_{l_4k_1} U^*_{l_1k_2} U^*_{l_2k_3} U^*_{l_3k_4} \Big) \\
& + \Xi^*_{l_1l_2l_3l_4} \Big(V^*_{l_1k_1} V^*_{l_2k_2} V^*_{l_3k_3} U^*_{l_4k_4} - V^*_{l_1k_1} V^*_{l_2k_2} U^*_{l_4k_3} V^*_{l_3k_4} \\
& \quad + V^*_{l_1k_1} U^*_{l_4k_2} V^*_{l_2k_3} V^*_{l_3k_4} - U^*_{l_4k_1} V^*_{l_1k_2} V^*_{l_2k_3} U^*_{l_3k_4} \Big) \Big] \,, \qquad \text{(C.2h)} \\
O^{04}_{k_1k_2k_3k_4} = \sum_{l_1l_2l_3l_4} \Big[& \Theta_{l_1l_2l_3l_4} \Big(U_{l_3k_1} U_{l_4k_2} V_{l_2k_3} V_{l_1k_4} - U_{l_3k_1} V_{l_2k_2} U_{l_4k_3} V_{l_1k_4} + U_{l_3k_1} V_{l_2k_2} V_{l_1k_3} U_{l_4k_4} \\
& \quad - V_{l_2k_1} U_{l_3k_2} V_{l_1k_3} U_{l_4k_4} + V_{l_2k_1} V_{l_1k_2} U_{l_3k_3} U_{l_4k_4} + V_{l_2k_1} U_{l_3k_2} U_{l_4k_3} V_{l_1k_4} \Big) \\
& + \Xi_{l_1l_2l_3l_4} \Big(V_{l_1k_1} V_{l_2k_2} V_{l_3k_3} U_{l_4k_4} - V_{l_1k_1} V_{l_2k_2} U_{l_4k_3} V_{l_3k_4} \\
& \quad + V_{l_1k_1} U_{l_4k_2} V_{l_2k_3} V_{l_3k_4} - U_{l_4k_1} V_{l_1k_2} V_{l_2k_3} V_{l_3k_4} \Big) \\
& + \Xi^*_{l_1l_2l_3l_4} \Big(V_{l_4k_1} U_{l_3k_2} U_{l_2k_3} U_{l_1k_4} - U_{l_3k_1} V_{l_4k_2} U_{l_2k_3} U_{l_1k_4} \\
& \quad + U_{l_3k_1} U_{l_2k_2} V_{l_4k_3} U_{l_1k_4} - U_{l_3k_1} U_{l_2k_2} U_{l_1k_3} V_{l_4k_4} \Big) \Big] \,. \qquad \text{(C.2i)}
\end{aligned}
$$

The above expressions make use of four one- and two-body operators whose matrix elements are given in an arbitrary single-particle basis by

$$\Lambda_{pq} \equiv \Lambda^{1N}_{pq} + \Lambda^{2N}_{pq} + \Lambda^{3N}_{pq} \tag{C.3a}$$
$$= o^{1N}_{pq} + \sum_{rs} \bar{o}^{2N}_{psqr}\rho_{rs} + \frac{1}{2}\sum_{rstu} \bar{o}^{3N}_{prsqtu}\left(\rho_{us}\rho_{tr} + \frac{1}{2}\kappa^*_{rs}\kappa_{tu}\right) , \tag{C.3b}$$
$$\Upsilon_{pq} \equiv \Upsilon^{2N}_{pq} + \Upsilon^{3N}_{pq} \tag{C.3c}$$
$$= \frac{1}{2}\sum_{rs} \bar{o}^{2N}_{pqrs}\kappa_{rs} + \frac{1}{2}\sum_{rstu} \bar{o}^{3N}_{rpqstu}\rho_{sr}\kappa_{tu} , \tag{C.3d}$$
$$\Theta_{pqrs} \equiv \bar{o}^{2N}_{pqrs} + \sum_{tu} \bar{o}^{3N}_{pqtrsu}\rho_{ut} , \tag{C.3e}$$
$$\Xi_{pqrs} \equiv \frac{1}{2}\sum_{tu} \bar{o}^{3N}_{pqrstu}\kappa_{tu} . \tag{C.3f}$$

It is easy to verify the following properties

$$\Lambda^{2N}_{pq} = \Lambda^{2N*}_{qp} , \tag{C.4a}$$
$$\Lambda^{3N}_{pq} = \Lambda^{3N*}_{qp} , \tag{C.4b}$$
$$\Upsilon^{2N}_{pq} = -\Upsilon^{2N}_{qp} , \tag{C.4c}$$
$$\Upsilon^{3N}_{pq} = -\Upsilon^{3N}_{qp} , \tag{C.4d}$$
$$\Theta_{pqrs} = -\Theta_{pqsr} = \Theta_{qpsr} = -\Theta_{qprs} , \tag{C.4e}$$
$$\Theta_{pqrs} = \Theta^*_{rspq} , \tag{C.4f}$$
$$\Xi_{pqrs} = -\Xi_{qprs} = \Xi_{qrps} = -\Xi_{prqs} = \Xi_{rpqs} = -\Xi_{rqps} , \tag{C.4g}$$

as will be the case for the other operators to follow.

C.2. Grand canonical potential Ω

One can derive the normal-ordered matrix elements of Ω using the expressions above and four one- and two-body operators whose matrix elements are given in an arbitrary single-particle basis by

$$\Lambda_{pq} \equiv h_{pq} - \lambda\delta_{pq} \tag{C.5a}$$
$$\equiv t_{pq} - \lambda\,\delta_{pq} + \Gamma^{2N}_{pq} + \Gamma^{3N}_{pq} \tag{C.5b}$$
$$= t_{pq} - \lambda\,\delta_{pq} + \sum_{rs} \bar{v}_{psqr}\rho_{rs} + \frac{1}{2}\sum_{rstu} \bar{w}_{prsqtu}\left(\rho_{us}\rho_{tr} + \frac{1}{2}\kappa^*_{rs}\kappa_{tu}\right) , \tag{C.5c}$$
$$\Upsilon_{pq} \equiv \Delta^{2N}_{pq} + \Delta^{3N}_{pq} \tag{C.5d}$$
$$= \frac{1}{2}\sum_{rs} \bar{v}_{pqrs}\kappa_{rs} + \frac{1}{2}\sum_{rstu} \bar{w}_{rpqstu}\rho_{sr}\kappa_{tu} , \tag{C.5e}$$
$$\Theta_{pqrs} \equiv \bar{v}_{pqrs} + \sum_{tu} \bar{w}_{pqtrsu}\rho_{ut} , \tag{C.5f}$$
$$\Xi_{pqrs} \equiv \frac{1}{2}\sum_{tu} \bar{w}_{pqrstu}\kappa_{tu} . \tag{C.5g}$$

C.3. Hamiltonian operator H

Similarly to the grand potential case, one uses, along with the expressions in App. C.1, four one- and two-body operators whose matrix elements are given in an arbitrary single-particle basis by

$$\Lambda_{pq} \equiv h_{pq} \tag{C.6a}$$
$$\equiv t_{pq} + \Gamma^{2N}_{pq} + \Gamma^{3N}_{pq} \tag{C.6b}$$
$$= t_{pq} + \sum_{rs} \bar{v}_{psqr}\rho_{rs} + \frac{1}{2}\sum_{rstu} \bar{w}_{prsqtu}\left(\rho_{us}\rho_{tr} + \frac{1}{2}\kappa^*_{rs}\kappa_{tu}\right) , \tag{C.6c}$$
$$\Upsilon_{pq} \equiv \Delta^{2N}_{pq} + \Delta^{3N}_{pq} \tag{C.6d}$$
$$= \frac{1}{2}\sum_{rs} \bar{v}_{pqrs}\kappa_{rs} + \frac{1}{2}\sum_{rstu} \bar{w}_{rpqstu}\rho_{sr}\kappa_{tu} , \tag{C.6e}$$
$$\Theta_{pqrs} \equiv \bar{v}_{pqrs} + \sum_{tu} \bar{w}_{pqtrsu}\rho_{ut} , \tag{C.6f}$$
$$\Xi_{pqrs} \equiv \frac{1}{2}\sum_{tu} \bar{w}_{pqrstu}\kappa_{tu} . \tag{C.6g}$$

C.4. Particle number operator A

The particle number operator A can be written using the work accomplished for a generic operator in App. C.1, making use of one-body operators whose matrix elements are given in an arbitrary single-particle basis by

$$\Lambda_{pq} \equiv a_{pq} \tag{C.7a}$$
$$= \delta_{pq} , \tag{C.7b}$$
$$\Upsilon_{pq} \equiv 0 , \tag{C.7c}$$
$$\Theta_{pqrs} \equiv 0 , \tag{C.7d}$$
$$\Xi_{pqrs} \equiv 0 . \tag{C.7e}$$

C.5. A^2 operator

The A^2 operator defined in Eq. (2.75) can be written using the work accomplished for a generic operator in App. C.1, making use of one- and two-body operators whose matrix elements are

given in an arbitrary single-particle basis by

$$\Lambda_{pq} \equiv a^{(1)}_{pq} + \sum_{rs} \bar{a}^{(2)}_{psqr}\rho_{rs} \tag{C.8a}$$

$$= \delta_{pq} + \sum_{rs} 2(\delta_{pr}\delta_{qs} - \delta_{ps}\delta_{qr})\rho_{rs} \ , \tag{C.8b}$$

$$\Upsilon_{pq} \equiv \frac{1}{2}\sum_{rs} \bar{a}^{(2)}_{pqrs}\kappa_{rs} \tag{C.8c}$$

$$= \sum_{rs} (\delta_{pr}\delta_{qs} - \delta_{ps}\delta_{qr})\kappa_{rs} \ , \tag{C.8d}$$

$$\Theta_{pqrs} \equiv \bar{a}^{(2)}_{pqrs} \tag{C.8e}$$

$$= 2(\delta_{pr}\delta_{qs} - \delta_{ps}\delta_{qr}) \ , \tag{C.8f}$$

$$\Xi_{pqrs} \equiv 0 \ . \tag{C.8g}$$

D. Diagrammatic contributions at BMBPT(2)

D.1. $n(\tau)$ at BMBPT(2)

Applying the diagrammatic rules explicated in Sec. 2.4.3 to the two second-order BMBPT diagrams contributing to $n(\tau)$ and displayed in Fig. 2.4 gives

$$\mathrm{PN2.1} = \lim_{\tau\to\infty} +\frac{1}{2}\sum_{k_1k_2}\frac{\Omega^{20}_{k_1k_2}\Omega^{02}_{k_1k_2}}{E_{k_1}+E_{k_2}}\left[\tau - \frac{1-e^{-\tau(E_{k_1}+E_{k_2})}}{E_{k_1}+E_{k_2}}\right] ,$$

$$\mathrm{PN2.2} = \lim_{\tau\to\infty} +\frac{1}{4!}\sum_{k_1k_2k_3k_4}\frac{\Omega^{40}_{k_1k_2k_3k_4}\Omega^{04}_{k_1k_2k_3k_4}}{E_{k_1}+E_{k_2}+E_{k_3}+E_{k_4}}\left[\tau - \frac{1-e^{-\tau(E_{k_1}+E_{k_2}+E_{k_3}+E_{k_4})}}{E_{k_1}+E_{k_2}+E_{k_3}+E_{k_4}}\right] ,$$

which reduce in the large τ limit to

$$\mathrm{PN2.1} = \lim_{\tau\to\infty} +\frac{1}{2}\sum_{k_1k_2}\frac{\Omega^{20}_{k_1k_2}\Omega^{02}_{k_1k_2}}{E_{k_1}+E_{k_2}}\left[\tau - \frac{1}{E_{k_1}+E_{k_2}}\right] ,$$

$$\mathrm{PN2.2} = \lim_{\tau\to\infty} +\frac{1}{4!}\sum_{k_1k_2k_3k_4}\frac{\Omega^{40}_{k_1k_2k_3k_4}\Omega^{04}_{k_1k_2k_3k_4}}{E_{k_1}+E_{k_2}+E_{k_3}+E_{k_4}}\left[\tau - \frac{1}{E_{k_1}+E_{k_2}+E_{k_3}+E_{k_4}}\right] .$$

D.2. $o(\tau)$ at BMBPT(2)

Applying diagrammatic rules to the eleven zero-, first- and second-order BMBPT connected/linked diagrams contributing to $o(\tau)$ and displayed in Fig. 2.6 gives

$$\mathrm{PO0.1} = +O^{00} \ ,$$

$$\mathrm{PO1.1} = \lim_{\tau\to\infty} -\frac{1}{2}\sum_{k_1k_2}\frac{O^{20}_{k_1k_2}\Omega^{02}_{k_1k_2}}{E_{k_1}+E_{k_2}}\left[1-e^{-\tau(E_{k_1}+E_{k_2})}\right] \ ,$$

$$\mathrm{PO1.2} = \lim_{\tau\to\infty} -\frac{1}{4!}\sum_{k_1k_2k_3k_4}\frac{O^{40}_{k_1k_2k_3k_4}\Omega^{04}_{k_1k_2k_3k_4}}{E_{k_1}+E_{k_2}+E_{k_3}+E_{k_4}}\left[1-e^{-\tau(E_{k_1}+E_{k_2}+E_{k_3}+E_{k_4})}\right] \ ,$$

$$\mathrm{PO2.1} = \lim_{\tau\to\infty} +\sum_{k_1k_2k_3}\frac{O^{20}_{k_1k_2}\breve{\Omega}^{11}_{k_3k_1}\Omega^{02}_{k_3k_2}}{E_{k_3}-E_{k_1}}\left[\frac{1-e^{-\tau\left(E_{k_1}+E_{k_2}\right)}}{E_{k_1}+E_{k_2}}-\frac{1-e^{-\tau\left(E_{k_2}+E_{k_3}\right)}}{E_{k_2}+E_{k_3}}\right] \ ,$$

$$\mathrm{PO2.2} = \lim_{\tau\to\infty} +\frac{1}{4}\sum_{k_1k_2k_3k_4}\frac{O^{20}_{k_1k_2}\Omega^{22}_{k_3k_4k_1k_2}\Omega^{02}_{k_3k_4}}{E_{k_3}+E_{k_4}-E_{k_1}-E_{k_2}}\left[\frac{1-e^{-\tau\left(E_{k_1}+E_{k_2}\right)}}{E_{k_1}+E_{k_2}}-\frac{1-e^{-\tau\left(E_{k_3}+E_{k_4}\right)}}{E_{k_3}+E_{k_4}}\right] \ ,$$

$$\mathrm{PO2.3} = \lim_{\tau\to\infty} +\frac{1}{4}\sum_{k_1k_2k_3k_4}\frac{O^{20}_{k_1k_2}\Omega^{04}_{k_1k_2k_3k_4}\Omega^{20}_{k_3k_4}}{E_{k_3}+E_{k_4}}\left[\frac{1-e^{-\tau\left(E_{k_1}+E_{k_2}\right)}}{E_{k_1}+E_{k_2}}-\frac{1-e^{-\tau\left(E_{k_1}+E_{k_2}+E_{k_3}+E_{k_4}\right)}}{E_{k_1}+E_{k_2}+E_{k_3}+E_{k_4}}\right] \ ,$$

$$\mathrm{PO2.4} = \lim_{\tau\to\infty} +\frac{1}{8}\sum_{k_1k_2k_3k_4}\frac{O^{40}_{k_1k_2k_3k_4}\Omega^{02}_{k_1k_4}\Omega^{02}_{k_2k_3}}{\left(E_{k_1}+E_{k_4}\right)\left(E_{k_2}+E_{k_3}\right)}\left(1-e^{-\tau\left(E_{k_2}+E_{k_3}\right)}\right)\left(1-e^{-\tau\left(E_{k_1}+E_{k_4}\right)}\right) \ ,$$

$$\mathrm{PO2.5} = \lim_{\tau\to\infty} +\frac{1}{6}\sum_{k_1k_2k_3k_4k_5}\frac{O^{40}_{k_1k_2k_3k_4}\Omega^{13}_{k_5k_1k_2k_3}\Omega^{02}_{k_5k_4}}{E_{k_5}-E_{k_1}-E_{k_2}-E_{k_3}}\left[\frac{1-e^{-\tau\left(E_{k_1}+E_{k_2}+E_{k_3}+E_{k_4}\right)}}{E_{k_1}+E_{k_2}+E_{k_3}+E_{k_4}}-\frac{1-e^{-\tau\left(E_{k_4}+E_{k_5}\right)}}{E_{k_4}+E_{k_5}}\right] \ ,$$

$$\mathrm{PO2.6} = \lim_{\tau\to\infty} +\frac{1}{6}\sum_{k_1k_2k_3k_4k_5}\frac{O^{40}_{k_1k_2k_3k_4}\Omega^{04}_{k_1k_2k_3k_5}\breve{\Omega}^{11}_{k_5k_4}}{E_{k_5}-E_{k_4}}\left[\frac{1-e^{-\tau\left(E_{k_1}+E_{k_2}+E_{k_3}+E_{k_4}\right)}}{E_{k_1}+E_{k_2}+E_{k_3}+E_{k_4}}-\frac{1-e^{-\tau\left(E_{k_1}+E_{k_2}+E_{k_3}+E_{k_5}\right)}}{E_{k_1}+E_{k_2}+E_{k_3}+E_{k_5}}\right] \ ,$$

$$\mathrm{PO2.7} = \lim_{\tau\to\infty} +\frac{1}{6}\sum_{k_1k_2k_3k_4k_5}\frac{O^{20}_{k_1k_2}\Omega^{31}_{k_3k_4k_5k_1}\Omega^{04}_{k_3k_4k_5k_2}}{E_{k_3}+E_{k_4}+E_{k_5}-E_{k_1}}\left[\frac{1-e^{-\tau\left(E_{k_1}+E_{k_2}\right)}}{E_{k_1}+E_{k_2}}-\frac{1-e^{-\tau\left(E_{k_2}+E_{k_3}+E_{k_4}+E_{k_5}\right)}}{E_{k_2}+E_{k_3}+E_{k_4}+E_{k_5}}\right] \ ,$$

$$\mathrm{PO2.8} = \lim_{\tau\to\infty} +\frac{1}{8}\sum_{k_1k_2k_3k_4k_5k_6}\frac{O^{40}_{k_1k_2k_3k_4}\Omega^{22}_{k_5k_6k_2k_3}\Omega^{04}_{k_1k_5k_6k_4}}{E_{k_5}+E_{k_6}-E_{k_2}-E_{k_3}}\left[\frac{1-e^{-\tau\left(E_{k_1}+E_{k_2}+E_{k_3}+E_{k_4}\right)}}{E_{k_1}+E_{k_2}+E_{k_3}+E_{k_4}}-\frac{1-e^{-\tau\left(E_{k_1}+E_{k_4}+E_{k_5}+E_{k_6}\right)}}{E_{k_1}+E_{k_4}+E_{k_5}+E_{k_6}}\right] \ ,$$

which reduce in the large τ limit to

$$\mathrm{PO0.1} = +O^{00} \,,$$

$$\mathrm{PO1.1} = -\frac{1}{2}\sum_{k_1k_2}\frac{O^{20}_{k_1k_2}\Omega^{02}_{k_1k_2}}{E_{k_1}+E_{k_2}} \,,$$

$$\mathrm{PO1.2} = -\frac{1}{4!}\sum_{k_1k_2k_3k_4}\frac{O^{40}_{k_1k_2k_3k_4}\Omega^{04}_{k_1k_2k_3k_4}}{E_{k_1}+E_{k_2}+E_{k_3}+E_{k_4}} \,,$$

$$\mathrm{PO2.1} = +\sum_{k_1k_2k_3}\frac{O^{20}_{k_1k_2}\breve{\Omega}^{11}_{k_3k_1}\Omega^{02}_{k_3k_2}}{(E_{k_1}+E_{k_2})\,(E_{k_2}+E_{k_3})} \,,$$

$$\mathrm{PO2.2} = +\frac{1}{4}\sum_{k_1k_2k_3k_4}\frac{O^{20}_{k_1k_2}\Omega^{22}_{k_3k_4k_1k_2}\Omega^{02}_{k_3k_4}}{(E_{k_1}+E_{k_2})\,(E_{k_3}+E_{k_4})} \,,$$

$$\mathrm{PO2.3} = +\frac{1}{4}\sum_{k_1k_2k_3k_4}\frac{O^{20}_{k_1k_2}\Omega^{04}_{k_1k_2k_3k_4}\Omega^{20}_{k_3k_4}}{(E_{k_1}+E_{k_2})\,(E_{k_1}+E_{k_2}+E_{k_3}+E_{k_4})} \,,$$

$$\mathrm{PO2.4} = +\frac{1}{8}\sum_{k_1k_2k_3k_4}\frac{O^{40}_{k_1k_2k_3k_4}\Omega^{02}_{k_1k_4}\Omega^{02}_{k_2k_3}}{(E_{k_1}+E_{k_4})\,(E_{k_2}+E_{k_3})} \,,$$

$$\mathrm{PO2.5} = +\frac{1}{6}\sum_{k_1k_2k_3k_4k_5}\frac{O^{40}_{k_1k_2k_3k_4}\Omega^{13}_{k_5k_1k_2k_3}\Omega^{02}_{k_5k_4}}{(E_{k_1}+E_{k_2}+E_{k_3}+E_{k_4})\,(E_{k_4}+E_{k_5})} \,,$$

$$\mathrm{PO2.6} = +\frac{1}{6}\sum_{k_1k_2k_3k_4k_5}\frac{O^{40}_{k_1k_2k_3k_4}\Omega^{04}_{k_1k_2k_3k_5}\breve{\Omega}^{11}_{k_5k_4}}{(E_{k_1}+E_{k_2}+E_{k_3}+E_{k_4})\,(E_{k_1}+E_{k_2}+E_{k_3}+E_{k_5})} \,,$$

$$\mathrm{PO2.7} = +\frac{1}{6}\sum_{k_1k_2k_3k_4k_5}\frac{O^{20}_{k_1k_2}\Omega^{31}_{k_3k_4k_5k_1}\Omega^{04}_{k_3k_4k_5k_2}}{(E_{k_1}+E_{k_2})\,(E_{k_2}+E_{k_3}+E_{k_4}+E_{k_5})} \,,$$

$$\mathrm{PO2.8} = +\frac{1}{8}\sum_{k_1k_2k_3k_4k_5k_6}\frac{O^{40}_{k_1k_2k_3k_4}\Omega^{22}_{k_5k_6k_2k_3}\Omega^{04}_{k_1k_5k_6k_4}}{(E_{k_1}+E_{k_2}+E_{k_3}+E_{k_4})\,(E_{k_1}+E_{k_4}+E_{k_5}+E_{k_6})} \,.$$

D.3. $\omega(\tau)$ at BMBPT(2)

Using the results of D.2 and replacing O with Ω, one obtains, for the diagrams contributing to $\omega(\tau)$,

$$\mathrm{P}\Omega 0.1 = +\Omega^{00} \ ,$$

$$\mathrm{P}\Omega 1.1 = \lim_{\tau\to\infty} -\frac{1}{2}\sum_{k_1k_2}\frac{\Omega^{20}_{k_1k_2}\Omega^{02}_{k_1k_2}}{E_{k_1}+E_{k_2}}\left[1-e^{-\tau(E_{k_1}+E_{k_2})}\right] \ ,$$

$$\mathrm{P}\Omega 1.2 = \lim_{\tau\to\infty} -\frac{1}{4!}\sum_{k_1k_2k_3k_4}\frac{\Omega^{40}_{k_1k_2k_3k_4}\Omega^{04}_{k_1k_2k_3k_4}}{E_{k_1}+E_{k_2}+E_{k_3}+E_{k_4}}\left[1-e^{-\tau(E_{k_1}+E_{k_2}+E_{k_3}+E_{k_4})}\right] \ ,$$

$$\mathrm{P}\Omega 2.1 = \lim_{\tau\to\infty} +\sum_{k_1k_2k_3}\frac{\Omega^{20}_{k_1k_2}\breve{\Omega}^{11}_{k_3k_1}\Omega^{02}_{k_3k_2}}{E_{k_3}-E_{k_1}}\left[\frac{1-e^{-\tau\left(E_{k_1}+E_{k_2}\right)}}{E_{k_1}+E_{k_2}}-\frac{1-e^{-\tau\left(E_{k_2}+E_{k_3}\right)}}{E_{k_2}+E_{k_3}}\right] \ ,$$

$$\mathrm{P}\Omega 2.2 = \lim_{\tau\to\infty} +\frac{1}{4}\sum_{k_1k_2k_3k_4}\frac{\Omega^{20}_{k_1k_2}\Omega^{22}_{k_3k_4k_1k_2}\Omega^{02}_{k_3k_4}}{E_{k_3}+E_{k_4}-E_{k_1}-E_{k_2}}\left[\frac{1-e^{-\tau\left(E_{k_1}+E_{k_2}\right)}}{E_{k_1}+E_{k_2}}-\frac{1-e^{-\tau\left(E_{k_3}+E_{k_4}\right)}}{E_{k_3}+E_{k_4}}\right] \ ,$$

$$\mathrm{P}\Omega 2.3 = \lim_{\tau\to\infty} +\frac{1}{4}\sum_{k_1k_2k_3k_4}\frac{\Omega^{20}_{k_1k_2}\Omega^{04}_{k_1k_2k_3k_4}\Omega^{20}_{k_3k_4}}{E_{k_3}+E_{k_4}}\left[\frac{1-e^{-\tau\left(E_{k_1}+E_{k_2}\right)}}{E_{k_1}+E_{k_2}}-\frac{1-e^{-\tau\left(E_{k_1}+E_{k_2}+E_{k_3}+E_{k_4}\right)}}{E_{k_1}+E_{k_2}+E_{k_3}+E_{k_4}}\right] \ ,$$

$$\mathrm{P}\Omega 2.4 = \lim_{\tau\to\infty} +\frac{1}{8}\sum_{k_1k_2k_3k_4}\frac{\Omega^{40}_{k_1k_2k_3k_4}\Omega^{02}_{k_1k_4}\Omega^{02}_{k_2k_3}}{\left(E_{k_1}+E_{k_4}\right)\left(E_{k_2}+E_{k_3}\right)}\left(1-e^{-\tau\left(E_{k_2}+E_{k_3}\right)}\right)\left(1-e^{-\tau\left(E_{k_1}+E_{k_4}\right)}\right) \ ,$$

$$\mathrm{P}\Omega 2.5 = \lim_{\tau\to\infty} +\frac{1}{6}\sum_{k_1k_2k_3k_4k_5}\frac{\Omega^{40}_{k_1k_2k_3k_4}\Omega^{13}_{k_5k_1k_2k_3}\Omega^{02}_{k_5k_4}}{E_{k_5}-E_{k_1}-E_{k_2}-E_{k_3}}\left[\frac{1-e^{-\tau\left(E_{k_1}+E_{k_2}+E_{k_3}+E_{k_4}\right)}}{E_{k_1}+E_{k_2}+E_{k_3}+E_{k_4}}-\frac{1-e^{-\tau\left(E_{k_4}+E_{k_5}\right)}}{E_{k_4}+E_{k_5}}\right] \ ,$$

$$\mathrm{P}\Omega 2.6 = \lim_{\tau\to\infty} +\frac{1}{6}\sum_{k_1k_2k_3k_4k_5}\frac{\Omega^{40}_{k_1k_2k_3k_4}\Omega^{04}_{k_1k_2k_3k_5}\breve{\Omega}^{11}_{k_5k_4}}{E_{k_5}-E_{k_4}}\left[\frac{1-e^{-\tau\left(E_{k_1}+E_{k_2}+E_{k_3}+E_{k_4}\right)}}{E_{k_1}+E_{k_2}+E_{k_3}+E_{k_4}}-\frac{1-e^{-\tau\left(E_{k_1}+E_{k_2}+E_{k_3}+E_{k_5}\right)}}{E_{k_1}+E_{k_2}+E_{k_3}+E_{k_5}}\right] \ ,$$

$$\mathrm{P}\Omega 2.7 = \lim_{\tau\to\infty} +\frac{1}{6}\sum_{k_1k_2k_3k_4k_5}\frac{\Omega^{20}_{k_1k_2}\Omega^{31}_{k_3k_4k_5k_1}\Omega^{04}_{k_3k_4k_5k_2}}{E_{k_3}+E_{k_4}+E_{k_5}-E_{k_1}}\left[\frac{1-e^{-\tau\left(E_{k_1}+E_{k_2}\right)}}{E_{k_1}+E_{k_2}}-\frac{1-e^{-\tau\left(E_{k_2}+E_{k_3}+E_{k_4}+E_{k_5}\right)}}{E_{k_2}+E_{k_3}+E_{k_4}+E_{k_5}}\right] \ ,$$

$$\mathrm{P}\Omega 2.8 = \lim_{\tau\to\infty} +\frac{1}{8}\sum_{k_1k_2k_3k_4k_5k_6}\frac{\Omega^{40}_{k_1k_2k_3k_4}\Omega^{22}_{k_5k_6k_2k_3}\Omega^{04}_{k_1k_5k_6k_4}}{E_{k_5}+E_{k_6}-E_{k_2}-E_{k_3}}\left[\frac{1-e^{-\tau\left(E_{k_1}+E_{k_2}+E_{k_3}+E_{k_4}\right)}}{E_{k_1}+E_{k_2}+E_{k_3}+E_{k_4}}-\frac{1-e^{-\tau\left(E_{k_1}+E_{k_4}+E_{k_5}+E_{k_6}\right)}}{E_{k_1}+E_{k_4}+E_{k_5}+E_{k_6}}\right] \ ,$$

which reduce in the large τ limit to

$$
\begin{aligned}
\mathrm{P}\Omega 0.1 &= +\Omega^{00} \,, \\
\mathrm{P}\Omega 1.1 &= -\frac{1}{2}\sum_{k_1k_2}\frac{\Omega^{20}_{k_1k_2}\Omega^{02}_{k_1k_2}}{E_{k_1}+E_{k_2}} \,, \\
\mathrm{P}\Omega 1.2 &= -\frac{1}{4!}\sum_{k_1k_2k_3k_4}\frac{\Omega^{40}_{k_1k_2k_3k_4}\Omega^{04}_{k_1k_2k_3k_4}}{E_{k_1}+E_{k_2}+E_{k_3}+E_{k_4}} \,, \\
\mathrm{P}\Omega 2.1 &= +\sum_{k_1k_2k_3}\frac{\Omega^{20}_{k_1k_2}\breve{\Omega}^{11}_{k_3k_1}\Omega^{02}_{k_3k_2}}{(E_{k_1}+E_{k_2})\,(E_{k_2}+E_{k_3})} \,, \\
\mathrm{P}\Omega 2.2 &= +\frac{1}{4}\sum_{k_1k_2k_3k_4}\frac{\Omega^{20}_{k_1k_2}\Omega^{22}_{k_3k_4k_1k_2}\Omega^{02}_{k_3k_4}}{(E_{k_1}+E_{k_2})\,(E_{k_3}+E_{k_4})} \,, \\
\mathrm{P}\Omega 2.3 &= +\frac{1}{4}\sum_{k_1k_2k_3k_4}\frac{\Omega^{20}_{k_1k_2}\Omega^{04}_{k_1k_2k_3k_4}\Omega^{20}_{k_3k_4}}{(E_{k_1}+E_{k_2})\,(E_{k_1}+E_{k_2}+E_{k_3}+E_{k_4})} \,, \\
\mathrm{P}\Omega 2.4 &= +\frac{1}{8}\sum_{k_1k_2k_3k_4}\frac{\Omega^{40}_{k_1k_2k_3k_4}\Omega^{02}_{k_1k_4}\Omega^{02}_{k_2k_3}}{(E_{k_1}+E_{k_4})\,(E_{k_2}+E_{k_3})} \,, \\
\mathrm{P}\Omega 2.5 &= +\frac{1}{6}\sum_{k_1k_2k_3k_4k_5}\frac{\Omega^{40}_{k_1k_2k_3k_4}\Omega^{13}_{k_5k_1k_2k_3}\Omega^{02}_{k_5k_4}}{(E_{k_1}+E_{k_2}+E_{k_3}+E_{k_4})\,(E_{k_4}+E_{k_5})} \,, \\
\mathrm{P}\Omega 2.6 &= +\frac{1}{6}\sum_{k_1k_2k_3k_4k_5}\frac{\Omega^{40}_{k_1k_2k_3k_4}\Omega^{04}_{k_1k_2k_3k_5}\breve{\Omega}^{11}_{k_5k_4}}{(E_{k_1}+E_{k_2}+E_{k_3}+E_{k_4})\,(E_{k_1}+E_{k_2}+E_{k_3}+E_{k_5})} \,, \\
\mathrm{P}\Omega 2.7 &= +\frac{1}{6}\sum_{k_1k_2k_3k_4k_5}\frac{\Omega^{20}_{k_1k_2}\Omega^{31}_{k_3k_4k_5k_1}\Omega^{04}_{k_3k_4k_5k_2}}{(E_{k_1}+E_{k_2})\,(E_{k_2}+E_{k_3}+E_{k_4}+E_{k_5})} \,, \\
\mathrm{P}\Omega 2.8 &= +\frac{1}{8}\sum_{k_1k_2k_3k_4k_5k_6}\frac{\Omega^{40}_{k_1k_2k_3k_4}\Omega^{22}_{k_5k_6k_2k_3}\Omega^{04}_{k_1k_5k_6k_4}}{(E_{k_1}+E_{k_2}+E_{k_3}+E_{k_4})\,(E_{k_1}+E_{k_4}+E_{k_5}+E_{k_6})} \,.
\end{aligned}
$$

D.4. $a(\tau)$ at BMBPT(2)

Using the results of D.2 and replacing O with A, one obtains, for the diagrams contributing to $a(\tau)$,

$$\mathrm{PA0.1} = +A^{00} \ ,$$

$$\mathrm{PA1.1} = \lim_{\tau\to\infty} -\frac{1}{2}\sum_{k_1k_2}\frac{A^{20}_{k_1k_2}\Omega^{02}_{k_1k_2}}{E_{k_1}+E_{k_2}}\left[1-e^{-\tau\left(E_{k_1}+E_{k_2}\right)}\right] \ ,$$

$$\mathrm{PA1.2} = 0 \ ,$$

$$\mathrm{PA2.1} = \lim_{\tau\to\infty} +\sum_{k_1k_2k_3}\frac{A^{20}_{k_1k_2}\breve{\Omega}^{11}_{k_3k_1}\Omega^{02}_{k_3k_2}}{E_{k_3}-E_{k_1}}\left[\frac{1-e^{-\tau\left(E_{k_1}+E_{k_2}\right)}}{E_{k_1}+E_{k_2}}-\frac{1-e^{-\tau\left(E_{k_2}+E_{k_3}\right)}}{E_{k_2}+E_{k_3}}\right] \ ,$$

$$\mathrm{PA2.2} = \lim_{\tau\to\infty} +\frac{1}{4}\sum_{k_1k_2k_3k_4}\frac{A^{20}_{k_1k_2}\Omega^{22}_{k_3k_4k_1k_2}\Omega^{02}_{k_3k_4}}{E_{k_3}+E_{k_4}-E_{k_1}-E_{k_2}}\left[\frac{1-e^{-\tau\left(E_{k_1}+E_{k_2}\right)}}{E_{k_1}+E_{k_2}}-\frac{1-e^{-\tau\left(E_{k_3}+E_{k_4}\right)}}{E_{k_3}+E_{k_4}}\right] \ ,$$

$$\mathrm{PA2.3} = \lim_{\tau\to\infty} +\frac{1}{4}\sum_{k_1k_2k_3k_4}\frac{A^{20}_{k_1k_2}\Omega^{04}_{k_1k_2k_3k_4}\Omega^{20}_{k_3k_4}}{E_{k_3}+E_{k_4}}\left[\frac{1-e^{-\tau\left(E_{k_1}+E_{k_2}\right)}}{E_{k_1}+E_{k_2}}-\frac{1-e^{-\tau\left(E_{k_1}+E_{k_2}+E_{k_3}+E_{k_4}\right)}}{E_{k_1}+E_{k_2}+E_{k_3}+E_{k_4}}\right] \ ,$$

$$\mathrm{PA2.4} = 0 \ ,$$

$$\mathrm{PA2.5} = 0 \ ,$$

$$\mathrm{PA2.6} = 0 \ ,$$

$$\mathrm{PA2.7} = \lim_{\tau\to\infty} +\frac{1}{6}\sum_{k_1k_2k_3k_4k_5}\frac{A^{20}_{k_1k_2}\Omega^{31}_{k_3k_4k_5k_1}\Omega^{04}_{k_3k_4k_5k_2}}{E_{k_3}+E_{k_4}+E_{k_5}-E_{k_1}}\left[\frac{1-e^{-\tau\left(E_{k_1}+E_{k_2}\right)}}{E_{k_1}+E_{k_2}}-\frac{1-e^{-\tau\left(E_{k_2}+E_{k_3}+E_{k_4}+E_{k_5}\right)}}{E_{k_2}+E_{k_3}+E_{k_4}+E_{k_5}}\right] \ ,$$

$$\mathrm{PA2.8} = 0 \ ,$$

which reduce in the large τ limit to

$$\mathrm{PA0.1} = +A^{00} \ ,$$

$$\mathrm{PA1.1} = -\frac{1}{2}\sum_{k_1k_2}\frac{A^{20}_{k_1k_2}\Omega^{02}_{k_1k_2}}{E_{k_1}+E_{k_2}} \ ,$$

$$\mathrm{PA1.2} = 0 \ ,$$

$$\mathrm{PA2.1} = +\sum_{k_1k_2k_3}\frac{A^{20}_{k_1k_2}\breve{\Omega}^{11}_{k_3k_1}\Omega^{02}_{k_3k_2}}{(E_{k_1}+E_{k_2})\,(E_{k_2}+E_{k_3})} \ ,$$

$$\mathrm{PA2.2} = +\frac{1}{4}\sum_{k_1k_2k_3k_4}\frac{A^{20}_{k_1k_2}\Omega^{22}_{k_3k_4k_1k_2}\Omega^{02}_{k_3k_4}}{(E_{k_1}+E_{k_2})\,(E_{k_3}+E_{k_4})} \ ,$$

$$\mathrm{PA2.3} = +\frac{1}{4}\sum_{k_1k_2k_3k_4}\frac{A^{20}_{k_1k_2}\Omega^{04}_{k_1k_2k_3k_4}\Omega^{20}_{k_3k_4}}{(E_{k_1}+E_{k_2})\,(E_{k_1}+E_{k_2}+E_{k_3}+E_{k_4})} \ ,$$

$$\mathrm{PA2.4} = 0 \ ,$$

$$\mathrm{PA2.5} = 0 \ ,$$

$$\mathrm{PA2.6} = 0 \ ,$$

$$\mathrm{PA2.7} = +\frac{1}{6}\sum_{k_1k_2k_3k_4k_5}\frac{A^{20}_{k_1k_2}\Omega^{31}_{k_3k_4k_5k_1}\Omega^{04}_{k_3k_4k_5k_2}}{(E_{k_1}+E_{k_2})\,(E_{k_2}+E_{k_3}+E_{k_4}+E_{k_5})} \ ,$$

$$\mathrm{PA2.8} = 0 \ .$$

D.5. $a^2(\tau)$ at BMBPT(2)

Using the results of D.2 and replacing O with A^2, one obtains, for the diagrams contributing to $a^2(\tau)$,

$$\text{PA2 } 0.1 = +A^{2.00}_{} \ ,$$

$$\text{PA2 } 1.1 = \lim_{\tau\to\infty} -\frac{1}{2}\sum_{k_1k_2} \frac{A^{2.20}_{k_1k_2}\Omega^{02}_{k_1k_2}}{E_{k_1}+E_{k_2}}\left[1-e^{-\tau(E_{k_1}+E_{k_2})}\right] \ ,$$

$$\text{PA2 } 1.2 = \lim_{\tau\to\infty} -\frac{1}{4!}\sum_{k_1k_2k_3k_4} \frac{A^{2.40}_{k_1k_2k_3k_4}\Omega^{04}_{k_1k_2k_3k_4}}{E_{k_1}+E_{k_2}+E_{k_3}+E_{k_4}}\left[1-e^{-\tau(E_{k_1}+E_{k_2}+E_{k_3}+E_{k_4})}\right] \ ,$$

$$\text{PA2 } 2.1 = \lim_{\tau\to\infty} +\sum_{k_1k_2k_3} \frac{A^{2.20}_{k_1k_2}\breve{\Omega}^{11}_{k_3k_1}\Omega^{02}_{k_3k_2}}{E_{k_3}-E_{k_1}}\left[\frac{1-e^{-\tau\left(E_{k_1}+E_{k_2}\right)}}{E_{k_1}+E_{k_2}}-\frac{1-e^{-\tau\left(E_{k_2}+E_{k_3}\right)}}{E_{k_2}+E_{k_3}}\right] \ ,$$

$$\text{PA2 } 2.2 = \lim_{\tau\to\infty} +\frac{1}{4}\sum_{k_1k_2k_3k_4} \frac{A^{2.20}_{k_1k_2}\Omega^{22}_{k_3k_4k_1k_2}\Omega^{02}_{k_3k_4}}{E_{k_3}+E_{k_4}-E_{k_1}-E_{k_2}}\left[\frac{1-e^{-\tau\left(E_{k_1}+E_{k_2}\right)}}{E_{k_1}+E_{k_2}}-\frac{1-e^{-\tau\left(E_{k_3}+E_{k_4}\right)}}{E_{k_3}+E_{k_4}}\right] \ ,$$

$$\text{PA2 } 2.3 = \lim_{\tau\to\infty} +\frac{1}{4}\sum_{k_1k_2k_3k_4} \frac{A^{2.20}_{k_1k_2}\Omega^{04}_{k_1k_2k_3k_4}\Omega^{20}_{k_3k_4}}{E_{k_3}+E_{k_4}}\left[\frac{1-e^{-\tau\left(E_{k_1}+E_{k_2}\right)}}{E_{k_1}+E_{k_2}} -\frac{1-e^{-\tau\left(E_{k_1}+E_{k_2}+E_{k_3}+E_{k_4}\right)}}{E_{k_1}+E_{k_2}+E_{k_3}+E_{k_4}}\right] \ ,$$

$$\text{PA2 } 2.4 = \lim_{\tau\to\infty} +\frac{1}{8}\sum_{k_1k_2k_3k_4} \frac{A^{2.40}_{k_1k_2k_3k_4}\Omega^{02}_{k_1k_4}\Omega^{02}_{k_2k_3}}{\left(E_{k_1}+E_{k_4}\right)\left(E_{k_2}+E_{k_3}\right)}\left(1-e^{-\tau\left(E_{k_2}+E_{k_3}\right)}\right)\left(1-e^{-\tau\left(E_{k_1}+E_{k_4}\right)}\right) \ ,$$

$$\text{PA2 } 2.5 = \lim_{\tau\to\infty} +\frac{1}{6}\sum_{k_1k_2k_3k_4k_5} \frac{A^{2.40}_{k_1k_2k_3k_4}\Omega^{13}_{k_5k_1k_2k_3}\Omega^{02}_{k_5k_4}}{E_{k_5}-E_{k_1}-E_{k_2}-E_{k_3}}\left[\frac{1-e^{-\tau\left(E_{k_1}+E_{k_2}+E_{k_3}+E_{k_4}\right)}}{E_{k_1}+E_{k_2}+E_{k_3}+E_{k_4}} -\frac{1-e^{-\tau\left(E_{k_4}+E_{k_5}\right)}}{E_{k_4}+E_{k_5}}\right] \ ,$$

$$\text{PA2 } 2.6 = \lim_{\tau\to\infty} +\frac{1}{6}\sum_{k_1k_2k_3k_4k_5} \frac{A^{2.40}_{k_1k_2k_3k_4}\Omega^{04}_{k_1k_2k_3k_5}\breve{\Omega}^{11}_{k_5k_4}}{E_{k_5}-E_{k_4}}\left[\frac{1-e^{-\tau\left(E_{k_1}+E_{k_2}+E_{k_3}+E_{k_4}\right)}}{E_{k_1}+E_{k_2}+E_{k_3}+E_{k_4}} -\frac{1-e^{-\tau\left(E_{k_1}+E_{k_2}+E_{k_3}+E_{k_5}\right)}}{E_{k_1}+E_{k_2}+E_{k_3}+E_{k_5}}\right] \ ,$$

$$\text{PA2 } 2.7 = \lim_{\tau\to\infty} +\frac{1}{6}\sum_{k_1k_2k_3k_4k_5} \frac{A^{2.20}_{k_1k_2}\Omega^{31}_{k_3k_4k_5k_1}\Omega^{04}_{k_3k_4k_5k_2}}{E_{k_3}+E_{k_4}+E_{k_5}-E_{k_1}}\left[\frac{1-e^{-\tau\left(E_{k_1}+E_{k_2}\right)}}{E_{k_1}+E_{k_2}} -\frac{1-e^{-\tau\left(E_{k_2}+E_{k_3}+E_{k_4}+E_{k_5}\right)}}{E_{k_2}+E_{k_3}+E_{k_4}+E_{k_5}}\right] \ ,$$

$$\text{PA2 } 2.8 = \lim_{\tau\to\infty} +\frac{1}{8}\sum_{k_1k_2k_3k_4k_5k_6} \frac{A^{2.40}_{k_1k_2k_3k_4}\Omega^{22}_{k_5k_6k_2k_3}\Omega^{04}_{k_1k_5k_6k_4}}{E_{k_5}+E_{k_6}-E_{k_2}-E_{k_3}}\left[\frac{1-e^{-\tau\left(E_{k_1}+E_{k_2}+E_{k_3}+E_{k_4}\right)}}{E_{k_1}+E_{k_2}+E_{k_3}+E_{k_4}} -\frac{1-e^{-\tau\left(E_{k_1}+E_{k_4}+E_{k_5}+E_{k_6}\right)}}{E_{k_1}+E_{k_4}+E_{k_5}+E_{k_6}}\right] \ ,$$

which reduce in the large τ limit to

$$\text{PA2 } 0.1 = +A^{2.00} \ ,$$

$$\text{PA2 } 1.1 = -\frac{1}{2}\sum_{k_1k_2}\frac{A^{2.20}_{k_1k_2}\Omega^{02}_{k_1k_2}}{E_{k_1}+E_{k_2}} \ ,$$

$$\text{PA2 } 1.2 = -\frac{1}{4!}\sum_{k_1k_2k_3k_4}\frac{A^{2.40}_{k_1k_2k_3k_4}\Omega^{04}_{k_1k_2k_3k_4}}{E_{k_1}+E_{k_2}+E_{k_3}+E_{k_4}} \ ,$$

$$\text{PA2 } 2.1 = +\sum_{k_1k_2k_3}\frac{A^{2.20}_{k_1k_2}\breve{\Omega}^{11}_{k_3k_1}\Omega^{02}_{k_3k_2}}{(E_{k_1}+E_{k_2})\,(E_{k_2}+E_{k_3})} \ ,$$

$$\text{PA2 } 2.2 = +\frac{1}{4}\sum_{k_1k_2k_3k_4}\frac{A^{2.20}_{k_1k_2}\Omega^{22}_{k_3k_4k_1k_2}\Omega^{02}_{k_3k_4}}{(E_{k_1}+E_{k_2})\,(E_{k_3}+E_{k_4})} \ ,$$

$$\text{PA2 } 2.3 = +\frac{1}{4}\sum_{k_1k_2k_3k_4}\frac{A^{2.20}_{k_1k_2}\Omega^{04}_{k_1k_2k_3k_4}\Omega^{20}_{k_3k_4}}{(E_{k_1}+E_{k_2})\,(E_{k_1}+E_{k_2}+E_{k_3}+E_{k_4})} \ ,$$

$$\text{PA2 } 2.4 = +\frac{1}{8}\sum_{k_1k_2k_3k_4}\frac{A^{2.40}_{k_1k_2k_3k_4}\Omega^{02}_{k_1k_4}\Omega^{02}_{k_2k_3}}{(E_{k_1}+E_{k_4})\,(E_{k_2}+E_{k_3})} \ ,$$

$$\text{PA2 } 2.5 = +\frac{1}{6}\sum_{k_1k_2k_3k_4k_5}\frac{A^{2.40}_{k_1k_2k_3k_4}\Omega^{13}_{k_5k_1k_2k_3}\Omega^{02}_{k_5k_4}}{(E_{k_1}+E_{k_2}+E_{k_3}+E_{k_4})\,(E_{k_4}+E_{k_5})} \ ,$$

$$\text{PA2 } 2.6 = +\frac{1}{6}\sum_{k_1k_2k_3k_4k_5}\frac{A^{2.40}_{k_1k_2k_3k_4}\Omega^{04}_{k_1k_2k_3k_5}\breve{\Omega}^{11}_{k_5k_4}}{(E_{k_1}+E_{k_2}+E_{k_3}+E_{k_4})\,(E_{k_1}+E_{k_2}+E_{k_3}+E_{k_5})} \ ,$$

$$\text{PA2 } 2.7 = +\frac{1}{6}\sum_{k_1k_2k_3k_4k_5}\frac{A^{2.20}_{k_1k_2}\Omega^{31}_{k_3k_4k_5k_1}\Omega^{04}_{k_3k_4k_5k_2}}{(E_{k_1}+E_{k_2})\,(E_{k_2}+E_{k_3}+E_{k_4}+E_{k_5})} \ ,$$

$$\text{PA2 } 2.8 = +\frac{1}{8}\sum_{k_1k_2k_3k_4k_5k_6}\frac{A^{2.40}_{k_1k_2k_3k_4}\Omega^{22}_{k_5k_6k_2k_3}\Omega^{04}_{k_1k_5k_6k_4}}{(E_{k_1}+E_{k_2}+E_{k_3}+E_{k_4})\,(E_{k_1}+E_{k_4}+E_{k_5}+E_{k_6})} \ .$$

E. Coupled-cluster-like amplitudes at BMBPT(2)

The algebraic expressions of coupled-cluster-like Goldstone amplitudes defined in Eq. (2.65) and computed up to second order in BMBPT using rules detailed in Sec. 2.8 are

$$\mathcal{T}^{\dagger(1)}_{k_1k_2}(\tau) \equiv -\frac{\Omega^{02}_{k_1k_2}}{E_{k_1}+E_{k_2}}\left[1-e^{-\tau\left(E_{k_1}+E_{k_2}\right)}\right] , \tag{E.1a}$$

$$\mathcal{T}^{\dagger(1)}_{k_1k_2k_3k_4}(\tau) \equiv -\frac{\Omega^{04}_{k_1k_2k_3k_4}}{E_{k_1}+E_{k_2}+E_{k_3}+E_{k_4}}\left[1-e^{-\tau\left(E_{k_1}+E_{k_2}+E_{k_3}+E_{k_4}\right)}\right] , \tag{E.1b}$$

$$\begin{aligned}
\mathcal{T}^{\dagger(2)}_{k_1k_2}(\tau) \equiv\ & \mathcal{T}^{\dagger(1)}_{k_1k_2}(\tau) \\
& + P(k_1/k_2)\sum_{k_3}\frac{\breve{\Omega}^{11}_{k_3k_1}\Omega^{02}_{k_3k_2}}{E_{k_3}-E_{k_1}}\left[\frac{1-e^{-\tau\left(E_{k_1}+E_{k_2}\right)}}{E_{k_1}+E_{k_2}}-\frac{1-e^{-\tau\left(E_{k_2}+E_{k_3}\right)}}{E_{k_2}+E_{k_3}}\right] \\
& + \frac{1}{2}\sum_{k_3k_4}\frac{\Omega^{22}_{k_3k_4k_1k_2}\Omega^{02}_{k_3k_4}}{E_{k_3}+E_{k_4}-E_{k_1}-E_{k_2}}\left[\frac{1-e^{-\tau\left(E_{k_1}+E_{k_2}\right)}}{E_{k_1}+E_{k_2}}-\frac{1-e^{-\tau\left(E_{k_3}+E_{k_4}\right)}}{E_{k_3}+E_{k_4}}\right] \\
& + \frac{1}{2}\sum_{k_3k_4}\frac{\Omega^{04}_{k_1k_2k_3k_4}\Omega^{20}_{k_3k_4}}{E_{k_3}+E_{k_4}}\left[\frac{1-e^{-\tau\left(E_{k_1}+E_{k_2}\right)}}{E_{k_1}+E_{k_2}}-\frac{1-e^{-\tau\left(E_{k_1}+E_{k_2}+E_{k_3}+E_{k_4}\right)}}{E_{k_1}+E_{k_2}+E_{k_3}+E_{k_4}}\right] \\
& + \frac{1}{3!}P(k_1/k_2)\sum_{k_3k_4k_5}\frac{\Omega^{31}_{k_3k_4k_5k_1}\Omega^{04}_{k_3k_4k_5k_2}}{E_{k_3}+E_{k_4}+E_{k_5}-E_{k_1}}\left[\frac{1-e^{-\tau\left(E_{k_1}+E_{k_2}\right)}}{E_{k_1}+E_{k_2}}\right. \\
& \qquad \left. -\frac{1-e^{-\tau\left(E_{k_2}+E_{k_3}+E_{k_4}+E_{k_5}\right)}}{E_{k_2}+E_{k_3}+E_{k_4}+E_{k_5}}\right] ,
\end{aligned} \tag{E.1c}$$

$$
\begin{aligned}
\mathcal{T}^{\dagger(2)}_{k_1k_2k_3k_4}(\tau) \equiv\ & \mathcal{T}^{\dagger(1)}_{k_1k_2k_3k_4}(\tau) \\
& + P(k_1k_2k_3/k_4) \sum_{k_5} \frac{\Omega^{13}_{k_5k_1k_2k_3}\Omega^{02}_{k_5k_4}}{E_{k_5}-E_{k_1}-E_{k_2}-E_{k_3}} \left[\frac{1-e^{-\tau\left(E_{k_1}+E_{k_2}+E_{k_3}+E_{k_4}\right)}}{E_{k_1}+E_{k_2}+E_{k_3}+E_{k_4}} \right. \\
& \qquad \left. - \frac{1-e^{-\tau\left(E_{k_4}+E_{k_5}\right)}}{E_{k_4}+E_{k_5}} \right] \\
& + P(k_1k_2k_3/k_4) \sum_{k_5} \frac{\Omega^{04}_{k_1k_2k_3k_5}\breve{\Omega}^{11}_{k_5k_4}}{E_{k_5}-E_{k_4}} \left[\frac{1-e^{-\tau\left(E_{k_1}+E_{k_2}+E_{k_3}+E_{k_4}\right)}}{E_{k_1}+E_{k_2}+E_{k_3}+E_{k_4}} \right. \\
& \qquad \left. - \frac{1-e^{-\tau\left(E_{k_1}+E_{k_2}+E_{k_3}+E_{k_5}\right)}}{E_{k_1}+E_{k_2}+E_{k_3}+E_{k_5}} \right] \\
& + \frac{1}{2} P(k_1k_4/k_2k_3) \sum_{k_5k_6} \frac{\Omega^{22}_{k_5k_6k_2k_3}\Omega^{04}_{k_1k_5k_6k_4}}{E_{k_5}+E_{k_6}-E_{k_2}-E_{k_3}} \left[\frac{1-e^{-\tau\left(E_{k_1}+E_{k_2}+E_{k_3}+E_{k_4}\right)}}{E_{k_1}+E_{k_2}+E_{k_3}+E_{k_4}} \right. \\
& \qquad \left. - \frac{1-e^{-\tau\left(E_{k_1}+E_{k_4}+E_{k_5}+E_{k_6}\right)}}{E_{k_1}+E_{k_4}+E_{k_5}+E_{k_6}} \right] ,
\end{aligned}
\tag{E.1d}
$$

introducing permutation operators $P(\alpha\beta/\gamma\delta/\ldots)$ where the notation denotes that α, β and γ, δ are equivalent pairs, but are distinct from each other and from the remaining indices. As a result, all possible permutations among labels, except for those involving labels in the same group, are implied. The ordering of the groups within the parentheses is irrelevant, e.g. $P(\alpha\beta/\gamma\delta/\ldots) = P(\gamma\delta/\alpha\beta/\ldots)$. The permutation operators needed in Eq. (E.1) are

$$P(\alpha/\beta) \equiv 1 - P_{\alpha\beta} \ , \tag{E.2a}$$

$$P(\alpha\beta\gamma/\delta) \equiv 1 - P_{\alpha\delta} - P_{\beta\delta} - P_{\gamma\delta} \ , \tag{E.2b}$$

$$P(\alpha\beta/\gamma\delta) \equiv 1 - P_{\alpha\gamma} - P_{\alpha\delta} - P_{\beta\gamma} - P_{\beta\delta} + P_{\alpha\gamma}P_{\beta\delta} \ . \tag{E.2c}$$

These amplitudes reduce in the infinite time limit to

$$\mathcal{T}^{\dagger(1)}_{k_1k_2}(\infty) \equiv -\frac{\Omega^{02}_{k_1k_2}}{E_{k_1}+E_{k_2}} \ , \tag{E.3a}$$

$$\mathcal{T}^{\dagger(1)}_{k_1k_2k_3k_4}(\infty) \equiv -\frac{\Omega^{04}_{k_1k_2k_3k_4}}{E_{k_1}+E_{k_2}+E_{k_3}+E_{k_4}} \ , \tag{E.3b}$$

$$\begin{aligned}\mathcal{T}^{\dagger(2)}_{k_1k_2}(\infty) \equiv\ & \mathcal{T}^{\dagger(1)}_{k_1k_2}(\infty) \\ & + P(k_1/k_2)\sum_{k_3}\frac{\breve{\Omega}^{11}_{k_3k_1}\Omega^{02}_{k_3k_2}}{(E_{k_1}+E_{k_2})(E_{k_2}+E_{k_3})} \\ & + \frac{1}{2}\sum_{k_3k_4}\frac{\Omega^{22}_{k_3k_4k_1k_2}\Omega^{02}_{k_3k_4}}{(E_{k_1}+E_{k_2})\,(E_{k_3}+E_{k_4})} \\ & + \frac{1}{2}\sum_{k_3k_4}\frac{\Omega^{04}_{k_1k_2k_3k_4}\Omega^{20}_{k_3k_4}}{(E_{k_1}+E_{k_2})\,(E_{k_1}+E_{k_2}+E_{k_3}+E_{k_4})} \\ & + \frac{1}{3!}P(k_1/k_2)\sum_{k_3k_4k_5}\frac{\Omega^{31}_{k_3k_4k_5k_1}\Omega^{04}_{k_3k_4k_5k_2}}{(E_{k_1}+E_{k_2})\,(E_{k_2}+E_{k_3}+E_{k_4}+E_{k_5})} \ ,\end{aligned} \tag{E.3c}$$

$$\begin{aligned}\mathcal{T}^{\dagger(2)}_{k_1k_2k_3k_4}(\infty) \equiv\ & \mathcal{T}^{\dagger(1)}_{k_1k_2k_3k_4}(\infty) \\ & + P(k_1k_2k_3/k_4)\sum_{k_5}\frac{\Omega^{13}_{k_5k_1k_2k_3}\Omega^{02}_{k_5k_4}}{(E_{k_1}+E_{k_2}+E_{k_3}+E_{k_4})\,(E_{k_4}+E_{k_5})} \\ & + P(k_1k_2k_3/k_4)\sum_{k_5}\frac{\Omega^{04}_{k_1k_2k_3k_5}\breve{\Omega}^{11}_{k_5k_4}}{(E_{k_1}+E_{k_2}+E_{k_3}+E_{k_4})\,(E_{k_1}+E_{k_2}+E_{k_3}+E_{k_5})} \\ & + \frac{1}{2}P(k_1k_4/k_2k_3)\sum_{k_5k_6}\frac{\Omega^{22}_{k_5k_6k_2k_3}\Omega^{04}_{k_1k_5k_6k_4}}{(E_{k_1}+E_{k_2}+E_{k_3}+E_{k_4})\,(E_{k_1}+E_{k_4}+E_{k_5}+E_{k_6})} \ .\end{aligned} \tag{E.3d}$$

F. Slater determinant limit of the contributions at BMBPT(2)

Applying the relations of Sec. 2.11 to the diagrams in App. D.2, one obtains for an operator O

$$\mathrm{PO0.1} = +\sum_{i}\left[\Lambda^{O,1N}_{ii} + \frac{1}{2}\Lambda^{O,2N}_{ii} + \frac{1}{3}\Lambda^{O,3N}_{ii}\right] ,$$

$$\mathrm{PO1.1} = -\sum_{ai}\frac{\Lambda^{O}_{ai}h_{ia}}{\epsilon^{a}_{i}} ,$$

$$\mathrm{PO1.2} = -\frac{1}{4}\sum_{abij}\frac{\Theta^{O}_{abji}\Theta^{\Omega}_{jiab}}{\epsilon^{ab}_{ij}} ,$$

$$\mathrm{PO2.1} = +\sum_{aij}\frac{\Lambda^{O}_{ai}h_{ij}h_{ja}}{\epsilon^{a}_{i}\epsilon^{a}_{j}} - \sum_{abi}\frac{\Lambda^{O}_{ai}h_{ba}h_{ib}}{\epsilon^{a}_{i}\epsilon^{b}_{i}} ,$$

$$\mathrm{PO2.2} = -\sum_{abij}\frac{\Lambda^{O}_{ai}\Theta^{\Omega}_{biaj}h_{jb}}{\epsilon^{a}_{i}\epsilon^{b}_{j}} ,$$

$$\mathrm{PO2.3} = -\sum_{abij}\frac{\Lambda^{O}_{ai}\Theta^{\Omega}_{jiab}h_{bj}}{\epsilon^{a}_{i}\epsilon^{ab}_{ij}} ,$$

$$\mathrm{PO2.4} = +\frac{1}{2}\sum_{abij}\frac{\Theta^{O}_{abij}h_{ia}h_{jb}}{\epsilon^{a}_{i}\epsilon^{b}_{j}} ,$$

$$\mathrm{PO2.5} = +\frac{1}{2}\left[\sum_{abijk}\frac{\Theta^{O}_{baji}\Theta^{\Omega}_{jiak}h_{kb}}{\epsilon^{ab}_{ij}\epsilon^{b}_{k}} + \sum_{abcij}\frac{\Theta^{O}_{abji}\Theta^{\Omega}_{ciab}h_{jc}}{\epsilon^{ab}_{ij}\epsilon^{c}_{j}}\right] ,$$

$$\mathrm{PO2.6} = +\frac{1}{2}\left[\sum_{abcij}\frac{\Theta^{O}_{abji}\Theta^{\Omega}_{jiac}h_{cb}}{\epsilon^{ab}_{ij}\epsilon^{ac}_{ij}} - \sum_{abijk}\frac{\Theta^{O}_{abji}\Theta^{\Omega}_{kiab}h_{jk}}{\epsilon^{ab}_{ij}\epsilon^{ab}_{ik}}\right] ,$$

$$\mathrm{PO2.7} = -\frac{1}{2}\left[\sum_{abijk}\frac{\Lambda^{O}_{ai}\Theta^{\Omega}_{bikj}\Theta^{\Omega}_{kjba}}{\epsilon^{a}_{i}\epsilon^{ab}_{jk}} - \sum_{abcij}\frac{\Lambda^{O}_{ai}\Theta^{\Omega}_{cbja}\Theta^{\Omega}_{ijbc}}{\epsilon^{a}_{i}\epsilon^{bc}_{ij}}\right] ,$$

$$\mathrm{PO2.8} = +\frac{1}{8}\sum_{abcdij}\frac{\Theta^{O}_{abji}\Theta^{\Omega}_{cdab}\Theta^{\Omega}_{jicd}}{\epsilon^{ab}_{ij}\epsilon^{cd}_{ij}} + \frac{1}{8}\sum_{abijkl}\frac{\Theta^{O}_{abji}\Theta^{\Omega}_{ijkl}\Theta^{\Omega}_{lkab}}{\epsilon^{ab}_{ij}\epsilon^{ab}_{kl}} + \sum_{abcijk}\frac{\Theta^{O}_{abji}\Theta^{\Omega}_{cjbk}\Theta^{\Omega}_{ikac}}{\epsilon^{ab}_{ij}\epsilon^{ac}_{ik}} ,$$

where matrix elements with upper index O have to be adapted to the operator of interest, while those with upper index Ω can be taken from App. C.2. Let it be noticed that in the Slater determinant limit, every BMBPT diagram conserves the number of particles.

For instance, one obtains for the grand potential diagrams, i.e. when replacing O with the

potential Ω without pairing, and with one- and two-body forces only

$$
\begin{aligned}
\mathrm{P}\Omega 0.1 &= +\sum_i \left[t_{ii} - \lambda + \frac{1}{2}\sum_j \bar{v}_{ijij} \right] \ , \\
\mathrm{P}\Omega 1.1 &= -\sum_{ai} \frac{h'_{ai}h'_{ia}}{\epsilon_i^a} \ , \\
\mathrm{P}\Omega 1.2 &= -\frac{1}{4}\sum_{abij} \frac{\bar{v}_{abji}\bar{v}_{jiab}}{\epsilon_{ij}^{ab}} \ , \\
\mathrm{P}\Omega 2.1 &= +\sum_{aij} \frac{h'_{ai}h'_{ij}h'_{ja}}{\epsilon_i^a\epsilon_j^a} - \sum_{abi} \frac{h'_{ai}h'_{ba}h'_{ib}}{\epsilon_i^a\epsilon_i^b} \ , \\
\mathrm{P}\Omega 2.2 &= -\sum_{abij} \frac{h'_{ai}\bar{v}_{biaj}h'_{jb}}{\epsilon_i^a\epsilon_j^b} \ , \\
\mathrm{P}\Omega 2.3 &= -\sum_{abij} \frac{h'_{ai}\bar{v}_{jiab}h'_{bj}}{\epsilon_i^a\epsilon_{ij}^{ab}} \ , \\
\mathrm{P}\Omega 2.4 &= +\frac{1}{2}\sum_{abij} \frac{\bar{v}_{abij}h'_{ia}h'_{jb}}{\epsilon_i^a\epsilon_j^b} = +\sum_{abij} \frac{\bar{v}_{abij}h'_{ia}h'_{jb}}{\epsilon_i^a\epsilon_{ij}^{ab}} \ , \\
\mathrm{P}\Omega 2.5 &= +\frac{1}{2}\left[\sum_{abijk} \frac{\bar{v}_{baji}\bar{v}_{jiak}h'_{kb}}{\epsilon_{ij}^{ab}\epsilon_k^b} + \sum_{abcij} \frac{\bar{v}_{abji}\bar{v}_{ciab}h'_{jc}}{\epsilon_{ij}^{ab}\epsilon_j^c} \right] \ , \\
\mathrm{P}\Omega 2.6 &= +\frac{1}{2}\left[\sum_{abcij} \frac{\bar{v}_{abji}\bar{v}_{jiac}h'_{cb}}{\epsilon_{ij}^{ab}\epsilon_{ij}^{ac}} - \sum_{abijk} \frac{\bar{v}_{abji}\bar{v}_{kiab}h'_{jk}}{\epsilon_{ij}^{ab}\epsilon_{ik}^{ab}} \right] \ , \\
\mathrm{P}\Omega 2.7 &= -\frac{1}{2}\left[\sum_{abijk} \frac{h'_{ai}\bar{v}_{bikj}\bar{v}_{kjba}}{\epsilon_i^a\epsilon_{jk}^{ab}} - \sum_{abcij} \frac{h'_{ai}\bar{v}_{cbja}\bar{v}_{ijbc}}{\epsilon_i^a\epsilon_{ij}^{bc}} \right] \ , \\
\mathrm{P}\Omega 2.8 &= +\frac{1}{8}\sum_{abcdij} \frac{\bar{v}_{abji}\bar{v}_{cdab}\bar{v}_{jicd}}{\epsilon_{ij}^{ab}\epsilon_{ij}^{cd}} + \frac{1}{8}\sum_{abijkl} \frac{\bar{v}_{abji}\bar{v}_{ijkl}\bar{v}_{lkab}}{\epsilon_{ij}^{ab}\epsilon_{kl}^{ab}} + \sum_{abcijk} \frac{\bar{v}_{abji}\bar{v}_{cjbk}\bar{v}_{ikac}}{\epsilon_{ij}^{ab}\epsilon_{ik}^{ac}} \ ,
\end{aligned}
$$

where $h'_{pq} \equiv h_{pq} - \epsilon_p\delta_{pq}$. For the BMBPT diagram labelled PΩ2.4, recovering the MBPT expression actually necessitates the use of relation

$$
\frac{1}{\epsilon_i^a\epsilon_{ij}^{ab}} + \frac{1}{\epsilon_j^b\epsilon_{ij}^{ab}} = \frac{1}{\epsilon_i^a\epsilon_j^b} \ , \tag{F.1}
$$

and relabelling of the indices, thus linking the symmetric structure of the BMBPT Feynman diagram with the non-symmetric one of the MBPT Goldstone diagram and explaining the change in the symmetry factor.

G. Structure of the *ADG* program

The previously described methodology has been implemented to build a *Python 2.7* program called `ADG` for `Automatic Diagram Generator`. This program uses the external Python packages *NumPy* for matrix-related operations and *NetworkX* for producing and manipulating diagrams. Python allows us to develop an easy-to-use, low-maintenance program without having to tamper directly with low-level concepts such as memory allocation. The wide ecosystem of open-source packages available helps focus on physics-related parts of the code. Furthermore, the possibility to use object-oriented programming has proven useful to design a program that could easily be extended to a various range of many-body diagrammatic theories. For readability and maintainability purposes, the program has been separated into different modules, the functions of which are detailed below.

G.1. Main script

The main function, contained in file *main.py*, organizes the whole program and makes use of the other modules when needed. The function first parses the command-line options enterred by the user, asking them for keyboard input if needed. The calling options comprises the theory being used, the two- or three-body operator character of the operators as well as other features regarding output formatting.

The function is designed to be as theory-agnostic as possible, calling for wrapper functions defined in the *run* module to generate the appropriate adjacency matrices, which are then recasted as *NumPy* matrices and fed to *NetworkX* to produce graphs that are then used to initialize the actual *Diagram* objects that the program uses. A few tests are applied to make sure only appropriate matrices are kept (corresponding to connected graphs, etc.) before MBPT or BMBPT diagrams are produced, which encapsulate the *NetworkX* graph as well as other related properties stored as attributes (two- or three-body character, various tags, degrees of the vertices,...).

Checks for topologically identical diagrams are then performed. As this part of the program scales factorially with the number of diagrams considered, it constitutes the more time-costly part of the program when going to higher orders. Especially, the `is_isomorphic` interface of *NetworkX* is itself time-costly as it performs permutations between the graph nodes. Consequently, the algorithm has been optimize to call it as rarely as possible. Diagrams are therefore first selected based on their two- or three-body character and Hartree-Fock or non-Hartree-Fock status, such that comparisons are done within a smaller set of diagrams. Additionally, checks on the set of in- and out-degrees of the vertices of the two graphs are made, leaving the need for a call to `is_isomorphic` to the fewest possible cases.

Once only topologically distinct diagrams are kept, the program extracts the expressions associated to the diagrams depending of the formalism involved, and stores them as attributes

of the diagram objects.

Finally, output LaTeX files are produced, the exact content and formatting of which depend on user's input. Computer-readable files are available as well for MBPT diagrams. Compilation of the main LaTeX file is then proposed to the user, and useless files produced by the program and the LaTeX compilation are deleted before exiting.

G.2. Run management module

The *run.py* file contains routines related to run management, command-line interface and managing the code output.

G.2.1. Routines

The routines of the module are:

- `parse_command_line` sets up the calculation depending on the used command-line flags.
- `interactive_interface` sets up the calculation using keyboard input when `ADG` has been called with the flag `-i`.
- `attribute_directory` creates the appropriate folder for the output of the program, depending of the theory, order and other options.
- `generate_diagrams` is used as a wrapper for the different class-dependent diagram creation routines.
- `order_diagrams` is used as a wrapper for the different class-dependent diagram ordering routines.
- `print_diags_numbers` prints out information about the produced diagram on the terminal.
- `prepare_drawing_instructions` launches the production of graph-related drawing instructions.
- `create_feynmanmp_files` then stores the instructions in an appropriately-labelled text file.
- `write_file_header` takes care of writing the beginning of the LaTeX output file with the appropriate formatting options.
- `compile_manager` takes care of compiling the LaTeX file with PDFLaTeX.
- `clean_folders` then deletes the auxiliary files that are no longer needed.

G.3. Generic diagram module

The *diag.py* file contains various routines for diagrams that can be used regardless of the theory of interest, i.e., tests on the degree of vertices in a matrix, tests for topologically identical diagrams, or routines used to label the vertices and propagators of a diagram. It also contains the routines that are used to produce the FeynMP instructions starting from a *NetworkX* graph and various routines used for the production of the LaTeX output files. Finally, it contains the definition of a `Diagram` abstract class that is inherited by the classes associated to MBPT and BMBPT diagrams.

G.3.1. Routines

Let us now describe briefly the different routines of the module:

- `no_trace` takes as input a list of matrices and returns it without any matrix with a non-zero diagonal matrix element.
- `check_vertex_degree` checks the degree of a specific vertex. It is used during the matrix generation to remove ill-defined matrices.
- `topologically_distinct_diagrams` checks a list of `Diagram` objects and removes the topologically equivalent ones.
- `label_vertices` is used to attribute labels to the nodes in a *NetworkX* graph depending on their general operator or grand canonical potential character.
- `feynmf_generator` is the routine used to generate the *FeynMP* drawing instructions starting from a *NetworkX* graph.
- `propagator_style` selects the appropriate drawing instructions for propagators.
- `draw_diagram` recovers the drawing instructions of a given diagram and copies them in the LaTeX file.
- `to_skeleton` returns only the non-redundant links in a diagram, i.e., only the minimal set of edges to infer the time relations. It is mostly used for time-structure diagrams, though its scope could be more general.
- `extract_denom` returns the appropriate denominator for a diagram using the subgraph rule.
- `print_adj_matrices` prints a computer-readable file with the adjacency matrices of the diagrams.

G.3.2. `Diagram` class

The `Diagram` class is used to describe a general diagram and comprises the following attributes:

- `graph`, the *NetworkX* graph associated to the diagram.
- `unsort_degrees`, a tuple with the graph vertex degrees.
- `degrees`, a sorted tuple with the degrees of the graph's vertices.
- `unsort_io_degrees`, a tuple with the in- and out-degrees of the vertices.
- `io_degrees`, that correspond to a sorted version of `unsort_io_degrees`.
- `max_degree`, the highest vertex degree in the graph.
- `tags`, a list of integers associated with the graph to keep track of topologically identical diagrams.
- `adjacency_mat`, a *NumPy* array with the adjacency matrix of the graph.

The `Diagram` class has two methods described below:

- `__init__` takes as input a *NetworkX* graph that it stores in `graph` and uses to initialize the other attributes.
- `write_graph`, an abstract method for drawing the graph using *FeynMP* instructions.

G.4. MBPT module

This *mbpt.py* file contains the routines that are related to MBPT diagrams, be it the generation of the adjacency matrices associated to them or the treatment of the MBPT expressions, as well as producing a computer-readable output suitable for automated calculation frameworks [169]. It also contains the `MbptDiagram` class that inherits from the `Diagram` class defined in the *diag* module.

G.4.1. Routines

Let us now describe briefly the different routines of the module:

- `diagrams_generation` produces all the adjacency matrices associated to MBPT diagrams of a given order.
- `write_diag_exp` writes the expression associated to a diagram in the LaTeX file.
- `write_header` writes the appropriate header for the LaTeX output file.
- `print_cd_output` prints a computer-readable output file.
- `order_diagrams` order the diagrams depending on their excitation level.

- `attribute_conjugate` searches for the conjugate partner of a diagram in the list of all diagrams.
- `extract_cd_denom` extracts the denominator of the graph and writes it in a computer-readable format.

G.4.2. `MbptDiagram` class

Additionnally to the attributes defined in the class `Diagram`, the class `MbptDiagram` possesses the following attributes:

- `incidence`, a *NumPy* array with the incidence matrix of the graph.
- `excitation_level`, an integer coding for the single, double, etc., character of the diagram.
- `complex_conjugate`, the tag of the conjugate partner of the diagram.
- `expr` a string that stores the expression associated to a diagram.
- `cd_expr`, the expression associated to the graph in a computer-readable format.

The methods of the `MbptDiagram` class are described below:

- Its constructor `__init__` calls the `Diagram` class constructor and additionnaly inializes the diagram `tags` before calling `attribute_expressions`.
- `attribute_expression` is used to generate the expression associated with the MBPT diagram and stores it in its attribute `expr`.
- `calc_excitation` returns the integer associated with the excitation level of the diagram.
- `count_hole_lines` returns the number of hole lines in the graph.
- `is_complex_conjug_of` returns True if a diagram is the complex conjugate diagram of the object.
- `attribute_ph_labels` attributes the appropriate particle or hole label to the lines of the diagram.
- `extract_denominator` returns a string with the denominator associated to the diagram.
- `cd_denominator` returns a string with the denominator associated to the graph in a computer-readable format.
- `extract_numerator` returns the numerator associated to the diagram.
- `cd_numerator` returns the numerator associated to the diagram in a computer-readable format.
- `loops_number` returns the number of loops in the diagram, using a specific convention for reading its representation.
- `write_section` writes the information associated to the graph in the LaTeX output file.

G.5. BMBPT module

The `bmbpt.py` file contains the routines related to BMBPT diagrams: generation of the associated adjacency matrices, some on-the-fly tests for this generation, tests used to characterize the BMBPT diagrams with respect to their two- or three-body operator or Hartree-Fock character, different routines for the extraction of the associated numerators, denominators and different symmetry factors, and finally routines used to format the output files. This module also defines a `BmbptFeynmanDiagram` class, similar to the `MbptDiagram` one.

G.5.1. Routines

Let us now describe briefly the different routines of the module:

- `diagrams_generation` generates all the adjacency matrices associated to BMBPT diagrams of a given order.
- `check_unconnected_spawn` is used by `BMBPT_generation` to avoid producing matrices that would in the end correspond to unconnected diagrams.
- `write_header` takes care of the appropriate formatting of the output LaTeX file in the case `ADG` has been called for BMBPT.
- `produce_expressions` produces and stores the expressions associated to the BMBPT diagrams.
- `order_diagrams` order the diagrams depending on their use of two- or three-body forces and their Hartree-Fock character, and discard topologically equivalent diagrams.

G.5.2. `BmbptFeynmanDiagram` class

Additionnally to the attributes defined in the class `Diagram`, the class `BmbptFeynmanDiagram` possesses the following attributes:

- `two_or_three_body` that stores as an integer the two-body-only or three-body character of the operators comprised in the diagram.
- `time_tag` is an integer that keep track of the associated time-structure diagram.
- `tsd_is_tree` is set to True if the associated TSD has a tree structure, False if it has not.
- `feynman_exp`, a string that stores the time-dependent expression associated to a diagram.
- `diag_exp`, a string that stores the time-independent expression associated to a diagram.
- `vert_exp`, a list of strings that stores the expressions associated to each vertex.
- `hf_type`, a string that says if a diagram is of Hartree-Fock character, Hartree-Fock if the generic operator is replaced by the grand canonical potential, or non-Hartree-Fock.

The `BmbptFeynmanDiagram` class has fifteen methods described below:

- Its constructor `__init__` calls the `Diagram` class constructor and initializes the other attributes.
- `attribute_expressions` is used to generate the time-dependent and time-independent expressions associated with the BMBPT diagram and stores it in its attributes `feynman_exp` and `diag_exp`.
- `vertex_expression` returns the expression associated to a given vertex of the BMBPT diagram.
- `write_graph` writes the graph and its associated TSD to the LaTeX file.
- `write_tsd_info` writes information relative to the TSD associated to the diagram in the output file.
- `write_section` writes sections and subsections in the output file.
- `write_vertices_values` writes the quasiparticle energies associated to each vertex of the graph in the output file.
- `write_diag_exps` writes the expressions associated to a diagram in the LaTeX file.
- `vertex_exchange_sym_factor` returns the symmetry factor associated with vertex exchange.
- `extract_integral` returns as a string the integral part of the Feynman expression of the graph.
- `attribute_qp_labels` is used to attribute the appropriate quasiparticle label to the edges of the *NetworkX* graph.
- `extract_numerator` returns as a string the numerator associated to the graph.
- `has_crossing_sign` returns True if there is a minus sign associated with crossing propagators in the graph.
- `multiplicity_symmetry_factor` returns the symmetry factor associated with propagators multiplicity.
- `time_tree_denominator` returns as a string the time-integrated denominator associated to a BMBPT graph that has a tree time-structure.

G.6. TSD module

Finally, the *tsd.py* file contains routines related to time-structure diagrams (TSDs). Though designed specifically for TSDs related to BMBPT diagrams, it could be extended to encompass other types of TSDs. The various routines this module contains deal with the production of a TSD diagram out of a BMBPT diagram, different tests on BMBPT diagrams with respect to their associated TSD, extraction of the denominator resulting from the time integration

associated with the TSD, and production of the corresponding section of the output file, including the drawing of the TSD. Finally, it contains a `TimeStructureDiagram` class that inherits from the `Diagram` class, with its constructor that generates a TSD starting from a BMBPT diagram.

G.6.1. Routines

Let us now describe briefly the different routines of the module:

- `time_structure_graph` returns the time-structure graph associated to a BMBPT graph.
- `tree_time_structure_den` returns the denominator associated to a tree time-structure graph.
- `equivalent_labelled_TSDs` returns the list of labelled TSDs corresponding to the equivalent tree TSDs of a previously given non-tree TSD.
- `write_section` takes care of the proper formatting of the section devoted to TSDs in the output LaTeX file.
- `disentangle_cycle` is used by `treat_cycle` to separate a cycle in a sum of trees.
- `find_cycle` returns the start and end nodes of an elementary cycle and is called by `disentangle_cycle`.
- `treat_tsds` orders the TSDs, produces their expressions and returns the number of tree TSDs.

G.6.2. `TimeStructureDiagram` class

Additionnally to the attributes defined in the class `Diagram`, the class `TimeStructureDiagram` possesses the following attributes:

- `perms`, a dictionnary of permutations necessary for the treatment of expressions for topologically equivalent TSDs.
- `equivalent_trees`, a list of integers to keep track of the topologically equivalent TSDs.
- `is_tree`, set to True if the TSD is a tree, False if it not.
- `expr`, a string to store the denominator associated with the TSD.
- `resum`, the resummation power of the tree TSD stored has an integer.

The `TimeStructureDiagram` class has four methods described below:

- Its constructor `__init__` calls the `Diagram` class constructor and then initializes the other attributes.
- `treat_cycles` finds and treat the cycles in a non-tree TSD.

- `draw_equivalent_tree_tsds` draws the equivalent tree TSDs of a given non-tree TSD.
- `resummation_power` returns the resummation power associated to a tree TSD.

H. Résumé

Plus de quarante ans après la remise du prix Nobel à Bohr, Mottelson et Rainwater, la physique nucléaire reste à bien des égards un champ de recherche actif au sein duquel de nombreux changements se sont opérés ces quinze dernières années. Du fait de la complexité du noyau atomique, depuis la description des propriétés liées à son état fondamental (masse, rayon...) jusqu'à son comportement lors de réactions (diffusion, fission...), de son caractère mésoscopique interdisant à la fois traitement statistique et méthode exacte dans la plupart des cas, et d'une interaction nucléaire encore appréhendée avec difficulté, aucun modèle n'a su s'ériger en modèle standard de la physique nucléaire. Si le modèle de la goutte liquide se montre suffisant pour la plupart des applications civiles comme militaires, une description fine de l'ensemble des propriétés du noyau reste hors d'atteinte dans ce cadre. Diverses approches théoriques ont donc été développées pour parer à cet inconvénient. Si le modèle en couche et les fonctionnelles énergie de la densité se sont imposés par leur capacité à reproduire les résultats expérimentaux, l'impossibilité de les améliorer de manière systématique conduit à une approche de type essai-erreur et à une multiplication des modèles. A l'opposé, les méthodes de type *ab initio* ont été conçues avec l'idée d'améliorabilité systématique au cœur de leur approche, mais ont longtemps été limitées au secteur A$\sim$ 12 en raison de temps de calcul factoriels ou exponentiels.

Les années 2000 ont toutefois bouleversé cet état de fait, avec le développement concomitants d'hamiltoniens issus de la théorie effective des champs chirale, de méthodes *ab initio* dont le temps de calcul croît polynomialement avec le nombre de particules ainsi que la possibilité d'effectuer un pré-traitement de l'hamiltonien pour réduire le temps de calcul final, via notamment le groupe de renormalisation de similarité. Ces progrès simultanés dans la modélisation de l'hamiltonien, les méthodes à N corps et les méthodes de calculs ont permis l'extension rapide du domaine des méthodes *ab initio* aux noyaux de masse moyenne jusqu'à A$\sim$ 100. En particulier, des extensions de ces méthodes polynomiales ont permis l'accès aux noyaux à simple couche ouverte.

Une des particularités des méthodes polynomiales précédemment citées est qu'elles sont non-perturbatives, au sens où elles resomment des classes infinies de diagrammes obtenus par l'emploi de la théorie de perturbation. L'usage de la théorie de perturbation à N corps (MBPT) avait été abandonné plusieurs décennies plus tôt pour son incapacité à traiter convenablement l'hamiltonien nucléaire. Or, le développement des méthodes de pré-traitement de l'hamiltonien a rendu à nouveau possible l'emploi de MBPT pour les noyaux à couche fermée, obtenant des résultats similaires à ceux des méthodes non perturbatives pour une fraction du temps de calcul. Pour pouvoir étendre cette approche aux noyaux à couche ouverte en conservant la simplicité d'une approche à simple référence comme MBPT, il était nécessaire de développer une théorie de perturbation à N corps brisant des symétries, en particulier la symétrie associée au nombre de particules dans le cas des noyaux à simple couche ouverte. Ce sont ce travail de développement et son application ultérieure qui sont détaillés dans le présent document.

Le Chapitre 1 détaille les ingrédients nécessaires à l'établissement du formalisme de la

théorie de perturbation à N corps de Bogolioubov (BMBPT), à commencer par l'hamiltonien à trois corps dont les éléments de matrice ont été antisymétrisés. Le formalisme repose sur l'usage de la notion de brisure de symétrie afin d'incorporer les corrélations traditionnellement associées au phénomène de superfluidité au sein du noyau. La brisure de la symétrie $U(1)$, associée à la conservation du nombre de particule, est discutée en détail. On introduit ensuite les opérateurs associés à l'algèbre de Bogolioubov, en particulier les opérateurs de création et d'annihilation de quasiparticules, obtenus par transformation unitaire des opérateurs de création et d'annihilation de particules. L'opérateur d'évolution, qui permet d'obtenir les états évolués en temps imaginaire est ensuite introduit, ainsi que les étapes permettant de développer les kernels d'opérateurs. Enfin, les différents opérateurs d'intérêt sont réexprimés dans la base des opérateurs de création et d'annihilation de quasiparticules, en ordre normal vis-à-vis de l'état de référence, permettant une écriture plus compacte du formalisme par la suite. La représentation diagrammatique d'un opérateur exprimé en ordre normal dans la base des opérateurs de quasiparticule est introduite pour clore ce chapitre.

Le Chapitre 2 introduit le formalisme de la théorie de perturbation à N corps de Bogolioubov à proprement parler. Le potentiel grand-canonique Ω, qui permet de résoudre l'équation de Schrödinger en exerçant une contrainte sur le nombre de particule du système, est partitionné en une partie non perturbée Ω_0 et une partie résiduelle Ω_1, de telle sorte que ces deux parties de l'opérateur ne commutent pas avec l'opérateur A associé au nombre de particules. La résolution de l'équation de Schrödinger à N corps pour Ω_0 et l'état de référence $|\Phi\rangle$ permet d'obtenir les énergies associées aux différents états de la base de quasiparticule. Le cas particulier où l'état de référence est solution des équations Hartree-Fock-Bogolioubov est ensuite discuté en détails. Un tel choix de vide de référence conduit naturellement à l'annulation de certaines composantes du potentiel grand-canonique et à une simplification du formalisme. Les propagateurs de quasiparticules sont ensuite présentés, et l'opérateur d'évolution est ensuite réexprimé en fonction des parties non-perturbative et résiduelle du potentiel grand-canonique.

Tous les éléments nécessaires étant désormais disponibles, les kernels d'opérateur peuvent être développés en perturbation. Les corrections en perturbation au premier et au second ordre sont dérivées pour le kernel de norme comme pour un kernel d'opérateur générique. La possibilité de refactoriser les diagrammes et obtenir directement l'expression d'une observable associée à un opérateur à partir du développement de son kernel réduit connecté est établie. En particulier, l'étude détaillée des contributions analytiques obtenues en appliquant le théorème de Wick conduit à la formulation des règles nécessaires à la génération et à l'évaluation des diagrammes BMBPT.

Différents sujets sont ensuite développés. Le caractère réel ou complexe des diagrammes obtenus est discuté en détails ainsi que la méthode pour obtenir l'observable, réelle par nature, à partir des diagrammes BMBPT. Le lien entre théorie de perturbation à N corps de Bogolioubov et théorie du cluster couplé de Bogolioubov est ensuite abordé, et les approximations des amplitudes de cluster au premier et au deuxième ordre en perturbation sont obtenues. La contrainte à exercer pour maintenir le nombre de particules moyen du système ainsi que la mesure de la variance du nombre de particules sont ensuite discutées. Pour finir, il est vérifié que les résultats de la théorie de perturbation à N corps de Bogolioubov correspondent aux résultats de la théorie de perturbation à N corps standard dans le cas d'un système à couche fermée, ce qui est une propriété du formalisme par construction.

Une fois le formalisme de la théorie de perturbation à N corps de Bogolioubov établi et

appliqué au premier et au second ordre, reste la question de son application à des ordres plus élevés. Par nature, les méthodes à N corps dites *ab initio* sont construites pour se rapprocher ordre par ordre de la solution exacte, et donc être applicables à l'ordre le plus élevé possible. Le cas des théories de perturbation est particulier parmi elles, car aucun théorème n'assure la convergence de la série vers la solution exacte de l'équation de Schrödinger à N corps. Il est donc nécessaire de vérifier *a posteriori* cette convergence en effectuant des calculs ordre par ordre. Par ailleurs, l'obtention de résultats BMBPT à des ordres supérieurs permettrait également l'incorporation d'effets physiques liés aux excitations triples et quadruples de quasiparticules.

Or, l'utilisation à des ordres plus élevés de BMBPT se heurte à une double difficulté. La première est celle de la génération de l'ensemble des diagrammes BMBPT à un ordre donné, liée à la difficulté à capturer l'ensemble des topologies de diagrammes possibles. La seconde est celle de l'évaluation de ces diagrammes. A chaque diagramme d'ordre p est en effet associé une intégrale en temps p-tuple, et la difficulté associée à la résolution de cette intégrale va donc croissante avec l'ordre de perturbation.

Le chapitre 3 est consacré à la mise en place d'outils automatisés permettant de résoudre cette double difficulté. La première partie est consacrée à l'usage des matrices d'adjacence, objets issus de la théorie des graphes, pour générer l'ensemble des diagrammes BMBPT possibles à un certain ordre. Les règles diagrammatiques discutées au sein du chapitre 2 sont traduites en termes de contraintes à exercer sur la forme des matrices d'adjacence, et les grands principes des algorithmes de génération des matrices sont discutés en détails, ainsi que la traduction des matrices en instructions de dessin des diagrammes.

La seconde partie est consacrée à la formulation et à l'étude des propriétés des diagrammes de structure en temps (TSD). Ces objets sont introduits comme représentation graphique de l'intégrale p-tuple en temps associée à un diagramme BMBPT d'ordre p, c'est-à-dire une représentation graphique des liens d'ordonnancement en temps entre les différents vertex. Une étude approfondie des propriétés de ces TSD permet de démontrer récursivement les règles diagrammatiques permettant l'extraction de l'expression intégrée en temps associée à un diagramme BMBPT. En particulier, la règle diagrammatique utilisée pour les diagrammes BMBPT dépendants du temps apparaît comme la généralisation de la règle diagrammatique de Goldstone utilisée pour les diagrammatiques indépendantes du temps.

La partie suivante est consacrée à mettre en perspective formalismes dépendant et indépendant du temps et leur diagrammatique associée. Il apparaît que la théorie de perturbation à N corps de Bogolioubov présente un cas particulièrement favorable, l'usage combiné d'un formalisme exprimé en termes de quasiparticules et d'une diagrammatique dépendante du temps conduisant à une réduction importante du nombre de diagrammes apparaissant à chaque ordre de la théorie et donc du nombre de diagrammes à implémenter dans un code de calcul numérique. La capacité d'un diagramme BMBPT dépendant du temps à resommer les contributions associées à plusieurs diagrammes BMBPT indépendants du temps est en particulier étudiée en détails.

Les deux innovations permettant la génération et l'évaluation des diagrammes BMBPT à un ordre quelconque ont été implémentées au sein d'un programme informatique appelé ADG pour Automated Diagram Generator, rédigé en Python 2 et rendu disponible sous licence libre GPLv3. La présentation de ce programme, de son installation et de son utilisation constituent la dernière section du chapitre 3.

Le chapitre 4 présente ensuite les premiers résultats numériques obtenus pour BMBPT après un travail collectif d'implémentation des diagrammes BMBPT du premier et du deuxième

ordre et appliqué aux chaînes isotopiques de l'oxygène, du calcium et du nickel. L'étude de l'évolution ordre par ordre de l'énergie de l'état fondamental et de l'énergie de séparation à deux neutrons obtenus par BMBPT montre que la plupart des corrélations sont capturées par BMBPT dès le premier ordre, les corrections au deuxième ordre étant plus faibles d'un ordre de grandeur pour l'énergie de l'état fondamental. Des telles signes de convergence de la série perturbative devront être confirmées par des calculs BMBPT menés à des ordres plus élevés.

Les résultats au premier ordre sont ensuite comparés à ceux obtenus pour un ensemble de méthodes *ab initio* non perturbatives, correspondant à l'état de l'art pour les noyaux de masse moyenne. Les résultats obtenus pour BMBPT sont très proches de ceux obtenus pour les autres méthodes, en particulier pour le modèle en couche sans cœur avec troncature en importance, méthode quasi-exacte, pour les isotopes de l'oxygène. Ce constat reste vrai pour les isotopes du calcium et du nickel, où l'écart aux résultats expérimentaux est lié à l'Hamiltonien. De tels résultats font de BMPBT la méthode *ab initio* qui présente le meilleur ratio exactitude / temps de calcul.

Enfin, les temps de calcul pour BMBPT sont comparés à ceux de méthodes non-perturbatives pour les chaînes de l'oxygène, du calcium, du nickel et de l'étain. L'indépendance du temps de calcul par rapport au nombre de masse du système est vérifié, celui-ci étant fixé par la taille de la base de quasiparticules. Par ailleurs, les temps de calculs pour BMBPT au premier ordre sont deux ordres de magnitude inférieurs à ceux des autres méthodes pour l'ensemble de ces systèmes. Une réduction du temps de calcul est constatée pour les systèmes à double couche fermée, liée à l'annulation de certaines composantes des équations sans utilisation de méthode d'optimisation dédiée.

Cette combinaison de résultats en accord avec des méthodes *ab initio* non perturbatives et de temps de calculs deux ordres de magnitudes inférieurs établit BMBPT comme une méthode de choix pour des études des noyaux à couche ouverte à grande échelle, qu'il s'agisse de prédire ou post-dire des propriétés expérimentales de ces noyaux ou bien de tester de nouveaux Hamiltoniens nucléaires, issus par exemple de théorie effective des champs chirale.

Les annexes rassemblent ensuite divers document utiles à la compréhension du manuscrit : identités employées pour la résolution des intégrales en temps, définitions de théorie des graphes, éléments de matrice d'opérateurs en produit normal, contributions BMBPT au premier et au deuxième ordre, amplitudes de cluster pour la théorie du cluster couplé de Bogolioubov, contributions BMBPT dans le cas d'un état de référence déterminant de Slater, et enfin description détaillée des routines composant le programme ADG.

Le formalisme de la théorie de perturbation à N corps de Bogolioubov étant maintenant solidement établi, et son implémentation numérique ayant été couronnée de succès, l'objectif est d'étendre BMBPT dans plusieurs directions dans un futur proche. La première étape est de mettre en place la contrainte sur le nombre de particules, non implémentée pour le moment, ce qui nécessite une évaluation itérative des équations Hartree-Fock-Bogolioubov, de la mise en ordre normal des opérateurs ainsi que des corrections perturbatives. Une étude détaillée sur ce sujet, ainsi qu'une analyse de la sensibilité des résultats numériques à des changements de paramètres de l'espace de modélisation ainsi que de la transformation de l'Hamiltonien sous le groupe de remormalisation de similarité seront au coeur d'une prochaine publication. L'étape suivante consistera en la réalisation de calcul haute précision au troisième ordre des perturbations, ce qui permettra également de vérifier les propriétés de convergence de BMBPT. Il sera également intéressant de tester des états de référence de Bogolioubov qui ne sont pas

optimisés pour la résolution des équations HFB, ce qui impliquera la résolution des diagrammes dits non-canoniques. Alors que la première application était limitée aux propriétés de l'état fondamental, le formalisme est actuellement en cours d'extension vers de nouvelles observables, telles que les rayons de charge, les énergies d'excitations basses ainsi que les transitions électromagnétiques. Étant donnée notre capacité à générer et évaluer automatiquement des diagrammes BMBPT pour des opérateurs à trois corps, il sera également intéressant de vérifier la validité de l'approximation à deux corps en ordre normal de l'interaction nucléaire à trois corps.

Au-delà, notre objectif à moyen terme est d'implémenter la théorie de perturbation à N corps de Bogolioubov avec restauration du nombre de particules (PNP-BMBPT), ce qui nécessitera un développement complet du formalisme ainsi qu'une extension conséquente du programme ADG. PNP-BMBPT pourra être employée pour l'étude des contaminations liées à la brisure de symétrie pour différents systèmes et observables. En parallèle, l'extension non-perturbative de BMBPT sous la forme de la théorie du cluster connecté de Bogolioubov sera implémentée afin de pouvoir obtenir des résultats réalistes. Là encore, ADG devrait s'avérer être un outil particulièrement important. Sur le long terme, il sera important d'implémenter une théorie de perturbation à N corps qui brise et restaure à la fois les symétries $U(1)$ et $SU(2)$ afin de pouvoir étudier les noyaux à double couche ouverte. Par ailleurs, en parallèle de son extension à PNP-BMBPT, ADG devrait être étendu pour développer les fonctions auto-cohérentes de Green-Gorkov au niveau de troncature $ADC(3)$.

Figures and Tables

List of Figures

List of Tables

Bibliography

[1] N. Ishii, S. Aoki, and T. Hatsuda, "The Nuclear Force from Lattice QCD," *Phys. Rev. Lett.* **99** (2007) 022001, arXiv:nucl-th/0611096 [nucl-th]. 1

[2] **HAL QCD** Collaboration, S. Aoki, T. Doi, T. Hatsuda, Y. Ikeda, T. Inoue, N. Ishii, K. Murano, H. Nemura, and K. Sasaki, "Lattice QCD approach to Nuclear Physics," *PTEP* **2012** (2012) 01A105, arXiv:1206.5088 [hep-lat]. 1

[3] U. van Kolck, "Few-Nucleon Systems in a Quirky World: Lattice Nuclei in Effective Field Theory," *Few Body Syst.* **56** no. 11-12, (2015) 745–752, arXiv:1505.06323 [nucl-th]. 1

[4] H. Witala, W. Gloeckle, D. Huber, J. Golak, and H. Kamada, "The Cross-section minima in elastic Nd scattering: A 'Smoking gun' for three nucleon force effects," *Phys. Rev. Lett.* **81** (1998) 1183–1186, arXiv:nucl-th/9801018 [nucl-th]. 1

[5] S. Nemoto, K. Chmielewski, S. Oryu, and P. U. Sauer, "Discrepancy in the cross section minimum of elastic nucleon-deuteron scattering," *Phys. Rev. C* **58** (1998) 2599–2602. 1

[6] S. Kistryn *et al.*, "Systematic study of three-nucleon force effects in the cross section of the deuteron-proton breakup at 130-MeV," *Phys. Rev. C* **72** (2005) 044006, arXiv:nucl-ex/0508012 [nucl-ex]. 1

[7] A. Nogga, H. Kamada, and W. Gloeckle, "Modern nuclear force predictions for the alpha particle," *Phys. Rev. Lett.* **85** (2000) 944–947, arXiv:nucl-th/0004023 [nucl-th]. 1

[8] A. Nogga, S. K. Bogner, and A. Schwenk, "Low-momentum interaction in few-nucleon systems," *Phys. Rev. C* **70** (2004) 061002, arXiv:nucl-th/0405016 [nucl-th]. 1

[9] A. Faessler, S. Krewald, and G. J. Wagner, "Is there evidence of three-body forces from violation of the Koltun energy sum rule?," *Phys. Rev. C* **11** (1975) 2069–2072. 1

[10] J. Fujita and H. Miyazawa, "Pion Theory of Three-Body Forces," *Prog. Theor. Phys.* **17** (1957) 360–365. 1

[11] B. A. Loiseau and Y. Nogami, "Three-nucleon force," *Nucl. Phys. B* **2** (1967) 470–478. 1

[12] W. Zuo, I. Bombaci, and U. Lombardo, "Asymmetric nuclear matter from extended Brueckner-Hartree-Fock approach," *Phys. Rev. C* **60** (1999) 024605, arXiv:nucl-th/0102035 [nucl-th]. 1

[13] A. Lejeune, U. Lombardo, and W. Zuo, "Nuclear matter EOS with a three-body force," *Phys. Lett. B* **477** (2000) 45, arXiv:nucl-th/0102038 [nucl-th]. 1

[14] W. Zuo, A. Lejeune, U. Lombardo, and J. F. Mathiot, "Interplay of three-body interactions in the EOS of nuclear matter," *Nucl. Phys. A* **706** (2002) 418–430, arXiv:nucl-th/0202076 [nucl-th]. 1

[15] W. Zuo, A. Lejeune, U. Lombardo, and J. F. Mathiot, "Microscopic three-body force for asymmetric nuclear matter," *Eur. Phys. J. A* **14** (2002) 469–475, arXiv:nucl-th/0202077 [nucl-th]. 1

[16] F. Coester, S. Cohen, B. Day, and C. M. Vincent, "Variation in Nuclear-Matter Binding Energies with Phase-Shift-Equivalent Two-Body Potentials," *Phys. Rev. C* **1** (1970) 769–776. 1

[17] R. Brockmann and R. Machleidt, "Relativistic nuclear structure. 1: Nuclear matter," *Phys. Rev. C* **42** (1990) 1965–1980. 1

[18] H. Muther, R. Machleidt, and R. Brockmann, "Relativistic nuclear structure. 2: Finite nuclei," *Phys. Rev. C* **42** (1990) 1981–1988. 1

[19] G. Audi, F. G. Kondev, M. Wang, W. J. Huang, and S. Naimi, "The NUBASE2016 evaluation of nuclear properties," *Chin. Phys. C* **41** no. 3, (2017) 030001. 1

[20] O. Sorlin and M. G. Porquet, "Nuclear magic numbers: New features far from stability," *Prog. Part. Nucl. Phys.* **61** (2008) 602–673, arXiv:0805.2561 [nucl-ex]. 2

[21] I. Tanihata, H. Hamagaki, O. Hashimoto, Y. Shida, N. Yoshikawa, K. Sugimoto, O. Yamakawa, T. Kobayashi, and N. Takahashi, "Measurements of Interaction Cross-Sections and Nuclear Radii in the Light p Shell Region," *Phys. Rev. Lett.* **55** (1985) 2676–2679. 2

[22] I. Tanihata *et al.*, "Measurements of Interaction Cross-Sections and Radii of He Isotopes," *Phys. Lett. B* **160** (1985) 380–384. 2

[23] M. Fukuda *et al.*, "Neutron halo in 11 Be studied via reaction cross sections," *Phys. Lett. B* **268** (1991) 339–344. 2

[24] P. G. Hansen and B. Jonson, "The Neutron halo of extremely neutron-rich nuclei," *Europhys. Lett.* **4** (1987) 409–414. 2

[25] A. S. Jensen, K. Riisager, D. V. Fedorov, and E. Garrido, "Structure and reactions of quantum halos," *Rev. Mod. Phys.* **76** (2004) 215–261. 2

[26] B. Blank and M. Ploszajczak, "Two-proton radioactivity," *Rept. Prog. Phys.* **71** (2008) 046301, arXiv:0709.3797 [nucl-ex]. 2

[27] K. Blaum, "High-accuracy mass spectrometry with stored ions," *Phys. Rept.* **425** no. 1, (2006) 1 – 78. 2

[28] B. Schlitt, K. Beckert, T. Beha, H. Eickhoff, B. Franzke, H. Geissel, H. Irnich, H. C. Jung, T. F. Kerscher, O. Klepper, K. E. G. Löbner, G. Münzenberg, F. Nolden, Y. Novikov, T. Radon, H. Reich, A. Schwinn, M. Steck, K. Sümmerer, T. Winkler, and H. Wollnik, "Schottky mass spectrometry at the heavy ion storage ring ESR," *Hyperfine Interactions* **99** no. 1, (1996) 117–125. 2

[29] M. Wang, G. Audi, B. Pfeiffer, and F. G. Kondev, "The atomic mass evaluation: Present and future," *J. Phys. Conf. Ser.* **312** (2011) 092064. 2

[30] N. Paul *et al.*, "Are There Signatures of Harmonic Oscillator Shells Far from Stability? First Spectroscopy of ^{110}Zr," *Phys. Rev. Lett.* **118** no. 3, (2017) 032501. 2

[31] H. Frisk, "Systematics of rotational bands with K=0 in odd-odd nuclei," *Z. Phys. A* **330** no. 3, (1988) 241–248. 2

[32] M. Ionescu-Bujor *et al.*, "Shape coexistence in neutron-deficient Pb nuclei probed by quadrupole moment measurements," *Phys. Lett. B* **650** (2007) 141–147. 2

[33] K. Heyde and J. L. Wood, "Shape coexistence in atomic nuclei," *Rev. Mod. Phys.* **83** (2011) 1467–1521. 2

[34] K. H. Schmidt *et al.*, "Relativistic radioactive beams: A New access to nuclear fission studies," *Nucl. Phys. A* **665** (2000) 221–267. 2

[35] M. A. Caprio, "Structure of collective modes in transitional and deformed nuclei," `arXiv:nucl-ex/0502004 [nucl-ex]`. 2

[36] D. Ackermann, "Superheavy elements at GSI - present and future," *Nucl. Phys. A* **787** (2007) 353–362. 2

[37] G. Royer and G. Gautier, "Coefficients and terms of the liquid drop model and mass formula," *Phys. Rev. C* **73** (2006) 067302, `arXiv:nucl-th/0608064 [nucl-th]`. 2

[38] J. L. Friar, G. L. Payne, V. G. J. Stoks, and J. J. de Swart, "Triton calculations with the new Nijmegen potentials," *Phys. Lett. B* **311** (1993) 4, `arXiv:nucl-th/9307010 [nucl-th]`. 3

[39] W. Glöckle and H. Kamada, "Alpha-particle binding energies for realistic nucleon-nucleon interactions," *Phys. Rev. Lett.* **71** (1993) 971–974. 3

[40] A. Nogga, D. Huber, H. Kamada, and W. Gloeckle, "Benchmark calculations for the triton binding energy for modern N N forces and the pi pi exchange three nucleon force," *Phys. Lett. B* **409** (1997) 19–25, `arXiv:nucl-th/9704001 [nucl-th]`. 3

[41] B. S. Pudliner, V. R. Pandharipande, J. Carlson, S. C. Pieper, and R. B. Wiringa, "Quantum Monte Carlo calculations of nuclei with A <= 7," *Phys. Rev. C* **56** (1997) 1720–1750, `arXiv:nucl-th/9705009 [nucl-th]`. 3

[42] R. B. Wiringa, "Quantum Monte Carlo calculations for light nuclei," *Nucl. Phys. A* **631** (1998) 70–90. 3

[43] R. B. Wiringa, S. C. Pieper, J. Carlson, and V. R. Pandharipande, "Quantum Monte Carlo calculations of A = 8 nuclei," *Phys. Rev. C* **62** (2000) 014001, arXiv:nucl-th/0002022 [nucl-th]. 3

[44] P. Navratil and B. R. Barrett, "Shell model calculations for the three nucleon system," *Phys. Rev. C* **57** (1998) 562–568, arXiv:nucl-th/9711027 [nucl-th]. 3

[45] P. Navratil and B. R. Barrett, "Large basis shell model calculations for p shell nuclei," *Phys. Rev. C* **57** (1998) 3119–3128, arXiv:nucl-th/9804014 [nucl-th]. 3

[46] P. Navratil, G. P. Kamuntavicius, and B. R. Barrett, "Few nucleon systems in translationally invariant harmonic oscillator basis," *Phys. Rev. C* **61** (2000) 044001, arXiv:nucl-th/9907054 [nucl-th]. 3

[47] S. Quaglioni and P. Navratil, "Ab initio no-core shell model and microscopic reactions: Recent achievements," *Few Body Syst.* **44** (2008) 337–339, arXiv:0712.0855 [nucl-th]. 3

[48] P. Navratil, S. Quaglioni, I. Stetcu, and B. R. Barrett, "Recent developments in no-core shell-model calculations," *J. Phys. G* **36** (2009) 083101, arXiv:0904.0463 [nucl-th]. 3, 4

[49] K. Kowalski, D. J. Dean, M. Hjorth-Jensen, T. Papenbrock, and P. Piecuch, "Coupled cluster calculations of ground and excited states of nuclei," *Phys. Rev. Lett.* **92** (2004) 132501, arXiv:nucl-th/0310082 [nucl-th]. 3, 113

[50] R. J. Bartlett and M. Musial, "Coupled-cluster theory in quantum chemistry," *Rev. Mod. Phys.* **79** (2007) 291–352. 3, 113

[51] G. Hagen, T. Papenbrock, D. J. Dean, and M. Hjorth-Jensen, "Ab initio coupled-cluster approach to nuclear structure with modern nucleon-nucleon interactions," *Phys. Rev. C* **82** (2010) 034330, arXiv:1005.2627 [nucl-th]. 3, 113

[52] P. Piecuch, J. R. Gour, and M. Włoch, "Left-eigenstate completely renormalized equation-of-motion coupled-cluster methods: Review of key concepts, extension to excited states of open-shell systems, and comparison with electron-attached and ionized approaches," *Int. J. Quantum Chem.* **109** no. 14, (2009) 3268–3304. 3, 113

[53] S. Binder, J. Langhammer, A. Calci, and R. Roth, "Ab Initio Path to Heavy Nuclei," *Phys. Lett. B* **736** (2014) 119–123, arXiv:1312.5685 [nucl-th]. 3, 6, 107, 108, 109, 113

[54] W. H. Dickhoff and C. Barbieri, "Selfconsistent Green's function method for nuclei and nuclear matter," *Prog. Part. Nucl. Phys.* **52** (2004) 377–496, arXiv:nucl-th/0402034 [nucl-th]. 3, 4, 113

[55] A. Cipollone, C. Barbieri, and P. Navrátil, "Chiral three-nucleon forces and the evolution of correlations along the oxygen isotopic chain," *Phys. Rev. C* **92** no. 1, (2015) 014306, arXiv:1412.0491 [nucl-th]. 3, 4, 113

[56] A. Carbone, A. Cipollone, C. Barbieri, A. Rios, and A. Polls, "Self-consistent Green's functions formalism with three-body interactions," *Phys. Rev. C* **88** no. 5, (2013) 054326, arXiv:1310.3688 [nucl-th]. 3, 4, 30, 113

[57] K. Tsukiyama, S. K. Bogner, and A. Schwenk, "In-Medium Similarity Renormalization Group for Nuclei," *Phys. Rev. Lett.* **106** (2011) 222502, arXiv:1006.3639 [nucl-th]. 3, 4, 109, 113

[58] H. Hergert, S. K. Bogner, S. Binder, A. Calci, J. Langhammer, R. Roth, and A. Schwenk, "In-medium similarity renormalization group with chiral two- plus three-nucleon interactions," *Phys. Rev. C* **87** no. 3, (2013) 034307. 3, 4, 113

[59] T. D. Morris, N. Parzuchowski, and S. K. Bogner, "Magnus expansion and in-medium similarity renormalization group," *Phys. Rev. C* **92** no. 3, (2015) 034331. 3, 4

[60] H. Hergert, S. K. Bogner, T. D. Morris, A. Schwenk, and K. Tsukiyama, "The In-Medium Similarity Renormalization Group: A Novel Ab Initio Method for Nuclei," *Phys. Rept.* **621** (2016) 165–222, arXiv:1512.06956 [nucl-th]. 3, 4, 6, 109, 113

[61] I. Shavitt and R. J. Bartlett, *Many-Body Methods in Chemistry and Physics: MBPT and Coupled-Cluster Theory*. Cambridge Molecular Science. Cambridge University Press, 2009. 3, 7, 52, 54, 62, 65, 66, 67, 93, 96, 113, 157

[62] K. A. Brueckner, "Many-Body Problem for Strongly Interacting Particles. 2. Linked Cluster Expansion," *Phys. Rev.* **100** (1955) 36–45. 3

[63] J. Hubbard, "The description of collective motions in terms of many-body perturbation theory," *Proc. Roy. Soc. A* **240** no. 1223, (1957) 539–560. 3

[64] F. Coester, "Bound states of a many-particle system," *Nucl. Phys.* **7** (1958) 421 – 424. 3

[65] F. Coester and H. Kümmel, "Short-range correlations in nuclear wave functions," *Nucl. Phys.* **17** (1960) 477 – 485. 3

[66] J. Čížek, "On the Correlation Problem in Atomic and Molecular Systems. Calculation of Wavefunction Components in Ursell-Type Expansion Using Quantum-Field Theoretical Methods," *J. Chem. Phys.* **45** no. 11, (1966) 4256–4266. 3

[67] J. Čížek, "On the Use of the Cluster Expansion and the Technique of Diagrams in Calculations of Correlation Effects in Atoms and Molecules," vol. 14 of *Advances in Chemical Physics*, ch. 2, pp. 35–89. Wiley-Blackwell, 1969. 3

[68] D. Mukherjee and S. Pal, "Use of Cluster Expansion Methods in the Open-Shell Correlation Problem," vol. 20 of *Advances in Quantum Chemistry*, pp. 291 – 373. Academic Press, 1989. 4, 6

[69] B. Jeziorski and J. Paldus, "Spin-adapted multireference coupled-cluster approach: Linear approximation for two closed-shell-type reference configurations," *J. Chem. Phys.* **88** no. 9, (1988) 5673–5687. 4, 6

[70] X. Li and J. Paldus, "Reduced multireference CCSD method: An effective approach to quasidegenerate states," *J. Chem. Phys.* **107** no. 16, (1997) 6257–6269. 4

[71] J. Paldus and X. Li, *A Critical Assessment of Coupled Cluster Method in Quantum Chemistry*, ch. 1, pp. 1–175. Wiley-Blackwell, 1999. 4

[72] M. Musiał, A. Perera, and R. J. Bartlett, "Multireference coupled-cluster theory: The easy way," *J. Chem. Phys.* **134** no. 11, (2011) 114108. 4, 6

[73] B. Adams, K. Jankowski, and J. Paldus, "Quasi-degeneracy and coupled-pair theories," *Chem. Phys. Lett.* **67** no. 1, (1979) 144 – 148. 4

[74] B. G. Adams and J. Paldus, "Symmetry-adapted coupled-pair approach to the many-electron correlation problem. i. LS-adapted theory for closed-shell atoms," *Phys. Rev. A* **24** (Nov, 1981) 2302–2315. 4

[75] B. G. Adams, K. Jankowski, and J. Paldus, "Symmetry-adapted coupled-pair approach to the many-electron correlation problem. iii. approximate coupled-pair approaches for the be atom," *Phys. Rev. A* **24** (Nov, 1981) 2330–2338. 4

[76] T. Duguet, "Symmetry broken and restored coupled-cluster theory: I. Rotational symmetry and angular momentum," *J. Phys. G* **42** no. 2, (2015) 025107, arXiv:1406.7183 [nucl-th]. 4, 6, 7, 8, 43, 113, 114

[77] T. Duguet and A. Signoracci, "Symmetry broken and restored coupled-cluster theory. II. Global gauge symmetry and particle number," *J. Phys. G* **44** no. 1, (2017) 015103, arXiv:1512.02878 [nucl-th]. 4, 6, 7, 8, 16, 46, 54, 108, 113, 114

[78] A. Signoracci, T. Duguet, G. Hagen, and G. Jansen, "Ab initio Bogoliubov coupled cluster theory for open-shell nuclei," *Phys. Rev. C* **91** no. 6, (2015) 064320, arXiv:1412.2696 [nucl-th]. 4, 6, 20, 54, 110, 113

[79] Y. Qiu, T. M. Henderson, J. Zhao, and G. E. Scuseria, "Projected coupled cluster theory," *J. Chem. Phys.* **147** no. 6, (2017) 064111. 4, 6

[80] Y. Qiu, T. M. Henderson, T. Duguet, and G. E. Scuseria, "Particle-number projected Bogoliubov coupled cluster theory. Application to the pairing Hamiltonian," arXiv:1810.11245 [nucl-th]. 4

[81] S. K. Bogner, R. J. Furnstahl, and R. J. Perry, "Similarity renormalization group for nucleon-nucleon interactions," *Phys. Rev. C* **75** (2007) 061001. 4, 106

[82] H. Hergert and R. Roth, "The Unitary correlation operator method from a similarity renormalization group perspective," *Phys. Rev. C* **75** (2007) 051001, arXiv:nucl-th/0703006 [nucl-th]. 4, 106

[83] R. Roth, S. Reinhardt, and H. Hergert, "Unitary Correlation Operator Method and Similarity Renormalization Group: Connections and Differences," *Phys. Rev. C* **77** (2008) 064003, arXiv:0802.4239 [nucl-th]. 4, 106

[84] S. K. Bogner, R. J. Furnstahl, and A. Schwenk, "From low-momentum interactions to nuclear structure," *Prog. Part. Nucl. Phys.* **65** (2010) 94–147, arXiv:0912.3688 [nucl-th]. 4, 106

[85] R. Roth, J. Langhammer, A. Calci, S. Binder, and P. Navratil, "Similarity-Transformed Chiral NN+3N Interactions for the Ab Initio Description of 12-C and 16-O," *Phys. Rev. Lett.* **107** (2011) 072501, arXiv:1105.3173 [nucl-th]. 4, 106

[86] E. D. Jurgenson, P. Maris, R. J. Furnstahl, P. Navratil, W. E. Ormand, and J. P. Vary, "Structure of p-shell nuclei using three-nucleon interactions evolved with the similarity renormalization group," *Phys. Rev. C* **87** no. 5, (2013) 054312, arXiv:1302.5473 [nucl-th]. 4, 106

[87] R. J. Furnstahl and K. Hebeler, "New applications of renormalization group methods in nuclear physics," *Rept. Prog. Phys.* **76** (2013) 126301, arXiv:1305.3800 [nucl-th]. 4, 106

[88] H. Hergert, "In-Medium Similarity Renormalization Group for Closed and Open-Shell Nuclei," *Phys. Scripta* **92** no. 2, (2017) 023002, arXiv:1607.06882 [nucl-th]. 4, 6, 108, 109

[89] H. Hergert, S. Binder, A. Calci, J. Langhammer, and R. Roth, "Ab Initio Calculations of Even Oxygen Isotopes with Chiral Two-Plus-Three-Nucleon Interactions," *Phys. Rev. Lett.* **110** no. 24, (2013) 242501, arXiv:1302.7294 [nucl-th]. 4, 6

[90] H. Hergert, S. K. Bogner, T. D. Morris, S. Binder, A. Calci, J. Langhammer, and R. Roth, "Ab initio multireference in-medium similarity renormalization group calculations of even calcium and nickel isotopes," *Phys. Rev. C* **90** no. 4, (2014) 041302, arXiv:1408.6555 [nucl-th]. 4

[91] B. R. Barrett, P. Navratil, and J. P. Vary, "Ab initio no core shell model," *Prog. Part. Nucl. Phys.* **69** (2013) 131–181. 4

[92] E. Gebrerufael, K. Vobig, H. Hergert, and R. Roth, "Ab Initio Description of Open-Shell Nuclei: Merging No-Core Shell Model and In-Medium Similarity Renormalization Group," *Phys. Rev. Lett.* **118** no. 15, (2017) 152503, arXiv:1610.05254 [nucl-th]. 4

[93] H. Hergert, J. Yao, T. D. Morris, N. M. Parzuchowski, S. K. Bogner, and J. Engel, "Nuclear Structure from the In-Medium Similarity Renormalization Group," in *Proceedings, 19th International Conference on Recent Progress in Many-Body Theories (RPMBT19): Pohang, Korea, June 25-30, 2017*, vol. 1041, p. 012007. 2018. arXiv:1805.09221 [nucl-th]. 4, 5, 108, 157

[94] C. Barbieri and A. Carbone, "Self-consistent Green's function approaches," *Lect. Notes Phys.* **936** (2017) 571–644, arXiv:1611.03923 [nucl-th]. 4, 5, 157

[95] V. Somà, T. Duguet, and C. Barbieri, "Ab-initio self-consistent Gorkov-Green's function calculations of semi-magic nuclei. I. Formalism at second order with a two-nucleon

interaction," *Phys. Rev. C* **84** (2011) 064317, arXiv:1109.6230 [nucl-th]. 5, 6, 8, 29, 109, 113

[96] V. Somà, A. Cipollone, C. Barbieri, P. Navrátil, and T. Duguet, "Chiral two- and three-nucleon forces along medium-mass isotope chains," *Phys. Rev. C* **89** no. 6, (2014) 061301, arXiv:1312.2068 [nucl-th]. 5, 6, 113

[97] M. Rosenbusch *et al.*, "Probing the N = 32 shell closure below the magic proton number Z = 20: Mass measurements of the exotic isotopes 52,53K," *Phys. Rev. Lett.* **114** (2015) 202501, arXiv:1506.00520 [nucl-ex]. 5

[98] T. Duguet, V. Somà, S. Lecluse, C. Barbieri, and P. Navrátil, "Ab initio calculation of the potential bubble nucleus ^{34}si," *Phys. Rev. C* **95** (2017) 034319, arXiv:1611.08570 [nucl-th]. 5

[99] V. Lapoux, V. Somà, C. Barbieri, H. Hergert, J. D. Holt, and S. Stroberg, "Radii and Binding Energies in Oxygen Isotopes: A Challenge for Nuclear Forces," *Phys. Rev. Lett.* **117** no. 5, (2016) 052501, arXiv:1605.07885 [nucl-ex]. 5

[100] **IS484** Collaboration, J. Papuga *et al.*, "Shell structure of potassium isotopes deduced from their magnetic moments," *Phys. Rev. C* **90** no. 3, (2014) 034321, arXiv:1410.0895 [nucl-ex]. 5

[101] T. Duguet, H. Hergert, J. D. Holt, and V. Somà, "Nonobservable nature of the nuclear shell structure: Meaning, illustrations, and consequences," *Phys. Rev. C* **92** (2015) 034313. 5

[102] E. Caurier, G. Martinez-Pinedo, F. Nowacki, A. Poves, and A. P. Zuker, "The Shell model as unified view of nuclear structure," *Rev. Mod. Phys.* **77** (2005) 427–488, arXiv:nucl-th/0402046 [nucl-th]. 5

[103] D. J. Dean, T. Engeland, M. Hjorth-Jensen, M. Kartamyshev, and E. Osnes, "Effective interactions and the nuclear shell-model," *Prog. Part. Nucl. Phys.* **53** (2004) 419–500, arXiv:nucl-th/0405034 [nucl-th]. 5

[104] A. Tichai, E. Gebrerufael, and R. Roth, "Open-Shell Nuclei from No-Core Shell Model with Perturbative Improvement," *Phys. Lett. B* **786** (2018) 448–452, arXiv:1703.05664 [nucl-th]. 6, 7, 107, 109, 113

[105] S. K. Bogner, H. Hergert, J. D. Holt, A. Schwenk, S. Binder, A. Calci, J. Langhammer, and R. Roth, "Nonperturbative shell-model interactions from the in-medium similarity renormalization group," *Phys. Rev. Lett.* **113** (2014) 142501, arXiv:1402.1407 [nucl-th]. 6

[106] G. R. Jansen, J. Engel, G. Hagen, P. Navratil, and A. Signoracci, "Ab-initio coupled-cluster effective interactions for the shell model: Application to neutron-rich oxygen and carbon isotopes," *Phys. Rev. Lett.* **113** no. 14, (2014) 142502, arXiv:1402.2563 [nucl-th]. 6

[107] G. R. Jansen, A. Signoracci, G. Hagen, and P. Navrátil, "Open *sd*-shell nuclei from first principles," *Phys. Rev. C* **94** no. 1, (2016) 011301, arXiv:1511.00757 [nucl-th]. 6

[108] Q. Wu, F. R. Xu, B. S. Hu, and J. G. Li, "*Ab initio* perturbation calculations of realistic effective interactions in the Hartree-Fock basis," arXiv:1806.09165 [nucl-th]. 6, 7

[109] P. Ring and P. Schuck, *The Nuclear Many-Body Problem*. Springer-Verlag, New-York, 1980. 6, 13, 15, 30, 31

[110] M. Bender, P.-H. Heenen, and P.-G. Reinhard, "Self-consistent mean-field models for nuclear structure," *Rev. Mod. Phys.* **75** (2003) 121–180. 6

[111] T. Duguet and J. Sadoudi, "Breaking and restoring symmetries within the nuclear energy density functional method," *J. Phys. G* **37** (2010) 064009, arXiv:1001.0673 [nucl-th]. 6

[112] T. Duguet, "The nuclear energy density functional formalism," *Lect. Notes Phys.* **879** (2014) 293–350, arXiv:1309.0440 [nucl-th]. 6, 19

[113] V. Somà, C. Barbieri, and T. Duguet, "Ab-initio Gorkov-Green's function calculations of open-shell nuclei," *Phys. Rev. C* **87** no. 1, (2013) 011303, arXiv:1208.2472 [nucl-th]. 6

[114] J. Goldstone, "Derivation of the Brueckner many-body theory," *Proc. Roy. Soc. A* **239** no. 1217, (1957) 267–279. 7, 43, 113

[115] N. Hugenholtz, "Perturbation theory of large quantum systems," *Physica* **23** no. 1, (1957) 481 – 532. 7, 113

[116] A. Tichai, J. Langhammer, S. Binder, and R. Roth, "Hartree-Fock Many-Body Perturbation Theory for Nuclear Ground-States," *Phys. Lett. B* **756** (2016) 283 – 288, arXiv:1601.03703 [nucl-th]. 7, 106, 107, 113

[117] B. Hu, F. Xu, Z. Sun, J. P. Vary, and T. Li, "*Ab initio* nuclear many-body perturbation calculations in the Hartree-Fock basis," *Phys. Rev. C* **94** no. 1, (2016) 014303, arXiv:1604.07146 [nucl-th]. 7, 113

[118] G. C. Wick, "The Evaluation of the Collision Matrix," *Phys. Rev.* **80** (1950) 268–272. 8, 20, 34

[119] J. Paldus and H. Wong, "Computer generation of Feynman diagrams for perturbation theory I. General algorithm," *Comput. Phys. Comm.* **6** no. 1, (1973) 1 – 7. 8, 69

[120] H. Wong and J. Paldus, "Computer generation of Feynman diagrams for perturbation theory II. Program description," *Comput. Phys. Comm.* **6** no. 1, (1973) 9 – 16. 8, 69

[121] U. Kaldor, "An algorithm for generating Goldstone and Bloch-Brandow diagrams," *J. Comput. Phys.* **20** no. 4, (1976) 432 – 441. 8, 69

[122] Z. Csépes and J. Pipek, "An effective recursive algorithm for generating many-body Hugenholtz and Goldstone diagrams," *J. Comput. Phys.* **77** no. 1, (1988) 1 – 17. 8, 69

[123] J. Lyons, D. Moncrieff, and S. Wilson, "Diagrammatic many body perturbation expansion for atoms and molecules: Automatic generation & analysis of 5th order Hugenholtz energy diagrams," *Comput. Phys. Comm.* **84** (1994) 91–101. 8, 69

[124] P. D. Stevenson, "Automatic Generation of Vacuum Amplitude Many-Body Perturbation Series," *Int. J. Mod. Phys. C* **14** no. 8, (2003) 1135–1141. 8, 69

[125] M. Kállay and P. R. Surján, "Higher excitations in coupled-cluster theory," *J. Chem. Phys.* **115** no. 7, (2001) 2945–2954. 8, 69

[126] M. Kállay, P. G. Szalay, and P. R. Surján, "A general state-selective multireference coupled-cluster algorithm," *J. Chem. Phys.* **117** no. 3, (2002) 980–990. 8, 69

[127] P. Arthuis, A. Tichai, and T. Duguet, "Bogoliubov Many-Body Perturbation Theory formalism," *in prep.* . 8, 16, 46, 107, 113

[128] D. J. Thouless, "Perturbation theory in statistical mechanics and the theory of superconductivity," *Annals of Physics* **10** no. 4, (1960) 553 – 588. 14, 30

[129] M. Bender, T. Duguet, and D. Lacroix, "Particle-Number Restoration within the Energy Density Functional Formalism," *Phys. Rev. C* **79** (2009) 044319, arXiv:0809.2045 [nucl-th]. 19

[130] R. Roth, S. Binder, K. Vobig, A. Calci, J. Langhammer, and P. Navratil, "Ab Initio Calculations of Medium-Mass Nuclei with Normal-Ordered Chiral NN+3N Interactions," *Phys. Rev. Lett.* **109** (2012) 052501, arXiv:1112.0287 [nucl-th]. 27, 106

[131] S. Binder, J. Langhammer, A. Calci, P. Navratil, and R. Roth, "*AbInitio* calculations of medium-mass nuclei with explicit chiral $3N$ interactions," *Phys. Rev. C* **87** no. 2, (2013) 021303, arXiv:1211.4748 [nucl-th]. 27, 106, 109

[132] V. Rotival and T. Duguet, "New analysis method of the halo phenomenon in finite many-fermion systems. First applications to medium-mass atomic nuclei," *Phys. Rev. C* **79** (2009) 054308, arXiv:nucl-th/0702050 [nucl-th]. 29

[133] N. C. Handy, J. A. Pople, M. Head-Gordon, K. Raghavachari, and G. W. Trucks, "Size-consistent Brueckner theory limited to double substitutions," *Chem. Phys. Lett.* **164** no. 2, (1989) 185 – 192. 30

[134] J. Dobaczewski, H. Flocard, and J. Treiner, "Hartree-Fock-Bogolyubov descriptions of nuclei near the neutrino dripline," *Nucl. Phys. A* **422** (1984) 103–139. 31

[135] C. Bloch, "Sur la détermination de l'état fondamental d'un système de particules," *Nucl. Phys.* **7** (1958) 451 – 458. 42

[136] K. Van Houcke, F. Werner, E. Kozik, N. Prokofev, B. Svistunov, M. Ku, A. Sommer, L. W. Cheuk, A. Schirotzek, and M. W. Zwierlein, "Feynman diagrams versus Fermi-gas Feynman emulator," *Nature Phys.* **8** (2012) 366, arXiv:1110.3747 [cond-mat.quant-gas]. 69

[137] K. Van Houcke, F. Werner, N. Prokof'ev, and B. Svistunov, "Bold diagrammatic Monte Carlo for the resonant Fermi gas," arXiv:1305.3901 [cond-mat.quant-gas]. 69

[138] A. Tichai, P. Arthuis, T. Duguet, H. Hergert, V. Somá, and R. Roth, "Bogoliubov Many-Body Perturbation Theory for Open-ShellNuclei," *Phys. Lett. B* **786** (2018) 195–200, arXiv:1806.10931 [nucl-th]. 70, 105, 114

[139] T. Ohl, "Drawing Feynman diagrams with Latex and Metafont," *Comput. Phys. Comm.* **90** (1995) 340–354, arXiv:hep-ph/9505351 [hep-ph]. 75

[140] A. A. Hagberg, D. A. Schult, and P. J. Swart, "Exploring Network Structure, Dynamics, and Function using NetworkX," in *Proceedings of the 7th Python in Science Conference*, G. Varoquaux, T. Vaught, and J. Millman, eds., pp. 11 – 15. Pasadena, CA USA, 2008. 75

[141] S. Weinberg, "Nuclear forces from chiral Lagrangians," *Phys. Lett. B* **251** no. 2, (1990) 288 – 292. 105, 113

[142] S. Weinberg, "Effective chiral lagrangians for nucleon-pion interactions and nuclear forces," *Nucl. Phys. B* **363** no. 1, (1991) 3 – 18. 105, 113

[143] E. Epelbaum, H.-W. Hammer, and U.-G. Meißner, "Modern Theory of Nuclear Forces," *Rev.Mod.Phys.* **81** (2008) 1773–1825, 0811.1338. 105, 113

[144] U.-G. Meißner, "The long and winding road from chiral effective Lagrangians to nuclear structure," *Phys. Scripta* **91** no. 3, (2016) 033005, arXiv:1510.03230 [nucl-th]. 105, 113

[145] E. Epelbaum, "Nuclear Chiral EFT in the Precision Era," in *8th International Workshop on Chiral Dynamics (CD 2015) Pisa, Italy, June 29-July 3, 2015*. 2015. arXiv:1510.07036 [nucl-th]. 105, 113

[146] S. Weinberg, "Phenomenological Lagrangians," *Physica A* **96** no. 1–2, (1979) 327 – 340. 106

[147] P. Navratil, "Local three-nucleon interaction from chiral effective field theory," *Few Body Syst.* **41** (2007) 117–140, arXiv:0707.4680 [nucl-th]. 106

[148] D. R. Entem and R. Machleidt, "Accurate charge dependent nucleon nucleon potential at fourth order of chiral perturbation theory," *Phys. Rev. C* **68** (2003) 041001, arXiv:nucl-th/0304018 [nucl-th]. 106

[149] E. Epelbaum, H. Krebs, and U. G. Meißner, "Improved chiral nucleon-nucleon potential up to next-to-next-to-next-to-leading order," *Eur. Phys. J. A* **51** no. 5, (2015) 53, arXiv:1412.0142 [nucl-th]. 106

[150] D. R. Entem, N. Kaiser, R. Machleidt, and Y. Nosyk, "Peripheral nucleon-nucleon scattering at fifth order of chiral perturbation theory," *Phys. Rev. C* **91** no. 1, (2015) 014002, arXiv:1411.5335 [nucl-th]. 106

[151] D. R. Entem, N. Kaiser, R. Machleidt, and Y. Nosyk, "Dominant contributions to the nucleon-nucleon interaction at sixth order of chiral perturbation theory," *Phys. Rev. C* **92** no. 6, (2015) 064001, arXiv:1505.03562 [nucl-th]. 106

[152] D. R. Entem, R. Machleidt, and Y. Nosyk, "High-quality two-nucleon potentials up to fifth order of the chiral expansion," *Phys. Rev. C* **96** no. 2, (2017) 024004, arXiv:1703.05454 [nucl-th]. 106

[153] A. Ekström *et al.*, "Optimized Chiral Nucleon-Nucleon Interaction at Next-to-Next-to-Leading Order," *Phys. Rev. Lett.* **110** no. 19, (2013) 192502, arXiv:1303.4674 [nucl-th]. 106

[154] A. Ekström, G. R. Jansen, K. A. Wendt, G. Hagen, T. Papenbrock, B. D. Carlsson, C. Forssén, M. Hjorth-Jensen, P. Navrátil, and W. Nazarewicz, "Accurate nuclear radii and binding energies from a chiral interaction," *Phys. Rev. C* **91** no. 5, (2015) 051301, arXiv:1502.04682 [nucl-th]. 106

[155] B. D. Carlsson, A. Ekström, C. Forssén, D. F. Strömberg, G. R. Jansen, O. Lilja, M. Lindby, B. A. Mattsson, and K. A. Wendt, "Uncertainty analysis and order-by-order optimization of chiral nuclear interactions," *Phys. Rev. X* **6** no. 1, (2016) 011019, arXiv:1506.02466 [nucl-th]. 106

[156] J. Hoppe, C. Drischler, R. J. Furnstahl, K. Hebeler, and A. Schwenk, "Weinberg eigenvalues for chiral nucleon-nucleon interactions," *Phys. Rev. C* **96** no. 5, (2017) 054002, arXiv:1707.06438 [nucl-th]. 106

[157] S. D. Glazek and K. G. Wilson, "Renormalization of Hamiltonians," *Phys. Rev. D* **48** (1993) 5863–5872. 106

[158] F. Wegner, "Flow equations for Hamiltonians," *Annalen der Physik* **3** no. 77, (1994) 77–91. 106

[159] R. Roth and J. Langhammer, "Pade-resummed high-order perturbation theory for nuclear structure calculations," *Phys. Lett. B* **683** (2010) 272–277, arXiv:0910.3650 [nucl-th]. 106

[160] G. Hagen, T. Papenbrock, D. J. Dean, A. Schwenk, A. Nogga, M. Włoch, and P. Piecuch, "Coupled-cluster theory for three-body Hamiltonians," *Phys. Rev. C* **76** (2007) 034302, arXiv:0704.2854 [nucl-th]. 106

[161] S. Binder, P. Piecuch, A. Calci, J. Langhammer, P. Navrátil, and R. Roth, "Extension of coupled-cluster theory with a noniterative treatment of connected triply excited clusters to three-body Hamiltonians," *Phys. Rev. C* **88** no. 5, (2013) 054319, arXiv:1309.1123 [nucl-th]. 106, 109

[162] M. Wang, G. Audi, A. Wapstra, F. Kondev, M. MacCormick, X. Xu, and B. Pfeiffer, "The AME2012 atomic mass evaluation," *Chin. Phys. C* **36** no. 12, (2012) 1603. http://stacks.iop.org/1674-1137/36/i=12/a=003. 108, 110

[163] A. Tichai, J. Müller, K. Vobig, and R. Roth, "Natural orbitals for ab initio no-core shell modelcalculations," arXiv:1809.07571 [nucl-th]. 109

[164] J. Schirmer, L. S. Cederbaum, and O. Walter, "New approach to the one-particle Green's function for finite Fermi systems," *Phys. Rev. A* **28** (1983) 1237–1259. 109

[165] P. Piecuch and M. Włoch, "Renormalized coupled-cluster methods exploiting left eigenstates of the similarity-transformed Hamiltonian," *J. Chem. Phys.* **123** no. 22, (2005) 224105. 109

[166] P. Arthuis, T. Duguet, A. Tichai, R.-D. Lasseri, and J.-P. Ebran, "ADG: Automated generation and evaluation of many-body diagrams I. Bogoliubov many-body perturbation theory," *Comput. Phys. Comm.* (2018) , arXiv:1809.01187 [nucl-th]. 114

[167] F. Raimondi and C. Barbieri, "Algebraic diagrammatic construction formalism with three-body interactions," *Phys. Rev. C* **97** no. 5, (2018) 054308, arXiv:1709.04330 [nucl-th]. 114

[168] B. Bollobás, *Modern Graph Theory*. Springer New York, 1998. 117

[169] C. Drischler, K. Hebeler, and A. Schwenk, "Chiral interactions up to N^3LO and nuclear saturation," arXiv:1710.08220 [nucl-th]. 144

université PARIS-SACLAY | ÉCOLE DOCTORALE PHENIICS

Titre : Théorie de perturbation à N corps de Bogolioubov pour les noyaux: Génération et évaluation automatique des diagrammes et premiers calculs *ab initio*

Mots-clés : ab initio, théorie à N corps, théorie de perturbation, brisure de symétrie, outils automatisés

Résumé : Les dernières décennies ont donné lieu à un développement rapide des théories *ab initio* visant à décrire les propriétés des noyaux à partir de l'interaction nucléonique. Un tel développement a été rendu possible à la fois par la très importante croissance de la puissance de calcul et de nouveaux développements formels.
Le présent travail se consacre au développement de la théorie de perturbation à N corps de Bogoliubov récemment proposée, qui repose sur l'usage d'un état de référence brisant la symétrie associée au nombre de particules pour permettre une description des noyaux à simple couche ouverte. Le formalisme est tout d'abord décrit en détails, son lien avec la théorie de perturbation à N corps standard est établi, tout comme sa connexion avec la théorie de cluster couplés de Bogolioubov.
L'extension du formalisme à des ordres plus élevés à partir de méthodes de théorie des graphes est ensuite présentée ainsi que le programme ADG qui génère et évalue les diagrammes BMBPT à un ordre quelconque. Les implications de ce développement formel dépassent le cadre du présent travail, les techniques développées pouvant être appliquées à d'autres méthodes à N corps.
Pour terminer, de premiers résultats numériques pour les isotopes de l'oxygène, du calcium et du nickel sont présentés. Ces résultats établissent la théorie de perturbation à N corps de Bogolioubov comme une méthode de premier intérêt pour des calculs à grande échelle sur les chaînes isotopiques et isotoniques de masse moyenne.

Title: Bogoliubov Many-Body Perturbation Theory for Nuclei: Systematic Generation and Evaluation of Diagrams and First *ab initio* Calculations

Keywords: ab initio, many-body theory, perturbation theory, symmetry breaking, automated tools

Abstract: The last few decades in nuclear structure theory have seen a rapid expansion of *ab initio* theories, aiming at describing the properties of nuclei starting from the inter-nucleonic interaction. Such an expansion relied both on the tremendous growth of computing power and novel formal developments. This work focuses on the development of the recently proposed Bogoliubov Many-Body Perturbation Theory that relies on a particle-number-breaking reference state to tackle singly open-shell nuclei. The formalism is first described in details, and diagrammatic and algebraic contributions are derived up to second order. Its link to standard Many-Body Perturbation Theory is made explicit, as well as its connexion to Bogoliubov Coupled-Cluster theory.
An automated extension to higher orders based on graph theory methods is then detailed, and the ADG numerical program generating and evaluating BMBPT diagrams at arbitrary order is introduced. Such a formal development carries implications that are not restricted to the present work, as the developed techniques can be applied to other many-body methods.
Finally, first numerical results obtained for oxygen, calcium and nickel isotopes are presented. They establish BMBPT as a method of interest for large-scale computations of isotopic or isotonic chains in the mid-mass sector of the nuclear chart.

Université Paris-Saclay
Espace Technologique / Immeuble Discovery
Route de l'Orme aux Merisiers RD 128 / 91190 Saint-Aubin, France